Fabrication, Characterisation and Applications of Mid-Infrared Quantum Cascade Lasers

Longqi Zhou

Department of Electronic and Electrical Engineering

University of Sheffield

Submitted for the degree of Doctor of Philosophy

December 2022

Abstract

Quantum cascade lasers (QCLs) are unipolar semiconductor lasers based on intersubband transition, mainly operate in the mid-infrared (mid-IR), far-infrared (FIR), and terahertz (THz) region, i.e., the spectral range between ~3 and ~300 μm including the important molecular fingerprint region. In this work, a mid-IR QCL is developed with the aim of hybrid integration on the silicon platform and coupled with germanium waveguides for on-chip sensing applications.

In Chapter 1, the unique properties of QCLs and the attractive applications of mid-IR QCLs are introduced. Chapter 2 is dedicated to the theoretical basics of QCL and the description of QCL characterisation techniques. The main research works are then presented from Chapter 3 to Chapter 5.

Chapter 3 describes the development of a mid-IR QCL in our facility, starting from wafer growth by metal-organic vapour phase epitaxy (MOVPE). The laser is based on strain-compensated InGaAs/AlInAs material system on the InP substrate and adopts a two-phonon resonance active region design with an emission wavelength of ~5.7 μm. The wafers are then processed into double-trench waveguide structures specifically for hybrid integration. The finalised QCLs can operate in continuous-wave mode at room temperature (CW-RT) with over 100mW total optical power and a very low threshold current density of ~1 kA/cm^2. The nearly circular output beam profile shows a good match to the spatial mode in the Ge-on-Si waveguides.

During the development of the mid-IR QCL, we observed many spectral and spatial instabilities, such as spectrum splitting and beam steering. The fundamental mechanisms behind these unusual laser behaviours are then studied in Chapter 4. We found that the QCL

is the cradle of many interesting instabilities originating from Rabi oscillation, spatial hole burning, and the third-order nonlinearity $\chi^{(3)}$.

Finally, the novel applications based on the developed mid-IR QCLs are presented in Chapter 5. For the hybrid QCL integration project, the Ge-on-Si platform is developed on our collaborator's side at the University of Southampton. The QCLs are integrated onto the platform through a flip-chip bonding approach, which provides <0.5 µm alignment accuracy in the surface plane. Vertically, the laser and waveguide are passively aligned through a specifically designed support structure, which is directly defined and etched on the silicon wafer, providing ±10nm aligning accuracy. Furthermore, we find that our QCLs are also capable of being used for polymer selective laser sintering (SLS), i.e., 3D printing, since the emission wavelength matches a strong absorption peak of the polymer. We thereby built a QCL-based SLS system and successfully demonstrated polymer powder sintering.

Acknowledgement

First of all, I would like to express my deep appreciation to my supervisor Dr Ian Farrer and second supervisor Dr Kristian M Groom. Seven years ago, I came to Sheffield simply for snooker without a particularly interested field in semiconductors. Ian was the person that inspired my interest in low-dimensional semiconductor structures when I was a postgraduate student; later, I further found my passion in quantum cascade lasers (QCLs), which naturally became the research topic of my PhD. Kris helped me fabricate all QCLs with his masterly skills, which I did not really have a chance to get involved in due to the outbreak of COVID-19. In addition, I would like to thank the group leader, Prof. Jon Heffernan. Jon is not my supervisor on the registration form, but he still arranged extra meetings to support my research.

I must not forget to thank Dr Dmitry G Revin, a truly respectful researcher from whom I learnt a lot about QCL, and beyond QCL. I often visited Dmitry's lab when I was a QCL rookie and sometimes disrupted his work – I remembered that once, he was explaining something to me and forgot to turn on the cooling system for his expensive external-cavity QCL. Also, I need to acknowledge Dr Andrey B Krysa for growing high-quality QCL wafers, thanks to which I did not get struggling with making the lasers operate in continuous-wave mode at room temperature; instead, I could look into something more interesting, i.e., the nonlinear optics. It has been my pleasure to work with the first-generation QCL researchers in Sheffield.

I also received many bits of help from my colleagues and collaborators – Aris, Charlotte, Chufan, Ed, Elisa, Elizabeth, Henry, Max, Nassar, Paige, Yasaman, Young In; Mohammed, Ryan, Sarath from the department of mechanical engineering; and Colin, Goran from the

University of Southampton. I would like to thank all of them, without whom my progress would have been significantly delayed or not even achieved.

Finally, I would like to thank my parents, who always support my decisions. There are endless words to say, so let me just thank them in the reciprocal space :)
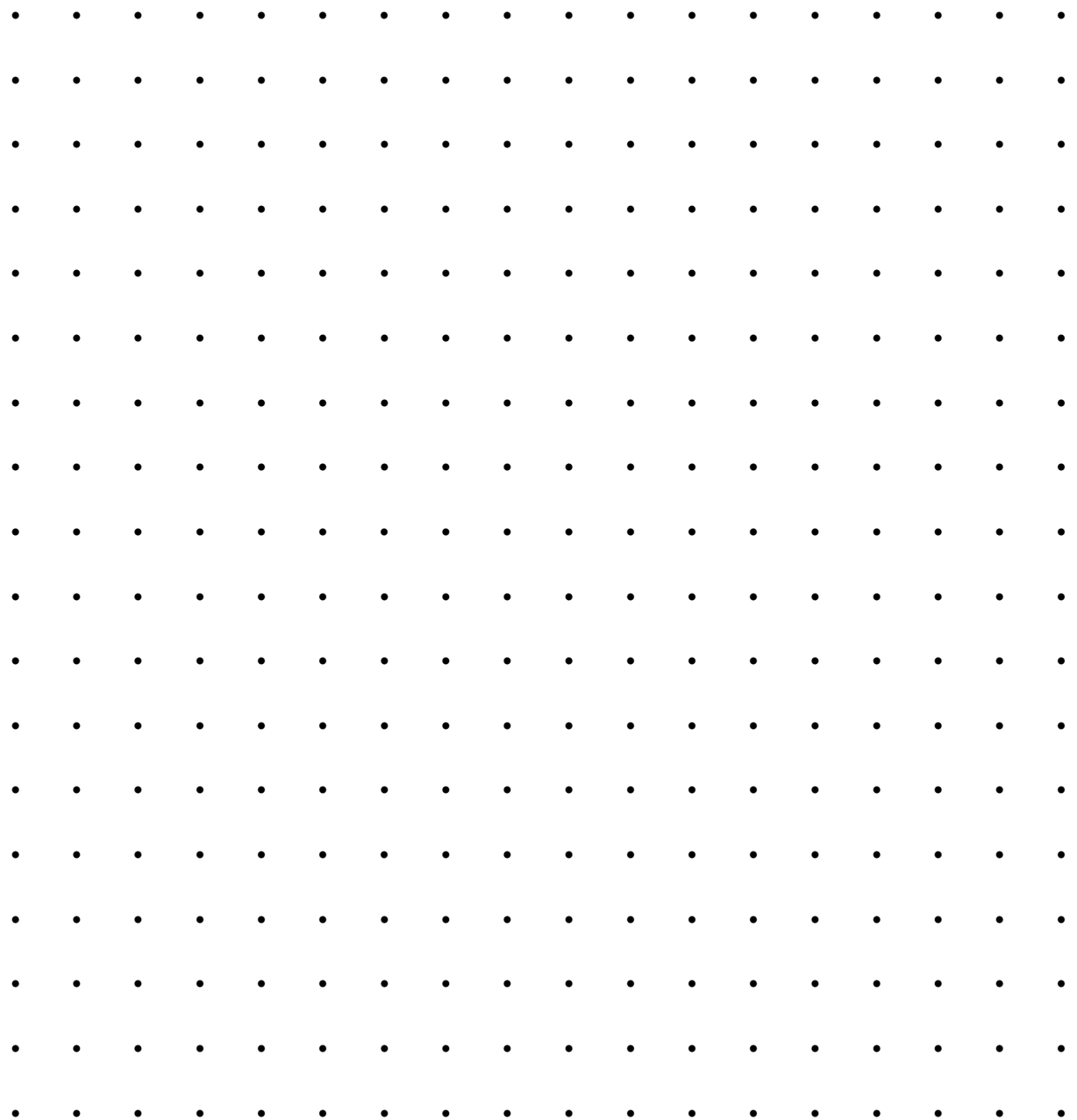
Oral Presentations

L. Zhou, K. M. Groom, I. Farrer, J. Heffernan, D. G. Revin, C. J. Mitchell, G. Mashanovich, Optimisation of beam quality for waveguide coupling of a CW quantum cascade laser, UK Semiconductors, Sheffield, 2022

Publications

C. J. Mitchell, A. Osman, K. Li, J. S. Penadés, M. Nedeljković, **L. Zhou**, K. M. Groom, J. Heffernan, G. Z. Mashanovich, "Hybrid integration methodology for quantum cascade lasers with germanium waveguides in mid-IR," *EPJ Web of Conferences*, vol. 266, p. 01008, 2022.

C. J. Mitchell, A. Osman, K. Li, J. S. Penadés, M. Nedeljković, **L. Zhou**, K. M. Groom, J. Heffernan, G. Z. Mashanovich, "Hybrid laser integration in the mid-IR for silicon photonics sensing applications," *Silicon Photonics XVIII*, vol. 12426, pp. 57–60, 2023.

L. Zhou, K. M. Groom, I. Farrer, D. G. Revin, J. Heffernan, "Complete synchronisation of multiple transverse modes in a CW quantum cascade laser," *In Preparation. Submitted to Physical Review Letter by the end of 2023.*

Table of Contents

1 Introduction

1.1 Laser Fundamentals

Laser, an acronym for *Light Amplification by Stimulated Emission of Radiation*, is a revolutionary light source that can emit beams with high intensity, remarkably narrow spectrum, and excellent directionality. Despite these unique features making lasers unsuitable for illumination purposes, they have played irreplaceable roles in many other areas, which include but are not limited to education, manufacturing, telecommunications, healthcare, and the military. Because of this, laser is considered one of the most influential inventions in the 20th century, among television, personal computer, aeroplane, radar, internet etc.

Laser has become a huge family since its birth in 1960 [1]. One can find many types of lasers in the market, such as gas lasers, solid-state lasers, fibre lasers, dye lasers etc. Nonetheless, any laser, regardless of its type or size, consists of two fundamental components [2]: a *gain medium* and a *resonating cavity*, as shown in Fig 1.1. The gain medium is where the light is amplified; the resonating cavity, which can be as simple as a pair of mirrors, provides optical feedback to the gain medium.

To understand how the gain medium works, let us first consider the electron optical transitions in a simple two-level system with a ground energy level E_1 and an excited energy level E_2, as shown in Fig 1.2. When an electron in the ground state $|E_1\rangle$ is exposed to an incident photon with energy $h\nu = E_2 - E_1$, the electron can absorb the photon energy and jump to the excited state $|E_2\rangle$. This process is termed *absorption*, i.e., Fig 1.2(a).
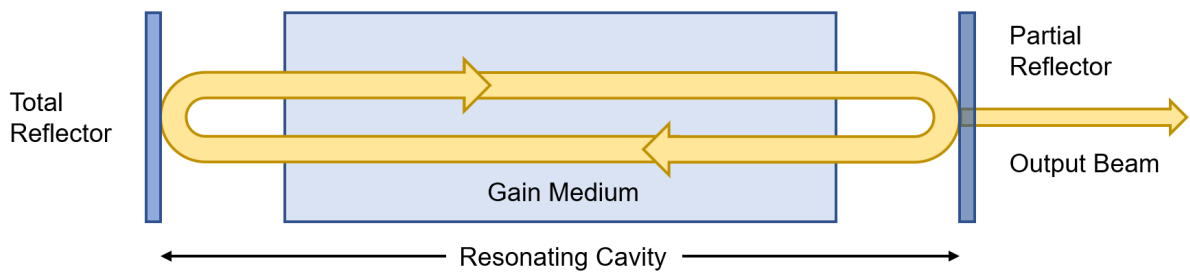
Fig 1.1 A simple laser model consists of (a) a gain medium for light amplification and (b) a set of parallel reflectors, which bounces the light back and forth through the gain medium.
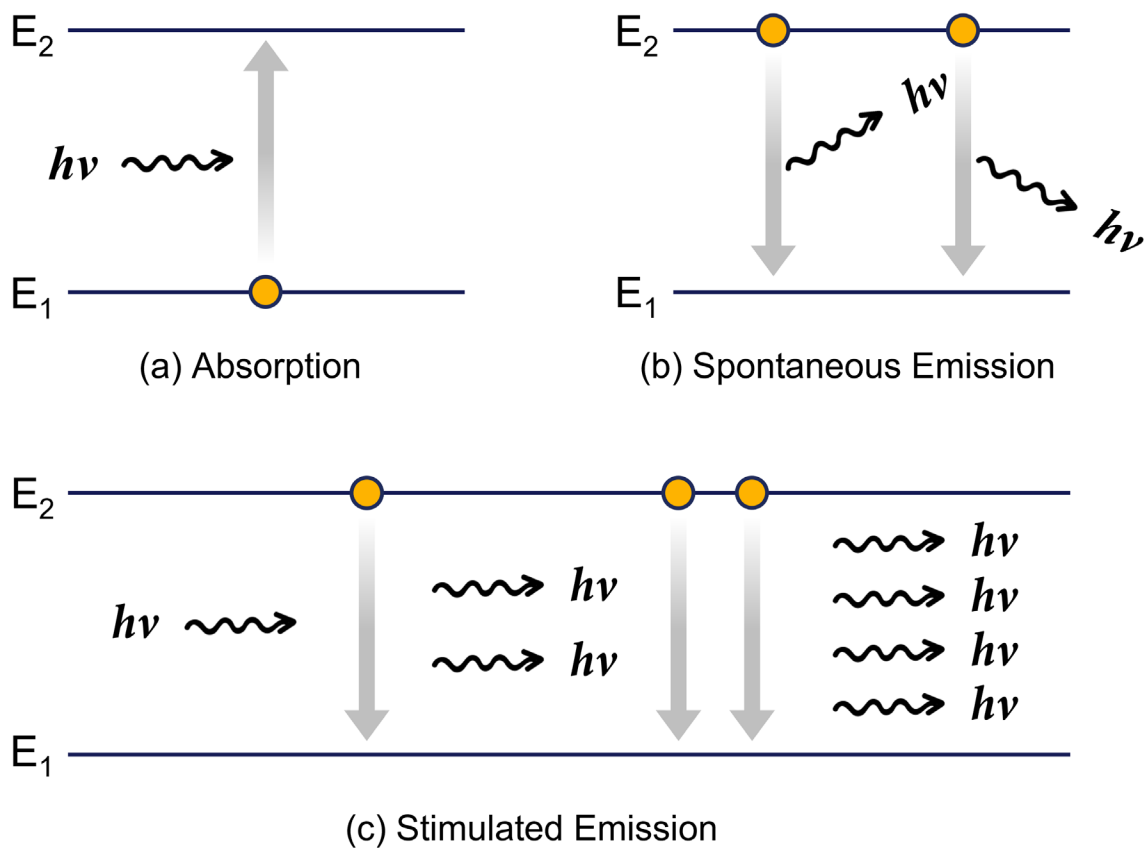
Fig 1.2 Optical transitions in a two-level system: (a) absorption, (b) spontaneous emission, and (c) stimulated emission, where $hv = E_2 - E_1$, v is the frequency of the photon, and h is Planck's constant.

Typically, the lifetime of electrons staying in the excited state $|E_2\rangle$ is very short, i.e., below or around nanoseconds [3]; therefore, they will fall back to the ground level soon, emitting photons with energy hv. This reverse process is referred to as *spontaneous emission*. The generation of light in light-emitting-diodes (LEDs) is based on such an optical process. It is worth highlighting that photons generated through spontaneous emission are isotropic, i.e., identical in energy but *random* in direction and phase, as shown in Fig 1.2(b). Thanks to this, LEDs can be used for illumination and display applications.

In contrast to spontaneous emission, *stimulated emission* is a more special optical process. In this type of transition, an electron in the state $|E_2\rangle$ is stimulated by an incident photon with energy hv to jump back to the ground state $|E_1\rangle$, resulting in two photons with exactly the same energy, direction, and phase as the incident photon, i.e., spatial and temporal coherence. When this process is turned into a chain reaction, as illustrated in Fig 1.2(c), the number of coherent photons increases massively. In a macroscopic sense, the light is amplified. This is the fundamental principle of any laser, which determines the high coherence nature of laser beams. However, under thermal equilibrium conditions, most electrons stay in the ground state; thus, absorption is the dominant optical process in the system. The essential condition for lasing is that the excited state $|E_2\rangle$ is occupied by more electrons than the ground state $|E_1\rangle$, i.e., electron *population inversion*, so that the stimulated emission process can overcome absorption, leading to net amplification of light. In order to create such a population inversion of electrons in the gain medium, additional pumping is required, which can be either optical or electrical.

1.2 Quantum Cascade Laser

Semiconductor lasers are a particularly popular type of laser due to their compact size, high reliability, high efficiency, mass producibility etc. Conventional semiconductor lasers are laser diodes (LDs) based on compound semiconductors [4] – one can consider them as light-emitting diodes with resonating cavities for simplicity. In this type of laser, light is generated through the recombination of free electrons and holes, i.e., interband transition: the upper lasing level is in the conduction band while the lower lasing level is in the valence band, as illustrated in Fig 1.3(a). Clearly, this is a cross-bandgap transition; therefore, the emission photon energy cannot be smaller than the bandgap energy and thus, there exists an upper limit of emission wavelength. In order to make laser diodes emit longer wavelengths, one has to find another material with a narrower bandgap as the active region. As a result, conventional semiconductor lasers operate up to the near-infrared (NIR) region.

(a) Interband   (b) Type-II interband   (c) Intersubband
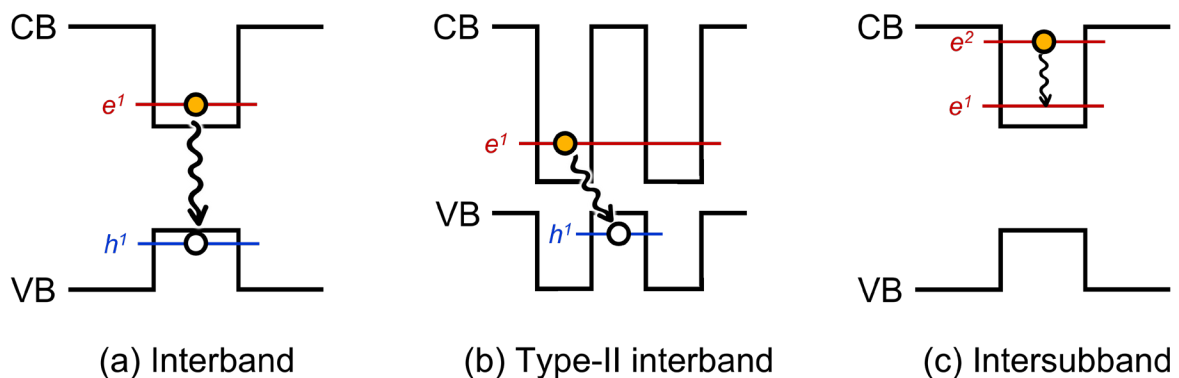
Fig 1.3 (a) Laser diodes based on interband transition, (b) ICLs based on interband transition in Type-II quantum wells, and (c) QCLs based on intersubband transition.

One approach to further extend the emission wavelength of interband semiconductor lasers is to employ the so-called Type-II heterostructure, as shown in Fig 1.3(b). In such a structure,

the bottom of the conduction band and the top of the valence band are located in different materials, forming a 'W' shaped band structure. Now that the forbidden energy gap is not defined by one material, thus the interband transition gap can be further reduced, resulting in longer emission wavelengths than in regular heterostructures (Type-I). Lasers based on Type-II interband transitions are known as *Interband Cascade Lasers* (ICLs) [5]. However, the extension of the emission wavelength by utilising type-II quantum wells is still limited; as shown in Fig 1.5, the emission wavelength of ICLs is between ~3 and ~11 μm [6][7], while that of most high-performance devices operate at ~3 – 4 μm [8].

Laser diodes and ICLs are both bipolar devices based on interband transition; in contrast, *Quantum Cascade Lasers* (QCLs) [9] work with a fundamentally different mechanism. QCLs are unipolar devices based on intersubband transition, i.e., the upper and lower lasing levels are both within the conduction band, and electrons are the only carrier. As shown in Fig 1.3(c), the intersubband transition does not cross the bandgap, and thus the emission wavelength is not limited by the bandgap energy. The active region of QCLs employs a superlattice structure, usually consisting of hundreds of alternating layers with elaborately designed thicknesses. In such structures, the energy states of the electrons are quantised rather than a continuum in the bulk materials, which allows intersubband radiative transitions to take place. Furthermore, these quantised electron states are manipulatable through layer thickness control, i.e., the width of quantum wells in the energy-distance (E-z) space. This leads to the most significant advantage of QCLs – they can emit different wavelengths based on the same material system by merely modifying the thickness of each layer in the superlattice structure [10].

Another key feature of QCLs is the cascading scheme. The total active region consists of tens of cascaded periods. In the E-z space, as shown in Fig 1.4(b), the electrons move similarly to a cascade waterfall, emitting one photon in one period and then relaxing to the next period for

another emission. In other words, electrons are recyclable for photon emission in QCLs. While in interband lasers, each electron can emit only one photon due to the electron-hole recombination mechanism and the optical transitions exhibit a parallel scheme, as illustrated in Fig 1.4(a). As a result, QCLs are no longer 'bandgap slaves', and the emission wavelength could cover mid-infrared (mid-IR), far-infrared (FIR) and even the terahertz (THz) region, i.e., from ~3 μm to ~300 μm. More technical details of the quantum well theory and QCL active region design are given in Chapter 2.
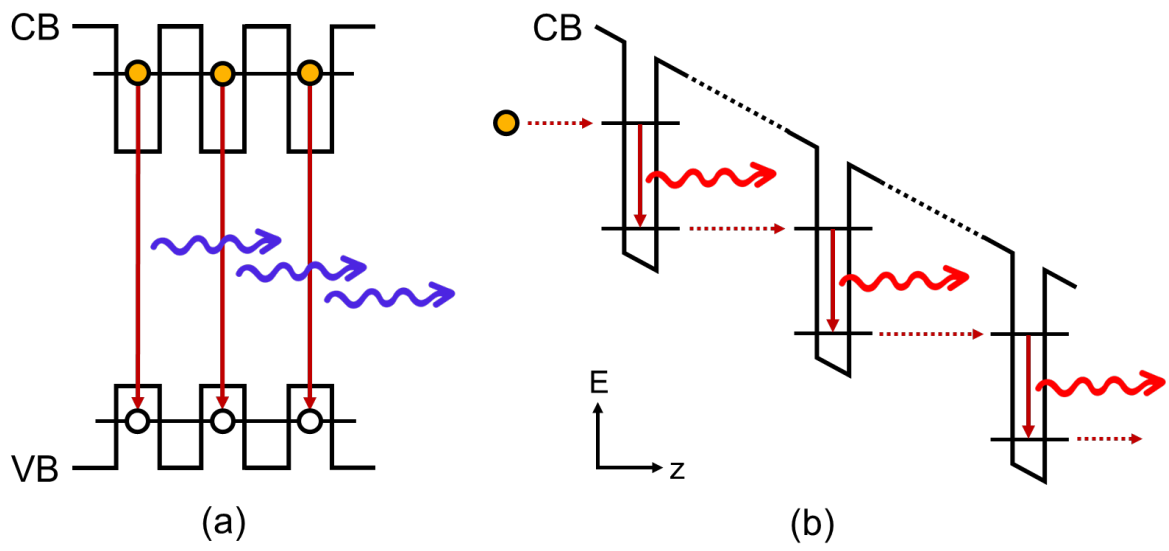
Fig 1.4 (a) Parallel transitions in a laser diode. (b) Cascade transitions in a QCL.

In addition to semiconductor lasers, a few other available mid-infrared coherent sources are also summarised in Fig 1.5 for comparison [11, pp. 7–8]. CO and CO_2 lasers are gas lasers with watt-level output power, but their emission wavelength is limited to a few specific lines. For example, CO_2 lasers typically operate at the wavelength of 9.6 μm or 10.6 μm. Lead salt lasers [12] based on ternary or quaternary lead compounds (e.g., $Pb_xSn_{1-x}Te$, $Pb_xEu_{1-x}Se_yTe_{1-y}$) can cover the whole mid-IR region thanks to their relatively small

bandgaps (<0.5 eV). However, using this type of laser is problematic because of its limited reliability, low power, and the necessity to operate at cryogenic temperature. The mid-infrared region is also accessible through nonlinear frequency down-conversion of near-infrared beams, e.g., utilising the difference frequency generation (DFG) [13] effect in a nonlinear crystal or employing an optical parametric oscillator (OPO) [14], but the high cost and complexity of these systems are unsatisfactory. Compared to these mid-IR candidates, QCLs offer huge advantages, i.e., much broader wavelength coverage, the ability to operate in continuous-wave (CW) mode at room temperature (RT) between ~3 and ~12 μm [15], compact size, and high reliability. For these reasons, QCLs have become the most popular coherent light source in mid-IR.
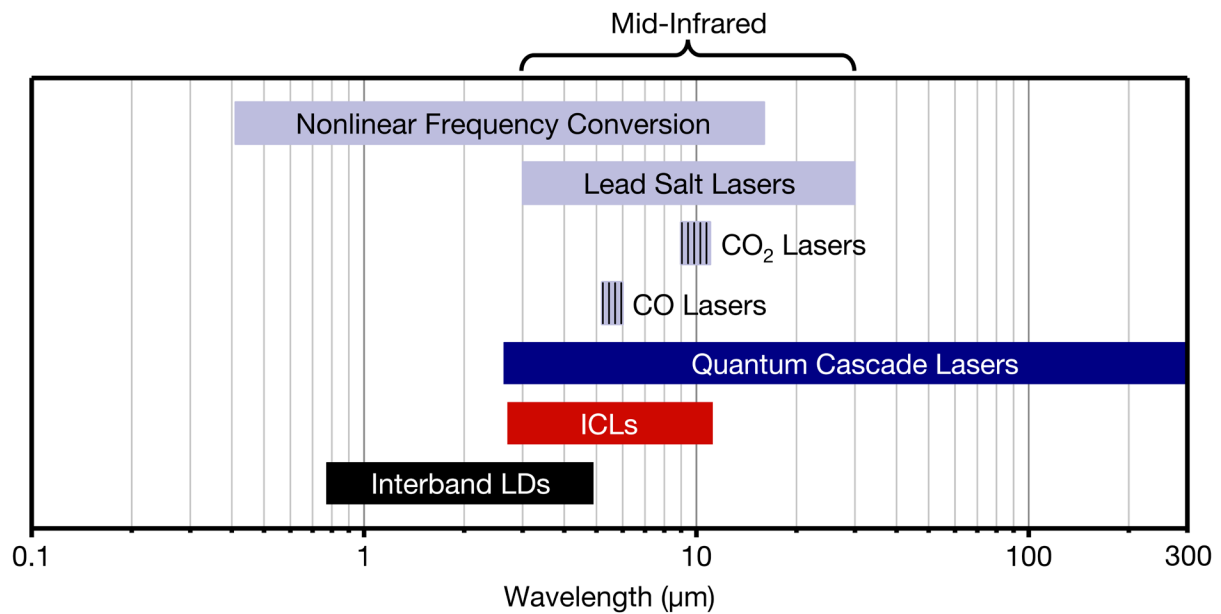
Fig 1.5 Wavelength coverage of various coherent sources in infrared [11, pp. 7–8]

1.3 Mid-Infrared Applications

High-performance mid-infrared coherent sources are desired simply because of the attractive applications of this wavelength region. This section mainly introduces three representative applications, i.e., gas sensing, free space telecommunication, and infrared countermeasures.

1.3.1 Gas Sensing

Many gas molecules exhibit strong absorptions in the mid-IR region due to their molecule fundamental vibrational modes [16], as shown in Fig 1.6. The fundamental vibrational transition $v_0 \rightarrow v_1$ features several orders of magnitude stronger absorption strength compared to transitions in other frequency bands (the overtones) because of the large oscillator strength. Hence, extremely high detection sensitivity can be achieved in mid-IR spectroscopy, and therefore, this wavelength region is also known as the 'fingerprint' region.
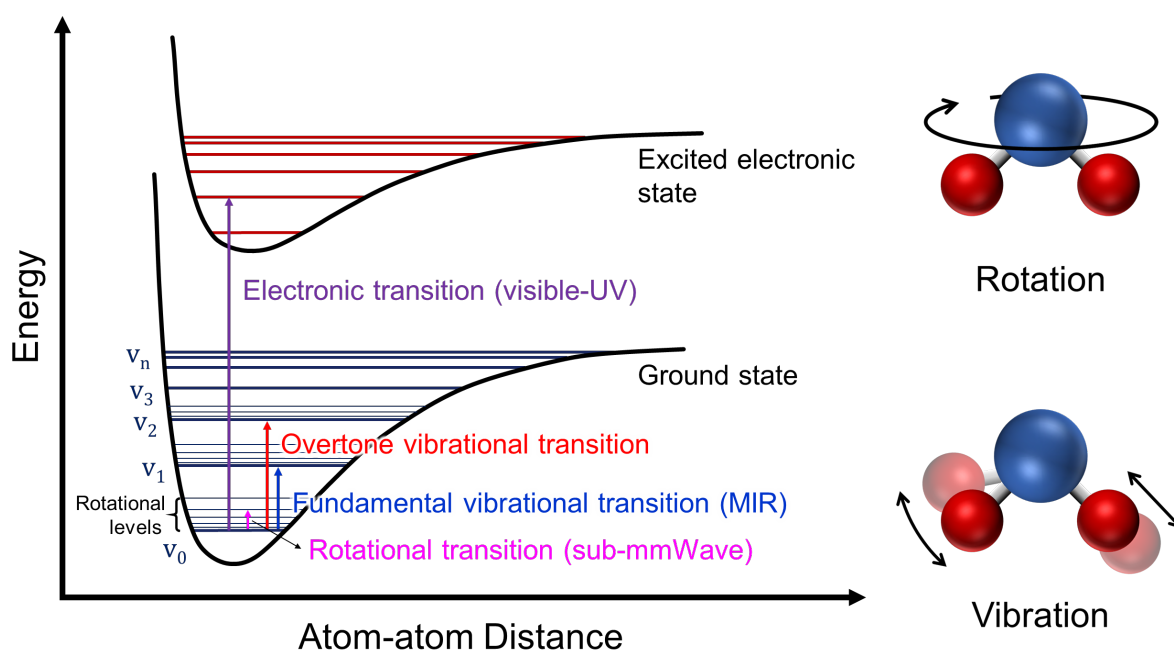
Fig 1.6 Rotational and vibrational transitions in molecules

The general setup of a gas sensing system is schematically shown in Fig 1.7, where a multi-pass cavity containing the gas sample is placed between the mid-IR laser and the corresponding detector. The total optical path, therefore, can be extended to several meters, tens of metres, or even hundreds of meters long, which significantly increases the detection sensitivity, allowing the detection of gas molecules at very low concentrations.
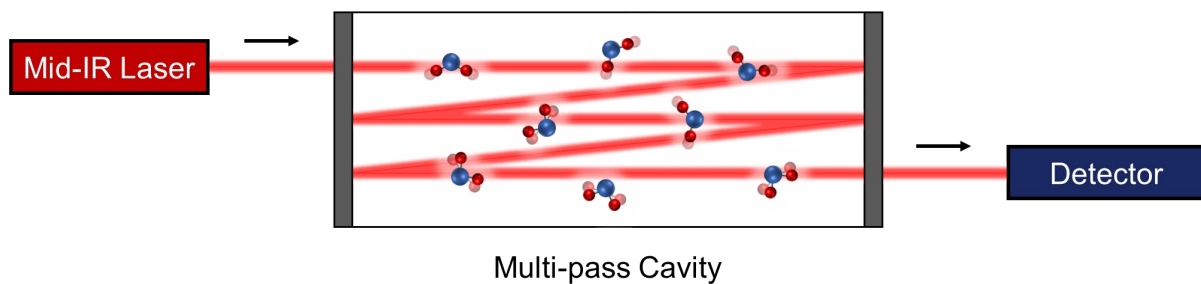
Fig 1.7 Schematic diagram of a gas sensing setup

With the general theory understood, we can now look at what gas sensing can actually do. In Fig 1.8, a number of common gas molecules are listed, which have strong characteristic absorption peaks in the mid-infrared region between 2.5 and 15 μm. The ultra-high precision detection of these gases brings many valuable and irreplaceable applications. For example, the 3 – 5 μm region is favoured for environmental monitoring applications such as the study of the greenhouse effect, ambient air quality monitoring, pollution monitoring etc. 7 – 10 μm gas sensing can be used for leakage detection in the industrial process. In addition, this region is also applicable for defence and security purposes, i.e., chemical and explosive threat detection. This is because chemicals such as TNT, H_2O_2, acetone and sarin also have strong characteristic absorptions in this region, which are not compiled in the figure due to space limitations. Gas sensing in the 8 – 12 μm region sees popular applications in medical

diagnosis for the particular reason that this is a non-invasive method. For instance, the concentration of acetone in the exhaled breath of diabetic patients is found to be remarkably increased [18]. Therefore, the detection of acetone in the exhaled breath can be used for the preliminary diagnosis of diabetes as the biomarker. Moreover, in contrast to another widely used breath analysis technique, gas chromatography, which usually requires multiple breaths, mid-infrared spectroscopy provides exceptionally higher sensitivity; thus, the total diagnosis time can be considerably shortened, and even single breath diagnostics could be possible.
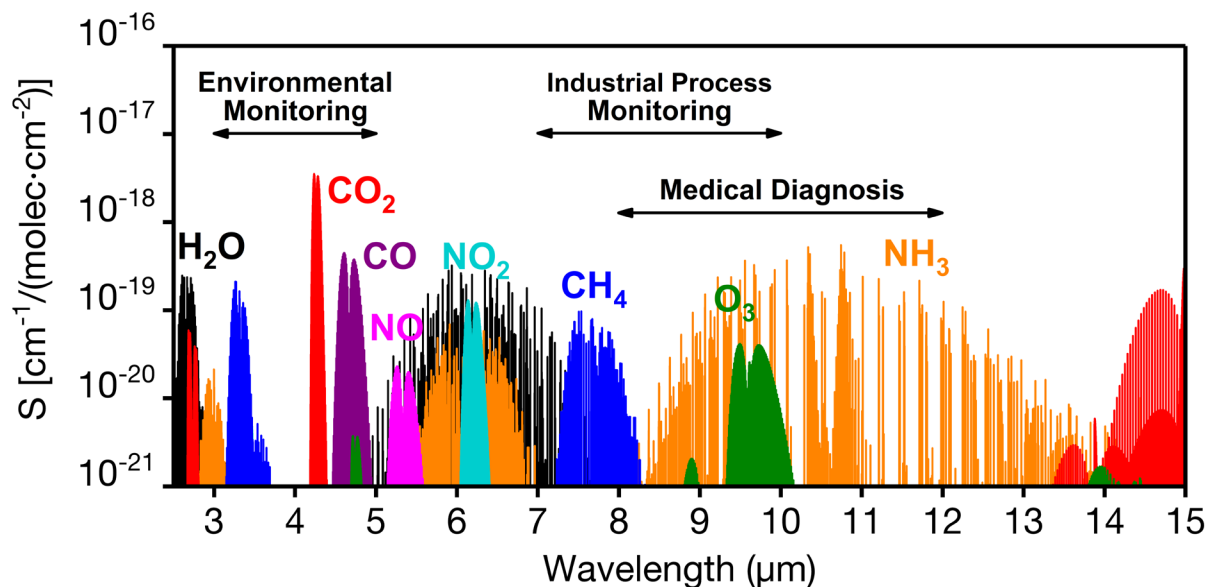
Fig 1.8 A number of gas molecules with strong absorption lines in the mid-infrared region between 2.5 and 15 μm. Molecule absorption data were compiled from the HITRAN2020 edition [17].

1.3.2 Free-space Communication

The most common and widely used optical telecommunication technology is fibre optic communication; however, regular glass optical fibres cannot transmit mid-infrared due to the

high absorption and mid-IR compatible fibres, such as As-Se fibres, are very expensive. On the other hand, as shown in Fig 1.9, the two atmospheric transmission windows in the mid-infrared region, i.e., 3 – 5 μm and 8 – 14 μm, allow mid-IR coherent sources to be used for free-space communication [19]. Compared to fibre optic communication, the transmission medium in this technique is simply the air; hence, the costs of optical fibre installation, maintenance, and repair can be saved, which is the most attractive feature of free-space communication. Besides, compared to near-IR or visible, mid-IR is safer for eyes, more distinct from the solar spectrum, and more insensitive to fog and urban haze due to the longer wavelength resulting in a reduced Rayleigh scattering effect [11, p. 271].
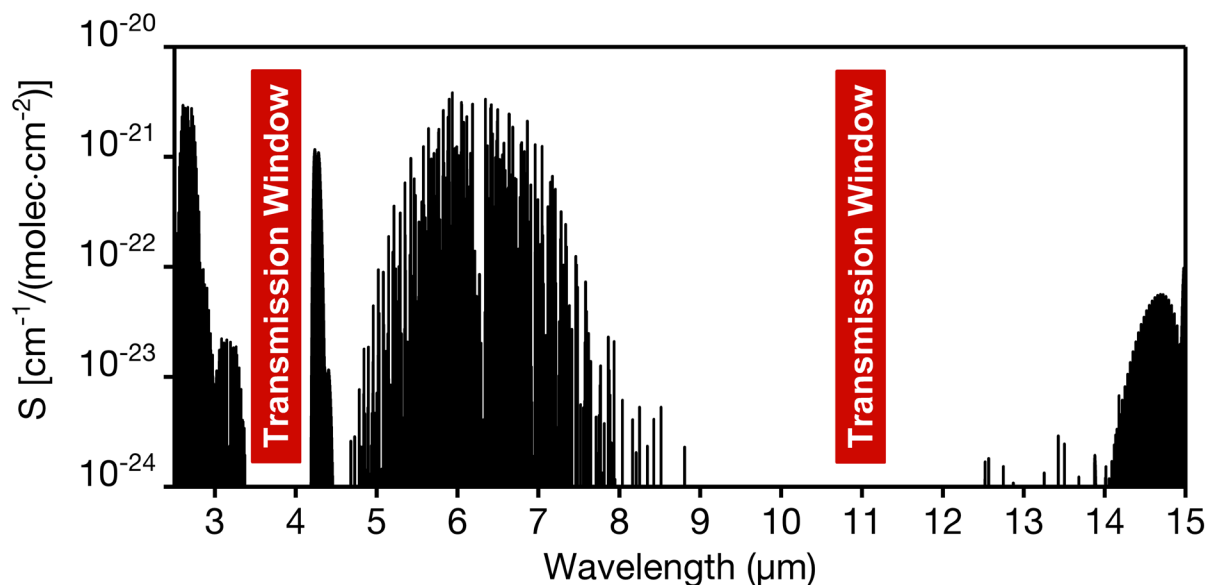
Fig 1.9 Atmospheric absorption spectrum in the mid-infrared region between 2.5 and 15 μm. Plotted data is based on a gas mixture model provided by HITRAN [20].

On the other hand, the link quality can still be affected by severe weather such as rain and snow; the beam divergence from mid-IR sources can also contribute to additional signal attenuation, which can affect viable communication distances. These are examples of the

limitations of free-space communication; it is, therefore, suitable for establishing optical data links in urban areas as a complement to fibre optics communication to provide temporary bandwidth increases.

1.3.3 Infrared Countermeasures

Coherent mid-infrared light also has been found to have important applications in the military. Aircraft with high-temperature engines emit very strong infrared signals as a result of blackbody radiation; therefore, they can be tracked and hit by infrared-guided missiles. To fight against these heat-seeking rockets, military aircraft are equipped with infrared countermeasure (IRCM) systems, which can emit even stronger infrared signals and mislead the heat-seekers. A common method is to deploy flares, which could simultaneously create numerous targets for the infrared-homing missile, thus confusing it.

In contrast, laser beams are highly directional, which obviously cannot 'broadcast' in the infrared band as flares do, but high-power infrared lasers also can be used to mislead infrared-guided missiles [21]. This is known as Directed Infrared Countermeasures (DIRCM). As shown in Fig 1.10, once alerted by the missile warning system, a bright infrared beam will be emitted, targeting the heat-seeking missile and disrupting its guide system.
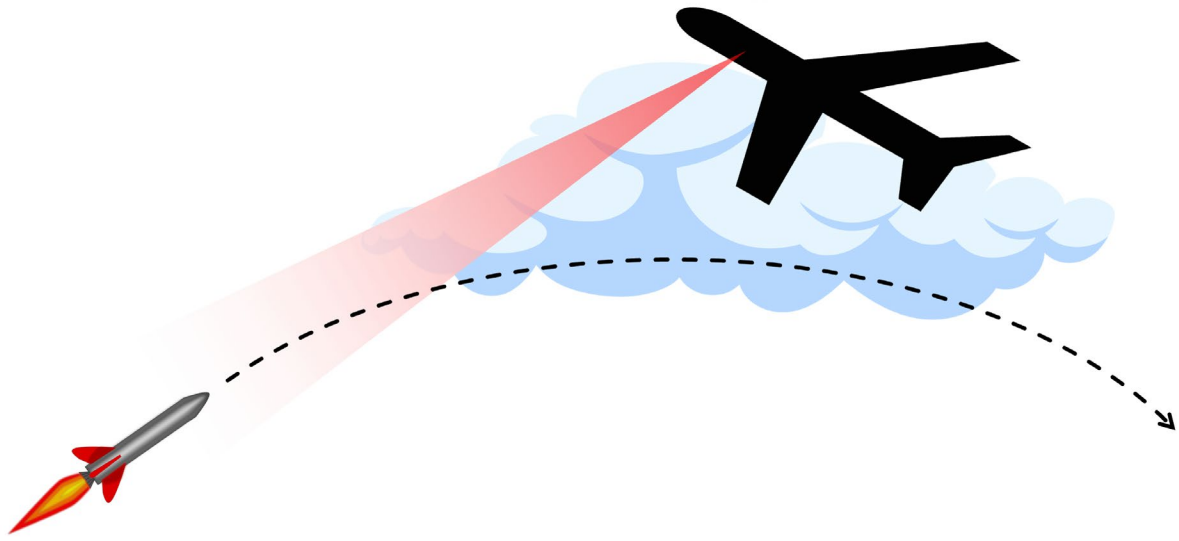
Fig 1.10 Directed Infrared Countermeasures (DIRCM) solutions protect aircraft against heat-seeking ground-to-air missiles

In addition to protecting aircraft against IR-guided missiles, high-power infrared lasers also can be utilised to blind the night vision cameras used in military equipment (e.g., helicopter, tank etc.) as these devices are usually based on infrared imaging.

1.4 Thesis Overview

This thesis presents a relatively rounded story of developing a mid-infrared quantum cascade laser, which covers device fabrication, device characterisation, discussion of nonlinear optics in QCLs, and novel applications based on the developed QCL.

```
┌─────────────────────────────────┐
│   Chapter 1: Introduction       │
└─────────────────────────────────┘
              │
              ▼
┌─────────────────────────────────┐
│        Chapter 2: Theory        │
│  ▪ Quantum cascade laser theory │
│  ▪ QCL Characterisation techniques│
└─────────────────────────────────┘
              │
              ▼
┌─────────────────────────────────┐         ┌──────────────────────────────────────┐
│  Chapter 3: Device Fabrication  │────────▶│ Chapter 4: Nonlinear Physics in QCL  │
│  ▪ Fabrication of λ ~5.7 µm QCLs │         │  ▪ Observation of spectral instability│
│  ▪ Characterisation of λ ~5.7 µm QCLs│      │  ▪ Observation of CW mode beam steering│
└─────────────────────────────────┘         └──────────────────────────────────────┘
              │
              ▼
┌─────────────────────────────────┐
│    Chapter 5: QCL Applications  │
│  ▪ Hybrid integration of QCLs on Si│
│  ▪ QCL based polymer sintering  │
└─────────────────────────────────┘
              │
              ▼
┌─────────────────────────────────┐
│     Chapter 6: Conclusion       │
└─────────────────────────────────┘
```

A complementary chapter to discuss the spectral and spatial instabilities observed during the development of the QCL.

Fig 1.11 Overview of the thesis

As schematically shown in Fig 1.11, the content of each chapter is organised as follows:

- The unique features of QCLs and their attractive applications have been generally introduced in this chapter.

- In Chapter 2, details of mid-IR QCL active region design will be presented by reviewing the milestones in the history of QCL development. In addition, the general QCL characterisation techniques and our experimental setups are described in the chapter.

- Chapter 3 presents the fabrication and characterisation works of developing a mid-IR QCL emitting at the wavelength of ~5.7 μm for hybrid integration on the silicon platform. The devices eventually achieved at room temperature (RT) in continuous-wave (CW) operation with excellent beam quality.

- During the development of this QCL, we observed a few fascinating spectral and spatial mode instabilities in several devices, which are further investigated and discussed in Chapter 4.

- Chapter 5 is dedicated to novel applications based on our developed QCLs. First, the developed QCLs are integrated onto the germanium-on-silicon (GoS) platform and coupled with germanium waveguides via the flip-chip bonding approach, which is a collaboration with the optoelectronics research centre at the University of Southampton. Besides, a mid-IR QCL-based prototype polymer 3D printing system is introduced, replacing the conventional CO_2 laser, and wavelength-selective polymer sintering is demonstrated.

- Finally, the thesis is concluded in Chapter 6, with an outlook of future works.

References

[1]   J. L. Bromberg, "The birth of the Laser," *Physics Today*, vol. 41, no. 10, pp. 26–33, 1988.

[2]   W. T. Silfvast, *Laser Fundamentals*. Cambridge: Cambridge University Press, 1996.

[3]   J. Wilson and J. F. B. Hawkes, *Lasers: Principles and applications*. New York; London: Prentice Hall, 1987, p. 11.

[4]   H. K. Choi, *Long-wavelength infrared semiconductor lasers*. Hoboken, New Jersey: Wiley, 2004.

[5]   R. Q. Yang, "Infrared laser based on intersubband transitions in quantum wells," *Superlattices and Microstructures*, vol. 17, no. 1, pp. 77–83, 1995.

[6]   C. L. Felix, W. W. Bewley, E. H. Aifer, I. Vurgaftman, J. R. Meyer, C. H. Lin, D. Zhang, S. J. Murry, R. Q. Yang, and S. S. Pei, "Low threshold 3 μm interband cascade 'W' laser," *Journal of Electronic Materials*, vol. 27, no. 2, pp. 77–80, 1998.

[7]   L. Li, H. Ye, Y. Jiang, R. Q. Yang, J. C. Keay, T. D. Mishima, M. B. Santos, and M. B. Johnson, "MBE-grown long-wavelength interband cascade lasers on InAs substrates," *Journal of Crystal Growth*, vol. 425, pp. 369–372, 2015.

[8]   I. Vurgaftman, R. Weih, M. Kamp, J. R. Meyer, C. L. Canedy, C. S. Kim, M. Kim, W. W. Bewley, C. D. Merritt, J. Abell, and S. Höfling, "Interband Cascade Lasers," *Journal of Physics D: Applied Physics*, vol. 48, no. 12, p. 123001, 2015.

[9]   J. Faist, F. Capasso, D. L. Sivco, C. Sirtori, A. L. Hutchinson, and A. Y. Cho, "Quantum Cascade Laser," *Science*, vol. 264, no. 5158, pp. 553–556, 1994.

[10]   N. Bandyopadhyay, Y. Bai, S. Slivken, and M. Razeghi, "High power operation of $\lambda \sim 5.2$–11 μm strain balanced quantum cascade lasers based on the same material composition," *Applied Physics Letters*, vol. 105, no. 7, p. 071106, 2014.

[11]   J. Faist, *Quantum Cascade Lasers*. Oxford: Oxford University Press, 2018.

[12]   M. Tacke, "New Developments and applications of tunable IR lead salt lasers," *Infrared Physics & Technology*, vol. 36, no. 1, pp. 447–463, 1995.

[13]   C. Erny, K. Moutzouris, J. Biegert, D. Kühlke, F. Adler, A. Leitenstorfer, and U. Keller, "Mid-infrared difference-frequency generation of ultrashort pulses tunable between 3.2 and 4.8 μm from a compact fiber source," *Optics Letters*, vol. 32, no. 9, pp. 1138–1140, 2007.

[14]   M. M. J. W. van Herpen, S. Li, S. E. Bisson, S. te Lintel Hekkert, and F. J. M. Harren, "Tuning and stability of a continuous-wave mid-infrared high-power single resonant optical parametric oscillator," *Applied Physics B: Lasers and Optics*, vol. 75, no. 2-3, pp. 329–333, 2002.

[15]   M. Razeghi, W. Zhou, S. Slivken, Q.-Y. Lu, D. Wu, and R. McClintock, "Recent progress of quantum cascade laser research from 3 to 12 μm at the center for quantum devices," *Applied Optics*, vol. 56, no. 31, pp. H30-H44, 2017.

[16]   A. Kosterev, G. Wysocki, Y. Bakhirkin, S. So, R. Lewicki, M. Fraser, F. Tittel, and R. F. Curl, "Application of quantum cascade lasers to trace gas analysis," *Applied Physics B*, vol. 90, no. 2, pp. 165–176, 2007.

[17]   HITRAN online: https://hitran.org/lbl/

[18]   R. Selvaraj, N. J. Vasa, S. M. Nagendra, and B. Mizaikoff, "Advances in mid-infrared spectroscopy-based sensing techniques for exhaled breath diagnostics," *Molecules*, vol. 25, no. 9, p. 2227, 2020.

[19]   R. Martini and E. A. Whittaker, "Quantum Cascade Laser-based Free Space Optical Communications," *Journal of Optical and Fiber Communications Reports*, vol. 2, no. 4, pp. 279–292, 2005.

[20]   HITRAN on the web: https://hitran.iao.ru/gasmixture/simlaunch

[21]   P. I. Abramov, E. V. Kuznetsov, and L. A. Skvortsov, "Prospects of using quantum-cascade lasers in optoelectronic countermeasure systems: Review," *Journal of Optical Technology*, vol. 84, no. 5, pp. 331–341, 2017.

2 Theory and Experimental Setups

2.1 Introduction

The first half of this chapter describes the theory of mid-IR QCL active region design and the working mechanism. The theoretical section starts from the fundamentals of semiconductor quantum wells since the active region of a QCL is essentially a multiple quantum well structure, which is also known as the superlattice structure. The evolution of mid-IR QCL active region design and several milestones in the development history of QCLs are then reviewed after understanding the quantum well basics. In the second half of the chapter, the characterisation techniques of QCL performance are described, i.e., the basic electrical and optical measurement, spectral measurement, and far-field beam profile measurement, including the experimental setup of each measurement in our laser laboratory.

2.2 Electronic States in Quantum Well

In bulk semiconductor materials, electrons and holes are free to move in the x, y, z-directions and exhibit continuous energy states. Numerous continuous energy levels eventually form the conduction band and valence band, as illustrated in Fig 2.1(a). Whilst when a thin layer of narrow-bandgap semiconductor is sandwiched between two layers of another semiconductor material with a larger bandgap, two potential wells are then created in the conduction and valence band due to the bandgap discontinuity, which are known as quantum wells. In

contrast to the bulk material, in this case, the motion freedom of the carriers is reduced to two dimensions, as they are still free to move in the x-y plane but are now confined in the z-direction because of the presence of the potential barriers. In particular, when the width of the potential well is comparable to the de Broglie wavelength of the electron/hole, strong quantum effects can be observed in the well, i.e., electronic states will become quantised, as shown in Figure 2.1(b). The relationship between the confined energy levels and the quantum well will be explained in this section.

(a) Bulk material　　　　　　　(b) Sheet material
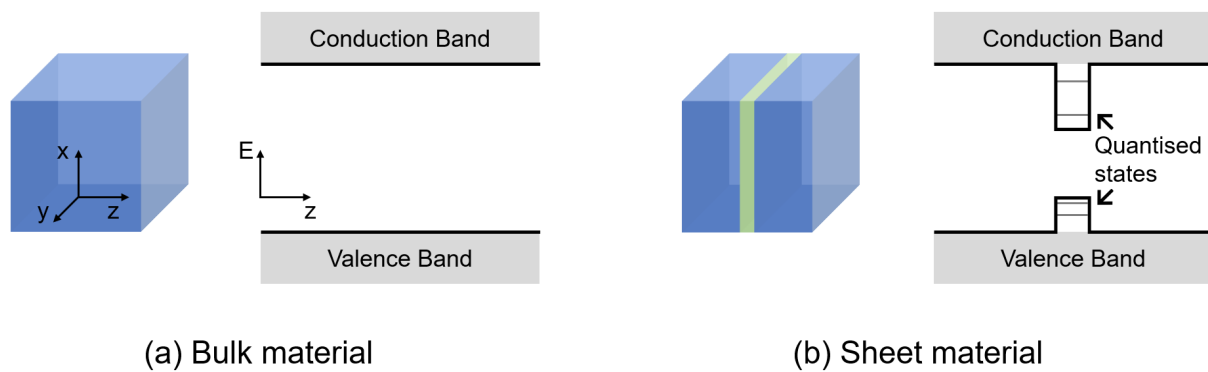
Fig 2.1 (a) Continuous electron/hole states in the bulk material. (b) Confined electron/hole in the 2D material has quantised energy states in the potential well.

2.2.1 Infinite Quantum Well

To quantitatively analyse the electronic states in a quantum well, we can start with a simplified model, i.e., the electron in a 1D infinite potential well, as illustrated in Fig 2.2(a). The potential is zero in the region $(0, a)$ and infinite in the region $(-\infty, a)$ and (a, ∞); hence, electrons will be confined in the $(0, a)$ interval.
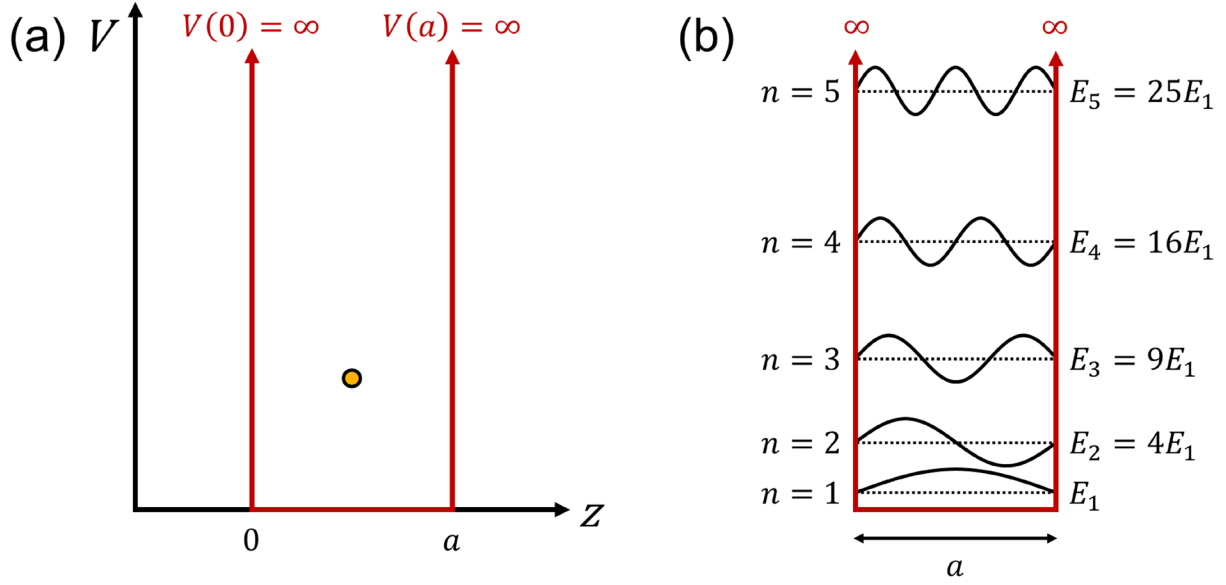
Fig 2.2 (a) Electron confined in a 1D infinite quantum well. (b) Electronic states in the 1D infinite quantum well calculated by the Schrödinger equation.

The problem can be easily solved using the time-independent Schrödinger equation:

$$\mathbf{H}|\psi(z)\rangle = E|\psi(z)\rangle \tag{2.1}$$

The Hamiltonian operator **H** represents the total energy of the system; in this case, it can be expanded into the sum of kinetic and potential energy operators:

$$\left[-\frac{\hbar^2}{2m}\frac{\partial^2}{\partial z^2} + V(z)\right]\psi(z) = E\psi(z) \tag{2.2}$$

where $\hbar$ is the reduced Planck's constant and m is the electron mass; in the following derivation, the effective electron mass will be used, denoted as m^*. As $V(z) = 0$ for $0 \leq z \leq a$, eq. (2.2) can be simplified to:

$$-\frac{\hbar^2}{2m^*}\frac{\partial^2}{\partial z^2}\psi(z) = E\psi(z) \tag{2.3}$$

Re-arrange the equation, we obtain:

$$\frac{\partial^2}{\partial z^2}\psi(z) = -\frac{2m^*E}{\hbar^2}\psi(z) \tag{2.4}$$

Here we can introduce $k = \frac{\sqrt{2m^*E}}{\hbar}$, and thus further simplifies the equation to:

$$\frac{\partial^2}{\partial z^2}\psi(z) = -k^2\psi(z) \tag{2.5}$$

The solution to this second differential equation has the general form:

$$\psi(z) = A\sin(kz) + B\cos(kz) \tag{2.6}$$

The wavefunction $\psi(z)$ is referred to as the *probability amplitude* and the amplitude square $|\psi(z)|^2$ describes the *probability density* at the position z. As electrons can only be found in the interval $(0, a)$, where $\psi(z) \neq 0$, the probability of finding electrons in other regions is zero, i.e., $\psi(z) = 0$ for $z \leq 0$ and $z \geq a$. Thus, we can apply the two boundary conditions required by wavefunction continuity to eq. (2.6), i.e., $\psi(0) = 0$ and $\psi(a) = 0$, to determine the values of coefficient A and B:

$$\psi(0) = A\sin(0) + B\cos(0) = 0 \quad \rightarrow \quad B = 0 \tag{2.7}$$

$$\psi(a) = A\sin(ka) + B\cos(ka) = 0 \quad \rightarrow \quad A\sin(ka) = 0 \tag{2.8}$$

For eq. (2.8), it would be meaningless if $A = 0$, hence this indicates that:

$$\sin(ka) = 0 \tag{2.9}$$

$$k = \frac{n\pi}{a}, n = 1, 2, 3, \dots \tag{2.10}$$

Recall that $k = \frac{\sqrt{2m^*E}}{\hbar}$, thus:

$$\frac{\sqrt{2m^*E}}{\hbar} = \frac{n\pi}{a} \tag{2.11}$$

Here we obtain the expression for the electronic energy levels:

$$E_n = \frac{n^2\pi^2\hbar^2}{2m^*a^2}, n = 1, 2, 3, \ldots \tag{2.12}$$

This implies that the electronic energy can only take certain discrete values in a potential well of width a, i.e., energy quantisation. In turn, we can find the corresponding wavefunctions for each energy eigenvalue:

$$\psi_n(z) = A\sin\left(\frac{n\pi z}{a}\right), n = 1, 2, 3, \ldots \tag{2.13}$$

The remaining unknown is the value of A, which is associated with the normalisation of the wavefunction. As mentioned above, $|\psi(z)|^2$ describes the probability density at the position z; considering that the total probability of finding the electron between 0 and a is 1, we have:

$$\int_0^a \left[A\sin\left(\frac{n\pi z}{a}\right)\right]^2 dz = 1 \tag{2.14}$$

$$A^2\left(\frac{a}{2}\right) = 1 \tag{2.15}$$

$$A = \sqrt{\frac{a}{2}} \tag{2.16}$$

Finally, we can sum up all the findings, which have been plotted in Fig 2.2(b). It can be easily found that in a quantum well, the ground electronic state is no longer at the band edge but at level E_1, which is associated with the electron mass and quantum well width a. The confined energy is proportional to the square of the level number. Similarly, hole states are also quantised, but they will be more closely spaced due to the larger effective mass of holes.

2.2.2 Finite Quantum Well

With the understanding of the simplest model, i.e., the infinite quantum well, now let us consider a practical quantum well, the potential barrier height of which is finite. Obviously, this is a more complicated case, but the analysis is similar to what we have done above – one needs to find general solutions to the Schrödinger equation in all three regions, i.e., left barrier, central well, and right barrier, and then apply the boundary conditions required by the continuity of wavefunctions at the heterointerface to determine the unknowns in the general solutions. Here a simple software **1D Poisson by Gregory Snider** [1] is used to calculate the quantum states in finite barrier quantum wells.

The program is basically a Schrödinger-Poisson solver, which solves the 1D Schrödinger and Poisson equations self-consistently. As demonstrated in the previous section, the Schrödinger equation is used to find the electronic states (i.e., energies and wavefunctions) in a given band profile. The Poisson equation, on the other hand, calculates the electrostatic potential based on the carrier density. Thus, the combination of both allows us to find the self-consistent solution of quantum states in the semiconductor structure, as shown in Fig 2.3: the electron energy levels and distributions (i.e., eigen energies E_n and the corresponding wavefunctions ψ_n) are calculated by resolving the Schrödinger equation with the given conduction band profile and then the result is fed back to the Poisson solver to update the electrostatic potential, followed by the band edge profile. Such iteration continues until the expected convergence is achieved and eventually a self-consistent solution is output.

Fig 2.4 shows an example of the quantised electronic states in a GaAs/Al$_{0.45}$Ga$_{0.55}$As finite barrier quantum well, calculated by the program.
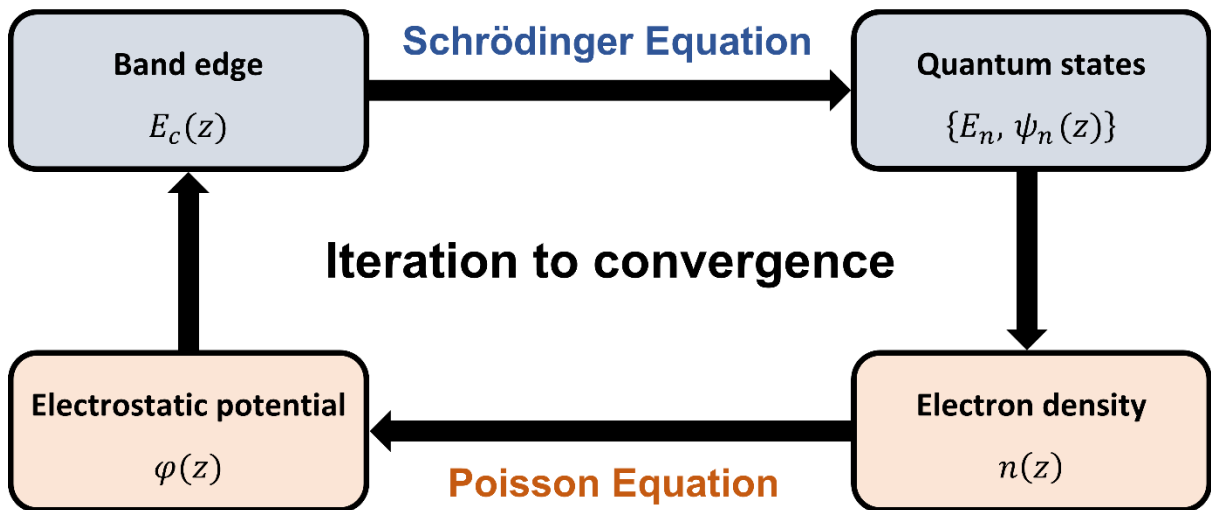
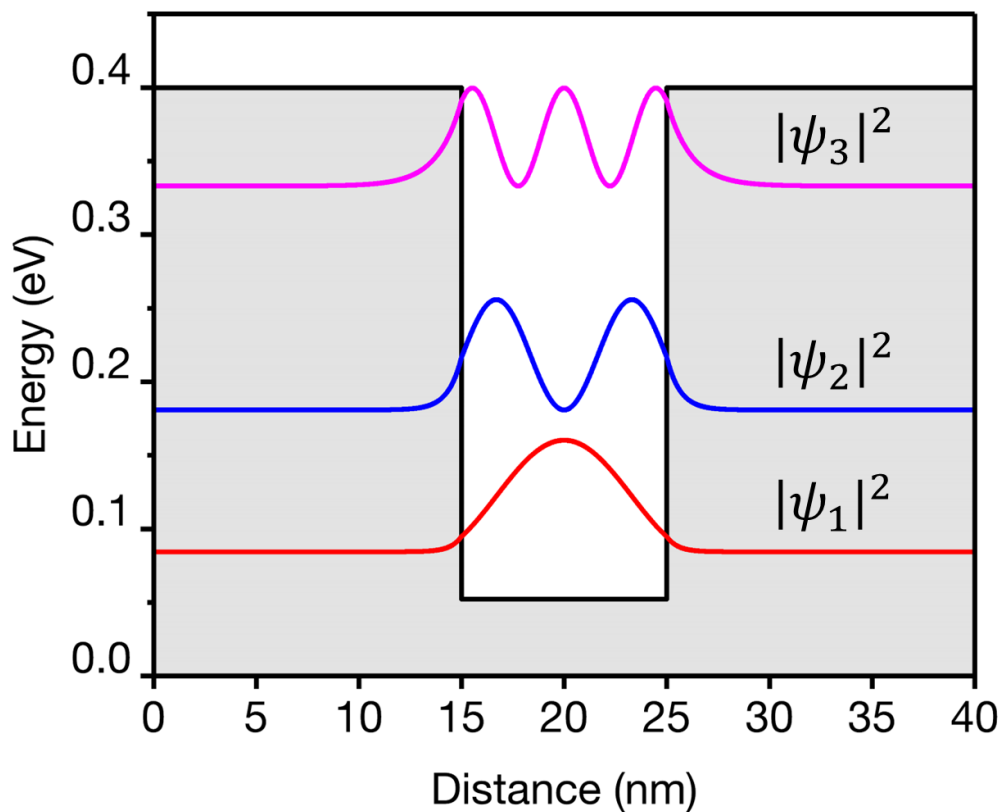**Fig 2.3** The self-consistent 1D Schrödinger-Poisson approach

Fig 2.4 Electronic states in a 10nm wide GaAs/Al$_{0.45}$Ga$_{0.55}$As quantum well

In contrast to the infinite quantum well model, in a finite model, the electron wavefunctions can penetrate into the potential barrier, indicating a probability of finding electrons in the barrier region, i.e., the confinement is no longer perfect. Furthermore, by comparing the calculated energy levels with the infinite model (see Fig 2.5), it can be easily seen that the energy levels in the finite model are lower due to the spread of wavefunction. They also no longer follow a strictly linear relationship as the infinite model when plotted in the E_n vs n^2 form. The nature of wavefunction penetration can further result in more interesting phenomena, i.e., quantum tunnelling, which will be covered in the next section.
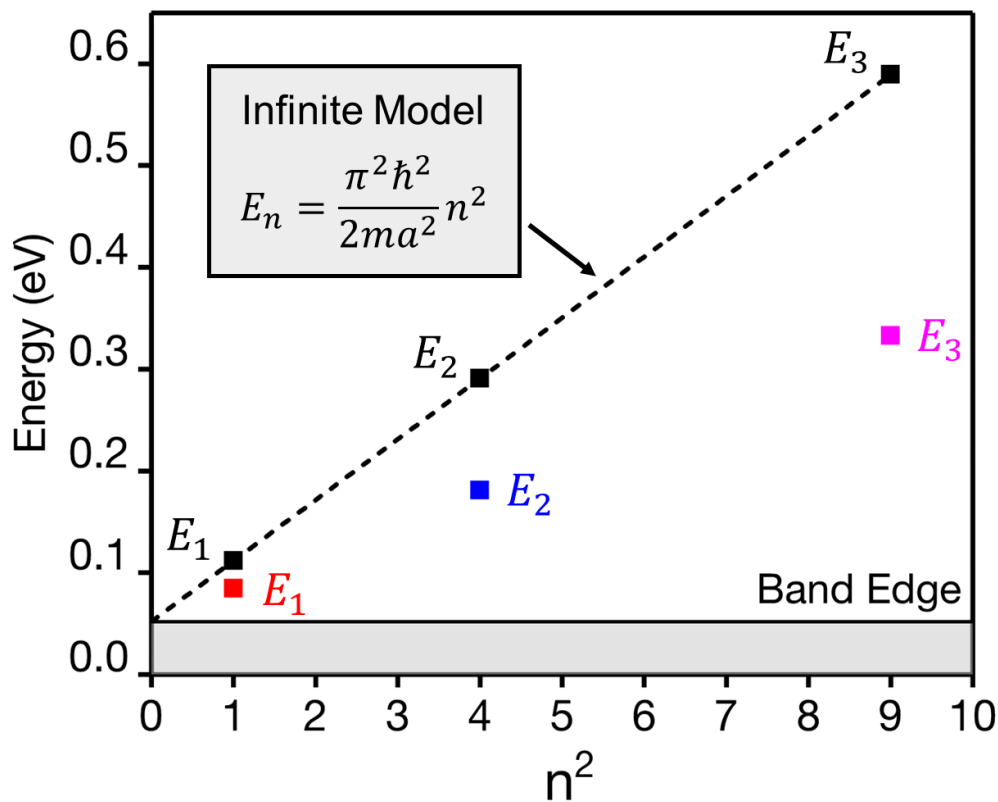
Fig 2.5 Comparison of electron energy levels between a 10nm infinite quantum well model (black) and a 10nm GaAs/Al$_{0.45}$Ga$_{0.55}$As quantum well (colour). $m = 0.067m_0$ is used in both models, which is the effective mass of electrons in GaAs.

2.2.3 Multiple Quantum Wells

Finally, we can have a look at an even more complex structure, i.e., multiple quantum wells (MQWs), which is very similar to a typical QCL structure. When two quantum wells are sufficiently distanced, one can simply treat them as two individual quantum wells, as we did in the last section. The two quantum wells will exhibit identical confined energy levels and wavefunctions, as displayed in Fig 2.6(a).
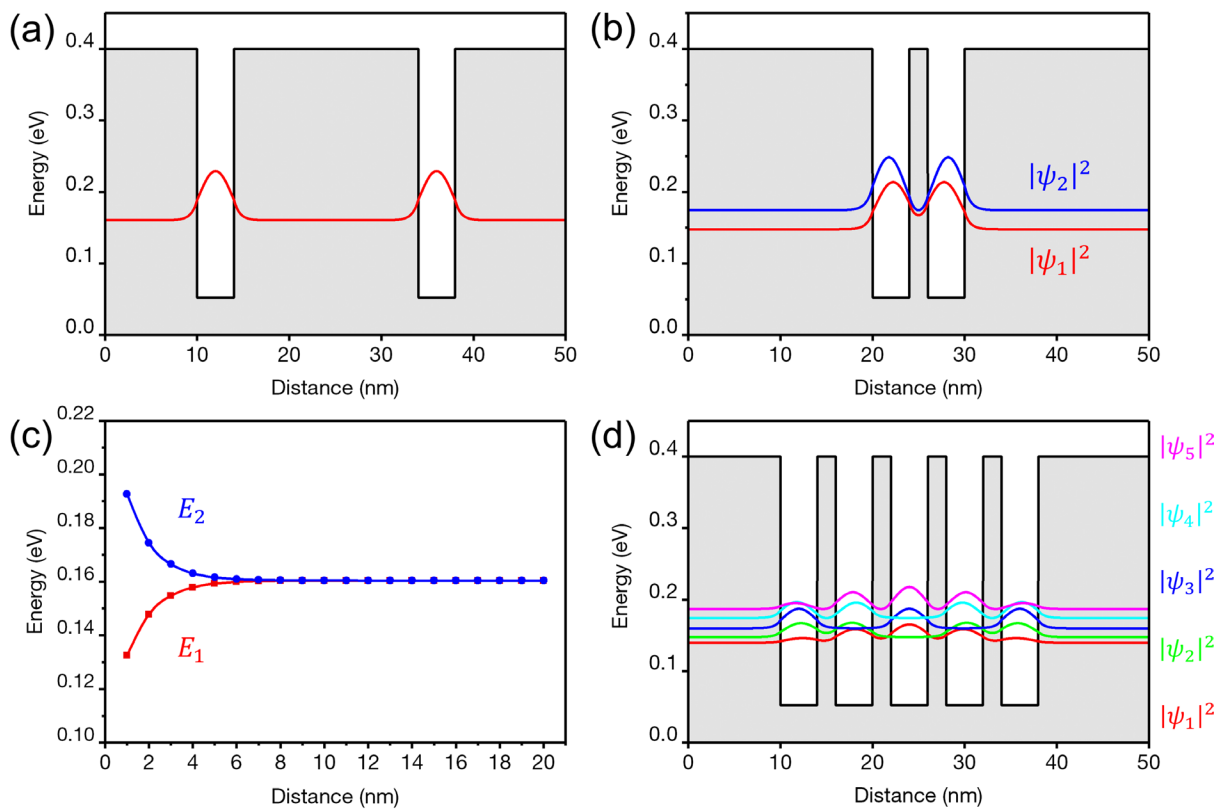
Fig 2.6 (a) Two 4nm GaAs/Al$_{0.45}$Ga$_{0.55}$As quantum wells separated by a 20nm thick barrier. (b) The barrier thickness reduces to 2nm. (c) Energies of the electron ground states vs barrier thickness in between. (d) Five 4nm GaAs/Al$_{0.45}$Ga$_{0.55}$As quantum well coupling.

However, when the two quantum wells are closely positioned, as shown in Fig 2.6(b), they exhibit a few coupling properties: (1) the wavefunctions spread over both wells, indicating an electron can move to the adjacent well despite the potential barrier, i.e., quantum tunnelling.

(2) The energy states are no longer at the same level; instead, they split in the energy space. The separation of the two energy levels is distance-related (barrier thickness), as shown in Fig 2.6(c).

Now, if we consider a case where more quantum wells are coupled, e.g., 5 QWs, as illustrated in Fig 2.6(d), we could find that five energy levels are slightly detuned in the energy space, the manifold of which thus form a quasi-continuous band, which is known as a miniband. One may notice that this is very analogous to the transition from the discrete energy levels of a single atom to the continuous energy band in the matter, where numerous atoms bonding together. Thus, electrons can move within the miniband just like in the conduction band, but most importantly, the profile of the miniband is artificially manipulated through band engineering.

2.3 Active Region of Mid-IR QCLs

This section presents a survey of a few typical active region designs of mid-IR QCLs in the development history of QCLs, such as the first QCL, the first QCL that achieved room-temperature continuous-wave operation and state-of-the-art high-power QCLs. In addition, several material systems for different emission wavelength QCLs are reviewed in section 2.3.2.
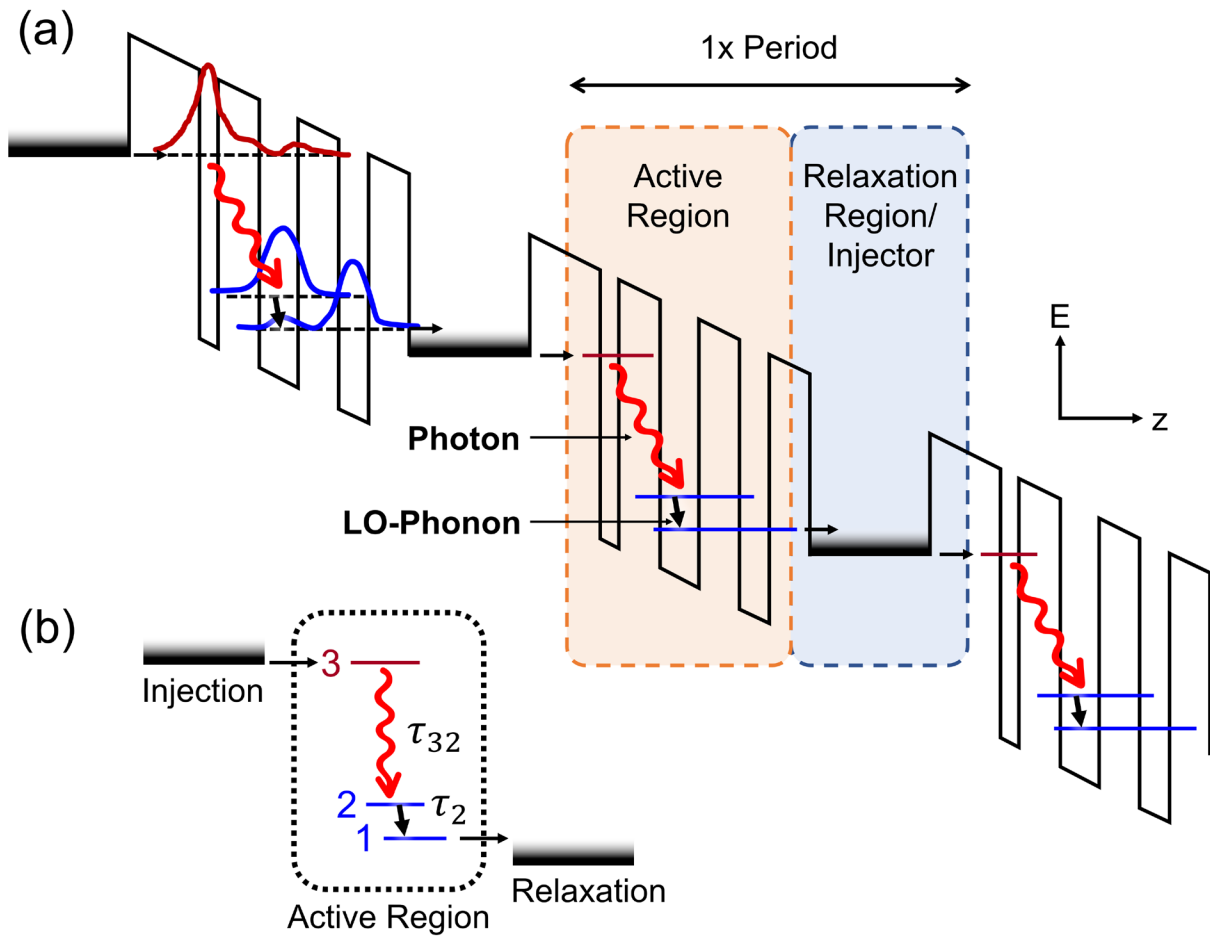
2.3.1 Active Region Design

The initial concept of a unipolar laser based on intersubband transition was proposed as early as in the 1970s by R. Kazarinov and R. Suris [2], whereas the experimental demonstration of such a laser was not succeeded until 1994 by J. Faist *et al.* [3] from F. Capasso's group at Bell Laboratories, i.e., the quantum cascade laser. Many technical or theoretical challenges prevented the realisation of such intersubband laser in the early days, one of the main difficulties being the establishment of effective population inversion within the conduction band. As a recall to Section 1.1 Laser Fundamentals, for any laser to obtain adequate optical gain to overcome losses, a sufficient population inversion between the upper and lower lasing states is required. Therefore, the active region design of QCL is all about how to create an effective population inversion between electronic levels. Nonetheless, obtaining electron population inversion within the conduction band is more problematic since the dominant intersubband transition is the ultra-fast longitudinal optical phonon (LO-phonon) scattering process, i.e., vibrations of lattice, leading to an electron lifetime at the picosecond level.

Three-Quantum-Well Design

The key to the success of the first QCL was the ingenious utilisation of LO-phonon scattering, in turn, as a depopulation measure for electron extraction of the lower lasing state, which is schematically shown in Fig 2.7. The QCL is based on $Al_{0.48}In_{0.52}As/Ga_{0.47}In_{0.53}As$ material system lattice matched to the InP substrate. The active region, where radiative transitions take place, consists of three coupled quantum wells, which therefore is also known as the three-quantum-well (3QW) design. Three confined energy levels are generated inside the active region. Level 3 and level 2 are the upper and lower lasing levels, respectively, the energy gap between which is designed to be the emission photon energy, corresponding to a wavelength of ~4.2 μm. As can be seen in the schematic diagram, the radiative transition is diagonal in the E-z space. Level 1 is the so-called depopulation level, and the energy gap between level 2 and 1 is one LO-phonon energy. Thus, electrons in level 2 will quickly relax to level 1 through electron-phonon scattering. In brief, electrons release energy *optically* when relaxing from level 3 to level 2 while *mechanically* from level 2 to 1. Thanks to this phonon-assisted depopulation approach, the lifetime of level 2 is decreased to a sub-picosecond level (τ_2 ~0.6 ps) while the lifetime of transition $3 \rightarrow 2$ remains at the picosecond level (τ_{32} ~4.3 ps). Hence, population inversion can be created between level 3 and 2.

Electrons at level 1 then tunnel into the relaxation region, which is also the injection region of the next cascade period. The relaxation/injection region is essentially a superlattice structure, which is bifunctional. On the one hand, it is transparent to the low-energy electrons at level 1 because of the internally generated miniband, so that electrons can relax to the bottom of the miniband and re-inject into the upper lasing level 3 of the next period. On the other hand, it acts as a Bragg reflector to the high-energy electrons at level 3, reducing the leakage of electrons into the continuum through quantum tunnelling.

Fig 2.7 (a) Band diagram of the first demonstrated quantum cascade laser emitting at the wavelength of ~4.2 μm; (b) Three-level active region design. The lifetime of the $3 \rightarrow 2$ transition is longer than the lifetime of level 2, i.e., $\tau_{32} > \tau_2$, so that population inversion can be achieved between level 3 and 2.

The successful demonstration of the first QCL validated the feasibility of the intersubband laser concept, but the device only operated in pulsed mode at cryogenic temperature with very high threshold current density, as several design aspects were still far from what is now known as optimal. On the other hand, many QCL designs were subsequently proposed, such as the 1QW design [4], 2QW design [5][6][7], optimised 3QW design [8], chirped superlattice design [9][10] etc., among which the *bound-to-continuum* design [11] and the *two-phonon resonance* design [12][13] brought dramatic improvements to the performance of QCLs.
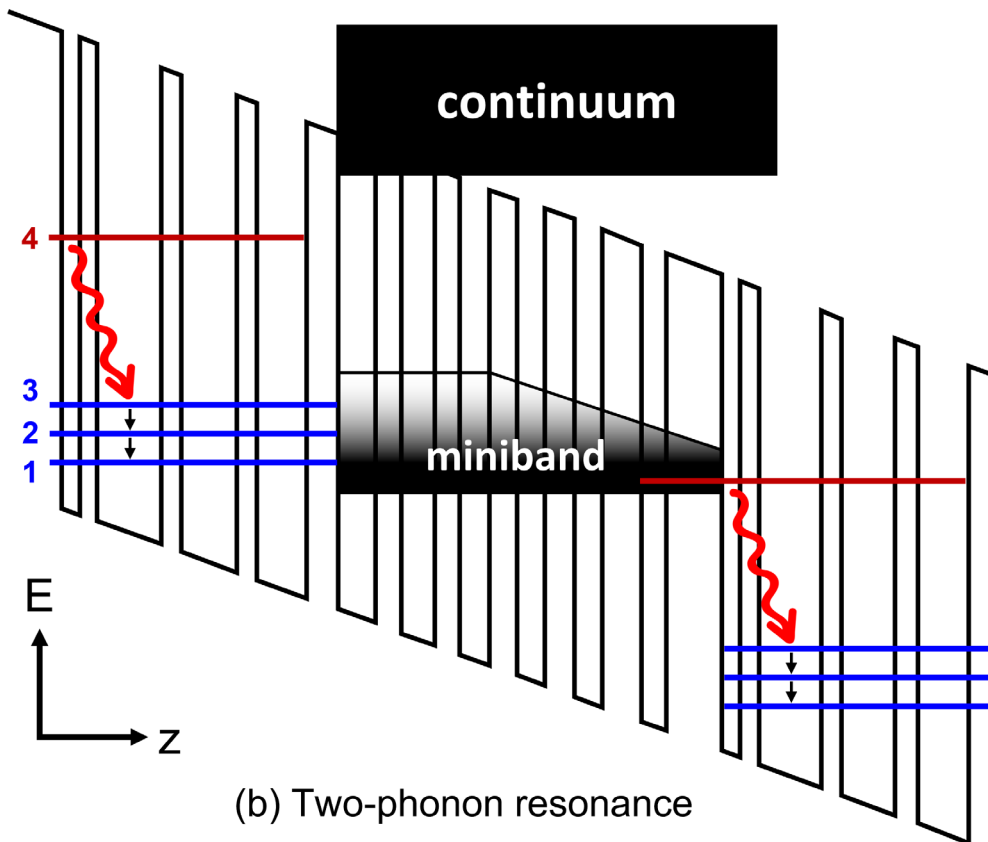
Bound-To-Continuum Design

To achieve better QCL performance, the active region design is required to (1) maximise the injection efficiency between the injection region and the upper lasing level, (2) mitigate the electron thermal escape of the upper lasing level, (3) minimise the lifetime of the lower lasing level, and (4) suppress the thermal backfilling of the lower lasing level etc. The classical 3QW design is considered to provide excellent injection efficiency thanks to the single upper lasing level design and resonant tunnelling injection, in particular with the improved funnel-shaped miniband injector [8]. However, a typical problem with this design is that although electrons can be efficiently extracted from level 2 to 1, the resonant tunnelling from level 1 to the relaxation region is found to be a much slower process, which thus becomes the bottleneck of electron transport. As a result, the achieved population inversion is not as effective as expected. In contrast, designs like the chirped superlattice do not suffer from such 'electron traffic jam', as electrons are depopulated through intra-miniband scattering – electrons can quickly relax to the bottom of the miniband and leave the miniband top relatively empty.

Combining the advantages of the 3QW design and the chirped superlattice design, the *bound-to-continuum* design was thus proposed in 2001 [11], as shown in Fig 2.8(a). Radiative transitions now no longer take place between two specific lasing levels but between the upper lasing level 1 and the energy levels at the top of the miniband. Because of that, the bound-to-continuum design is suitable for applications where broad gain bandwidth is needed, for example, broadband tuning external cavity QCL [14].

The initial QCL based on bound-to-continuum design operated in pulsed mode up to 150°C; later on, room temperature continuous-wave operations at various emission wavelengths were also reported [15][16][17].
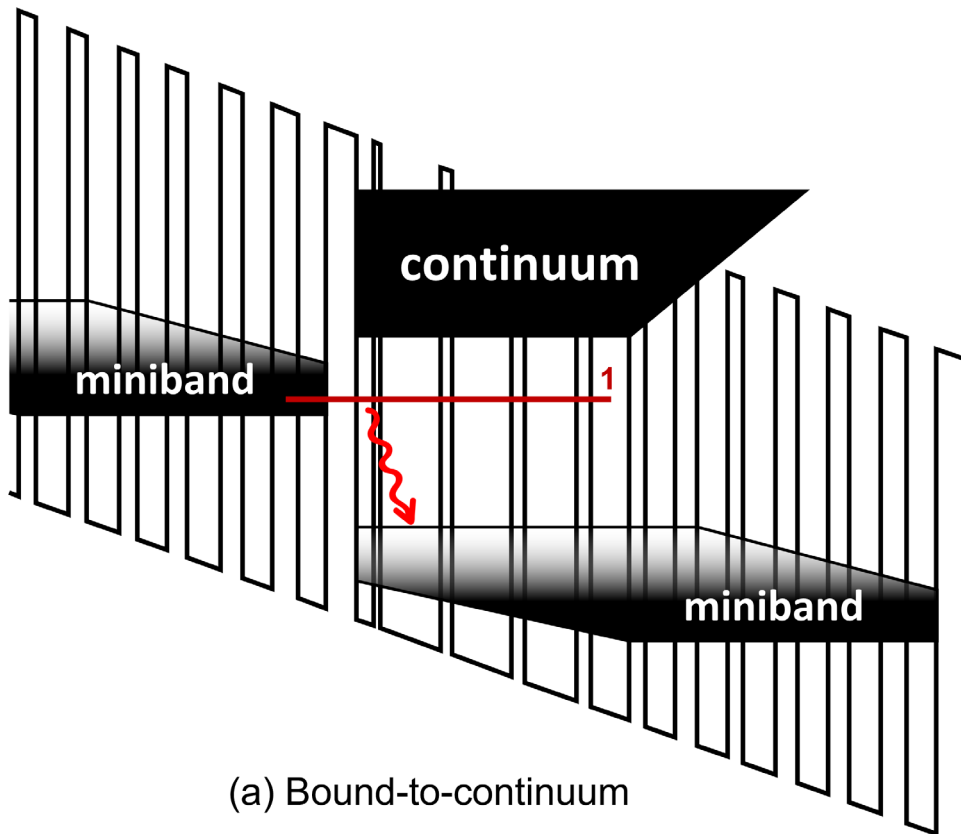
Fig 2.8 (a) Bound-to-continuum design, radiative transition takes place between the upper lasing level 1 and the miniband. (b) Two-phonon resonance design, radiative transition takes place between levels 4 and 3. $E_{32} = E_{21} = E_{LO}$.

Two-Phonon Resonance Design

Another approach to resolve the 'bottleneck' effect in the classical 3QW design is adding one more depopulation level in the active region, i.e., two-phonon resonance design. The active region of such design hence consists of four quantum wells, which is also known as a 4QW design, as shown in Fig 2.8(b). Similar to the 3QW design, the upper lasing level 4 is generated by a narrow quantum well next to the thick injection barrier. The other three wider quantum wells generate three lower coupled energy levels, 3, 2, and 1. The energy gap between every two adjacent levels is set to be one LO-phonon energy, i.e., $E_{32} = E_{21} = E_{LO}$. Compared to the single-phonon-assisted depopulation scheme, with the help of an additional depopulation state – the lifetime of the lower lasing level can be further shortened from ~0.8ps to ~0.5ps as estimated in the literature. Moreover, the lower lasing level is less affected by the electron thermal backfilling effect thanks to the additional 'buffer'. Finally, QCL based on this design with an emission wavelength of ~9.1 µm achieved continuous-wave operation at room temperature for the first time [18].

The ~9.1 µm QCL based on the two-phonon resonance design was still proposed using the lattice-matched material system, i.e., $Al_{0.48}In_{0.52}As/Ga_{0.47}In_{0.53}As/InP$. However, the 0.52 eV conduction band offset becomes somewhat less sufficient for a four-level active region design. The upper lasing state is close to the continuum, especially for shorter wavelength designs, resulting in enhanced electron leakage. Strain-compensated AlInAs/GaInAs systems were therefore started to be used in subsequential designs, in which the conduction band discontinuity is appropriately increased, reducing electron escape from the upper lasing level. Thanks to the use of strain compensated material system, the improved waveguide structure (buried-heterostructure), and optimised thermal management, many high-power QCLs have been reported based on the two-phonon resonance design [19][20][21], including the first QCL achieved over 1W output power in CW mode at room temperature [22].

Nonresonant Extraction Design

The two-phonon resonance active region design has seen tremendous success with a number of high-power QCLs reported, the highest RT CW power of which has reached 3.4W [23]. However, on the other hand, this design barely leaves free space for other structural optimisations, such as increasing the separation between levels 4 and 5 to reduce the thermal escape of electrons, because the active region thickness is virtually determined once the two optical phonon energy gaps and the radiative energy gap are defined. Furthermore, it also seems somehow 'misleading' the active region design to stick with such a phonon-assisted depopulation scheme.

To elaborate on this point, let us re-think the motivation for using the phonon-assisted depopulation approach. When the two energy levels are separated by one optical phonon energy (E_{LO}), as shown in Fig 2.9(a), the transition time τ_{21} will reach its minimum, and meanwhile, the extraction rate $\frac{1}{\tau_{21}}$ reaches its maximum, which is therefore considered the most efficient depopulation approach.
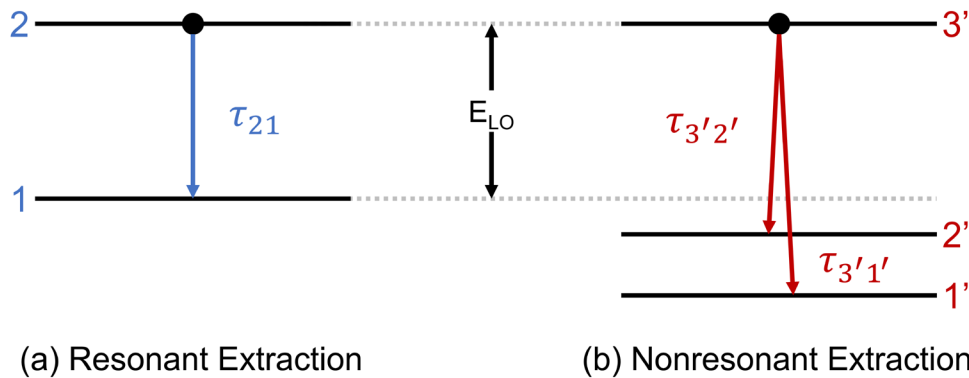

Fig 2.9 (a) Resonant extraction process. (b) Nonresonant extraction process.

Now, if we consider a three-level system, as shown in Fig 2.9(b), where $E_{3'1'} > E_{3'2'} > E_{LO}$. Due to the more significant energy separation, the transition times are also longer than the

phonon-resonance case, i.e., $\tau_{3'1'} > \tau_{3'2'} > \tau_{21}$. Despite that, we can still obtain an equivalent extraction rate of level $3'$ in this case, i.e., $\dfrac{1}{\tau_{3'1'}} + \dfrac{1}{\tau_{3'2'}} \approx \dfrac{1}{\tau_{21}}$. This is the principle behind the nonresonant extraction design, indicating that high-efficient electron depopulation can be maintained even after the removal of the resonant phonon levels, which whilst offers more design flexibility.

The band structure of a λ ~4.6 μm QCL [24] based on such active region design is schematically shown in Fig 2.10. The second phonon resonance level in a typical 4QW design is now replaced with two nonresonant levels 1 and $1'$, both have a large wavefunction overlap with level 2; therefore, the active region consists of five quantum wells, which leads to a large energy separation (100 meV) between level 3 and $1'$ under bias, thus obtaining an increased suppression of the thermal backfilling effect. The lifetime of level 2 is estimated to be ~0.34 ps, similar to that of a two-phonon resonance design.
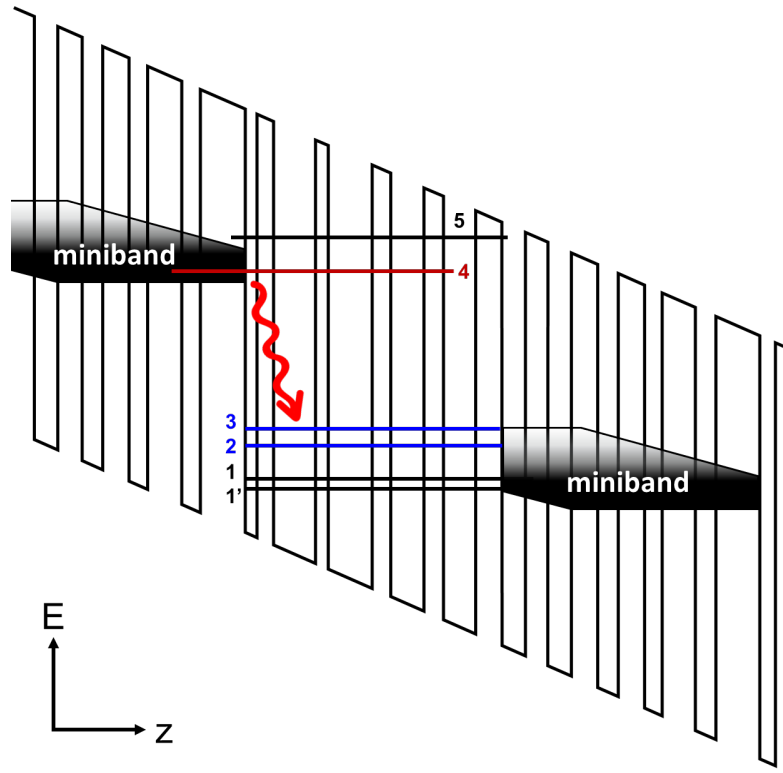
Fig 2.10 Nonresonant extraction active region design based on In$_{0.67}$Ga$_{0.33}$As/Al$_{0.64}$In$_{0.36}$As, where $E_{32} = E_{LO}$. Levels 1 and 1' are the nonresonant extraction levels, E_{21}=55 meV, $E_{21'}$=73 meV. E_{54}=63 meV. Emission wavelength ~4.6 μm [24].

Eventually, room temperature CW operation of a 5mm×11.6μm λ ~4.6 μm QCL with 3W output power and a wall-plug efficiency (WPE, defined as the ratio of optical power generation to electrical power consumption) of 12.7% was demonstrated based on this design, which was further improved to 4.5 W using a tapered waveguide geometry [25]. A λ ~9 μm QCL based on the nonresonant extraction design with 2W output power [26] was also reported shortly, proving the superiority of this design.

Shallow-Well Design

Shallow-well is another advanced active region design that can achieve watt-level output power, standing alongside the double LO-phonon resonance design and the nonresonant extraction design. In contrast to most QCL active region designs, which consist of two materials grown alternately, the shallow-well design [27] employs five materials in the active region, as shown in Fig 2.11.
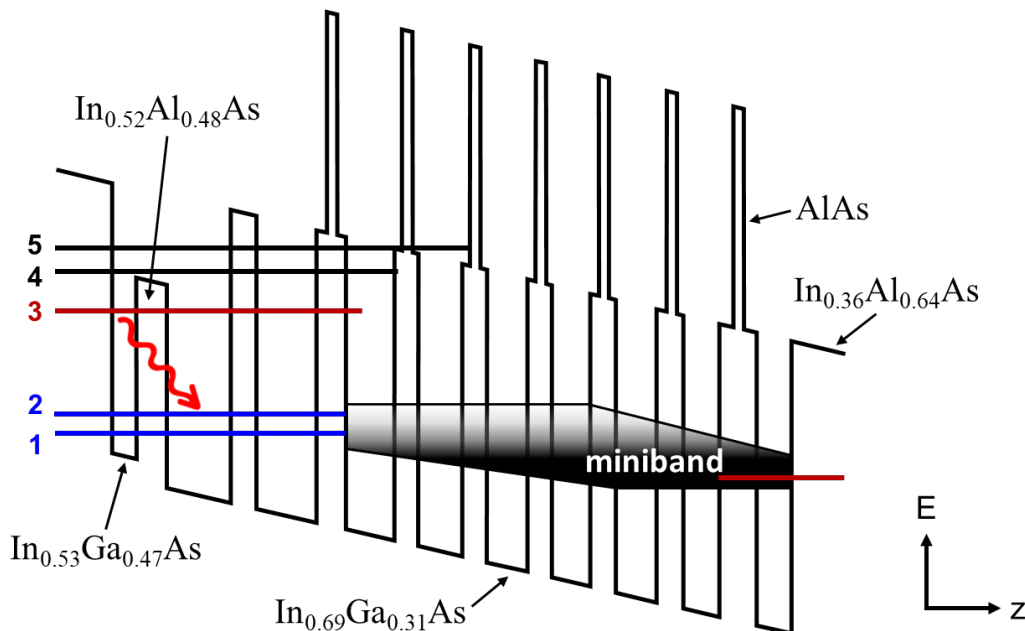
Fig 2.11 $In_{0.53}Ga_{0.47}As/In_{0.52}Al_{0.48}As/In_{0.69}Ga_{0.31}As/In_{0.36}Al_{0.64}As/AlAs$ based shallow-well active region design [27].

Provided with this extra design flexibility, several key parameters that determine the QCL performance are greatly improved in this design. The most pronounced feature in the band diagram is the particularly high potential barrier due to the use of AlAs inserts, which leads to stronger confinement of electronic states in the quantum wells, thus weakening their coupling to the continuum. The energy separation between the lower lasing level 2 and the bottom of the miniband (ground state) is 180 meV, obtaining better isolation against thermal backfilling. Furthermore, the energy spacing between the upper lasing level 4 and level 5 is up to 100 meV, which is remarkably larger than that of a two-phonon resonance design (~50 meV) and greatly prevents the thermal escape of electrons in the upper lasing state. In consequence, QCLs based on such a design show extremely high temperature insensitivity in operation.

Although this design is based on a single-phonon depopulation scheme, the outstanding suppression of thermal escape and thermal backfilling still results in a superb overall performance. In RT CW operation, a single facet output power of 3 W with a WPE of 16% was observed from an 8μm×5mm λ ~5 μm QCL based on this design. One year later, 5.1 W RT CW output power was reported [28], which held the record of the highest single facet output power obtained from a QCL for nearly ten years. In 2020, based on the same design, and by increasing the number of cascade stages from 40 to 45, a new record of 5.6 W RT CW output power was achieved with an impressive WPE of 22% [29].

2.3.2 Material Choice

Generally speaking, as described in the introduction chapter, the emission wavelength of QCLs is broadly tailorable and independent of the material bandgap due to the intersubband

transition nature; however, there remain several material-dependent considerations: (1) The shortest possible emission wavelength is clearly limited by the conduction band offset. (2) Radiative emission becomes inhibited when the designed photon energy is close to that of the optical phonon. For example, the LO-phonon energy in the GaAs/AlGaAs material system is ~36 meV; thus, GaAs-based QCLs are not capable of emitting around a corresponding wavelength of ~34.4 μm (~8.7 THz), leading to a spectral hole of the material system [30]. Furthermore, (3) different materials provide varied electron effective mass, an increase of which can result in a reduction of the oscillator strength, and thus a reduced intersubband gain [31]. For these reasons, one can find that QCLs operating in different spectral regions are based on different material systems. The four mainly used QCL material systems have been summarised in Table 2.1, provided with corresponding conduction band offset, electron effective mass, and wavelength region of common operations.

Table 2.1 Band offset and effective electron mass of different material systems

Well/Barrier Substrate	GaAs/AlGaAs GaAs	InGaAs/AlInAs InP	InGaAs/AlAsSb InP	InAs/AlSb InAs
C.B. Offset	0 – 0.35 eV	0.52 – 0.8 eV	1.6 eV	2.1 eV
Eff. Mass	0.067	0.043	0.043	0.023
Wavelength	Long MIR, THz	MIR	Short MIR	Broad

Mid-IR QCLs are typically based on the InGaAs/AlInAs material system on InP substrate and have achieved very high performance. Continuous-wave operation at room temperature has been demonstrated across the 3.8 – 12.5 μm spectral region, and particularly high-power QCLs can be realised at the wavelength around ~4.6 – 5 μm, as described in the previous section. Other than the properly large and flexible conduction band discontinuity offered by

the combination of InGaAs/AlInAs, these achievements are attributed to the use of InP, which acts not only as a substrate material but also as an ideal cladding material due to its lower refractive index. Moreover, it has excellent thermal conductivity. High-power QCLs therefore usually employ a buried-heterostructure (BH) waveguide, in which the active core is surrounded by InP, obtaining significantly improved heat dissipation and, eventually, a remarkable boost in the laser performance. More details on QCL waveguides and thermal management will be covered in the device fabrication section of Chapter 3.

GaAs/AlGaAs is a naturally lattice-matched material system despite the alloy composition of Al. Because of the small conduction band offset, it is only used for $\lambda > 8$ μm QCL designs [32][33][34], and especially for terahertz QCLs (THz-QCLs) [35]. However, the performance of GaAs-based QCLs cannot be compared to the exceptionally successful InP-based mid-IR QCLs as a result of the heavier electron effective mass, shallower barrier, worse thermal behaviour etc.

To further extend the wavelength coverage of QCLs in the shorter direction, a larger conduction band discontinuity is desired by the active region design, which can be realised by using antimonide materials. As a result, InGaAs/AlAsSb QCLs demonstrated an emission wavelength close to 3 μm for the first time [36].

InAs/AlSb is a more recent material system for QCLs. The 2.1 eV giant conduction band offset is even more extensive than that of the InGaAs/AlAsSb combination, which naturally reminds one of ultra-short wavelength QCL designs; and indeed, the shortest wavelength emitted from a QCL was demonstrated based on this material system, i.e., $\lambda \sim 2.6$ μm [37]; However, more interestingly, it also finds superiority in long wavelength QCL ($\lambda > 15$ μm) designs due to the small electron effective mass, which is promising for a high QCL gain as mentioned above. Surprisingly, room temperature continuous-wave operation of a $\lambda \sim 15$ μm

QCL was reported in 2016 [38] based on this material system, prior to which RT CW operations were only achieved by InP-based QCLs. Furthermore, RT CW operation of λ ~11 μm [39] and ~17.7 μm [40] InAs-based QCLs were also reported subsequently. Hence, the InAs/AlSb material system is seeing a replacement of the GaAs/AlGaAs material system for long wavelength mid-infrared QCLs.

# 2.4 Laser Characterisation Techniques

Laser performance is usually characterised by basic electrical and optical measurement, spectral measurement, and beam profile measurement. In this section, the setups for these characterisations are introduced.

2.4.1 Electrical and Optical Measurement

Basic electrical and optical measurement refers to the measurement of laser light-current (L-I) and voltage-current (V-I) characteristics. QCLs can be driven by a pulsed current source or continuous-wave (CW) current source, and therefore, this measurement can be conducted in pulsed mode or CW mode correspondingly. Pulsed mode is less challenging for QCL operation as very little heat will be generated in the core region compared to CW mode; thus, characterisations are usually started with a pulsed current.
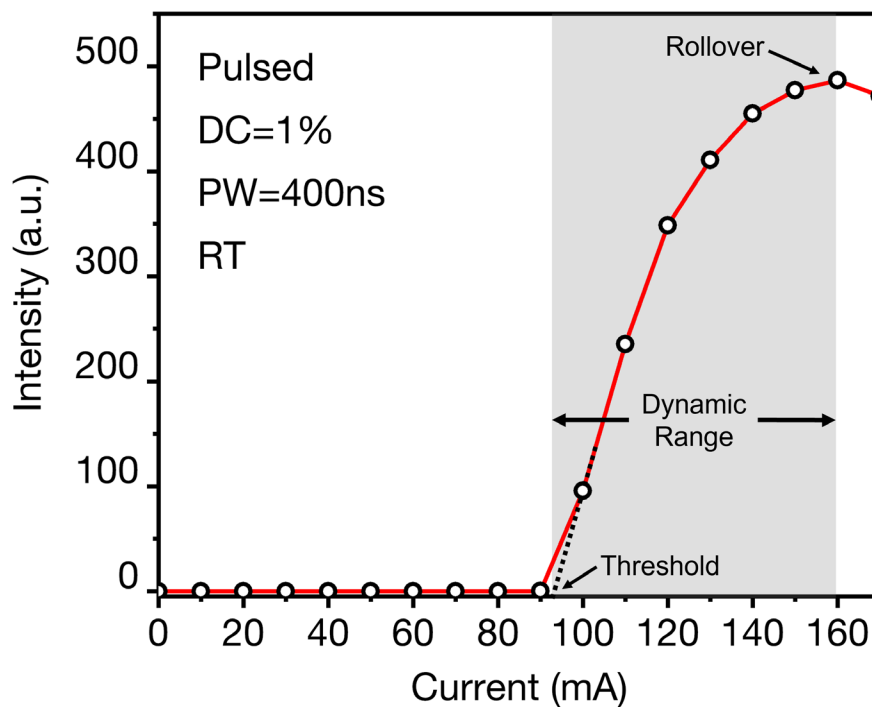
Pulsed L-I

The complete setup for pulsed mode QCL L-I measurement is schematically shown in Fig 2.12. The QCL is positioned on a temperature-controllable cooling stage and powered by the pulsed current source. The output light from the laser is collected by a thermoelectrically cooled mercury cadmium telluride (MCT) photovoltaic detector, sensitive to wavelengths between $3.2 - 9$ μm. Regular multi-meters are not suitable for pulsed mode measurement as they can only measure the time-averaged signal intensity; instead, a lock-in amplifier is used, which is connected with both the pulse source (as reference signal input) and the MCT detector (light signal input) to extract the pulsed signal from the noise.
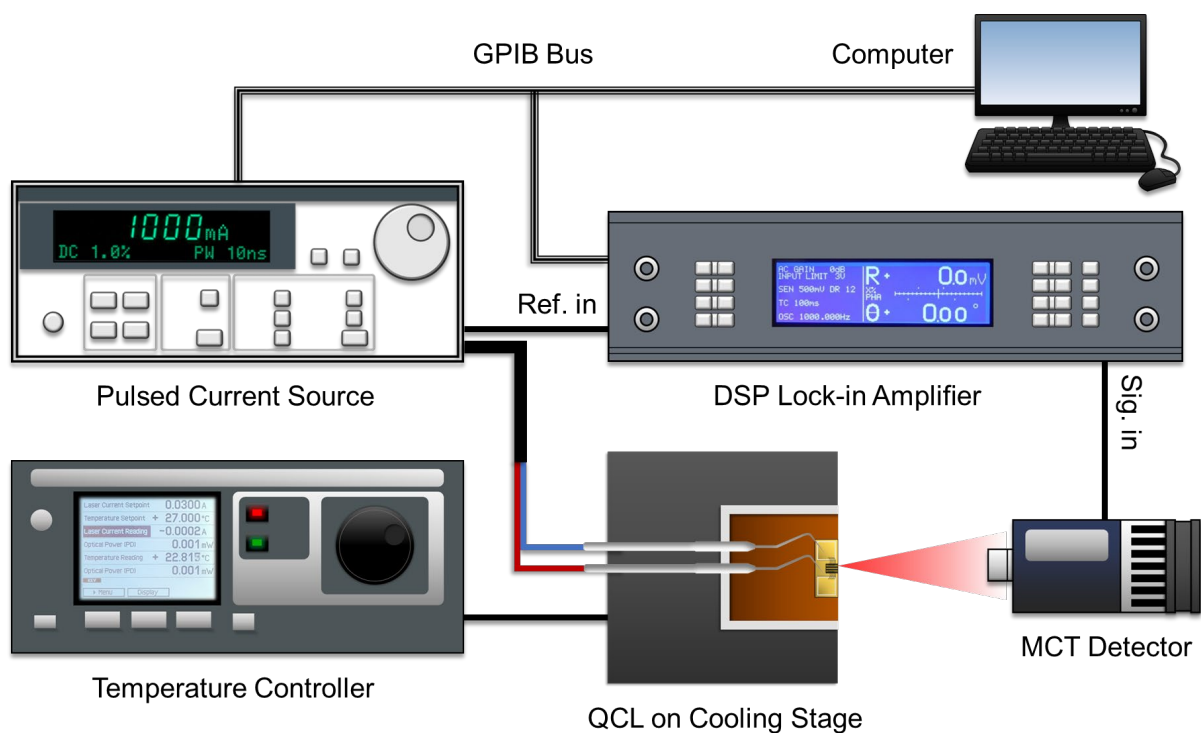
Fig 2.12 Complete setup for QCL pulsed L-I measurement. Pulsed current source model: ILX Lightwave LDP-3830. Temperature controller model: Thorlabs ITC4001. DSP lock-in amplifier model: Signal Recovery 7265. MCT Detector model: VIGO System S.A. PVI-4TE-8/MIPDC-F-20

A pulse current is defined by three parameters: current (I), pulse width (PW), and duty cycle (DC). The pulse width refers to the time duration of the current-on state in a period; the duty cycle describes the ratio of pulse width to the pulse period. For example, as shown in Fig 2.13, the L-I characteristic of a QCL is measured in pulsed mode, with 400ns pulse width and 1% duty cycle. The QCL starts to lase at a threshold current of ~93 mA, and the bias-induced rollover occurs at ~160 mA. The current range between the laser threshold and rollover is defined as the dynamic range.

Fig 2.13 Example of measured pulsed L-I data of a QCL. The device is driven by a pulsed current with 1% duty cycle and 400ns pulse width at room temperature. The threshold current is ~95 mA.

The detailed structure of the cooling stage is shown in Fig 2.14. A thermoelectric cooler (Peltier cooler) is adhered underneath the copper platform to transfer heat from the copper heatsink to a CPU liquid cooler. In the end, heat is dissipated by the fan and cooled liquid

flows back to the pump. The cooling stage can effectively control the surface temperature between 5°C and 70°C with an accuracy of 0.01°C thanks to the PID control settings of the temperature controller. Usually, cooling is not necessary for pulsed operation, but it could be helpful if one wants to characterise the pulsed mode T_0 value of a QCL via a plotting of threshold current vs heatsink temperature.
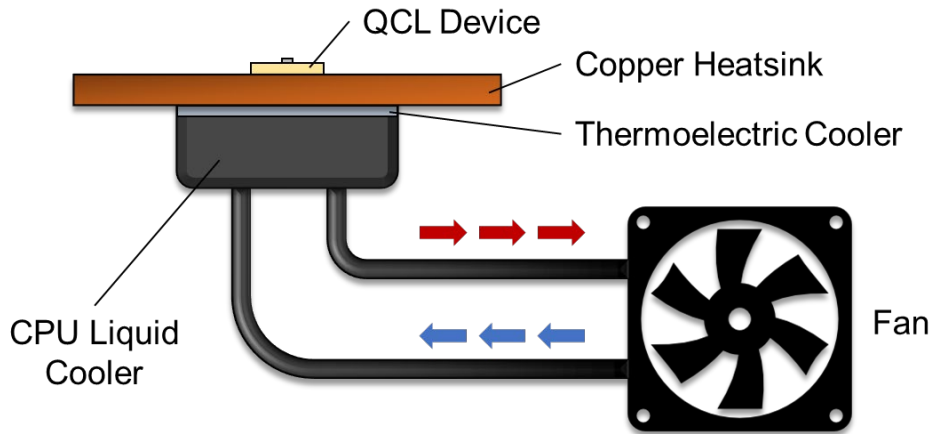
Fig 2.14 The cooling stage consists of the upper copper heatsink, a thermoelectric cooler controlled by a temperature controller, and a Corsair H60 CPU liquid cooler.

Continuous-wave L-I-V

The continuous-wave (CW) mode L-I-V measurement setup is relatively similar to the pulsed L-I setup, merely replacing the pulsed current source, MCT detector, and lock-in amplifier with a CW current source and a power meter, as shown in Fig 2.15. For CW operations, thermal management is critically important as tremendous heat will be generated in the laser core, causing electron thermal backfilling and escape, thus significantly decreasing the population inversion and increasing the lasing threshold. Hence, when the QCL device is positioned on the cooling stage, a thin layer of thermal grease is applied to the bottom of the device for better thermal contact at the interface.
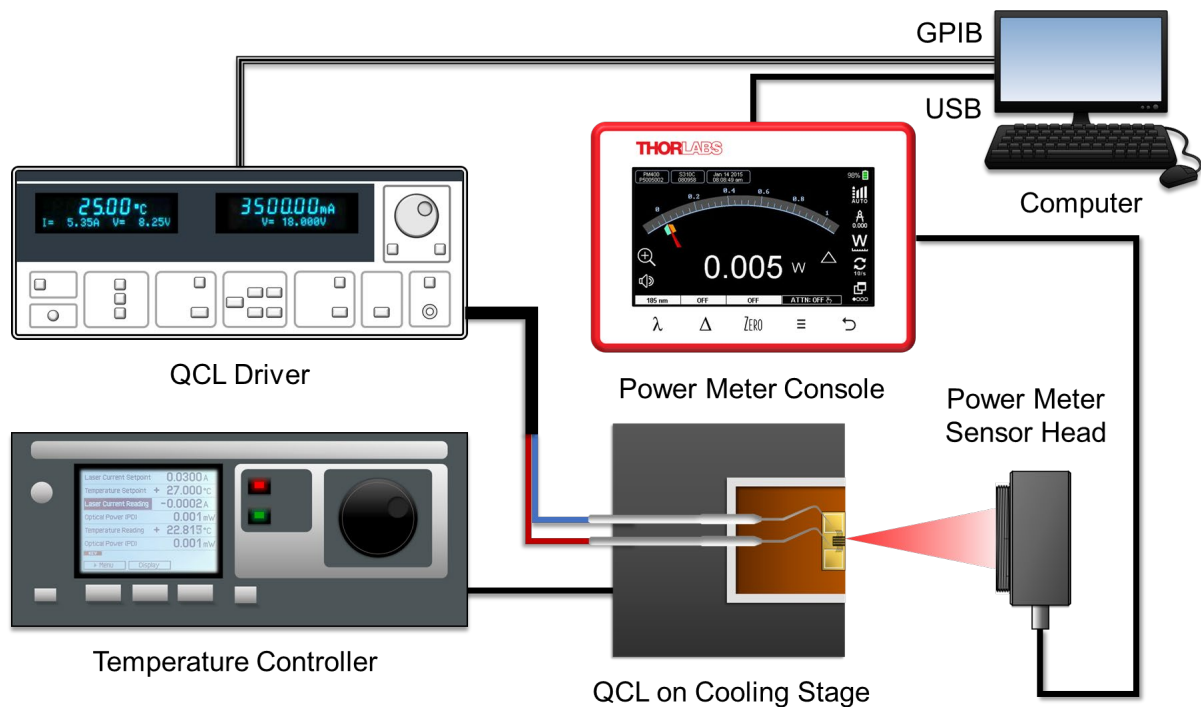
Fig 2.15 QCL CW mode L-I-V measurement setup. QCL driver model (CW source): ILX Lightwave LDC3736 quantum cascade laser controller. Temperature controller model: Thorlabs ITC4001. Power meter combination: Thorlabs PM400 optical power meter with S401C thermal power sensor.

Fig 2.16 shows the measured CW L-I-V data of two identical mid-IR uncoated FP-QCLs while the facet of device B is damaged. It can be seen that both devices have a standard QCL I-V characteristic, which is similar to that of a resonant tunnelling diode (RTD). Both devices require a certain large voltage to tilt the energy band so that all designed electronic states get aligned, before which they are super resistive. Also, an excessive voltage will lead to misalignment of electronic states again, resulting in increased resistance and degradation of laser performance, i.e., Stark-effect rollover or voltage rollover. However, for CW operations on a Peltier cooler, i.e., around room temperature, thermal rollover usually occurs before voltage rollover [41]. In contrast to the I-V characteristic of RTDs, QCLs typically operate before the negative differential resistance (NDR) region, i.e., the over-bias region.
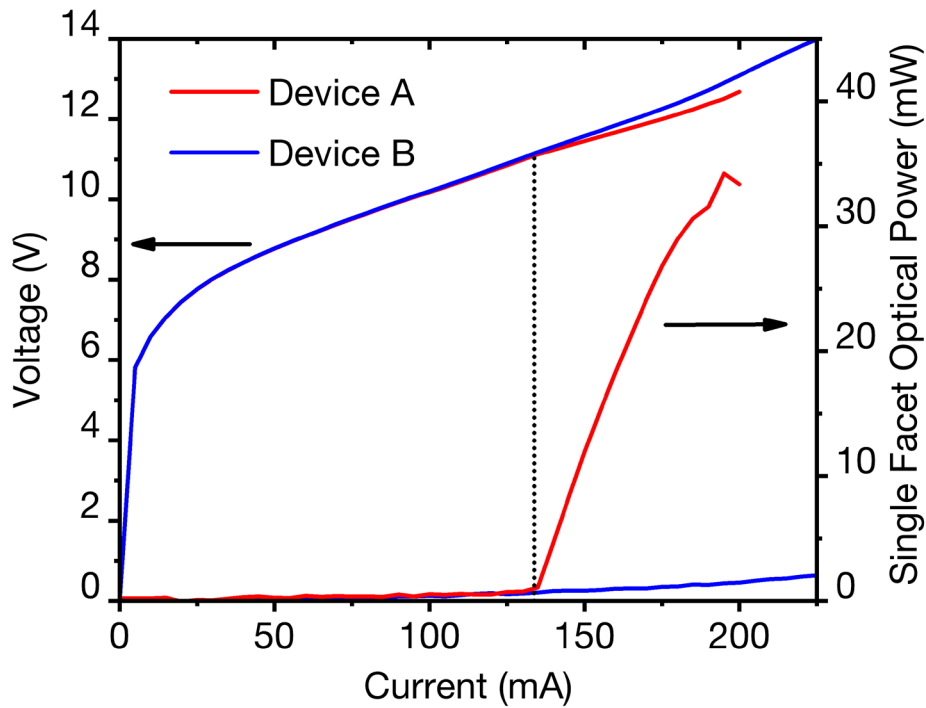
Fig 2.16 Example L-I-V data of two QCLs measured in CW mode at 15°C

The L-I curve corresponds to the coordinates on the right, and the maximum measured power of device A can be read as ~35mW. Note that this is the single-facet optical power. For these uncoated FP-QCLs, beams are emitted from both the front and back facets with the same power; therefore, the total optical power of device A is ~70mW. On the other hand, there is also a bit of emission from the dead device B caused by electroluminescence and blackbody radiation.

Although the two QCLs are from the same wafer, fabricated into the same size and packaging, and measured at the same temperature, one can notice that their I-V curves split after device A starts lasing, i.e., the lasing device tends to have a lower resistance. This is mainly caused by photon-driven transport [42], and such discontinuity of the voltage curve is even more pronounced in those high-power QCLs.

2.4.2 Spectral Measurement

The spectra of all QCL samples in this work are measured by Fourier-transform infrared spectroscopy (FT-IR), instrument model Nicolet iS50. Conventional spectrometers are based on a dispersive method: first, the beam will be spatially dispersed into different frequencies by a grating; then, a movable detector is used to measure the light intensity at different positions (frequency), which finally results in a full spectrum of the incident beam. FT-IR, in contrast, measures the beam spectrum in an indirect way, which features a number of advantages over the conventional technology, such as faster measuring speed, higher sensitivity, and simplified mechanical structure etc. The key part of the FT-IR system is the interferometer, as shown below.
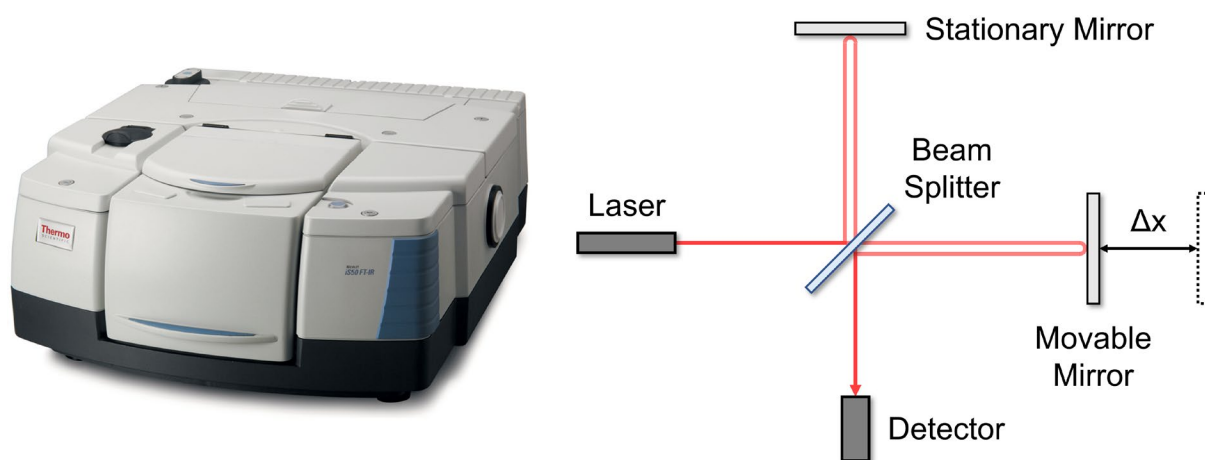

Fig 2.17 Nicolet iS50 FT-IR and the internal interferometer

A beam splitter is positioned at the centre of the interferometer, which splits the incident laser beam into two beams, 50% is reflected to the upper stationary mirror, and 50% passes through the beam splitter. The two separated beams are then reflected back by the two

mirrors and recombined at the beam splitter. As the upper mirror is stationary, the optical path of the vertical beam is also fixed. The other mirror, in contrast, is moveable within a small range (a few millimetres), and thus, the optical path of the lateral beam is correspondingly variable. Therefore, the two beams will interfere with each other when recombined at the beam splitter. Thus, the information directly collected by the detector is the interferogram, i.e., intensity vs mirror position. Then it can be converted into the spectrum (intensity vs frequency) by Fourier transformation.

Two detectors are equipped in the Nicolet iS50 FT-IR, i.e., MCT-A and DLaTGS, which are both capable of detecting light in the mid-infrared. MCT-A is a quantum detector, which provides very high detectivity, but the operation requires liquid nitrogen cooling. DLaTGS is a thermal detector with roughly two orders lower detectivity compared to MCT-A, but it can operate at room temperature. In this work, the DLaTGS detector is mainly used for spectral characterisations as the detectivity is still sufficiently high – even for the pulsed mode measurement; and most importantly, the cooling-free feature does offer considerable convenience.

An example spectrum of a 2mm-long FP-QCL measured by the FT-IR using the DLaTGS detector is shown in Fig 2.18. FP-QCLs usually emit a broad spectrum consisting of many evenly-spaced longitudinal modes due to the lack of wavelength selection. As the whole setup is not sealed and the laser is directly exposed to the air, one can see that a few longitudinal modes are suppressed or even missing as a result of air absorption. Recall Fig 1.8, the wavelength of ~5.7 μm is within the absorption region of water, and thus the signal loss is mainly because of moisture absorption.
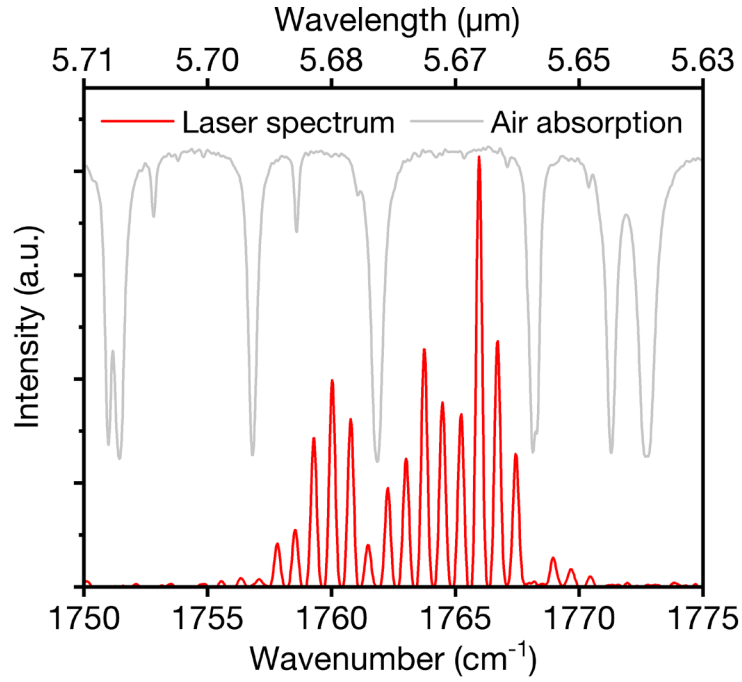
Fig 2.18 Example spectrum of a mid-IR FP-QCL measured by FT-IR. A few longitudinal modes are suppressed or missing due to air absorption.

The mode spacing gap, which is known as the free spectral range (FSR), is a cavity length (L) related term because, in an FP-laser, the light phase has to be the same after a round trip ($2L$):

$$m \frac{\lambda}{n_{eff}} = 2L \tag{2.17}$$

Where m is an integer, and n_{eff} is the effective refractive index of the laser core. For InGaAs/AlInAs-based QCLs, $n_{eff} \sim 3.3$. We may re-write the above relationship in the form of wavenumber ($1/\lambda$) because longitudinal modes are only evenly spaced in the frequency domain:

$$\frac{1}{\lambda} = \frac{m}{2 n_{eff} L} \tag{2.18}$$

For two adjacent longitudinal modes, we have:

$$\frac{1}{\lambda_0} = \frac{m}{2n_{eff}L} \tag{2.19}$$

$$\frac{1}{\lambda_1} = \frac{m+1}{2n_{eff}L} \tag{2.20}$$

From that, we can easily obtain the wavenumber difference between two adjacent modes, i.e., the FSR:

$$FSR = \frac{1}{\lambda_1} - \frac{1}{\lambda_0} = \frac{1}{2n_{eff}L} \tag{2.21}$$

Thus, we can use this simple equation to predict the mode spacing of 2mm and 3mm long mid-IR QCLs:

$$FSR_{2mm} = \frac{1}{2 \times 3.3 \times 0.2} = 0.758 \ cm^{-1} \tag{2.22}$$

$$FSR_{3mm} = \frac{1}{2 \times 3.3 \times 0.3} = 0.505 \ cm^{-1} \tag{2.23}$$

Consequently, a longer QCL will have a denser spectrum due to the smaller FSR. The FSR measured from the example spectrum of a 2mm QCL emitted at the wavelength of ~5.7 μm is ~0.742 cm^{-1}, which is reasonably close to the predicted value in eq. (2.22).

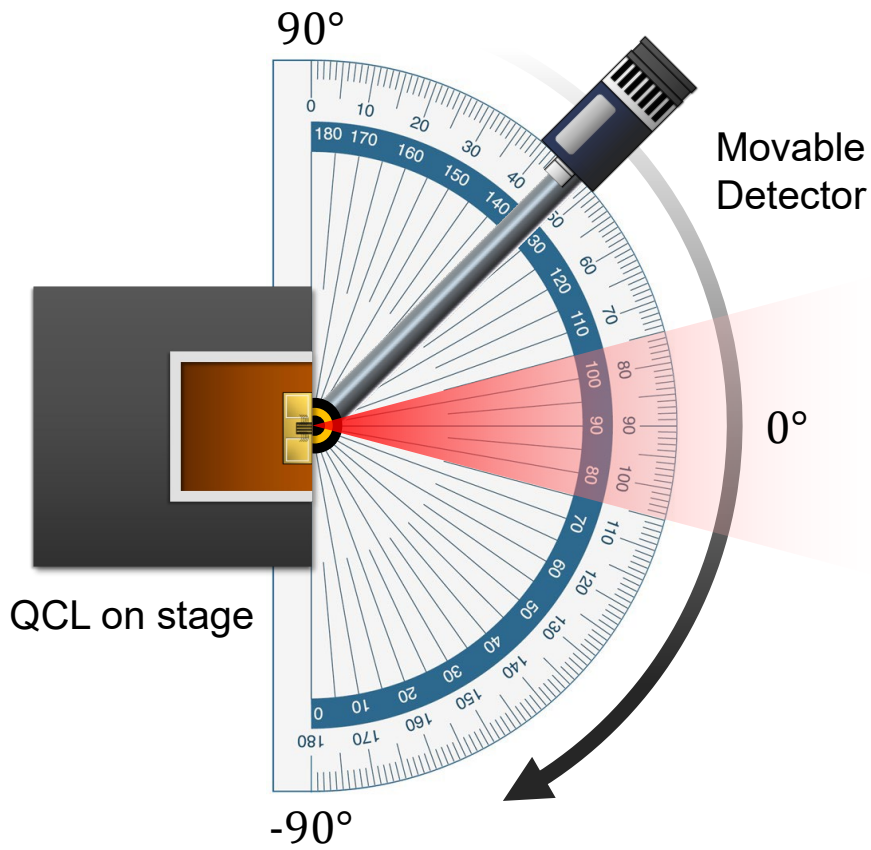## 2.4.3 Beam Profile Measurement

Beam profiles can be measured at near-field or far-field. The near-field pattern only extends over a very limited range from the laser facet, i.e., around the beam waist, which is typically measured using a specific technique called *near-field scanning optical microscope* (NSOM) [43]. NSOM employs a tapered fibre to scan the laser facet and thus collect the beam

intensity info at different positions. This technique, however, is not suitable for mid-infrared near-field measurement due to the difficult trade-off between the fibre aperture size and the delivered light intensity (smaller aperture for higher spatial resolution). Instead, one could find that the near-field of mid-IR QCLs is measured based on apertureless-NSOM [44], where an ultra-sharp tip (e.g., the AFM tip) is used to scan the laser facet, reflecting the near-field light to the far-field for analysis.

In contrast to near-field measurement, where sophisticated equipment is needed, the far-field angular distribution of a laser beam is remarkably simple to measure, the measurement setup for which can be easily built on the optical bench. In addition, the far-field pattern provides useful beam divergence information for laser users. A schematic diagram of our 'home-made' slow-axis (x-axis) far-field measurement setup is shown in Fig 2.19. The detector is mounted on a rotational rod and can therefore be moved in a circular path. The emitting facet of the QCL is positioned at the centre of the detector's motion orbit so that the beam intensity can be measured at a fixed distance at any angle. The angular position info of the detector is provided by the paper with a protractor printed on the bench surface. As the orbit radius increases, we can obtain a higher angular resolution, but meanwhile, the beam intensity decreases. Hence, there is also a trade-off between the measured signal accuracy and angular resolution, similar to the limitation of the NSOM technique in mid-IR but with less impact. In our measurement, this distance is set around 10 cm.

Fig 2.20 shows an example of measured far-field beam profile data, which was measured by a full 180° scan with a 5° step size. Single-mode lasers typically have a beam profile close to Gaussian distribution. The beam divergence is usually characterised by the FWHM (0.5 intensity) or the $1/e^2$ width (~0.135 intensity).

Fig 2.19 Setup for slow-axis far-field beam profile measurement.
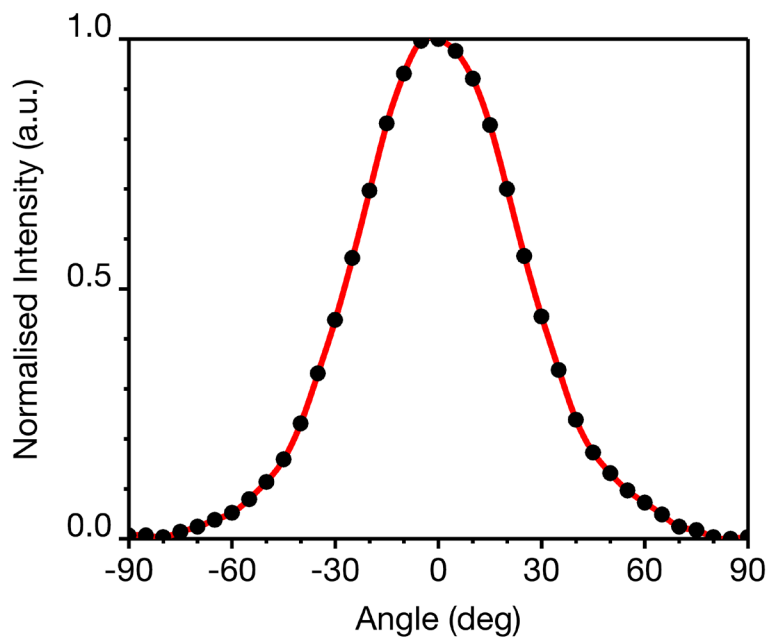
Fig 2.20 Example of a measured far-field beam pattern

2.5 Summary

This chapter mainly presented the working principle of quantum cascade lasers, starting from the introduction of quantum well theory. Electrons confined in the narrow potential well exhibit quantised energy states, which are manipulatable via well width control, i.e., layer thickness in real space. Based on this fundamental property, the active region of a QCL consists of multiple quantum wells and thus generating miniband and mini gap inside. The emission wavelength is independent of material but the active region layer thickness. The intersubband population inversion can be achieved by either resonant-phonon-assisted depopulation or intra-mini band relaxation. Several typical mid-IR QCL active region designs were reviewed, including advanced designs such as two-phonon resonance design, shallow well design, and nonresonant extraction design.

Also, three basic laser performance characterisation techniques for QCLs are introduced, i.e., L-I-V measurement, spectral measurement, and beam profile measurement. The QCL data presented later in this thesis are mainly based on these measurements.

References

[1]   1D Poisson by Gregory Snider: https://www3.nd.edu/~gsnider/

[2]   R. F. Kazarinov and R. A. Suris, "Possibility of the Amplification of Electromagnetic Waves in a Semiconductor with a Superlattice," *Soviet Physics Semiconductors*, vol. 5, no. 4, pp. 707–709, 1971.

[3]   J. Faist, F. Capasso, D. L. Sivco, C. Sirtori, A. L. Hutchinson, and A. Y. Cho, "Quantum Cascade Laser," *Science*, vol. 264, no. 5158, pp. 553–556, 1994.

[4]   J. Faist, F. Capasso, C. Sirtori, D. L. Sivco, A. L. Hutchinson, M. Hybertsen, and A. Y. Cho, "Quantum cascade lasers without intersubband population inversion," *Physical Review Letters*, vol. 76, pp. 411–414, 1996.

[5]   J. Faist, F. Capasso, C. Sirtori, D. L. Sivco, A. L. Hutchinson, and A. Y. Cho, "Vertical transition quantum cascade laser with Bragg confined excited state," *Applied Physics Letters*, vol. 66, pp. 538–540, 1995.

[6]   C. Sirtori, J. Faist, F. Capasso, D. L. Sivco, A. L. Hutchinson, S. G. Chu, and A. Y. Cho, "Continuous wave operation of mid-infrared (7.4–8.6 µm) quantum cascade lasers up to 110 K temperature," *Applied Physics Letters*, vol. 68, pp. 1745–1747, 1996.

[7]   C. Sirtori, J. Faist, F. Capasso, D. L. Sivco, A. L. Hutchinson, and A. Y. Cho, "Mid-infrared (8.5 µm) semiconductor lasers operating at room temperature," *IEEE Photonics Technology Letters*, vol. 9, pp. 294–296, 1997.

[8]   J. Faist, F. Capasso, C. Sirtori, D. L. Sivco, J. N. Baillargeon, A. L. Hutchinson, S. G. Chu, and A. Y. Cho, "High power mid-infrared ($\lambda{\sim}5\mu m$) quantum cascade lasers

operating above room temperature," *Applied Physics Letters*, vol. 68, no. 26, pp. 3680–3682, 1996.

[9]   A. Tredicucci, F. Capasso, C. Gmachl, D. L. Sivco, A. L. Hutchinson, and A. Y. Cho, "High performance interminiband quantum cascade lasers with graded superlattices," *Applied Physics Letters*, vol. 73, pp. 2101–2103, 1998.

[10]   A. Tredicucci, F. Capasso, C. Gmachl, D. L. Sivco, A. L. Hutchinson, A. Y. Cho, J. Faist, and G. Scamarcio, "High-power inter-miniband lasing in intrinsic superlattices," *Applied Physics Letters*, vol. 72, pp. 2388–2390, 1998.

[11]   J. Faist, M. Beck, T. Aellen, and E. Gini, "Quantum-cascade lasers based on a bound-to-continuum transition," *Applied Physics Letters*, vol. 78, no. 2, pp. 147–149, 2001.

[12]   D. Hofstetter, M. Beck, T. Aellen, and J. Faist, "High-temperature operation of distributed feedback quantum-cascade lasers at 5.3 μm," *Applied Physics Letters*, vol. 78, no. 4, pp. 396–398, 2001.

[13]   D. Hofstetter, M. Beck, T. Aellen, J. Faist, U. Oesterle, M. Ilegems, E. Gini, and H. Melchior, "Continuous wave operation of a 9.3 μm quantum cascade laser on a Peltier Cooler," *Applied Physics Letters*, vol. 78, no. 14, pp. 1964–1966, 2001.

[14]   R. Maulini, M. Beck, J. Faist, and E. Gini, "Broadband tuning of external cavity bound-to-continuum quantum-cascade lasers," *Applied Physics Letters*, vol. 84, no. 10, pp. 1659–1661, 2004.

[15]   S. Blaser, D. A. Yarekha, L. Hvozdara, Y. Bonetti, A. Muller, M. Giovannini, and J. Faist, "Room-temperature, continuous-wave, single-mode quantum-cascade lasers at λ~5.4 μm," *Applied Physics Letters*, vol. 86, no. 4, p. 041109, 2005.

[16]   A. Wittmann, M. Giovannini, J. Faist, L. Hvozdara, S. Blaser, D. Hofstetter, and E. Gini, "Room temperature, continuous wave operation of distributed feedback quantum cascade lasers with widely spaced operation frequencies," *Applied Physics Letters*, vol. 89, no. 14, p. 141116, 2006.

[17]   A. Mohan, A. Wittmann, A. Hugi, S. Blaser, M. Giovannini, and J. Faist, "Room-temperature continuous-wave operation of an external-cavity quantum cascade laser," *Optics Letters*, vol. 32, no. 19, p. 2792, 2007.

[18]   M. Beck, D. Hofstetter, T. Aellen, J. Faist, U. Oesterle, M. Ilegems, E. Gini, and H. Melchior, "Continuous wave operation of a mid-infrared semiconductor laser at room temperature," *Science*, vol. 295, no. 5553, pp. 301–305, 2002.

[19]   A. Evans, J. S. Yu, S. Slivken, and M. Razeghi, "Continuous-wave operation of λ∼4.8μm quantum-cascade lasers at room temperature," *Applied Physics Letters*, vol. 85, no. 12, pp. 2166–2168, 2004.

[20]   A. Evans, J. Nguyen, S. Slivken, J. S. Yu, S. R. Darvish, and M. Razeghi, "Quantum-cascade lasers operating in continuous-wave mode above 90°C at λ∼5.25μm," *Applied Physics Letters*, vol. 88, no. 5, p. 051105, 2006.

[21]   L. Diehl, D. Bour, S. Corzine, J. Zhu, G. Höfler, M. Lončar, M. Troccoli, and F. Capasso, "High-temperature continuous wave operation of strain-balanced quantum cascade lasers grown by metal organic vapor-phase epitaxy," *Applied Physics Letters*, vol. 89, no. 8, p. 081101, 2006.

[22]   Y. Bai, S. R. Darvish, S. Slivken, W. Zhang, A. Evans, J. Nguyen, and M. Razeghi, "Room temperature continuous wave operation of quantum cascade lasers with Watt-level optical power," *Applied Physics Letters*, vol. 92, no. 10, p. 101105, 2008.

[23] M. Razeghi, S. Slivken, Y. Bai, B. Gokden, and S. Ramezani Darvish, "High Power Quantum Cascade Lasers," *New Journal of Physics*, vol. 11, no. 12, p. 125017, 2009.

[24] A. Lyakh, R. Maulini, A. Tsekoun, R. Go, C. Pflügl, L. Diehl, Q. J. Wang, F. Capasso, and C. K. Patel, "3 W continuous-wave room temperature single-facet emission from quantum cascade lasers based on nonresonant extraction design approach," *Applied Physics Letters*, vol. 95, no. 14, p. 141113, 2009.

[25] A. Lyakh, R. Maulini, A. Tsekoun, R. Go, and C. K. Patel, "Tapered 4.7 μm quantum cascade lasers with highly strained active region composition delivering over 4.5 watts of continuous wave optical power," *Optics Express*, vol. 20, no. 4, p. 4382, 2012.

[26] A. Lyakh, R. Maulini, A. Tsekoun, R. Go, and C. K. Patel, "Multiwatt long wavelength quantum cascade lasers based on high strain composition with 70% injection efficiency," *Optics Express*, vol. 20, no. 22, p. 24272, 2012.

[27] Y. Bai, N. Bandyopadhyay, S. Tsao, E. Selcuk, S. Slivken, and M. Razeghi, "Highly temperature insensitive quantum cascade lasers," *Applied Physics Letters*, vol. 97, no. 25, p. 251104, 2010.

[28] Y. Bai, N. Bandyopadhyay, S. Tsao, S. Slivken, and M. Razeghi, "Room temperature quantum cascade lasers with 27% wall plug efficiency," *Applied Physics Letters*, vol. 98, no. 18, p. 181102, 2011.

[29] F. Wang, S. Slivken, D. H. Wu, and M. Razeghi, "Room temperature quantum cascade lasers with 22% wall plug efficiency in continuous-wave operation," *Optics Express*, vol. 28, no. 12, p. 17532, 2020.

[30]   N. Vukmirović, V. D. Jovanović, D. Indjin, Z. Ikonić, P. Harrison, and V. Milanović, "Optically pumped terahertz laser based on intersubband transitions in a Gan/AlGaN double quantum well," *Journal of Applied Physics*, vol. 97, no. 10, p. 103106, 2005.

[31]   E. Benveniste, A. Vasanelli, A. Delteil, J. Devenson, R. Teissier, A. Baranov, A. M. Andrews, G. Strasser, I. Sagnes, and C. Sirtori, "Influence of the material parameters on quantum cascade devices," *Applied Physics Letters*, vol. 93, no. 13, p. 131108, 2008.

[32]   C. Pflügl, W. Schrenk, S. Anders, G. Strasser, C. Becker, C. Sirtori, Y. Bonetti, and A. Muller, "High-temperature performance of GaAs-based bound-to-continuum quantum-cascade lasers," *Applied Physics Letters*, vol. 83, no. 23, pp. 4698–4700, 2003.

[33]   S. Anders, W. Schrenk, E. Gornik, and G. Strasser, "Room-temperature emission of GaAs/AlGaAs superlattice quantum-cascade lasers at 12.6 μm," *Applied Physics Letters*, vol. 80, no. 11, pp. 1864–1866, 2002.

[34]   J. Ulrich, J. Kreuter, W. Schrenk, G. Strasser, and K. Unterrainer, "Long wavelength (15 and 23 μm) GaAs/AlGaAs quantum cascade lasers," *Applied Physics Letters*, vol. 80, no. 20, pp. 3691–3693, 2002.

[35]   R. Köhler, A. Tredicucci, F. Beltram, H. E. Beere, E. H. Linfield, A. G. Davies, D. A. Ritchie, R. C. Iotti, and F. Rossi, "Terahertz semiconductor-heterostructure laser," *Nature*, vol. 417, no. 6885, pp. 156–159, 2002.

[36]   D. G. Revin, J. W. Cockburn, M. J. Steer, R. J. Airey, M. Hopkinson, A. B. Krysa, L. R. Wilson, and S. Menzel, "InGaAs/AlAsSb/InP quantum cascade lasers operating at wavelengths close to 3 μm," *Applied Physics Letters*, vol. 90, no. 2, p. 021108, 2007.

[37] O. Cathabard, R. Teissier, J. Devenson, J. C. Moreno, and A. N. Baranov, "Quantum cascade lasers emitting near 2.6 μm," *Applied Physics Letters*, vol. 96, no. 14, p. 141110, 2010.

[38] A. N. Baranov, M. Bahriz, and R. Teissier, "Room temperature continuous wave operation of InAs-based quantum cascade lasers at 15 μm," *Optics Express*, vol. 24, no. 16, p. 18799, 2016.

[39] Z. Loghmari, M. Bahriz, D. D. Thomas, A. Meguekam, H. N. Van, R. Teissier, and A. N. Baranov, "Room temperature continuous wave operation of InAs/AlSb-based quantum cascade laser at λ ~11 μm," *Electronics Letters*, vol. 54, no. 17, pp. 1045–1047, 2018.

[40] H. N. Van, Z. Loghmari, H. Philip, M. Bahriz, A. Baranov, and R. Teissier, "Long wavelength (λ > 17 μm) distributed feedback quantum cascade lasers operating in a continuous wave at room temperature," *Photonics*, vol. 6, no. 1, p. 31, 2019.

[41] S. S. Howard, Z. Liu, and C. F. Gmachl, "Thermal and Stark-effect roll-over of quantum-cascade lasers," *IEEE Journal of Quantum Electronics*, vol. 44, no. 4, pp. 319–323, 2008.

[42] H. Choi, L. Diehl, Z.-K. Wu, M. Giovannini, J. Faist, F. Capasso, and T. B. Norris, "Gain recovery dynamics and photon-driven transport in quantum cascade lasers," *Physical Review Letters*, vol. 100, no. 16, 2008.

[43] E. Betzig and J. K. Trautman, "Near-field optics: Microscopy, spectroscopy, and surface modification beyond the diffraction limit," *Science*, vol. 257, no. 5067, pp. 189–195, 1992.

[44]   N. Yu, L. Diehl, E. Cubukcu, C. Pflügl, D. Bour, S. Corzine, J. Zhu, G. Höfler, K. B. Crozier, and F. Capasso, "Near-field imaging of quantum cascade laser transverse modes," *Optics Express*, vol. 15, no. 20, pp. 13227–13235, 2007.

3 Device Growth, Fabrication and Characterisation

3.1 Introduction

This chapter describes the whole story of developing a mid-infrared quantum cascade laser within our facility, starting from wafer growth, laser fabrication to final laser characterisation. All QCL wafers presented in this thesis were grown by metal-organic vapour phase epitaxy (MOVPE) in the National Epitaxy Facility, where the world's first MOVPE-grown QCL was demonstrated [1]. More details of QCL growth are introduced in section 3.2, including a comparison of different QCL growth technologies. Then the materials were processed in our cleanroom, transforming raw wafers into double-trench ridge waveguide lasers. The standard wafer processing procedure is given in section 3.3. Fabricated devices were subsequently characterised by L-I-V, spectrum, and beam profile measurements. We found a few beam quality issues with the first fabricated QCLs (section 3.4), after which additional waveguide modelling work was carried out in section 3.5 to resolve the beam problem. Finally, the second fabrication work is presented in section 3.6, following the guidance of the simulation results.

3.2 Wafer Growth

The quantum cascade laser is a very typical example of band structure engineering, demonstrating human's ability to manipulate semiconductor energy bands with extreme precision. Nevertheless, the epitaxial growth of such sophisticated devices is not that easy. A mid-IR QCL typically consists of 30 – 40 periods of cascade active region and hundreds of ultra-thin layers, while for a THz-QCL, it can be hundreds of periods and over a thousand layers [2][3][4]. Sub-monolayer accuracy control of layer thickness, high precision control of layer composition and doping level, as well as abrupt interfaces are demanding requirements for the growth process. In addition, a stable growth rate over time is equally crucial to maintain uniformity from the first period to the last. Failure to precisely control any of these aspects could lead to a distortion of the bandstructure profile, followed by a misalignment of electron states, and finally, resulting in severe degradation of QCL performance or even non-operation. *Molecular Beam Epitaxy* (MBE) and *Metal-Organic Vapour Phase Epitaxy* (MOVPE) are the crystal growth technologies that meet these demanding and challenging conditions and are commonly used in manufacturing QCLs. Their different working mechanisms are described in this section.

3.2.1 Molecular Beam Epitaxy

The molecular beam epitaxy (MBE) [5] reactor is very similar to a thermal evaporator, though, of course, much more advanced. The internal structure of a typical MBE growth chamber is shown in Fig 3.1. The stainless steel chamber is pumped to vacuum and further surrounded by liquid nitrogen-cooled cryopanels at 77K, which act as an impurity sink in the vacuum, to create an ultra-high vacuum (UHV) environment for growth. A wafer is mounted

on the rotating substrate holder at the centre of the chamber, which is continuously rotated during the growth process for uniformity. Source elements, such as indium, gallium, arsenic, and aluminium, in ultra-pure form, are located in individual effusion cells, which can be heated and evaporated into a gas state. These gaseous-form elements then impinge and condense onto the wafer surface, forming compound semiconductors. The flux of each atomic beam can be controlled via the heating temperature, which determines the alloy composition of the epitaxial layer. The mechanical shutters can open/close to switch material and control the growth thickness. The typical growth rate in an MBE reactor is ~0.5–1μm per hour, i.e., ~0.5–1 monolayer per second.
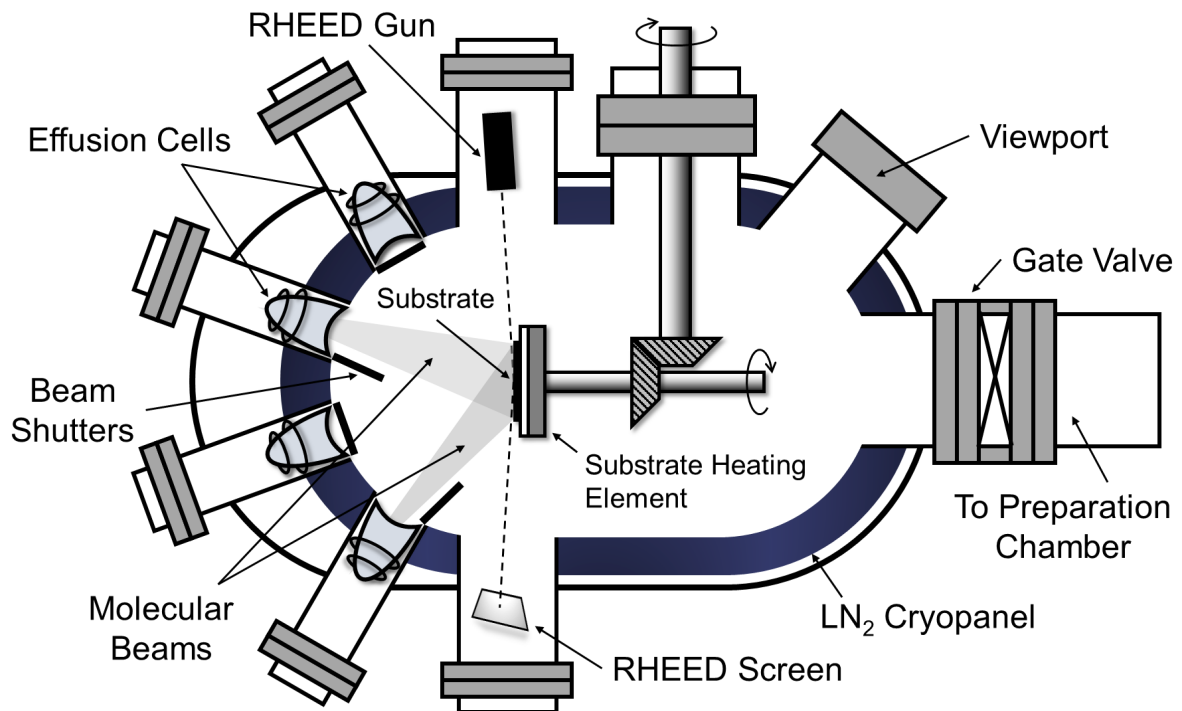
Fig 3.1 Schematic diagram of an MBE growth chamber

In addition, the growth chamber incorporates the reflection high-energy electron diffraction (RHEED) system for in-situ surface monitoring. The high-energy electron beam emitted from the electron gun will impinge the wafer surface with a grazing angle, and scattered electrons

are projected onto the fluorescent screen, forming diffraction patterns. The diffraction pattern reflects the surface quality and periodicity of layer growth.

3.2.2 Metal-Organic Vapour Phase Epitaxy

Active regions of early demonstrated QCLs were grown by either solid-source [6]-[10] or gas-source MBE [11]. Nearly ten years after its birth, the first QCL grown by metal-organic vapour phase epitaxy (MOVPE) [12] was demonstrated by the group at the University of Sheffield, which was a λ ~11.8μm QCL based on AlGaAs/GaAs material system [1], thus initiating research and development in this field [13]-[19].

Unlike the MBE system, in which elements are physically assembled to form the compound semiconductor, in the MOVPE system, epitaxial growth is achieved through the chemical reaction of reagent gases. Below is a simple example illustrating the fundamental difference in methods of forming GaAs in MBE and MOVPE systems.

- MBE: Ga + As → **GaAs**

- MOVPE: $Ga(CH_3)_3 + AsH_3 → $ **GaAs** $ + 3CH_4\uparrow$

The reagent gases are typically known as precursors in MOVPE. Organometallics are the commonly used group III precursors, such as trimethylgallium (TMGa), trimethylindium (TMIn), trimethylaluminum (TMAl) etc. And group V precursors are usually hydrides, e.g., arsine (AsH_3) and phosphine (PH_3). A schematic diagram of an MOVPE system is shown in Fig 3.2. Group III and V precursors are flowed into the reactor by a carrier gas, usually purified H_2 or N_2. SiH_4 is the dopant precursor used for n-doping in III-V compound semiconductors. In the quartz reactor, the substrate is positioned on a susceptor, which can be heated to the required chemical reaction temperature (~700°C) by surrounding RF coils. Thus,

precursors will pyrolyse on the heated substrate, and epitaxial growth naturally occurs. Alloy composition and epitaxial layer thickness are controlled by gas flow rates and source switching. Wasted gases are pumped into a scrubber for neutralisation before emission.
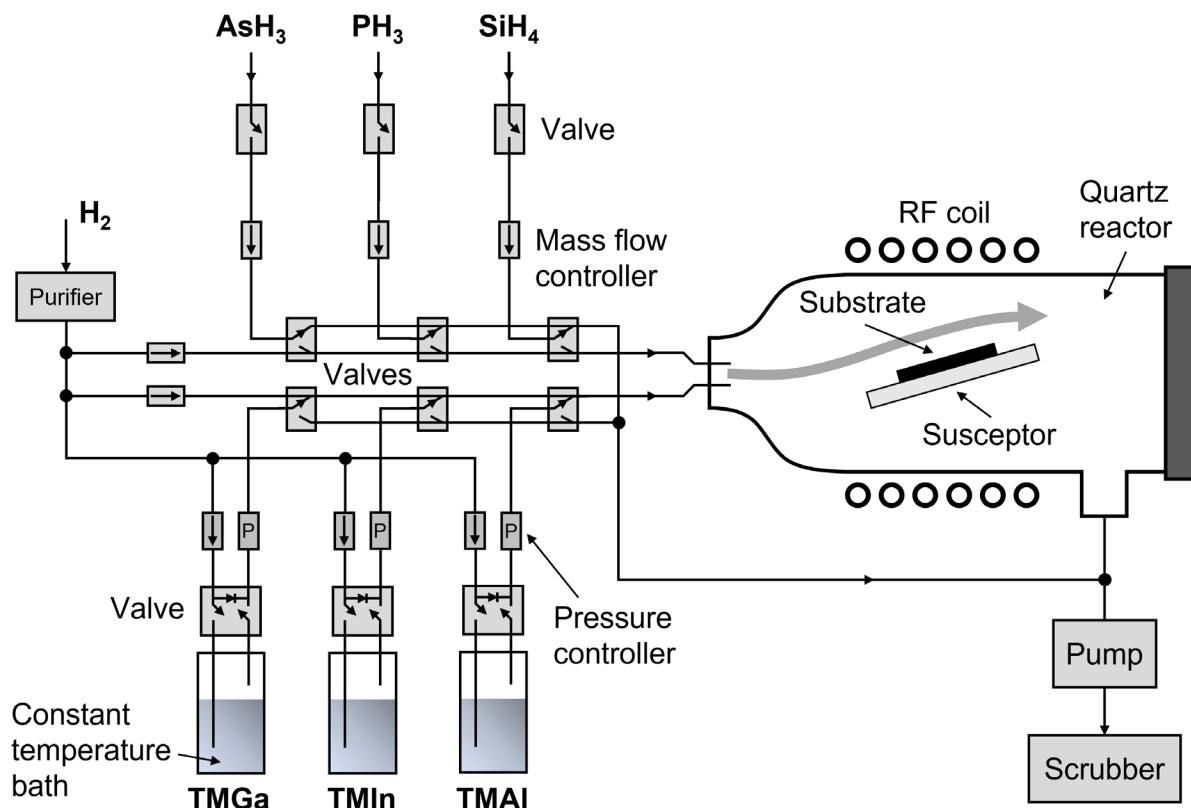

Fig 3.2 Schematic diagram of the MOVPE system with a horizontal flow reactor

In contrast to the MBE growth chamber, which employs a UHV environment, the MOVPE reactor operates at atmospheric pressure or below; thus, it cannot be equipped with the RHEED system but optical in-situ surface monitoring systems. On the other hand, MOVPE features a more stable growth rate thanks to the help of mass flow controllers. Furthermore, the growth rate of MOVPE can typically be 5–10 times faster than that of MBE, i.e., ~5 μm per hour, which is promising for the mass production and commercialisation of

semiconductor devices, thus generally favoured by the industry. As a matter of fact, MOVPE has been the mainstream platform for conventional p-n junction-based photonic device manufacturing. In addition, MOVPE also has demonstrated its capability to grow high-performance QCLs comparable to MBE-grown QCLs [20].

However, one common observation in MOVPE-grown QCLs is the more significant error between the actual emission wavelength and the predicted value than MBE-grown QCLs. For an identical λ ~9.3 µm design [21], MOVPE-grown QCLs from different groups exhibited a wavelength difference of 1.6 µm [22][23]. The main reason is that the alloy composition switching at the heterointerface in MOVPE is not as abrupt as MBE because of the precursor residence issue, which results in a compositionally graded interface, followed by slightly lower electronic energy levels, as shown below. The higher growth temperature is also suggested to contribute to this problem, considering that the growth temperature in MOVPE is typically ~100°C higher than that in MBE [24, p. 11].

(a) Abrupt interface   (b) Graded interface
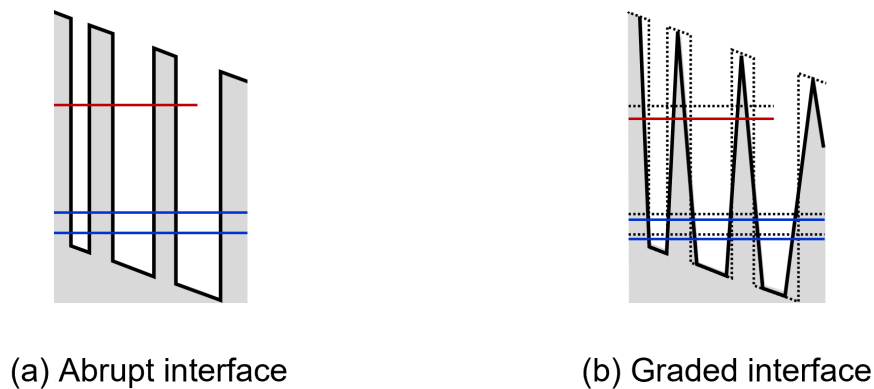
Fig 3.3 Electronic states in (a) abrupt interface and (b) graded interface active region

Eventually, MOVPE-grown QCLs with precise emission wavelengths as MBE-grown QCLs were ironically realised by growing at the 'MBE speed' with additional growth interruptions at each heterointerface [23]. From this perspective, it may seem to one that MOVPE is not

that superior to MBE in terms of growth efficiency. Nonetheless, the capability to grow InP cladding layers remains a huge advantage, given that phosphide growth in MBE is more of a problem. This dramatically simplifies the whole growth process as the active region and InP cladding of InP-based QCLs can be grown in a single run without transferring samples between different reactors. Furthermore, the selective area growth of insulating InP for buried heterostructure waveguide QCLs is also done in MOVPE, which is a crucial approach for high-performance InP-based mid-IR QCLs, as mentioned in Chapter 2.

In summary, both the MBE and MOVPE techniques can be used to grow the active region of mid-IR QCLs and achieve high performance. However, for any application where precision in wavelength is critically required, MBE-grown QCLs are the better choice.

3.2.3 Wafer Specs

Four QCL wafers were prepared for the work, which were all grown by a horizontal flow MR350 MOVPE reactor (similar to that in Fig 3.2 with a single 2-inch wafer capacity) in the EPSRC National Epitaxy Facility at the University of Sheffield and labelled as MR3877, MR3879, MR4241, MR4243 respectively. The four wafers have identical active region designs, i.e., two-phonon resonance based on strain-compensated $In_{0.6}Ga_{0.4}As/Al_{0.58}In_{0.42}As$ material system on InP. Fig 3.4(a) shows the band diagram of the active region simulated by nextnano.QCL, which is now known as nextnano.NEGF [25].

Nextnano.QCL is based on the non-equilibrium Green's function (NEGF) formalism, which is particularly suitable for describing open quantum systems, where particles can enter or leave the system (i.e., non-equilibrium), such as the electron transport in QCLs. Moreover, electron scattering effects are also considered, e.g., charged impurity scattering, interface

roughness scattering, alloy scattering, electron-electron scattering etc., which are described as self-energies in the NEGF approach as illustrated in Fig 3.4(b) [26]. The self-consistent NEGF solver starts from an initial guess of the lesser Green's function ($G^<$) from the Schrödinger equation; then the mean-field electrostatic potential can be obtained by resolving the Poisson equation; subsequently, the self-energies and the retarded Green's function can be further derived, followed by the update of the lesser Green's function $G^<$. Thus, $G^<$ can be iterated until the convergence is achieved. Finally, the current and optical gain can be calculated based on the electron density matrix, which is obtained from $G^<$.

With regards to the active region design, the thickness (nm) of each epitaxial layer in a single cascade period starting from the injection barrier is: **4.0**, 1.3, **1.3**, 5.1, **1.3**, 4.5, **1.4**, 4.0, **2.3**, 3.1, **1.8**, 2.8, **1.9**, 2.5, **2.0**, **2.4**, **2.2**, **2.3**, **2.8**, 2.2, where **Al$_{0.58}$In$_{0.42}$Ga** barrier layers are shown in **bold** and n-doped layers are underlined. The early demonstration work of this design, i.e., broad area lasers and pulsed operations, has been published in ref. [27][28].

(a)
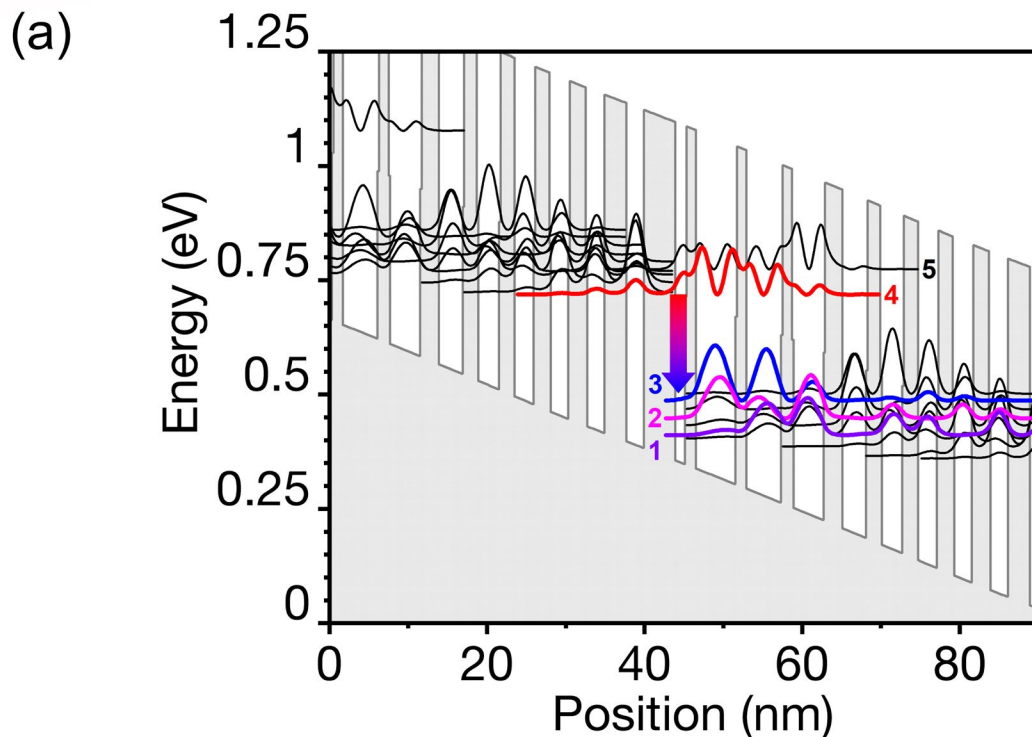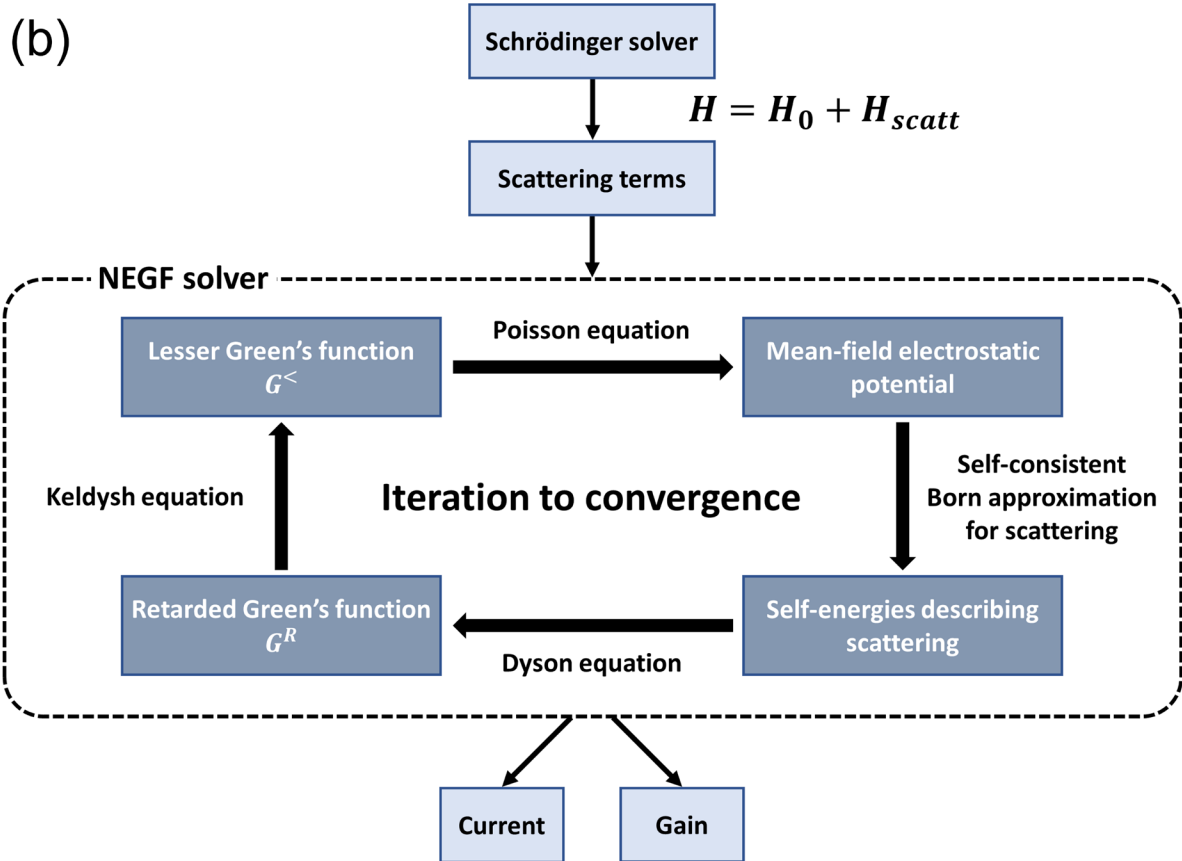
Fig 3.4 (a) Band diagram of the two-phonon resonance design QCL, emitting at a theoretical wavelength of ~5.4μm, simulated in nextnano.QCL [25] using the default material database with a 70kV/cm electric field applied. (b) Program flow of the NEGF solver [26].

Since the working principle of the two-phonon resonance design (4QW) has been elaborated in section 2.3 and ref. [27][28], it will not be repeated, except to highlight a few key parameters here: (1) Radiative transitions will take place between levels 4 and 3 with a designed emission photon energy of ~230 meV, corresponding to an emission wavelength of ~5.4 μm. (2) Levels 2 and 1 are the phonon-assisted depopulation states; hence the energy gap between levels 3→2 and 2→1 is equal to the optical phonon energy of ~40 meV. (3) The energy required for an electron to jump from level 4 to 5 is ~56 meV, which is greater than the electron's average thermal energy at room temperature (~25 meV), preventing electron thermal escape from the upper lasing state and thus facilitating operation above 300K.

In terms of growth, all the wafers possess 35 cascade active regions, and the main differences are in the doping level and the overgrowth process of the InP cladding layer, as underlined in Table 3.1. In brief, MR3879 has doubled n-doping level compared to other samples; the active region and the InP top cladding of wafers MR4241 and MR4243 were grown in separated runs. After the MOVPE growth process, wafer qualities were characterised; commonly used techniques are X-ray diffraction (XRD) [29] and transmission electron microscopy (TEM) [30].

Table 3.1 Summary of the four MOVPE-grown QCL wafers

| Wafer	Periods	Doping [cm^{-3}]	QCL Design	Material Well/Barrier	InP Clad Overgrowth
MR3877	35	1×10^{17}	$\lambda \sim 5.4$ µm, 4QW	In$_{0.6}$Ga$_{0.4}$As/Al$_{0.58}$In$_{0.42}$As	One run
MR3879	35	$\underline{2 \times 10^{17}}$	$\lambda \sim 5.4$ µm, 4QW	In$_{0.6}$Ga$_{0.4}$As/Al$_{0.58}$In$_{0.42}$As	One run
MR4241	35	1×10^{17}	$\lambda \sim 5.4$ µm, 4QW	In$_{0.6}$Ga$_{0.4}$As/Al$_{0.58}$In$_{0.42}$As	Separated run
MR4243	35	1×10^{17}	$\lambda \sim 5.4$ µm, 4QW	In$_{0.6}$Ga$_{0.4}$As/Al$_{0.58}$In$_{0.42}$As	Separated run

3.3 Device Fabrication

This section describes the fabrication procedures of ridge waveguide QCLs. All devices presented in this thesis were fabricated following the same procedures but different in ridge width. Laser packaging, i.e., chip mounting and wire bonding, is introduced after the fabrication section. Wafer processing and device packaging critically determine the optical loss and thermal management of the fabricated device, and thus the final device performance. Therefore, Device fabrication and wafer growth are equally crucial to the final performance.

## 3.3.1 Double-Trench Waveguide Processing

The QCLs were all fabricated into the ridge waveguide (RWG) structure. The RWG is defined by double-trench etching rather than the standard RWG processing, as required by the QCL hybrid integration project. More details of the integration scheme are introduced in Chapter 5. The process flow is schematically given in Fig 3.5. Firstly, (a) the 2-inch wafer is cleaved into smaller pieces using a diamond scriber and then bath cleaned through three solvents, i.e., n-butyl, acetone, and isopropyl alcohol (IPA), sequentially. This method will be used a few times in following fabrication procedures for sample cleaning. The cleaned wafer is then blown dry with nitrogen gas. Once the wafer is clean and dry, (b) ~1 μm thick SiO_2 is deposited onto the wafer surface by plasma-enhanced vapour deposition (PECVD) to form the hard mask. (c) A photoresist layer is further spun onto the surface (SPR350, 4000RPM, 30s), and (d) then a standard photolithography process is conducted to define the ridge waveguide pattern. (e) After hotplate baking, the ridge pattern is subsequently transferred from the solidified photoresist to the hard mask by inductively-coupled plasma (ICP) etching (Ar/CHF_3). Once the hard mask is completely open, the ridge waveguide can be shaped by another ICP etching of two trenches (f). Ar/$SiCl_4$ gases are used for the InP cladding and active region etching, and the process stops when the active region layer is laterally cut off by the trenches. (g) The remaining SiO_2 hard mask is then removed by hydrofluoric acid (HF). (h) Next, a ~500 nm thick silicon nitride (Si_3N_4) layer is deposited to cover the whole ridge in PECVD for electrical isolation. (i) The ridge top is re-opened for top contact formation by photolithography followed by selective reactive ion etching (RIE) of the exposed Si_3N_4, similar to the steps (c) – (e). After that, a ~20 nm thick titanium layer is deposited onto the top in the thermal evaporator, followed by ~200 nm gold deposition. The former acts as an adhesion layer between the semiconductor and gold. For the purpose of better heat dissipation, more uniform metal coverage of the sidewall and saving precious metals, the gold layer is

further thickened by 2 µm using the electroplating technique (j). After the completion of top structures, (k) the InP substrate is mechanically thinned to ~200 µm in the polisher to reduce the thermal dissipation path and finally (l) back ohmic contact is deposited with ~20 nm InGe layer and ~300 nm gold layer. The wafer is then ready for laser facet cleaving.
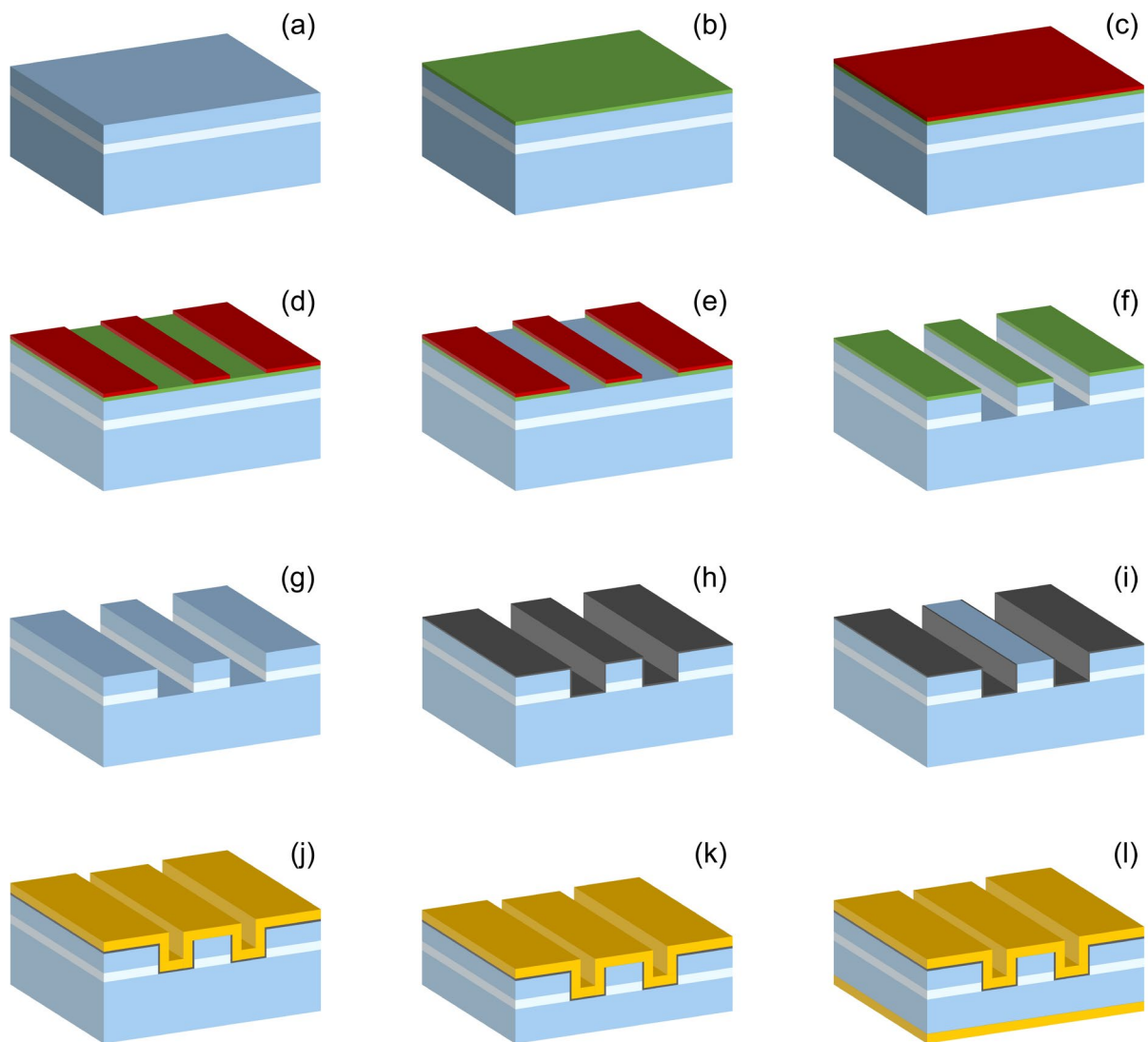
Fig 3.5 Fabrication procedures of double-trench ridge waveguide QCL. (a) wafer cleaving and cleaning, (b) silicon dioxide deposition, (c) photoresist coating, (d) photolithography, (e) hard mask formation, (f) double-trench etching, (g) hard mask removal and sample cleaning, (h) isolation layer deposition, (i) top contact window opening, (j) top contact deposition and electroplating, (k) wafer thinning, (l) back contact deposition.

As described above, the dry-etching method is used for the double-trench ridge waveguide formation. Compared to wet-etched ridges, dry-etched ridges have nearly vertical sidewalls thanks to the anisotropic etching rate in ICP, as illustrated in Fig 3.6 below.
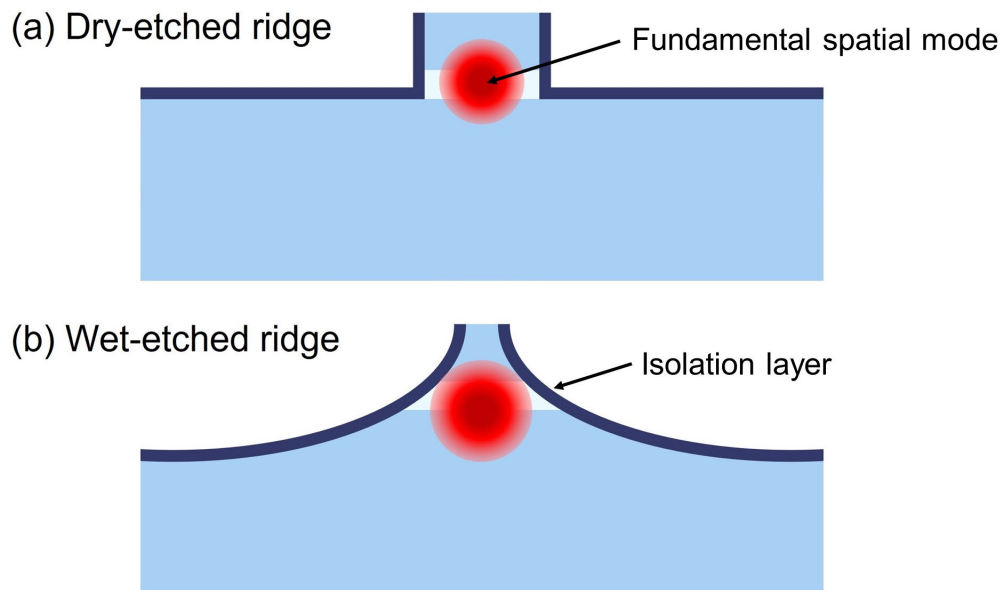
Fig 3.6 (a) Dry-etched and (b) wet-etched ridge waveguide at the same core width.

When the core width is sufficiently wide, e.g., 50 μm, the slope of sidewalls does not cause a significant difference in laser threshold or mode confinement. While in narrow wet-etched ridge lasers, the spatial mode will be pushed down to the InP substrate region due to the trapezoid shape of the laser core, which leads to a decrease of overlap between the laser beam and the active region, reducing the laser gain. Meanwhile, the spatial mode is very close to the isolation layer, causing surface plasmon mode coupling and resulting in a much higher waveguide loss [31]. In contrast, the fundamental spatial mode in the dry-etched ridge is located at the centre of the laser core and distanced from the lossy sidewalls. Therefore, for the fabrication of narrow-ridge lasers, wet-etched devices can have remarkably higher thresholds than dry-etched devices and thus disfavoured here.

For the first fabrication, four MOVPE-grown wafers were all processed but slightly different in the ridge width definition. MR3877 and MR4241 have a ridge width of 6.5 µm, while MR3879 and MR4243 have a ridge width of 8 µm. After wafer processing, ridges were cleaved into 2 mm long Fabry-Pérot (FP) cavities, in which the two cleaved facets naturally act as reflecting mirrors with a reflectivity of ~27%. Fig 3.7 shows the front facet of a QCL made from wafer MR3877 with a ~6.5 µm wide ridge, which was taken by scanning electron microscope (SEM). One can see that the practical device has a trapezoidal ridge, and it is labelled as 6.5 µm-wide, typically meaning that the core width (active region) is 6.5 µm.
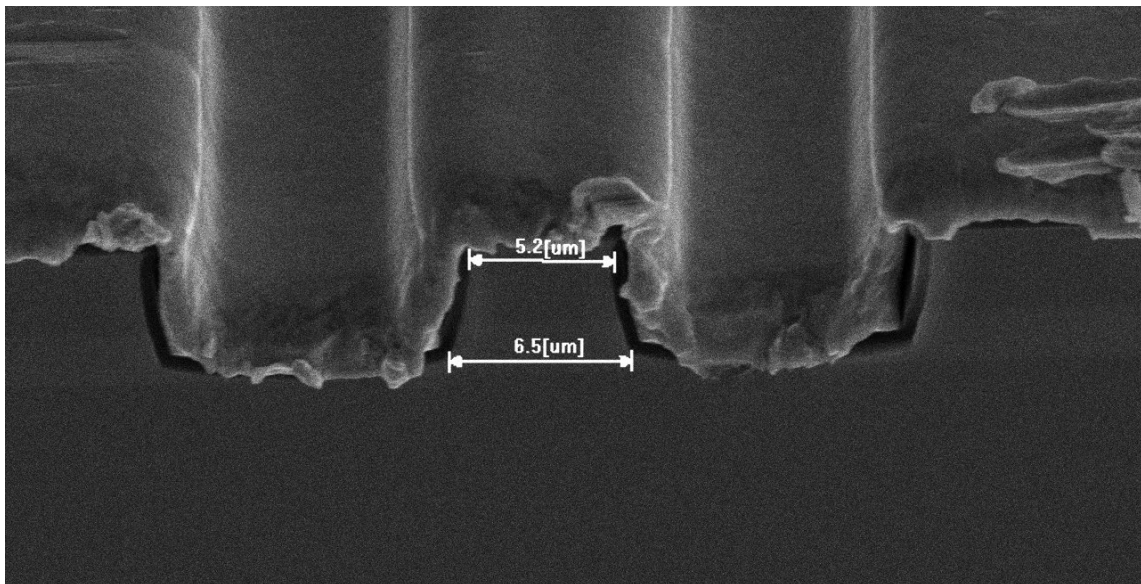

Fig 3.7 SEM photo of the cleaved facet of a 6.5µm-wide QCL from wafer MR3877.

3.3.2 Device Packaging

It has been elaborated in the QCL active region design section that the performance of semiconductor lasers is sensitive to temperature because, at a high temperature, the lower lasing states are occupied by more electrons (thermal backfilling) while the electrons in the

upper lasing state escape to higher energy levels or even into the continuum (thermal escape and leakage); thus, the population inversion is significantly reduced. In particular, in contrast to interband lasers, QCLs require a large voltage (>10V) to tilt the energy band for the alignment of electronic states, leading to a much higher thermal density in the core. Therefore, thermal management is critically important for maximising QCL performance.

For initial tests, i.e., pulsed L-I, a long laser bar of each wafer is mounted on a gold-coated ceramic tile, as shown in Fig 3.8(a). Although the ceramic tile is not ideal for thermal dissipation (see Table 3.2), the packaging provides the largest sample size for device quality inspection, which is therefore suitable for the preliminary test purpose. After that, smaller laser chips are epi-layer up mounted on oxygen-free high thermal conductivity (OFHC) copper and diamond heatspreader, as shown in Fig 3.8 (b) and (c), respectively, pursuing room-temperature (RT) continuous-wave (CW) operation. The chips are all indium soldered, and gold wires are ball-bonded between the laser top contact layer and an individually gold-coated region on the insulator, which forms the cathode. The conductive area under the QCL chip naturally forms the anode of the device.

(a) QCLs on Ceramic   (b) QCLs on Copper   (c) QCLs on Diamond
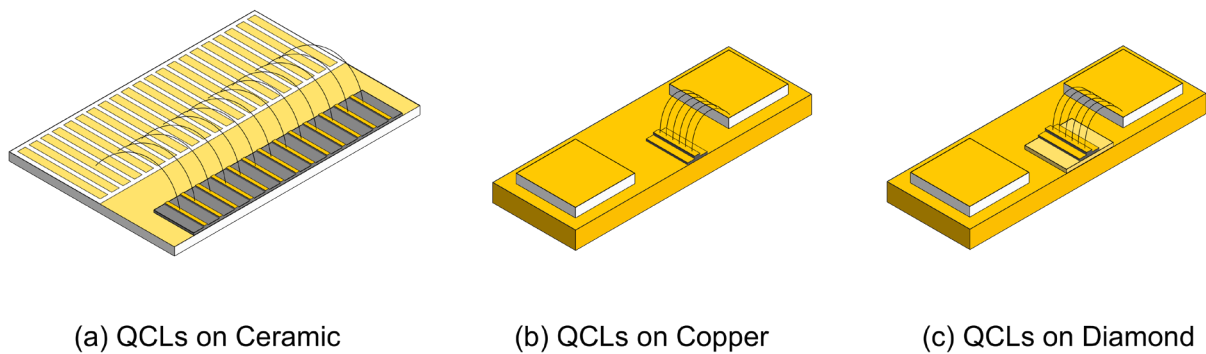
Fig 3.8 Different types of QCL packaging: (a) Long QCL bar mounted on ceramic tile, (b) QCL mounted on gold coated OFHC-copper, (c) QCLs mounted on a 3mm×3mm×300μm gold-coated sheet diamond heatspreader on the copper heatsink.

The thermal conductivity and coefficient of thermal expansion (CTE) parameters of the main materials used in an InP-based QCL are summarised in Table 3.2.

Table 3.2 Thermal conductivity and thermal expansion coefficient of main materials used in an InP-based QCL [24][32]

Material	Thermal Conductivity (W/m·K)	Thermal Expansion Coefficient ($\times 10^{-6}$/K)
InP	74	4.5
Ceramic (Al_2O_3)	32	7.2
OFHC-Copper	396	16.7
Diamond	1200	2.3
AlN	257	4.5

Despite the 'old school' style packaging of our QCLs, as described in the review of QCL development, the best performance of InP-based mid-IR QCLs is achieved by employing a buried-heterostructure waveguide with thick (~5 µm) electroplated gold top contact layer, epi-layer down mounted on diamond submount with indium solder [10]. InP features excellent thermal conductivity when compared to ternary compound semiconductors because acoustical phonon is the main heat carrier in QCLs, and the mean free path of phonon in binary material is much longer than that in ternary materials as a result of less alloy scattering [24]. This is the main reason that InP-based mid-IR QCLs can reach very high power and operate at room temperature in CW mode. In the buried-heterostructure QCL, the core is surrounded by InP, which is thus exceptionally effective for heat dissipation of the hot active region. Compared to the traditional epi-layer up mounting, the thermal path of epi-layer down mounting is greatly reduced as the generated heat no longer needs to travel through the ~100 – 200 µm thick InP substrate to the heatsink.

On the other hand, the drawback of this 'coolest' QCL packaging is the mismatch of the thermal expansion coefficient between InP (4.5) and diamond submount (2.3). This is why indium solder, a 'soft solder' that can adjust the strain in between, is specifically used in this packaging. Mismatching of the CTE can eventually lead to reliability problems for the device. An interesting fact reported in a QCL long-term reliability test [33] is that after tens of thousands of hours of operation, the degradation of QCL performance was actually caused by the degradation of laser packaging or even the power meter rather than the QCL chip. This implies that the laser chip is exceptionally robust, while the packaging can indeed cause problems. Therefore, many commercial mid-IR QCL products are mounted on an AlN submount using AuSn hard solder, which provides reasonably good thermal conductivity and a perfectly matched thermal expansion coefficient to the InP substrate [32]. A high-performance but low-reliability product, e.g., QCL mounted on diamond, would undoubtedly bring challenges to the product warranty service – not something most companies would expect; on the other hand, it is totally acceptable for us to test in the lab as a starting point and obtain a bit hint of the maximum possible output power we may achieve.

3.4 First Fabrication: Results and Discussion

This section presents the characterisation results of the first fabricated QCLs, i.e., 2mm×6.5μm MR3877, MR4241 and 2mm×8μm MR3879, MR4243. The devices mounted on ceramic tiles are first tested in the pulsed mode, and devices with low thresholds are promising candidates for continuous-wave operation.

3.4.1 Pulsed Mode

Four wafer samples mounted on ceramic tiles are first characterised in pulsed mode at room temperature (~20°C) with 1% duty cycle and 800ns pulse width. The pulsed L-I results are compiled in Fig 3.9. Since the lasers are in different dimensions, i.e., either 6.5μm×2mm or 8μm×2mm, the injection current is converted into current density for easier comparison.
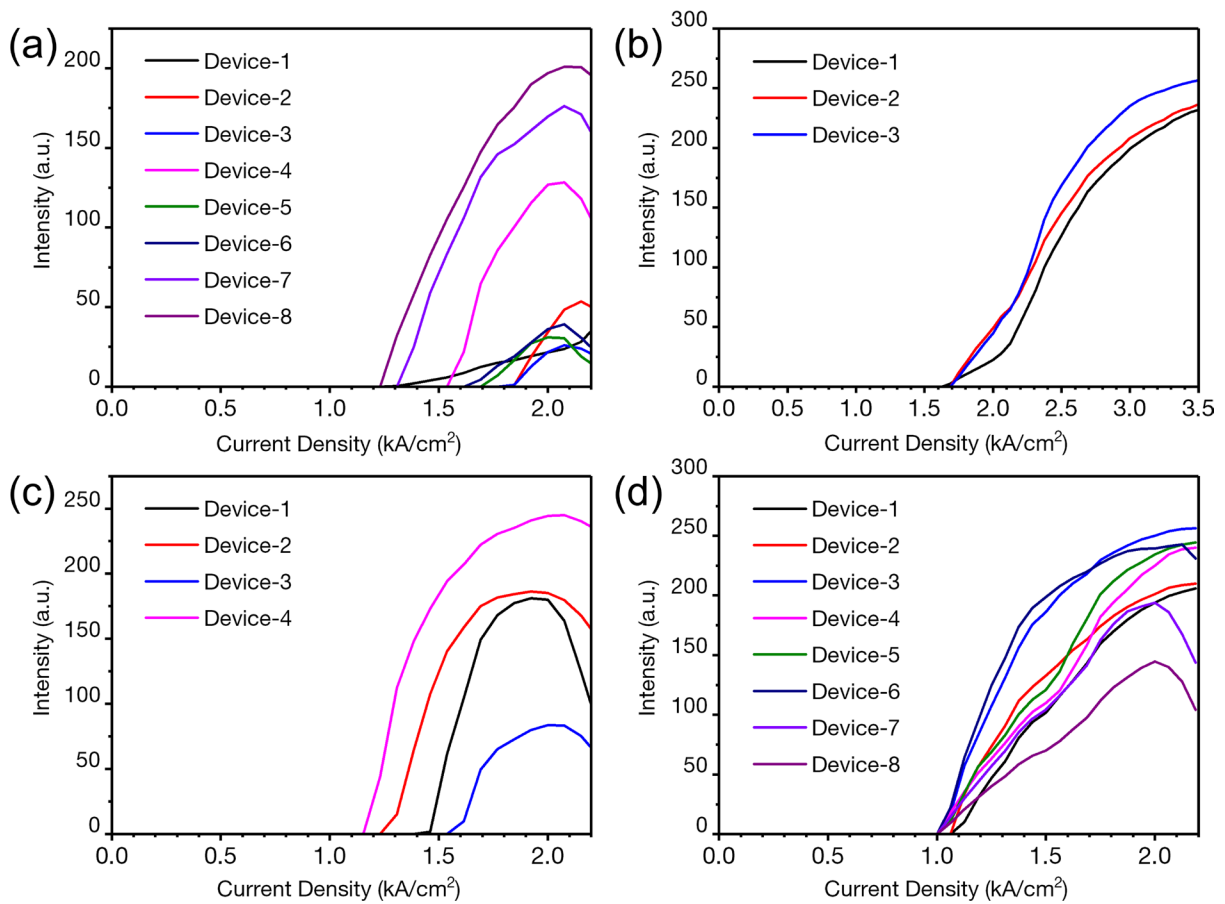
Fig 3.9 Pulsed L-I data. (a) MR3877, (b) MR3879, (c) MR4241, (d) MR4243.

As one can see in the bottom right, MR4243 QCLs have the lowest threshold current density among all samples, i.e., ~1 kA/cm^2, and the eight tested lasers exhibit relatively consistent performance. MR3879, i.e., Fig 3.9(b), is the wafer with doubled doping concentration compared to the rest wafers, and thus the threshold current is much higher (~1.7 kA/cm^2) as a

result of the increased carrier absorption. But on the other hand, the laser's dynamic range (threshold – rollover) is also dramatically increased, which is promising for high power. The devices from wafers MR3877 and MR4241, i.e., the left column, show higher thresholds and significantly individualised performance compared to MR4243. Furthermore, the dynamic range of these devices is also narrower than the latter. Considering that the InP cladding layer of wafers MR4241 and MR4243 (the bottom row) are grown separately, and both show lower thresholds than MR3877, the separate growth process may help, but not significant.

It was noticed that the measured L-I curves in Fig 3.9 more or less exhibit abnormal shapes compared to a standard QCL L-I curve; this was later found to be caused by laser beam instability (see Fig 3.10), which leads to variation in the power actually hitting the detector. In addition, the sensor of the MCT detector is relatively tiny, and thus it only collects a portion of the laser beam from a narrow angle. As a result, any change in the beam profile would distort the measured L-I curve. For these reasons, the measured intensity in Fig 3.9 is inaccurate, but the measured thresholds are reliable.

Laser beam instability is caused by the coupling of multiple transverse modes [34]-[37]. Intuitively, the light will only travel in a specific spatial mode in the laser cavity, i.e., the transverse mode with the lowest threshold gain. Nonetheless, multi-transverse mode operation becomes possible when the thresholds of different transverse modes are close to each other. The narrower lasers (MR3877 and MR4241, 6.5μm-wide) still emit a single beam but suffer from steering issues due to the presence of a low-composition first-order transverse mode TM_{01}. In contrast, the waveguides of the wider QCLs (MR3879 and MR4243, 8μm-wide) are completely dominated by the TM_{01} mode and thus emit two beams pointing at ±30°.
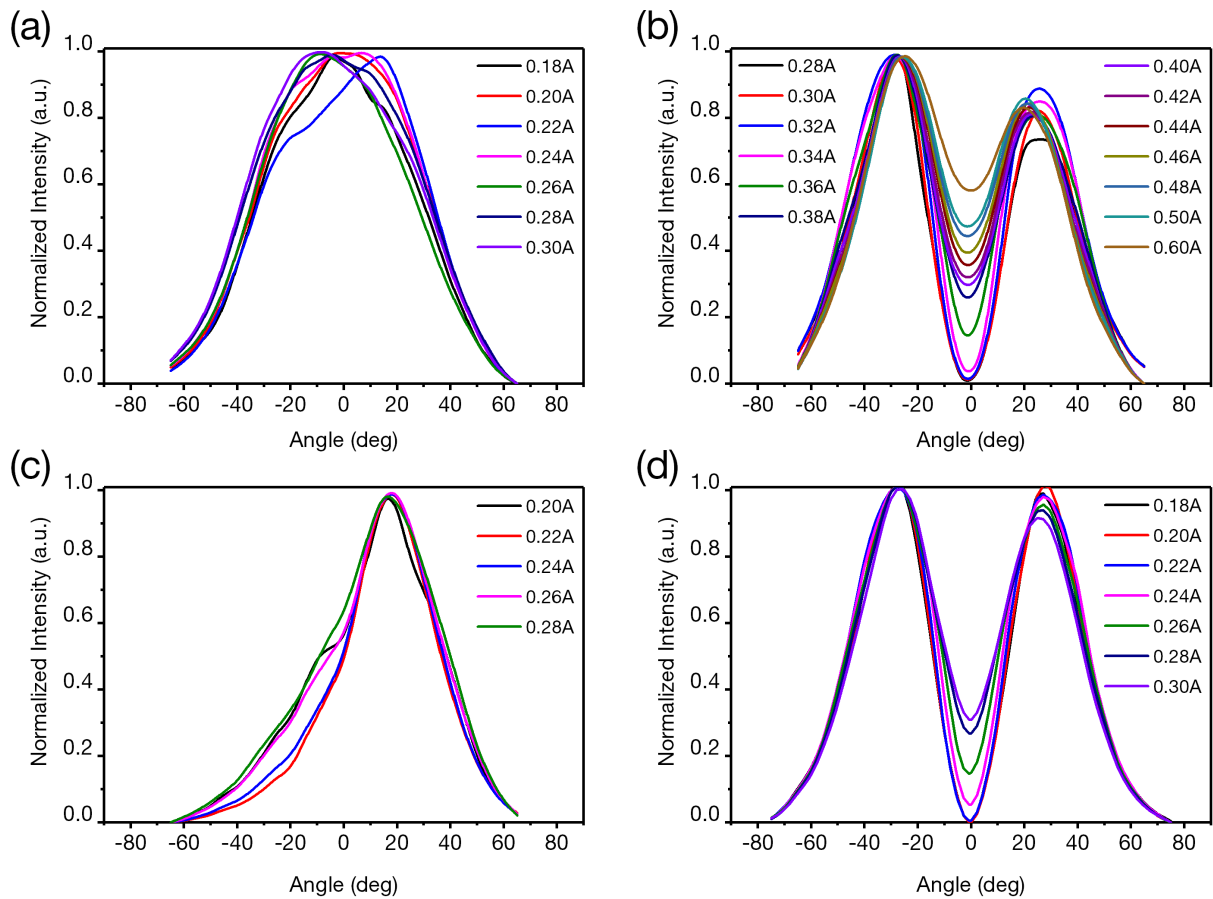
Fig 3.10 Normalised beam profile. (a) MR3877, (b) MR3879, (c) MR4241, and (d) MR4243

Finally, the emission wavelengths of the samples were measured using FT-IR. The pulse width is a crucial parameter in pulsed-mode spectroscopy. A long pulse width increases the heat in the core of the laser, with a subsequent thermal shift of longitudinal modes, which eventually leads to the smearing of the spectrum. Therefore, a short pulse width helps obtain a clear spectrum with discrete longitudinal modes. Fig 3.11 shows the spectral data, which was measured with a pulse width of 150ns. Recall that the designed wavelength is ~5.4 μm, and it is clear that the actual devices emit at longer wavelengths than the calculated value, varying from 5.49 to 5.75μm. This is mainly caused by the compositionally graded heterointerface during the MOPVE growth process, as mentioned in the growth section (3.2.2). Note that the emission wavelengths also vary between lasers from the same wafer.

For example, several MR3879 lasers exhibit a broad spectrum similar to that of the MR4241 in Fig 3.11.
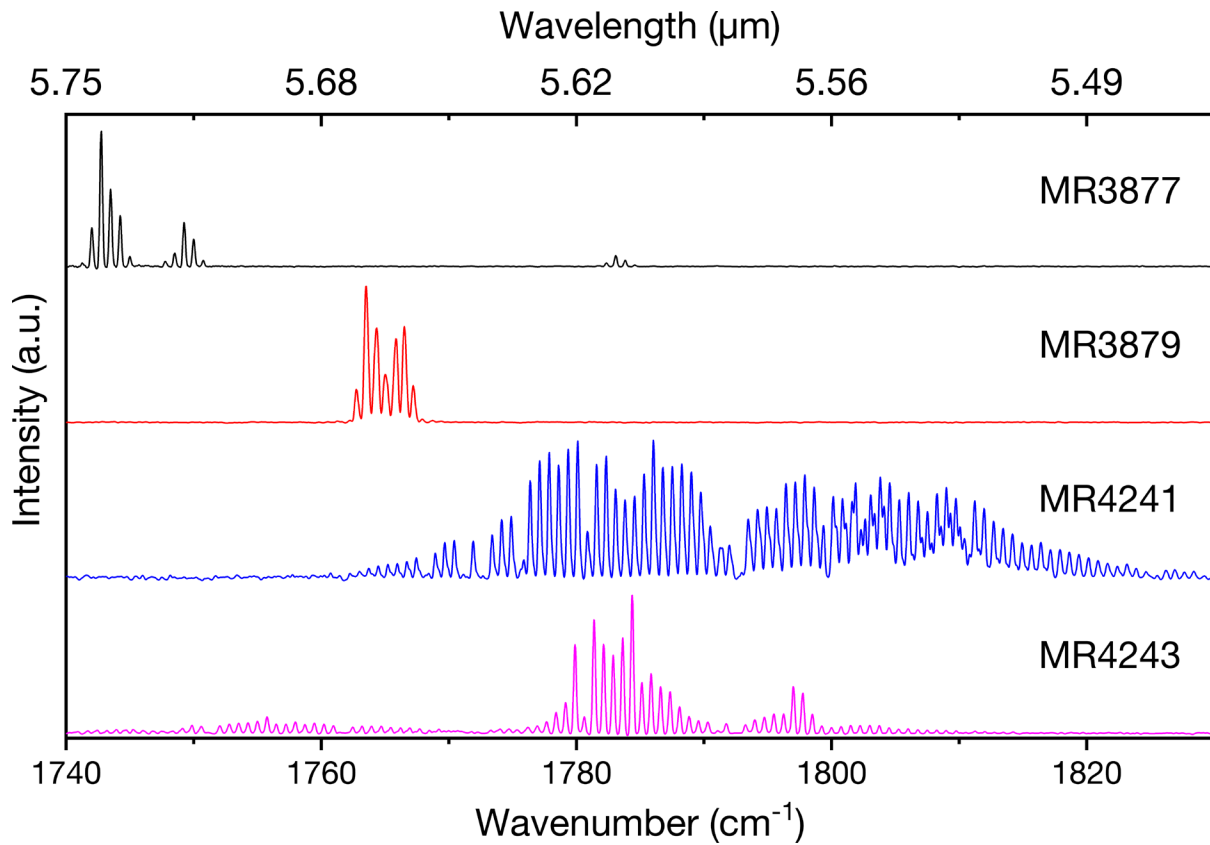

Fig 3.11 Spectra measured at room temperature with 5% duty cycle and 150ns pulse width.

In addition, one may have noticed that the spectrum of MR4241 does not show a clear spectral comb with evenly spaced longitudinal modes; instead, the right hump actually contains two closely located spectral combs. This is strong evidence of two co-existing transverse modes in the cavity, which have slightly different effective refractive indexes. More discussions on this will be given in Chapter 4.

3.4.2 Continuous-Wave Mode

For CW tests, devices with improved thermal management packaging are prepared, i.e., QCL-on-copper and QCL-on-diamond. Consistent with the previous pulsed L-I data analysis, we found that only devices made from wafer MR4243 can operate in CW mode, as shown below. The laser performances are characterised between 15°C and 30°C. Although the cooling stage can cool the lasers down to an even lower temperature and thus achieve better performance, they are rarely tested below 15°C for condensation concerns since the devices are directly exposed to the air.
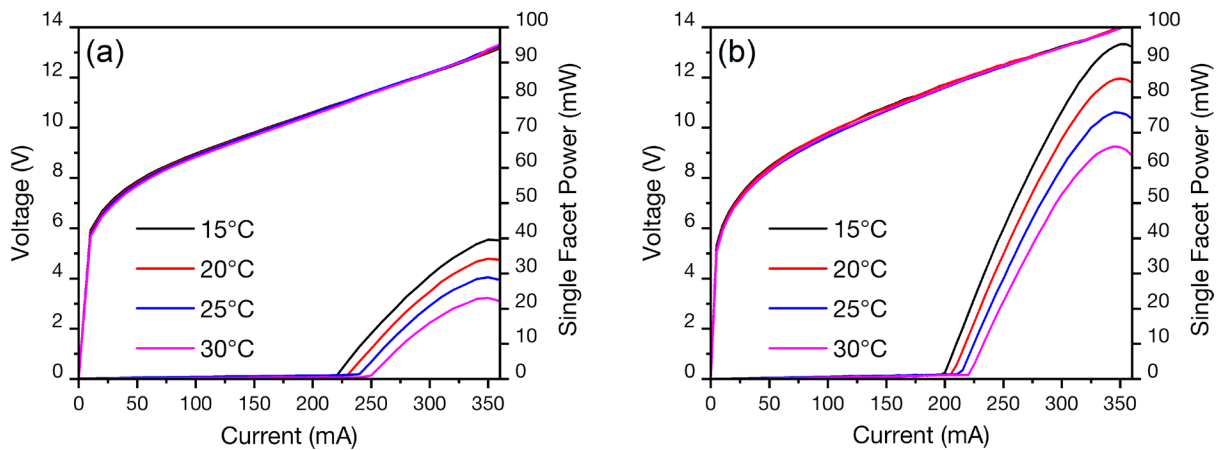

Fig 3.12 CW L-I-V of 8μm×2mm MR4243 QCL mounted on (a) copper and (b) diamond

From the CW L-I-V, we can see that these L-I curves are much straighter and smoother than the pulsed curves. This is mainly due to the much larger aperture (diameter ~10mm) of the thermal sensor, which is thus less sensitive to laser beam instability. Despite the poor beam quality, the performances of MR4243 QCLs are relatively satisfactory. Both the copper- and diamond-mounted QCLs can operate at room temperature in CW mode, with a threshold current density of ~1.48 kA/cm^2 and ~1.33 kA/cm^2, respectively. As the devices are uncoated and thus light is emitted from both the front and back facets, the maximum optical power of

the copper-mounted QCL at 15°C is ~80 mW while the diamond-mounted QCL outputs ~190

mW. Therefore, one can see how thermal management can have a significant impact on the

final laser performance. With the additional insertion of a 300μm thick diamond heatspreader

between the QCL chip and the copper heatsink, the QCL performance is improved by more

than 130%.

The QCL mounted on diamond was further tested between 10°C and 65°C to determine its

maximum CW operating temperature, and the result is shown in Fig 3.13(a). Note that the

laser was slightly moved away from the detector in the high-temperature test, which resulted

in ~1/3 power drop, but the thresholds of the L-I curves are consistent with Fig 3.12(b). As

one can see, the QCL continues to operate in CW mode at 65°C and the total optical power is

estimated to be ~15 mW. By plotting the heatsink temperature vs the corresponding threshold

current in Fig 3.13(b), we obtained a CW characteristic temperature T_0 of 124K.
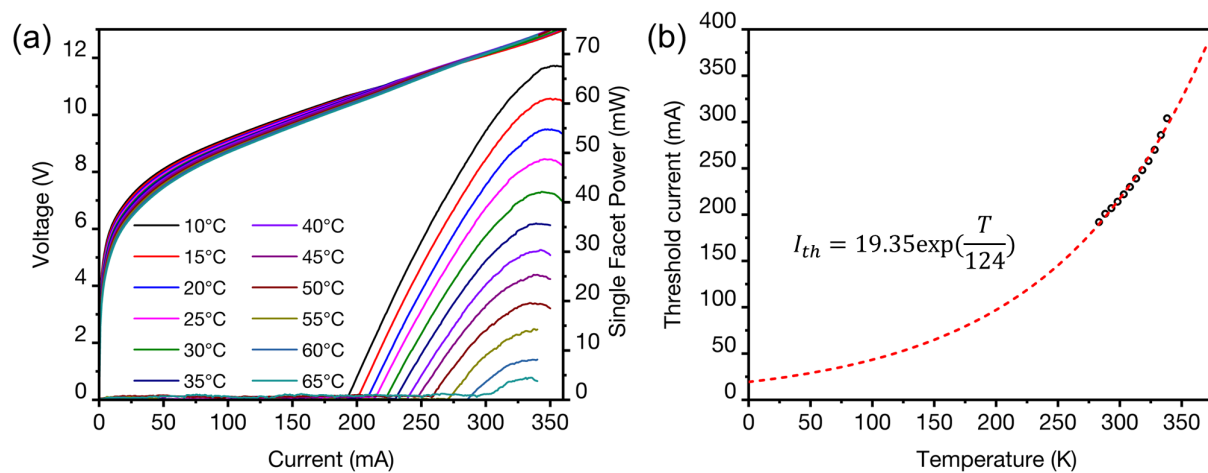
Fig 3.13 (a) CW L-I-V of the diamond-mounted QCL tested between 10°C and 65°C. (b)
Threshold current measured from (a) as a function of heatsink temperature. The fitting
equation is displayed next to the red fitting curve, indicating a T_0=124 K.

On the other hand, the beam steering issue continues to exist in the CW mode QCL, as shown

in Fig 3.14. The device is the same as the one in Fig 3.12(b), i.e., QCL mounted on a

diamond. The dissimilar L-I curves are caused by the different distances between the QCL and the thermal sensor. In the L-I-V measurement of Fig 3.12(b), the facet-sensor distance is 3mm, and virtually all the light can be collected, leading to a smooth L-I curve. While in the case of Fig 3.14(a), the QCL power is measured at a facet-sensor distance of 6.5mm; thus, the 10mm thermal sensor aperture is not large enough to collect the total power of the super divergent beam. Therefore, similar to the pulsed L-I case, the change of beam shape is directly reflected in the L-I curve.
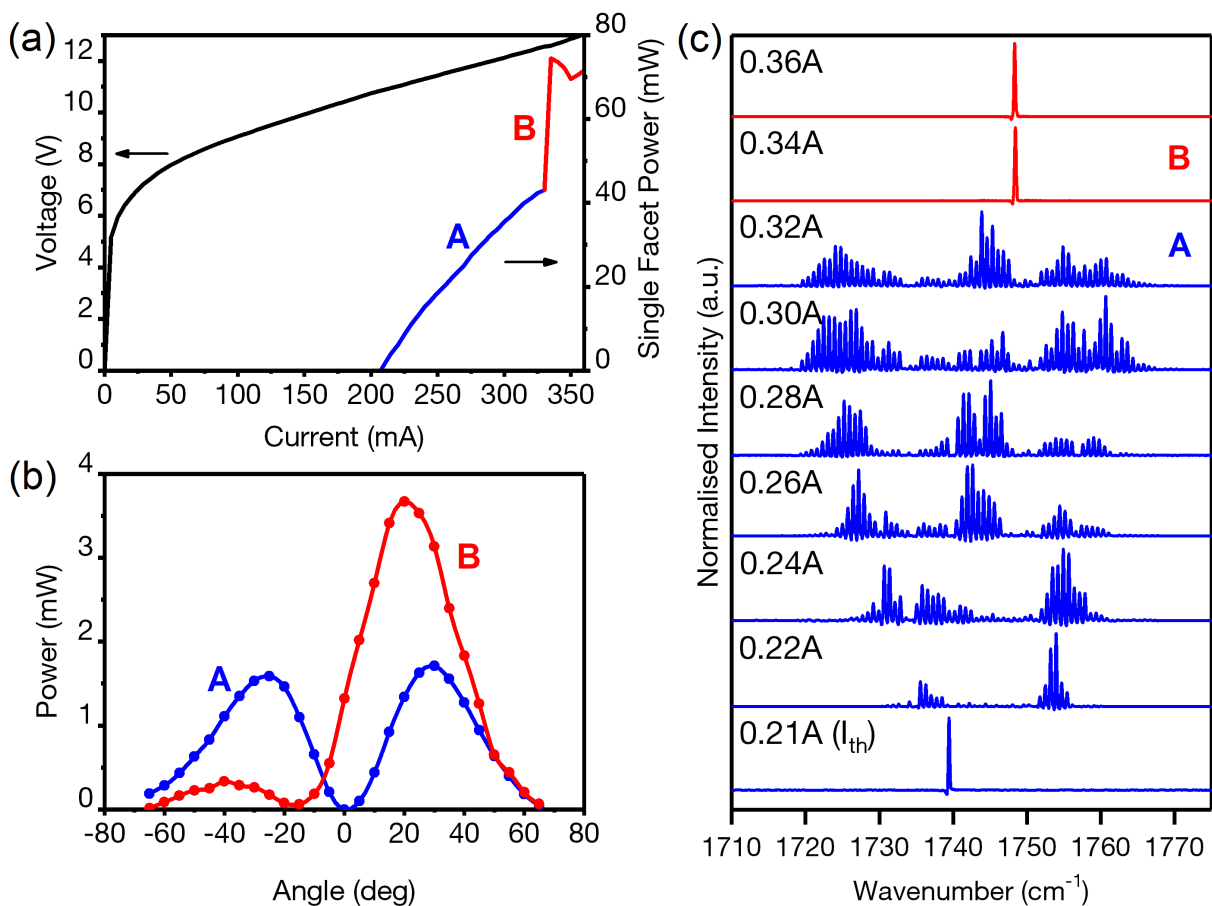

Fig 3.14 Complied data of the 8µm×2mm QCL mounted on diamond, operating in CW mode at 20°C. (a) L-I-V, (b) far-field beam profile, and (c) spectra.

The kink of the L-I curve is caused by a sudden change in beam profile, as one can see in Fig 3.14(b). In region A, the laser emits two beams pointing at ±30° direction, indicating that

TM$_{01}$ mode dominates the waveguide. Then the emission virtually becomes a single beam pointing at 20° direction in region B. The reduced beam divergence consequently results in more optical power delivery to the detector. Most interestingly, the laser switched to a fantastic single longitudinal mode above the L-I kink.

Furthermore, kinks also can be seen in the voltage curve – although not that pronounced in Fig 3.14(a). By differentiating the I-V curve, the kinks are clearer to observe from the dV/dI curve, as one can see in Fig 3.15. The first-order derivative curve shows two sudden changes of the I-V: the first kink at ~210 mA is the laser threshold, as introduced before (recall Fig 2.16); the second kink at ~330mA is the electrical response to the beam profile switch, i.e., a sudden voltage drop of ~0.05V. This implies that the output power is slightly increased. Similar observations, i.e., a sudden increase of optical output power accompanied by a small drop in voltage, can be seen in ref. [38], where the QCL is switched from the harmonic spectral mode to the dense spectral mode. In contrast, what we observed here is more related to transverse modes rather than longitudinal modes.
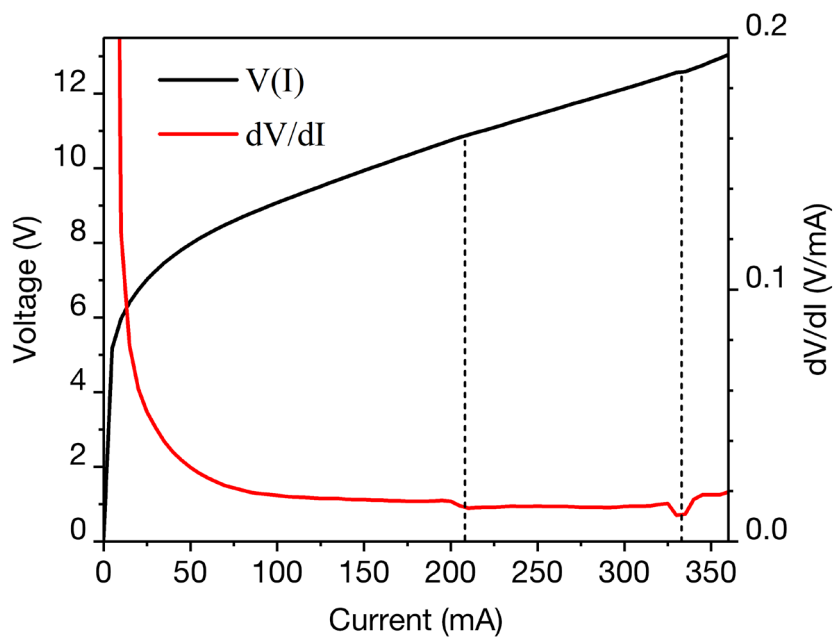
**Fig 3.15** I-V curve of the QCL and the corresponding first-order derivative curve

This interesting observation is suggested to be caused by the nonlinear coupling of multi-transverse modes [35][36][39], more details of which will be discussed in Chapter 4. With regards to device development, the next plan is clear, i.e., to eliminate the beam instability.

3.5 QCL Waveguide Modelling

In the previous section, the far-field measurement results have shown that both 6.5µm and 8µm-wide QCLs suffer from beam quality issues, i.e., beam steering, which is commonly seen in broad lasers. In general, it has little impact on the laser output power; however, it turns out to be a massive problem for any laser applications requiring precise alignment, focusing or pointing. For example, the directed infrared countermeasure (DIRCM) system will be unable to protect aircraft against heat-seeking missiles if there is an issue with laser pointing. In this work, QCLs are developed for waveguide coupling on silicon; thus, beam quality is critically important for achieving a high coupling efficiency. Consequently, it is necessary to reduce the ridge width in the following fabrication. In this section, waveguide simulations are performed to determine the optimal ridge width for our QCL using the commercial software package Lumerical. Additionally, a few other questions are investigated together, e.g., Why are higher-order transverse modes favoured in a wide-ridge laser? What is the difference between the conventional ridge waveguide and the buried-heterostructure waveguide in terms of transverse mode control?

First, we can consider a simple laser waveguide model, consisting of only waveguide loss (travelling loss in the waveguide) and mirror loss (reflection loss at facets), as shown below.
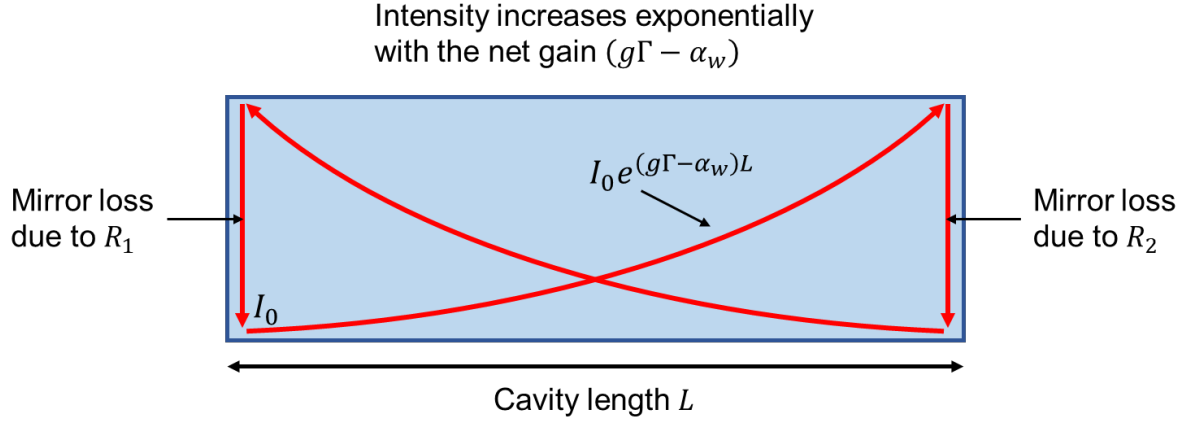
Fig 3.16 Evolution of light intensity of a round-trip in the FP-cavity

The initial light intensity at the bottom left corner is I_0, after travelling a distance of the full cavity length L to the right, the intensity is amplified to $I_0 e^{(g\Gamma - \alpha_w)L}$; once the light hits the right facet which has a reflectivity of R_2, there is a sudden intensity drop due to the transmission $(1 - R_2)$, and the remaining intensity is thus $R_2 I_0 e^{(g\Gamma - \alpha_w)L}$. Applying the same rule for the return trip, the final light intensity after a round-trip is $R_1 R_2 I_0 e^{(g\Gamma - \alpha_w)2L}$. Therefore, the lasing threshold condition, when the round-trip gain is equal to the round-trip loss, can be written as:

$$R_1 R_2 e^{(\Gamma g - \alpha_w)2L} = 1 \tag{3.1}$$

As our QCLs are uncoated at both facets, this can be simplified with $R_1 = R_2 = R$. Γ is the confinement factor, which is defined as the spatial overlap between the beam and the laser core, i.e., the gain medium. α_w is the waveguide loss and L is the laser cavity length, i.e., $2L$ for a round-trip. In consequence, this expression describes that the round-trip gain of light is 1. The gain g that satisfies this condition is called threshold gain, denoted as g_{th}.

Re-arrange the above equation, and we then obtain the expression of g_{th}:

$$g_{th} = \frac{\alpha_w - \frac{\ln R}{L}}{\Gamma} \tag{3.2}$$

The term $-\frac{\ln R}{L}$ is defined as the distributed mirror loss α_m

$$\alpha_m = -\frac{\ln(R)}{L} \tag{3.3}$$

Thus, the final expression of g_{th} is:

$$g_{th} = \frac{\alpha_w + \alpha_m}{\Gamma} \tag{3.4}$$

Clearly, the threshold gain is determined by three parameters – waveguide loss (α_w), mirror loss (α_m) and mode confinement factor (Γ). Different transverse modes will have different α_w, α_m and Γ values due to the different spatial distributions inside the waveguide, resulting in different g_{th}. The laser will start lasing in the transverse mode with the lowest g_{th}. The purpose of subsequent simulations is therefore clear – to calculate the gain threshold value g_{th} of each possible transverse mode at different waveguide widths, and find out the critical width below which the waveguide will stabilise the laser beam in TM$_{00}$ mode.

Now that the logic and goal of the task have been elaborated and we move on to the simulation. The simulation work is divided into two parts: (1) The transverse modes with corresponding waveguide loss α_w and confinement factor Γ are found using **Lumerical Finite-Difference Eigenmode (FDE) Solver**. (2) Facet reflectivity R, related to mirror loss, has to be calculated by a 3D electromagnetic solver; thus, **Lumerical Finite-Difference Time-Domain (FDTD) Solver** is used here.

3.5.1 Lumerical FDE

Lumerical FDE is a 2D mode solver [40]. By building the 2D waveguide structure in the software and defining the complex refractive index of each material, the solver can then find all the supported transverse modes in the waveguide. Fig 3.17 shows a simplified ridge waveguide QCL and a buried heterostructure QCL built in Lumerical with a rectangular core.
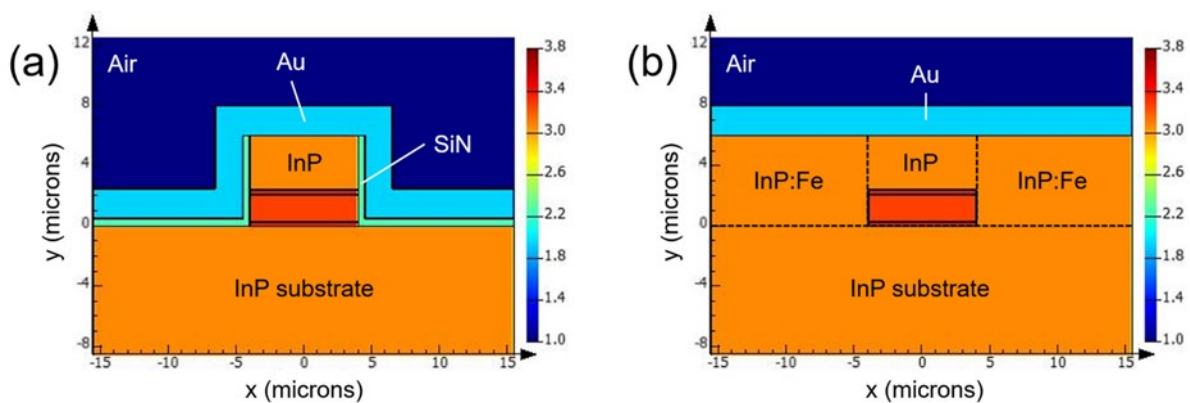
Fig 3.17 2D model of (a) ridge QCL and (b) buried heterostructure QCL in Lumerical FDE solver, the colour bar on the right refers to the real part of the refractive index.

The material refractive indexes (InP, QCL core, InGaAs) used in this simulation are from ref. [41], which are used in the simulation of a λ ~5.3 μm QCL with a similar two-phonon resonance active region design. One can find that the refractive indices of these materials vary slowly from 5.3 μm to 5.7 μm, i.e., $dn/d\lambda$ is close to zero in this range. Therefore, the index error caused by such a trivial wavelength difference can be neglected in this case. The complex index of each material is shown in Table 3.3, the real part of which is the regular refractive index, and the imaginary part is related to absorption or attenuation. Note that the Si_3N_4 insulating layer and the gold contact layer are remarkably lossier than the waveguide components.

Table 3.3 Complex refractive index of each material used in the simulation [41]

Material	Refractive Index
InP	3.0754 + 0.000144i
QCL Core	3.2773 + 0.000176i
InGaAs	3.3710 + 0.000077i
Si_3N_4	2.2608 + 0.017410i
Gold	1.9356 + 39.01700i

3.5.2 Lumerical FDTD

FDTD solver [42] is used to find the facet reflectivity (R) for each transverse mode. The QCL waveguide structure used in FDTD is identical to that in the FDE solver. A 2D sketch is shown in Fig 3.18 to illustrate the basic idea of the simulation.
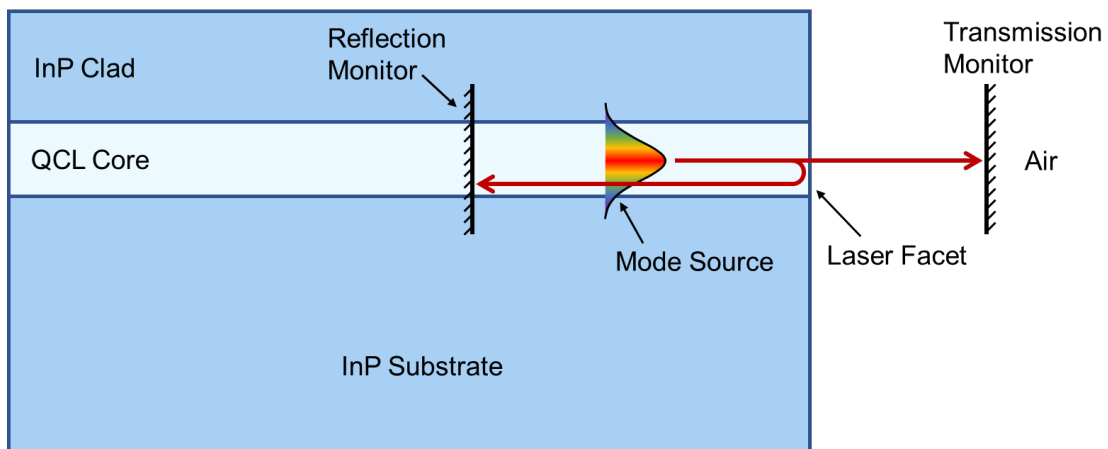
Fig 3.18 Sideview of facet reflectivity simulation in Lumerical FDTD

A transverse mode of the waveguide is used as the light source in this simulation, i.e., mode source, propagating to the right laser facet. The total power of the mode source is 1. Two power monitors are positioned at two sides of the mode source. The left one is in the cavity behind the mode source for light reflection monitoring, and the right one is outside the laser cavity in the air to measure the transmission power. Thus, the sum of the measured reflected power and transmitted power should be close to 1, the total power of the source. However, it is essential to emphasise that the facet reflectivity calculated here is not the total reflection but *the portion of light reflected back into the original transverse mode*. This is because not all facet reflected light contributes to the feedback – a similar conclusion is also seen in ref. [43]. Once the facet reflectivity is obtained from simulation, it can be converted into mirror loss α_m using eq. (3.3). *L* refers to the laser cavity length, i.e., 2mm in this case.

3.5.3 Results and Discussion

Now the waveguide loss (α_w) and confinement factor (Γ) found in Lumerical FDE and the facet reflectivity (R) obtained in Lumerical FDTD; finally, the threshold gain of each transverse mode at different laser widths can be calculated. The calculated results of ridge waveguide QCL and buried heterostructure QCL are summarised in Table 3.4 and 3.5, respectively. Note that in this case, only TM_{00} and TM_{01} modes are compared, but several of these structures also support the TM_{02} mode.

**Table 3.4** Threshold gain vs core width for λ ~5.7 μm ridge waveguide QCLs

Core Width	Mode	Waveguide Loss α_w (cm^{-1})	Mirror Loss α_m (cm^{-1})	Confinement Factor Γ	Threshold Gain g_{th}
8 μm	TM$_{00}$	3.926	6.892	0.6596	16.402
	TM$_{01}$	5.147	5.454	0.6506	16.296
7 μm	TM$_{00}$	4.093	6.778	0.6584	16.509
	TM$_{01}$	5.881	4.943	0.6442	16.802
6 μm	TM$_{00}$	4.374	6.590	0.6565	16.702
	TM$_{01}$	7.158	4.373	0.6299	18.306
5 μm	TM$_{00}$	4.891	6.307	0.6528	17.153
4 μm	TM$_{00}$	5.950	5.908	0.6447	18.393
3 μm	TM$_{00}$	8.502	5.484	0.6198	22.567

Table 3.5 Threshold gain vs core width for λ ~5.7 μm buried-heterostructure QCLs

Core Width	Mode	Waveguide Loss α_w (cm^{-1})	Mirror Loss α_m (cm^{-1})	Confinement Factor Γ	Threshold Gain g_{th}
8 μm	TM$_{00}$	3.554	7.009	0.6503	16.243
	TM$_{01}$	3.594	6.061	0.6090	15.855
7 μm	TM$_{00}$	3.556	6.944	0.6458	16.259
	TM$_{01}$	3.614	5.789	0.5856	16.058
6 μm	TM$_{00}$	3.559	6.847	0.6385	16.298
	TM$_{01}$	3.665	5.504	0.5451	16.822
5 μm	TM$_{00}$	3.563	6.709	0.6260	16.409
	TM$_{01}$	3.891	5.311	0.4646	19.806
4 μm	TM$_{00}$	3.571	6.528	0.6030	16.749
	TM$_{01}$	7.491	5.614	0.2331	56.213
3 μm	TM$_{00}$	3.595	6.344	0.5554	17.895

By plotting the calculated threshold gain vs ridge width data in Fig 3.19, we find that the simulation result is in relatively good agreement with the experimental observations. For 8μm-wide lasers, the threshold gain of TM$_{01}$ mode is lower than that of TM$_{00}$ mode; hence, TM$_{01}$ is the dominant mode in the waveguide. Nevertheless, the threshold gain of TM$_{00}$ mode is still remarkably close to TM$_{01}$, indicating that the laser will easily suffer from multi-transverse mode operations (beam steering), which is in agreement with what we observed in MR3879 and MR4243. When the ridge is narrowed down to ~6.5 μm, TM$_{01}$ mode becomes lossier than TM$_{00}$ due to the increased overlap with the sidewalls. As a result, TM$_{00}$

dominates the waveguide, but the laser is still unable to get rid of multi-transverse-mode operation as TM_{01} mode will be activated slightly above the threshold current. This matches our observation of samples MR3877 and MR4241. Therefore, the reliability of this model is validated. Below, we further investigate some interesting data details in the tables, which help to understand the transverse modes competition in different types of QCL waveguides.
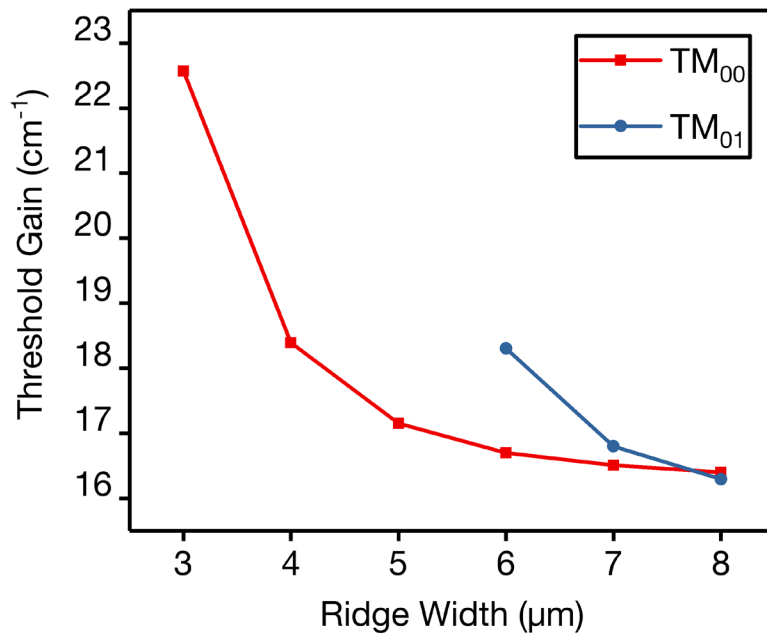

Fig 3.19 Threshold gain vs ridge width for TM_{00} and TM_{01} mode in ridge waveguide

The main difference between the ridge waveguide and buried heterostructure waveguide is the confinement factor and waveguide loss, as shown in Fig 3.20. The ridge laser has an abrupt index contrast waveguide, and all transverse modes are laterally confined within the ridge. As a result, the confinement factor of TM_{00} and TM_{01} modes are relatively close, i.e., ~0.65. Besides, it is relatively insensitive to the reduction of ridge width. On the contrary, buried heterostructure lasers are weakly index-guided; thus, higher-order transverse modes can easily penetrate into the InP region, significantly reducing the overlap between the laser

core and spatial mode. Furthermore, a narrower core width leads to a stronger mode penetration. For example, as shown in Table 3.5, the confinement factor of the TM_{01} drops to only ~0.23 at the core width of 4 µm. This difference is also visually noticeable in Fig 3.21.
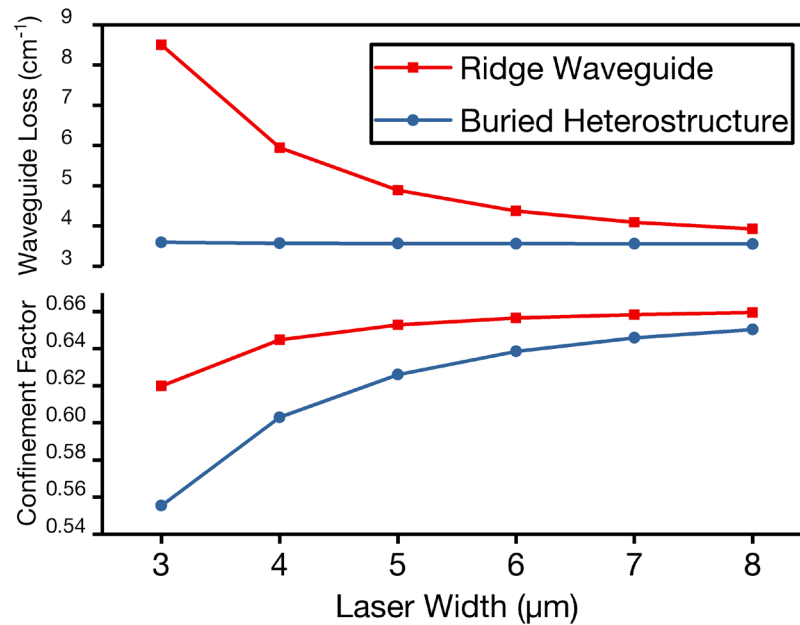
Fig 3.20 Comparison of the fundamental mode in the ridge waveguide and buried heterostructure in terms of waveguide loss and confinement factor as a function of laser core width.

On the other hand, the waveguide loss of buried heterostructure is much smaller than the ridge waveguide, especially at narrower core widths, due to the absence of a lossy Si_3N_4 insulating layer and a vertical gold wall. The ridge waveguide becomes super lossy when the core width is below 4µm, while the buried heterostructure waveguide exhibits nearly the same waveguide loss at 3µm and 8µm.
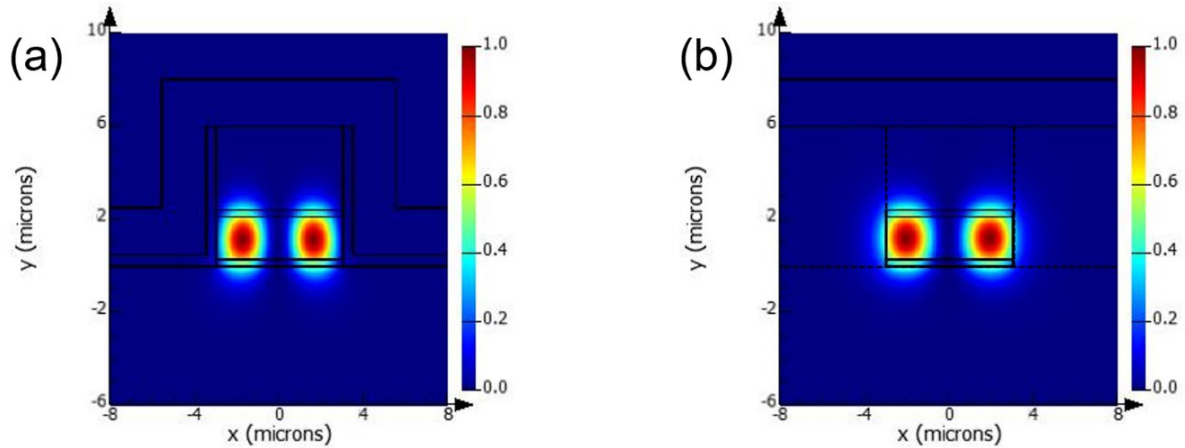
Fig 3.21 TM_{01} mode in (a) ridge QCL and (b) buried heterostructure QCL at 6μm width

Another interesting finding is that higher-order transverse modes always have lower mirror loss than the fundamental modes in both structures, which eventually leads to a lower threshold gain. This explains why lasers always prefer to operate in higher order mode when the width increases – the lower mirror loss is the main factor.

Finally, the optimal width for the QCL needs to be determined based on Fig 3.19. For ridge lasers, the threshold of higher-order modes significantly increases when the ridge width is narrower since there is more overlap between the transverse mode and lossy materials (Si_3N_4, Au). Therefore, the laser will prefer to operate in a less lossy mode, i.e., the fundamental mode. In theory, the laser can be stabilised in TM_{00} mode when the threshold gain difference between TM_{01} and TM_{00} mode is sufficiently significant, i.e., the higher order mode cannot reach the threshold within the dynamic range of the QCL. However, the threshold gain difference between the fundamental and first-order modes is insignificant, even at 6μm. Therefore, 5μm was chosen as the optimal QCL width for the subsequent fabrication, which theoretically does not support TM_{01} mode.

3.6 Second Fabrication: Results and Discussion

We have learnt from the waveguide modelling work that ~5 μm is the optimal core width for beam steering-free operations. Consequently, the next step is the fabrication of ridge width ~5 μm QCLs. The wafer processing (MR4243) is highly similar to the first fabrication, merely narrower ridge masks were used. However, we experienced some issues during the dry etching of the trenches, and the etched depth was not as deep as expected. This was then compensated by a further wet etching step, resulting in a slightly undercut ridge shape. The final core width measured by SEM is 4.5 μm, as shown below. The slightly narrower ridge leads to a small amount of power loss but still guarantees fundamental transverse mode operation. The latter is clearly more important for us as it will be used for hybrid integration on the silicon platform and coupled with germanium waveguides (see Chapter 5), where high beam quality is critically required. Despite the trivial ridge over-etching, the devices are relatively clean and well-processed.
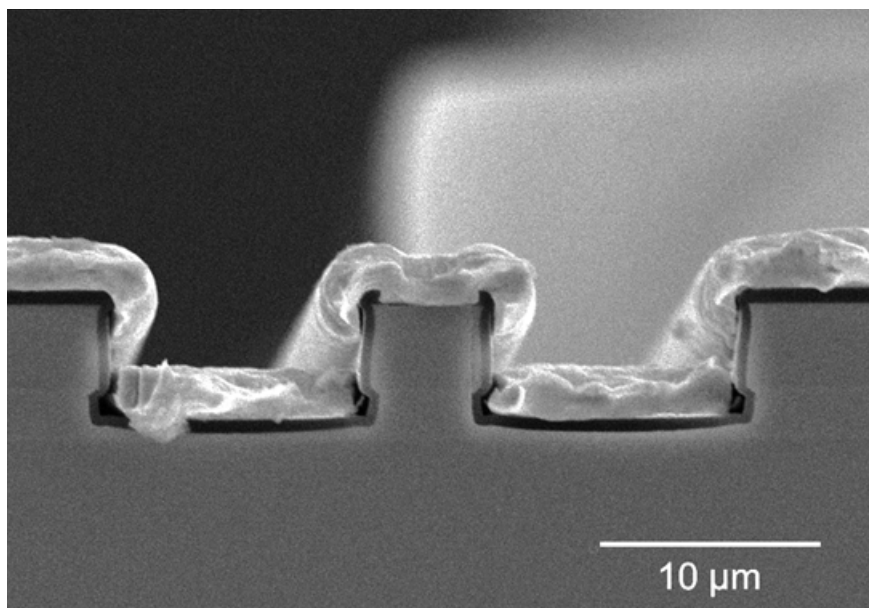
Fig 3.22 SEM photo of second fabricated QCLs, the measured core width is 4.5μm

The CW L-I-V, far-field beam profile, and spectra data of a 4.5μm×3mm uncoated device mounted on diamond are compiled in Fig 3.23. The total optical power of the device at 10°C is around 150mW, which remains comparable to previous 8μm-wide devices as the laser length is increased by 50%. But on the other hand, the CW threshold current density (J_{th}) of the new device is much lower than that of the previous devices, i.e., 0.926 kA/cm^2 at 10°C and around 1 kA/cm^2 at room temperature. This is mainly because the mirror loss α_m is a cavity length-dependent term, i.e., $-\frac{\ln R}{L}$. Clearly, increasing the cavity length L results in a reduced mirror loss and thus a smaller total loss, followed by a lower threshold gain.
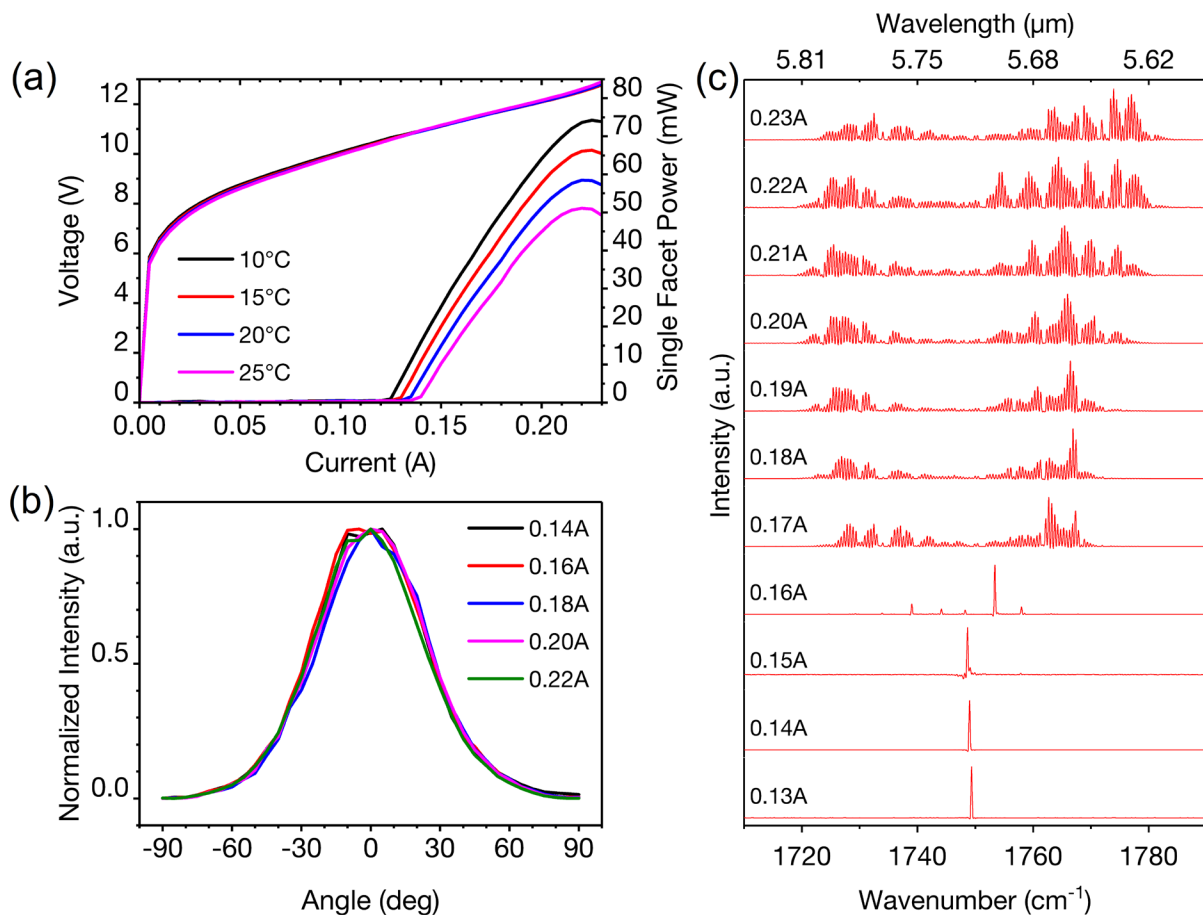
Fig 3.23 (a) CW L-I-V characteristics of a 4.5μm×3mm uncoated QCL mounted on diamond, (b) slow-axis beam profile, and (c) CW spectra measured at 15°C.

The slow-axis far-field pattern shows a consistent beam profile insensitive to the injection current, indicating a beam steering-free operation via the fundamental mode TM_{00}. The measured slow-axis FWHM beam divergence is ~55°. The fast-axis beam profile was also measured by rotating the cooling stage over 90°. The orthogonal beam profiles are shown in Fig 3.24(c), from which one can see that the vertical and parallel beam divergences are nearly the same, resulting in a circular output beam.
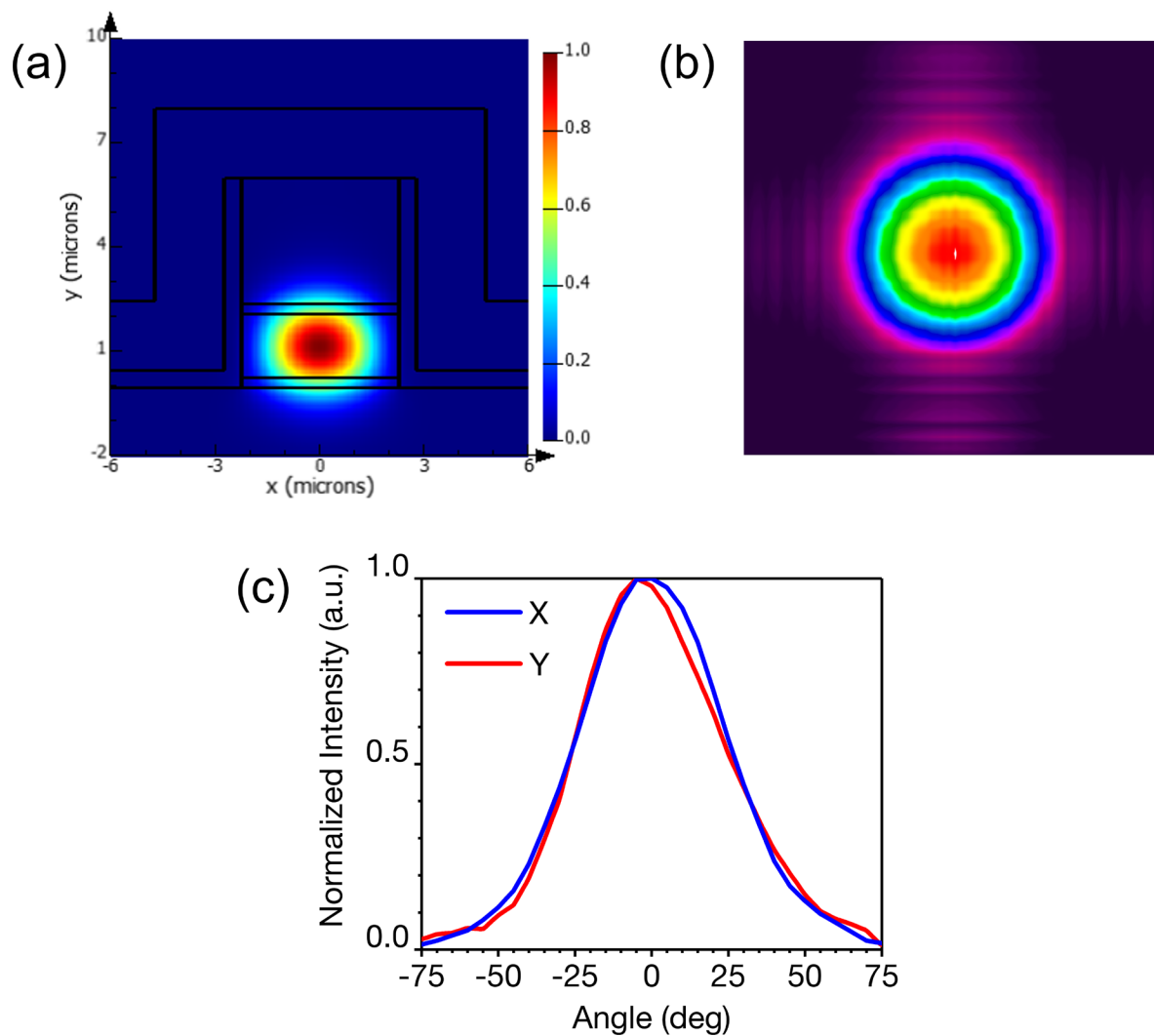
Fig 3.24 (a) TM_{00} transverse mode of the 4.5μm ridge QCL simulated by Lumerical. (b) 2D beam pattern measured by the scanning slit beam profiler. Model: NanoScan 2s Pyro/9/5. (c) The measured vertical and parallel angular far-field beam profiles of the 4.5μm×3mm QCL.

This was further confirmed by the 2D beam image from a beam profiler, as shown in Fig 3.24(b). The beam pattern was imaged by focusing the laser beam into a scanning slit beam profiler with the help of a germanium aspherical lens. The simulated transverse mode or near-field profile, as shown in Fig 3.24(a), is actually elliptical; however, due to the rectangular shape of the laser core ($1.8 \times 4.5 \mu m$), the vertical direction exhibits a stronger diffraction effect and thus a larger beam divergence, which eventually results in a circular beam spot in the far-field. In consequence, the simulated near-field mode is in good agreement with the measured far-field mode.

With regards to the emission spectrum, Fig 3.23(c) shows that the QCL operates in single frequency mode at $\lambda \sim 5.7$ μm when the injection current is slightly above the threshold, i.e., below $1.2 \times$ the threshold current. Then the spectrum splits into two clusters due to a combined effect of Rabi oscillation and spatial hole burning [44]-[47]. More details of this will be explained in the next chapter. The measured FSR is ~ 0.513 cm^{-1}, smaller than the previous samples as a result of the increased cavity length.

3.7 Summary

In conclusion, four QCL wafers based on strain compensated $In_{0.6}Ga_{0.4}As/Al_{0.58}In_{0.42}As$ material system on InP substrate with identical two-phonon resonance active region design ($\lambda \sim 5.7$ μm) were grown by MOVPE, i.e., MR3877, MR3879, MR4241, MR4243. The wafers were all fabricated into double-trench ridge waveguide structures for hybrid integration purposes. 6.5μm and 8μm-wide ridge FP-QCLs were first fabricated and characterised, which both suffered from the beam instability problem caused by multiple transverse modes

coupling. With regards to laser performance, MR4243 QCLs exhibit the lowest threshold current density in pulsed mode and are also the only group of devices that can operate in CW mode at room temperature with high performance. Moreover, it can continue to operate in CW mode at least above 338K (65°C). As wafers were processed together, the performance difference was less likely to be introduced in the fabrication process; thus, the fundamental difference between these devices should have been made during the growth process.

To solve the beam quality issue, the relationship between transverse modes and the waveguide dimension was then studied in the software Lumerical. Based on the theoretical analysis, we eventually fabricated 4.5 μm-wide QCLs that stably operate in the fundamental transverse mode with a nearly circular beam shape. The CW optical power of a 4.5μm×3mm uncoated FP-QCL epi-up mounted on diamond is around 100 mW at room temperature with a low threshold current density of ~1 kA/cm^2.

References

[1] J. S. Roberts, R. P. Green, L. R. Wilson, E. A. Zibik, D. G. Revin, J. W. Cockburn, and R. J. Airey, "Quantum cascade lasers grown by metalorganic vapor phase epitaxy," *Applied Physics Letters*, vol. 82, no. 24, pp. 4221–4223, 2003.

[2] R. Köhler, A. Tredicucci, F. Beltram, H. E. Beere, E. H. Linfield, A. G. Davies, D. A. Ritchie, R. C. Iotti, and F. Rossi, "Terahertz semiconductor-heterostructure laser," *Nature*, vol. 417, no. 6885, pp. 156–159, 2002.

[3] B. S. Williams, "Terahertz quantum-cascade lasers," *Nature Photonics*, vol. 1, no. 9, pp. 517–525, 2007.

[4] L. Li, L. Chen, J. Zhu, J. Freeman, P. Dean, A. Valavanis, A. G. Davies, and E. H. Linfield, "Terahertz quantum cascade lasers with >1 W output powers," *Electronics Letters*, vol. 50, no. 4, pp. 309–311, 2014.

[5] A. Y. Cho and J. R. Arthur, "Molecular beam epitaxy," *Progress in Solid State Chemistry*, vol. 10, part 3, pp. 157–191, 1975.

[6] J. Faist, F. Capasso, D. L. Sivco, C. Sirtori, A. L. Hutchinson, and A. Y. Cho, "Quantum cascade laser," *Science*, vol. 264, no. 5158, pp. 553–556, 1994.

[7] J. Faist, F. Capasso, C. Sirtori, D. L. Sivco, J. N. Baillargeon, A. L. Hutchinson, S. N. G. Chu, and A. Y. Cho, "High power mid-infrared ($\lambda \sim 5$ μm) quantum cascade lasers operating above room temperature," *Applied Physics Letters*, vol. 68, no. 26, pp. 3680–3682, 1996.

[8]   C. Sirtori, J. Faist, F. Capasso, D. L. Sivco, A. L. Hutchinson, and A. Y. Cho, "Mid-infrared (8.5 μm) semiconductor lasers operating at room temperature," *IEEE Photonics Technology Letters*, vol. 9, no. 3, pp. 294–296, 1997.

[9]   J. Faist, M. Beck, T. Aellen, and E. Gini, "Quantum-cascade lasers based on a bound-to-continuum transition," *Applied Physics Letters*, vol. 78, no. 2, pp. 147–149, 2001.

[10]   M. Beck, D. Hofstetter, T. Aellen, J. Faist, U. Oesterle, M. Ilegems, E. Gini, and H. Melchior, "Continuous wave operation of a mid-infrared semiconductor laser at room temperature," *Science*, vol. 295, no. 5553, pp. 301–305, 2002.

[11]   M. Razeghi, and S. Slivken, "High power quantum cascade lasers grown by GasMBE," *Opto-Electronics Review*, vol. 11, no. 2, pp. 85–91, 2003.

[12]   G. B. Stringfellow, *Organometallic vapor-phase epitaxy : theory and practice*, 2nd ed. San Diego: Academic Press, 1999.

[13]   R. P. Green, A. B. Krysa, J. S. Roberts, D. G. Revin, L. R. Wilson, E. A. Zibik, W. H. Ng, and J. W. Cockburn, "Room-temperature operation of InGaAs/AlInAs quantum cascade lasers grown by Metalorganic Vapor Phase Epitaxy," *Applied Physics Letters*, vol. 83, no. 10, pp. 1921–1922, 2003.

[14]   R. P. Green, L. R. Wilson, E. A. Zibik, D. G. Revin, J. W. Cockburn, C. Pflügl, W. Schrenk, G. Strasser, A. B. Krysa, J. S. Roberts, C. M. Tey, and A. G. Cullis, "High-performance distributed feedback quantum cascade lasers grown by Metalorganic Vapor Phase Epitaxy," *Applied Physics Letters*, vol. 85, no. 23, pp. 5529–5531, 2004.

[15]   X. J. Wang, J. Y. Fan, T. Tanbun-Ek, and F. S. Choa, "Low threshold quantum-cascade lasers of room temperature continuous-wave operation grown by metal-

organic chemical-vapor deposition," *Applied Physics Letters*, vol. 90, no. 21, p. 211103, 2007.

[16] K. Fujita, S. Furuta, A. Sugiyama, T. Ochiai, T. Edamura, N. Akikusa, M. Yamanishi, and H. Kan, "Room temperature, continuous-wave operation of quantum cascade lasers with single phonon resonance-continuum depopulation structures grown by metal organic vapor-phase epitaxy," *Applied Physics Letters*, vol. 91, no. 14, p. 141121, 2007.

[17] M. Troccoli, L. Diehl, D. P. Bour, S. W. Corzine, N. Yu, C. Y. Wang, M. A. Belkin, G. Hofler, R. Lewicki, G. Wysocki, F. K. Tittel, and F. Capasso, "High-performance quantum cascade lasers grown by metal-organic vapor phase epitaxy and their applications to trace gas sensing," *Journal of Lightwave Technology*, vol. 26, no. 21, pp. 3534–3555, 2008.

[18] C. A. Wang, R. K. Huang, A. Goyal, J. P. Donnelly, D. R. Calawa, S. G. Cann, F. O'Donnell, J. J. Plant, L. J. Missaggia, G. W. Turner, and A. Sanchez-Rubio, "OMVPE growth of highly strain-balanced GaInAs/AlInAs/InP for quantum cascade lasers," *Journal of Crystal Growth*, vol. 310, no. 23, pp. 5191–5197, 2008.

[19] F. Xie, C. Caneau, H. P. LeBlanc, N. J. Visovsky, S. C. Chaparala, O. D. Deichmann, L. C. Hughes, C. Zah, D. P. Caffey, and T. Day, "Room temperature CW operation of short wavelength quantum cascade lasers made of strain balanced $Ga_xIn_{1-x}As/Al_yIn_{1-y}As$ material on InP substrates," *IEEE Journal of Selected Topics in Quantum Electronics*, vol. 17, no. 5, pp. 1445–1452, 2011.

[20] L. Diehl, D. Bour, S. Corzine, J. Zhu, G. Höfler, B. G. Lee, C. Y. Wang, M. Troccoli, and F. Capasso, "Pulsed- and continuous-mode operation at high temperature of

strained quantum-cascade lasers grown by Metalorganic Vapor Phase Epitaxy," *Applied Physics Letters*, vol. 88, no. 4, p. 041102, 2006.

[21]   D. Hofstetter, M. Beck, T. Aellen, J. Faist, U. Oesterle, M. Ilegems, E. Gini, and H. Melchior, "Continuous wave operation of a 9.3 μm quantum cascade laser on a Peltier Cooler," *Applied Physics Letters*, vol. 78, no. 14, pp. 1964–1966, 2001.

[22]   L. Diehl, D. Bour, S. Corzine, J. Zhu, G. Höfler, M. Lončar, M. Troccoli, and F. Capasso, "High-power quantum cascade lasers grown by low-pressure metal organic vapor-phase epitaxy operating in continuous wave above 400K," *Applied Physics Letters*, vol. 88, no. 20, p. 201115, 2006.

[23]   C. A. Wang, B. Schwarz, D. F. Siriani, L. J. Missaggia, M. K. Connors, T. S. Mansuripur, D. R. Calawa, D. McNulty, M. Nickerson, J. P. Donnelly, K. Creedon, and F. Capasso, "MOVPE growth of LWIR AlInAs/GaInAs/InP quantum cascade lasers: Impact of growth and material quality on laser performance," *IEEE Journal of Selected Topics in Quantum Electronics*, vol. 23, no. 6, p. 1200413, 2017.

[24]   J. Faist, *Quantum Cascade Lasers*. Oxford: Oxford University Press, 2018.

[25]   Nextnano.NEGF: http://www.nextnano.com/nextnano.NEGF

[26]   H. Tanimura, S. Takagi, T. Kakuno, R. Hashimoto, K. Kaneko, and S. Saito, "Analyses of Optical Gains and Oscillation Wavelengths for Quantum Cascade Lasers Using the Nonequilibrium Green's Function Method," *Journal of Computer Chemistry, Japan -International Edition*, vol. 8, 2022.

[27]   I. I. Zasavitskii, N. Y. Kovbasa, N. A. Raspopov, A. V. Lobintsov, Y. V. Kurnyavko, P. V. Gorlachuk, A. B. Krysa, and D. G. Revin, "A GaInAs/AlInAs quantum cascade

laser with an emission wavelength of 5.6 μm," *Quantum Electronics*, vol. 48, no. 5, pp. 472–475, 2018.

[28] I. I. Zasavitskii, N. Y. Kovbasa, N. A. Raspopov, A. V. Lobintsov, Y. V. Kurnyavko, P. V. Gorlachuk, D. G. Revin, and A. B. Krysa, "GaInAs/AlInAs heteropair quantum cascade laser operating at a wavelength of 5.6 μm and temperature of above 300K," *KnE Engineering*, vol. 3, no. 6, pp. 236–243, 2018.

[29] A. B. Krysa, J. S. Roberts, R. P. Green, L. R. Wilson, H. Page, M. Garcia, and J. W. Cockburn, "MOVPE-grown quantum cascade lasers operating at ~9μm wavelength," *Journal of Crystal Growth*, vol. 272, no. 1-4, pp. 682–685, 2004.

[30] T. Walther and A. B. Krysa, "Transmission electron microscopy of AlGaAs/GaAs quantum cascade laser structures," *Journal of Microscopy*, vol. 268, no. 3, pp. 298–304, 2017.

[31] X. Huang, Y. Chiu, W. Charles, and C. Gmachl, "Ridge-width dependence of the threshold of long wavelength (λ ≈14 μm) quantum cascade lasers with sloped and vertical sidewalls", *Optics Express*, vol. 20, no. 3, p. 2539, 2012.

[32] A. Tsekoun, R. Go, M. Pushkarsky, M. Razeghi, and C. K. Patel, "Improved performance of quantum cascade lasers through a scalable, manufacturable epitaxial-side-down mounting process," *Proceedings of the National Academy of Sciences*, vol. 103, no. 13, pp. 4831–4835, 2006.

[33] F. Xie, H.-K. Nguyen, H. Leblanc, L. Hughes, J. Wang, J. Wen, D. J. Miller, and K. Lascola, "Long term reliability study and lifetime model of quantum cascade lasers," *Applied Physics Letters*, vol. 109, no. 12, p. 121111, 2016.

[34] N. Yu, L. Diehl, E. Cubukcu, D. Bour, S. Corzine, G. Höfler, A. K. Wojcik, K. B. Crozier, A. Belyanin, and F. Capasso, "Coherent coupling of multiple transverse modes in quantum cascade lasers," *Physical Review Letters*, vol. 102, no. 1, pp. 013901, 2009.

[35] N. Yu, "Nonlinear coupling of transverse modes in quantum cascade lasers," *Optical Engineering*, vol. 49, no. 11, p. 111114, 2010.

[36] A. K. Wójcik, N. Yu, F. Capasso, and A. Belyanin, "Nonlinear optical interactions of laser modes in quantum cascade lasers," *Journal of Modern Optics*, vol. 58, no. 9, pp. 727–742, 2011.

[37] Y. Yao, Y. Huang, X. Wang, and C. F. Gmachl, "Modal instability and beam steering in quantum cascade lasers," *CLEO:2011 – Laser Applications to Photonic Applications*, pp. 1–2, 2011.

[38] T. S. Mansuripur, C. Vernet, P. Chevalier, G. Aoust, B. Schwarz, F. Xie, C. Caneau, K. Lascola, C. Zah, D. P. Caffey, T. Day, L. J. Missaggia, M. K. Connors, C. A. Wang, A. Belyanin, and F. Capasso, "Single-mode instability in standing-wave lasers: The quantum cascade laser as a self-pumped parametric oscillator," *Physical Review A*, vol. 94, no. 6, p. 063807, 2016.

[39] A. K. Wójcik, N. Yu, L. Diehl, F. Capasso, and A. Belyanin, "Self-synchronization of laser modes and multistability in quantum cascade lasers," *Physical Review Letters*, vol. 106, no. 13, p. 133902, 2011.

[40] Lumerical MODE: https://optics.ansys.com/hc/en-us/articles/360020687354-MODE-product-reference-manual

[41] N. Yu, L. Diehl, E. Cubukcu, C. Pflügl, D. Bour, S. Corzine, J. Zhu, G. Höfler, K. B. Crozier, and F. Capasso, "Near-field imaging of quantum cascade laser transverse modes," *Optics Express*, vol. 15, no. 20, pp. 13227–13235, 2007.

[42] Lumerical FDTD: https://optics.ansys.com/hc/en-us/articles/360033154434-FDTD-product-reference-manual

[43] Z. Wang, F. Kapsalidis, R. Wang, M. Beck, and J. Faist, "Ultra-low threshold lasing through phase front engineering via a metallic circular aperture," *Nature Communications*, vol. 13, no. 230, pp. 1–6, 2022.

[44] C. Y. Wang, L. Diehl, A. Gordon, C. Jirauschek, F. X. Kärtner, A. Belyanin, D. Bour, S. Corzine, G. Höfler, M. Troccoli, J. Faist, and F. Capasso, "Coherent instabilities in a semiconductor laser with fast gain recovery," *Physical Review A*, vol. 75, no. 3, p. 031802(R), 2007.

[45] A. Gordon, C. Y. Wang, L. Diehl, F. X. Kärtner, A. Belyanin, D. Bour, S. Corzine, G. Höfler, H. C. Liu, H. Schneider, T. Maier, M. Troccoli, J. Faist, and F. Capasso, "Multimode regimes in quantum cascade lasers: From coherent instabilities to spatial hole burning," *Physical Review A*, vol. 77, no. 5, p. 053804, 2008.

[46] M. Bugajski, K. Pierscinski, D. Pierscinska, A. Szerling, and K. Kosiel, "Multimode instabilities in mid-infrared quantum cascade lasers," *Photonics Letters of Poland*, vol. 5, no. 3, pp. 85–87, 2013.

[47] N. N. Vukovic, J. Radovanovic, V. Milanovic, and D. L. Boiko, "Low-threshold RNGH instabilities in quantum cascade lasers," in *IEEE Journal of Selected Topics in Quantum Electronics*, vol. 23, no. 6, pp. 1–16, 2017.

# 4 Spectral and Spatial Instabilities in QCLs

4.1 Introduction

The performance of mid-IR QCLs was dramatically improved in the first decade after its invention in 1994. Thanks to this, many spectral and spatial instabilities subsequently started to be observed and reported as the sufficiently high intra-cavity light intensity results in a strong nonlinearity, such as the spectrum splitting [1], beam steering [2], and the more recent self-starting harmonic state [3], which was later proven to be essentially a frequency comb [4]. During the development of our λ ~5.7 μm QCL, we also observed several interesting phenomena, some of which slightly differed from what we have learned in the literature. These spectral and spatial instabilities are therefore explained and discussed in this chapter as complementary to Chapter 3. In section 4.2, we reviewed the theory of the QCL spectrum splitting issue; and in section 4.3, the QCL beam steering problem is discussed.

4.2 Spectral Mode Instability

During the spectral characterisation of our QCLs in CW mode, it was regularly observed that the lasers operated in single frequency mode when the injection current was just above the

threshold, but quickly the spectra became multimode and split into two clusters; the separation of the spectrum was enhanced with the increment of the injection current, i.e., increased laser power. The distance between the two clusters of longitudinal modes in the frequency domain eventually reached ~1 THz, as seen in Fig 4.1.
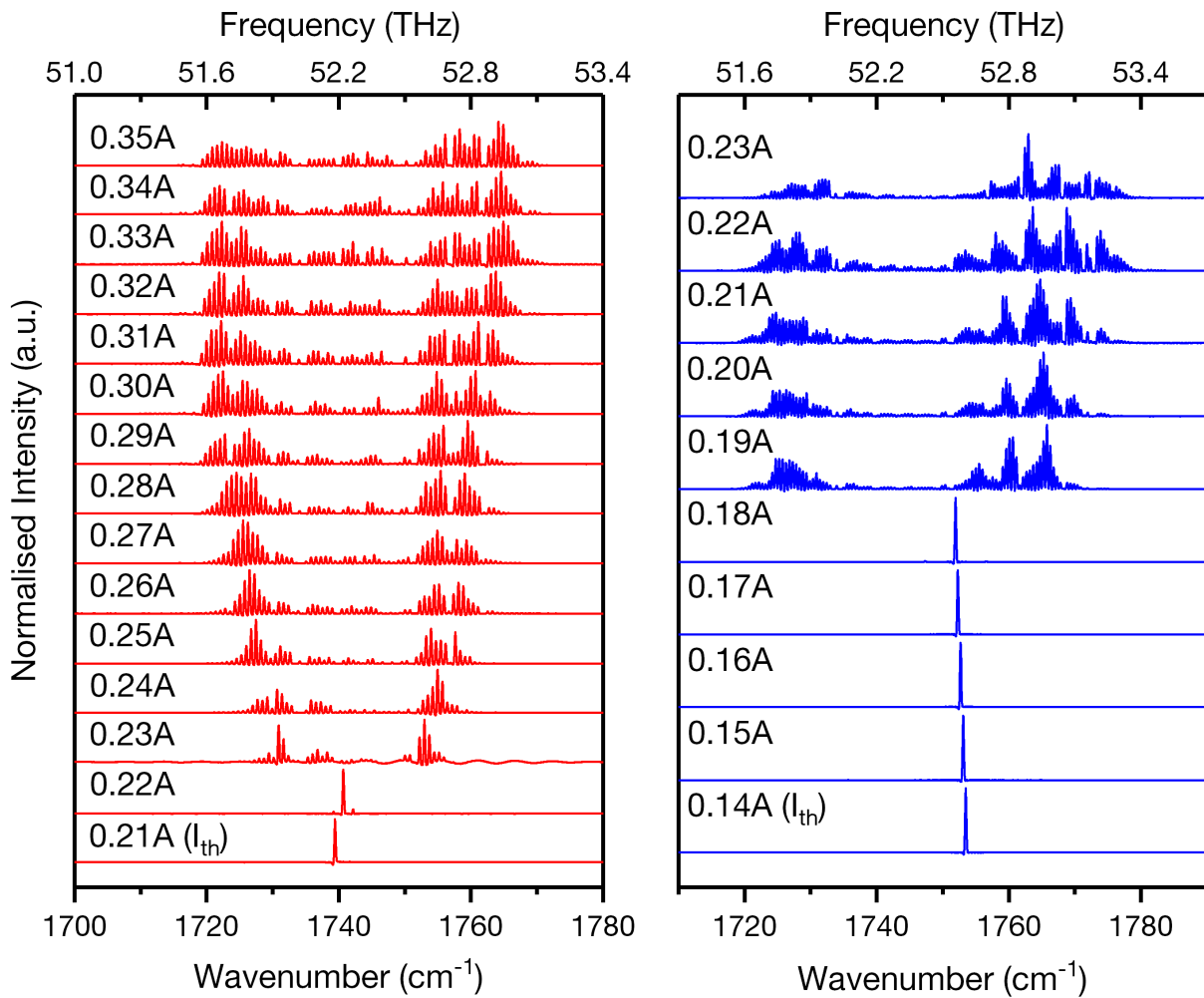

Fig 4.1 Spectrum splitting observed from a 2mm×8μm (red) and 3mm×4.5μm (blue) QCL operating in CW mode at 20°C. The corresponding L-I-V data is in Chapter 3.

This spectral instability in QCL has been investigated since fifteen years ago [1][5] and was usually described as the 'second threshold' of QCLs. The two main effects leading to the splitting spectra were believed to be *Rabi Oscillation* and *Spatial Hole Burning* (SHB). The mechanisms of these two effects are briefly introduced below.

4.2.1 Rabi Oscillation

As shown in Fig 4.2, in the case of resonant interaction between a strong electric field (e.g., a laser beam) and an atom, where the incident photon energy $\hbar\omega_0$ matches the energy gap $(E_2 - E_1)$ of two specific atomic energy levels, one can expect the electron to jump between the two energy states, absorbing or emitting photons.
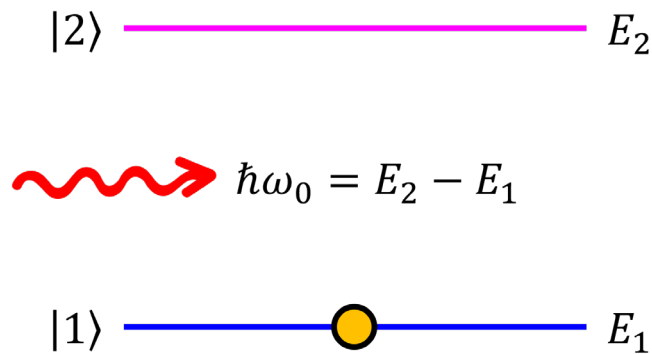
Fig 4.2 Resonant interaction between light and a two-level system

To quantitatively analyse the electron behaviour in this situation, firstly, we consider an electron in the superposition state $|\Psi\rangle$:

$$|\Psi\rangle = c_1|1\rangle + c_2|2\rangle \tag{4.1}$$

$$|c_1|^2 + |c_2|^2 = 1 \tag{4.2}$$

where $|c_1|^2$ and $|c_2|^2$ are the probabilities of finding the electron in state $|1\rangle$ and $|2\rangle$, respectively. Thus, if given that the total number of electrons in the system is N, the electron populations in state $|1\rangle$ and $|2\rangle$ are simply $|c_1|^2 N$ and $|c_2|^2 N$. Furthermore, once we could obtain the expressions of $c_1(t)$ and $c_2(t)$, we can then identify how the electron population of each state evolves over time. This problem can be solved using the time-dependent Schrödinger equation:

$$\mathbf{H}|\Psi\rangle = i\hbar\frac{\partial}{\partial t}|\Psi\rangle \tag{4.3}$$

The Hamiltonian for this system is:

$$\mathbf{H} = \mathbf{H_0} + \mathbf{V}(\mathrm{t}) \tag{4.4}$$

where $\mathbf{H_0}$ represents the atom energy in the dark, i.e., the intrinsic atomic energy, and $\mathbf{V}(\mathrm{t})$ describes the light-atom interaction energy, which is time-dependent. As a starting point, the space (z) and time (t) dependent wavefunctions of state $|1\rangle$ and $|2\rangle$ can be written as:

$$\mathbf{H_0}|1\rangle = i\hbar\frac{\partial}{\partial t}|1\rangle = E_1|1\rangle \longrightarrow \Psi_1(z,t) = \psi_1(z)e^{-\frac{iE_1t}{\hbar}} \tag{4.5}$$

$$\mathbf{H_0}|2\rangle = i\hbar\frac{\partial}{\partial t}|2\rangle = E_2|2\rangle \longrightarrow \Psi_2(z,t) = \psi_2(z)e^{-\frac{iE_2t}{\hbar}} \tag{4.6}$$

Thus, the wavefunction of the electron in a superposition state is:

$$\Psi = c_1\Psi_1 + c_2\Psi_2 = c_1\psi_1 e^{-\frac{iE_1t}{\hbar}} + c_2\psi_2 e^{-\frac{iE_2t}{\hbar}} \tag{4.7}$$

Expand the left and right terms of eq. (4.3) by substituting eq. (4.7) in:

$$\mathbf{H}|\Psi\rangle = (\mathbf{H_0} + \mathbf{V})\left(c_1\psi_1 e^{-\frac{iE_1t}{\hbar}} + c_2\psi_2 e^{-\frac{iE_2t}{\hbar}}\right)$$
$$= c_1 E_1\psi_1 e^{-\frac{iE_1t}{\hbar}} + c_2 E_2\psi_2 e^{-\frac{iE_2t}{\hbar}} + \mathbf{V}\left(c_1\psi_1 e^{-\frac{iE_1t}{\hbar}} + c_2\psi_2 e^{-\frac{iE_2t}{\hbar}}\right) \tag{4.8}$$

$$i\hbar\frac{\partial}{\partial t}|\Psi\rangle = i\hbar\frac{\partial}{\partial t}\left(c_1\psi_1 e^{-\frac{iE_1t}{\hbar}} + c_2\psi_2 e^{-\frac{iE_2t}{\hbar}}\right)$$
$$= E_1 c_1\psi_1 e^{-\frac{iE_1t}{\hbar}} + i\hbar\dot{c}_1\psi_1 e^{-\frac{iE_1t}{\hbar}} + E_2 c_2\psi_2 e^{-\frac{iE_2t}{\hbar}} + i\hbar\dot{c}_2\psi_2 e^{-\frac{iE_2t}{\hbar}} \tag{4.9}$$

Eq. (4.8) and eq. (4.9) are equal to each other; thus, a few terms can be cancelled, and we come to the following simplified equation:

$$\mathbf{V}\left(c_1\psi_1 e^{-\frac{iE_1t}{\hbar}} + c_2\psi_2 e^{-\frac{iE_2t}{\hbar}}\right) = i\hbar\dot{c}_1\psi_1 e^{-\frac{iE_1t}{\hbar}} + i\hbar\dot{c}_2\psi_2 e^{-\frac{iE_2t}{\hbar}} \tag{4.10}$$

Multiply ψ_1^* to both sides of eq. (4.10), then integrate over space z, and use $\langle \psi_1 | \psi_1 \rangle = 1$, $\langle \psi_1 | \psi_2 \rangle = 0$, we obtain:

$$c_1 \langle \psi_1 | \mathbf{V} | \psi_1 \rangle e^{-\frac{iE_1 t}{\hbar}} + c_2 \langle \psi_1 | \mathbf{V} | \psi_2 \rangle e^{-\frac{iE_2 t}{\hbar}}$$
$$= c_1 V_{11} e^{-\frac{iE_1 t}{\hbar}} + c_2 V_{12} e^{-\frac{iE_2 t}{\hbar}} = i\hbar \dot{c}_1 e^{-\frac{iE_1 t}{\hbar}} \tag{4.11}$$

where $V_{ij} = \langle \psi_i | \mathbf{V} | \psi_j \rangle$. Further multiply $e^{\frac{iE_2 t}{\hbar}}$ on two sides:

$$c_1 V_{11} e^{\frac{i(E_2 - E_1)t}{\hbar}} + c_2 V_{12} = i\hbar \dot{c}_1 e^{\frac{i(E_2 - E_1)t}{\hbar}} \tag{4.12}$$

$$c_1 V_{11} e^{i\omega_0 t} + c_2 V_{12} = i\hbar \dot{c}_1 e^{i\omega_0 t} \tag{4.13}$$

$$\dot{c}_1 = -\frac{i}{\hbar} \left(c_1 V_{11} + c_2 V_{12} e^{-i\omega_0 t} \right) \tag{4.14}$$

By multiplying ψ_2^* to eq. (4.10) and repeat the same procedures, we can have the expression of $\dot{c}_2$ as well:

$$\dot{c}_2 = -\frac{i}{\hbar} \left(c_2 V_{22} + c_1 V_{21} e^{i\omega_0 t} \right) \tag{4.15}$$

Now we need to deal with the terms V_{ij}. The perturbation $\mathbf{V}(t)$ is defined as [6]:

$$\mathbf{V}(t) = e \cdot \mathbf{z} \cdot \mathbf{E}(t) \tag{4.16}$$

where e is the electron charge, and $\mathbf{z}$ is the position operator. $\mathbf{E}(t)$ describes the oscillating E-field of the incident light. Assume that it is polarised in the z-direction with the amplitude E_0:

$$\mathbf{E}(t) = E_0 \cos \omega_0 t = E_0 \frac{e^{i\omega_0 t} + e^{-i\omega_0 t}}{2} \tag{4.17}$$

Thus:

$$\mathbf{V}(t) = e E_0 \frac{e^{i\omega_0 t} + e^{-i\omega_0 t}}{2} \cdot \mathbf{z} \tag{4.18}$$

$$V_{ij} = eE_0 \frac{e^{i\omega_0 t} + e^{-i\omega_0 t}}{2} \langle \psi_i | \mathbf{z} | \psi_j \rangle \tag{4.19}$$

The term $e\langle \psi_i | \mathbf{z} | \psi_j \rangle$ is known as the *dipole matrix element*, denoted as μ_{ij}. As $|1\rangle \to |1\rangle$ and $|2\rangle \to |2\rangle$ are forbidden transitions according to the selection rule [6], $z_{11} = z_{22} = 0$ and thus $\mu_{11} = \mu_{22} = 0$. In addition, the dipole matrix element is a measurable quantity in the SI unit of Debye (D), indicating that it should be a real number. Hence, we have $\mu_{12} = \mu_{21}$. Apply these conditions and eq. (4.19) to eq. (4.14) and eq. (4.15), finally we come to:

$$\dot{c}_1 = \frac{i}{\hbar} \mu_{12} E_0 \frac{e^{i\omega_0 t} + e^{-i\omega_0 t}}{2} e^{-i\omega_0 t} c_2 = i \frac{\mu_{12} E_0}{2\hbar} \left(1 + e^{-i2\omega_0 t}\right) c_2 \tag{4.20}$$

$$\dot{c}_2 = \frac{i}{\hbar} \mu_{12} E_0 \frac{e^{i\omega_0 t} + e^{-i\omega_0 t}}{2} e^{i\omega_0 t} c_1 = i \frac{\mu_{12} E_0}{2\hbar} \left(1 + e^{i2\omega_0 t}\right) c_1 \tag{4.21}$$

It is difficult to find the exact solutions to these differential equations. Hence, we need to play a trick at this step, i.e., applying the *rotating wave approximation* (RWA). Since the integral of a high-frequency oscillating term over a certain length of time is virtually 0, it thus contributes little to the expression of c_1 or c_2. In consequence, we can remove these terms and simplify the expressions to:

$$\dot{c}_1 = i \frac{\mu_{12} E_0}{2\hbar} c_2 \tag{4.22}$$

$$\dot{c}_2 = i \frac{\mu_{12} E_0}{2\hbar} c_1 \tag{4.23}$$

Differentiate eq. (4.22) and plug eq. (4.23) in:

$$\ddot{c}_1 = i \frac{\mu_{12} E_0}{2\hbar} \dot{c}_2 = -\left(\frac{\mu_{12} E_0}{2\hbar}\right)^2 c_1 \tag{4.24}$$

Assume that at the beginning ($t = 0$) the electron is in the eigen state $|1\rangle$, thus $c_1(0) = 1$ and $c_2(0) = 0$. We can quickly determine the solutions to be:

$$c_1(t) = \cos\left(\frac{\mu_{12}E_0}{2\hbar}t\right) \tag{4.25}$$

$$c_2(t) = i\sin\left(\frac{\mu_{12}E_0}{2\hbar}t\right) \tag{4.26}$$

Finally, the corresponding expressions of probability are:

$$|c_1(t)|^2 = \cos^2\left(\frac{\mu_{12}E_0}{2\hbar}t\right) \tag{4.27}$$

$$|c_2(t)|^2 = \sin^2\left(\frac{\mu_{12}E_0}{2\hbar}t\right) \tag{4.28}$$

As plotted in Fig 4.3, the probabilities are found to oscillate at the angular frequency of $\frac{\mu_{12}E_0}{\hbar}$, which is the so-called *Rabi frequency*, denoted as Ω_{Rabi}, and such oscillation is named *Rabi oscillation* after I. I. Rabi. In line with that, the electron population inversion, which is defined as $(|c_2|^2 - |c_1|^2)N$, also oscillates at the Rabi frequency.
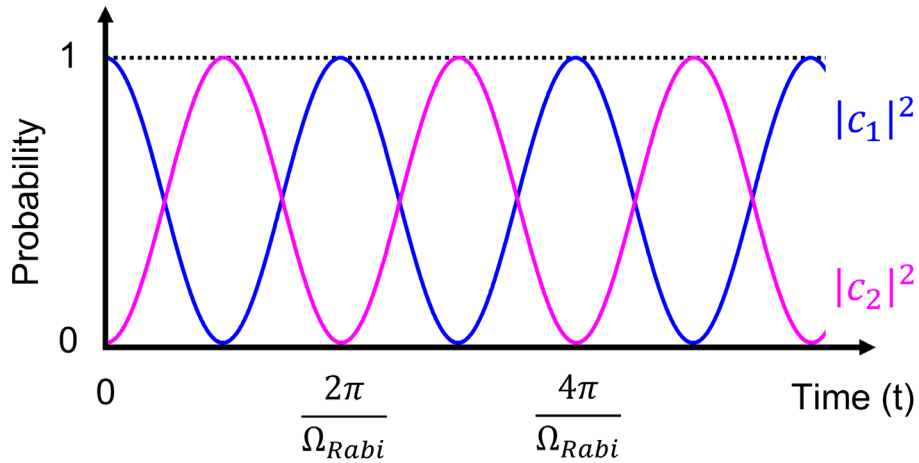
Fig 4.3 Probability of finding the electron in each state oscillates at the Rabi frequency

The above analysis allows us to develop a general understanding of the evolution of a closed two-level system when perturbed by resonant light. Nonetheless, such a model is an oversimplification. For a more practical case, we need to consider the damping effects in the

system further. On the one hand, electrons in the excited state $|2\rangle$ will naturally relax to state $|1\rangle$, e.g., by spontaneous emission, and thus disturb the Rabi oscillation. In other words, the lifetime of level 2 is limited, which is usually described by the longitudinal relaxation time T_1. One can simply imagine that if the Rabi oscillation period is longer than the lifetime of the upper state T_1, then it is unlikely that we would observe such oscillation. On the other hand, as one can see that all the theoretical derivations were based on eq. (4.1), implying the prerequisite for Rabi oscillation is the superposition state of electrons, or say, carrier coherence. Whilst in reality, due to spontaneous emission or atomic interactions with the surroundings, such as collisions and lattice vibrations, the atom can lose its superposition state. Correspondingly, the wavefunction $|\Psi\rangle$ collapses to either $|1\rangle$ or $|2\rangle$, thus disabling Rabi oscillation. The time that an electron can remain in the superposition state is characterised by the dephasing time T_2, also known as the transverse relaxation time. As a result, a necessary condition for the experimental observation of Rabi oscillation is:

$$\Omega_{Rabi} > \frac{1}{\sqrt{T_1 T_2}} \tag{4.29}$$

The gain medium of an operating laser is very similar to such a two-level system, with the upper and lower lasing states being the state $|2\rangle$ and $|1\rangle$, respectively, and near-resonantly interacting with the intracavity laser beam. The difference is that the laser gain medium is more of an open two-level system, with carriers flowing in and out, resulting in a dynamic population inversion. As a matter of fact, such population oscillation in a laser was predicted to cause single-mode instabilities in the 1960s, and it became known as the Risken-Nummedal-Graham-Haken (RNGH) instability [7][8], named after the four authors. When the laser operates just above the lasing threshold, the population inversion will remain at the threshold condition, which thus results in a constant gain, followed by a single-mode operation, as shown in Fig 4.4(a). Once the intracavity light intensity is sufficiently high, it

leads to a significant Rabi frequency that can overcome the damping effects in the cavity. Accordingly, the population inversion between the lasing levels can start oscillating at the Rabi frequency, leading to a periodically modulated gain. Finally, in analogy to the amplitude modulation (AM) technique, such oscillating amplification of light generates two side modes on either side of the primary mode at $\omega_0 \pm \Omega_{Rabi}$, as shown in Fig 4.4(b). The spectral distance between the two side modes is therefore equal to $2\Omega_{Rabi}$.
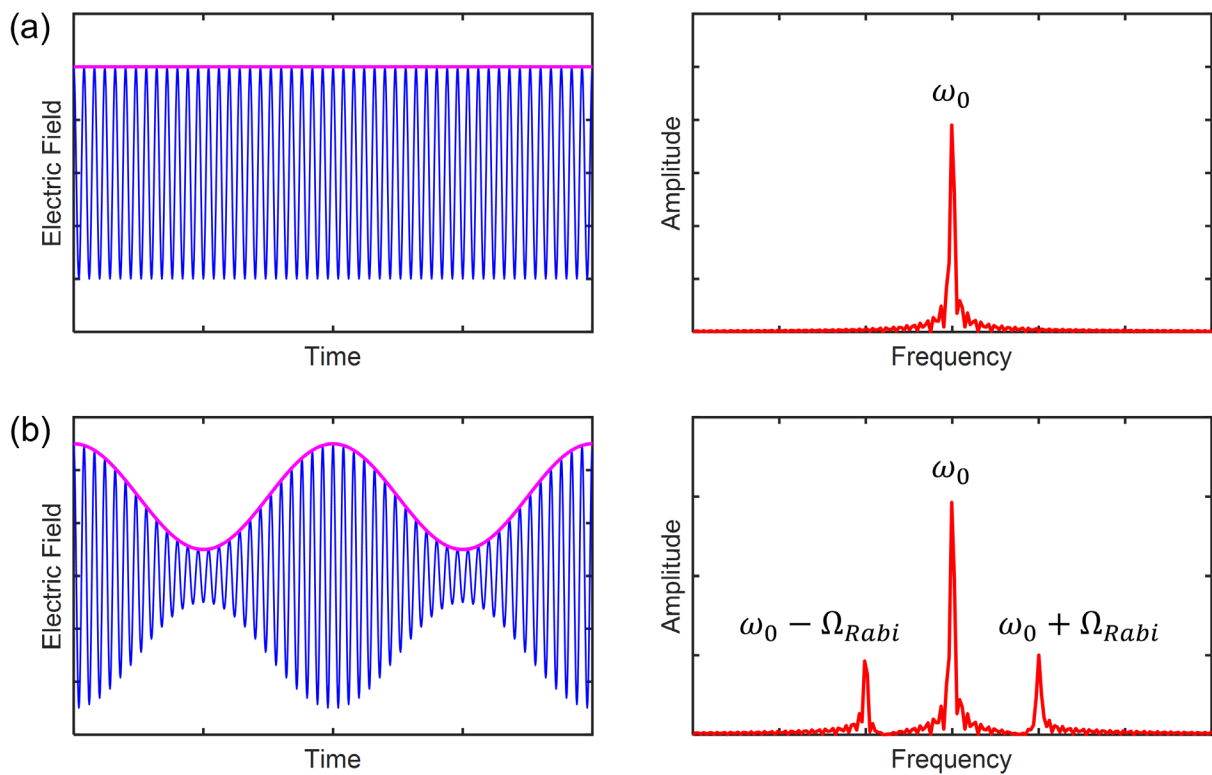
Fig 4.4 (a) E-field oscillates at the frequency of ω_0 with a constant amplitude and the corresponding spectrum converted by the Fourier transform. (b) E-field oscillates at the frequency of ω_0 with the amplitude modulated at the Rabi frequency Ω_{Rabi} and its corresponding spectrum.

But why is such spectrum splitting not previously seen in high-power conventional semiconductor lasers? The reason is still associated with the relative relationship between Ω_{Rabi} and T_1, T_2, i.e., eq. (4.29). The typical Rabi frequency of a laser diode is much smaller than the carrier dephasing rate T_2^{-1} [5]. In contrast, QCLs are intersubband lasers with a large

dipole matrix element (μ_{12}), which results in a large Rabi frequency compared to the relaxation rates $(T_1 T_2)^{-1}$ and thus allowing the single mode instability to be observed in high-power QCLs. However, on the other hand, the observed instability is slightly different in FP-QCLs and mainly in terms of two aspects: (1) In the case of QCLs, the central longitudinal mode (ω_0) disappears once the two side bands are generated; (2) The spectrum quickly splits when the injection current is only several tens of percent above the threshold I_{th}. For example, the splitting spectra of our QCLs are observed at $1.1 I_{th}$ and $1.36 I_{th}$ (see Fig 4.1), while in the early theoretical work, such instability only takes place when the driven current is nine times higher than the threshold current, i.e., $\sim 10 I_{th}$. The cause of the absence of the primary mode ω_0 has been widely recognised to be another co-existing mechanism exclusively in the FP-cavity – spatial hole burning (SHB), which will be covered in the next section, while the cause of the remarkably lowered threshold of RNGH instability in QCLs remains unclear and controversial [1][3][5][9]-[11].

Finally, to verify whether the spectrum splitting is indeed caused by Rabi oscillation, we can estimate the Rabi frequency based on the measured output power and compare that with the measured data. The time-averaged intracavity cavity intensity can be roughly estimated using the following equation based on the distributed loss approximation [3]:

$$I_{ave} = \frac{P_{out}}{\alpha_m LWH} \tag{4.30}$$

where P_{out} is the measured total output power. α_m is the mirror loss, the corresponding values can be found from previous waveguide simulations. L, W, H are the laser cavity length, core width and core thickness. Then the Rabi frequency f_{Rabi}, can be calculated:

$$f_{Rabi} = \frac{\Omega_{Rabi}}{2\pi} = \frac{\mu_{12} E}{2\pi \hbar} = \frac{e z_{34} \sqrt{\frac{2 I_{ave} \Gamma}{nc\epsilon_0}}}{h} \tag{4.31}$$

where e is the electron charge, z_{34} describes the coupling strength between the lower and upper lasing state (levels 3 and 4, see Fig 3.4), which can be found out from the previous nextnano.QCL simulation of the active region bandstructure (1.92 nm). Γ is the confinement factor, which has been determined to be ~0.65 in the waveguide simulation in Chapter 3. The reason for counting this in is that the light travelling outside the laser core does not contribute to the population flopping. n, c, and ϵ_0 are the effective refractive index of the laser core (~3.3), vacuum light speed, and vacuum permittivity, respectively.

Based on the above model, we can thus estimate the power-dependent Rabi frequency for both devices in Fig 4.1 and compare that with the measured splitting distance from the spectra. The result is shown in Fig 4.5. One can see a relatively good agreement between the theoretically calculated twice Rabi frequency and the measured spectral splitting distance between two sidebands, validating the fundamental cause of spectrum splitting to be the population oscillation at the Rabi frequency.
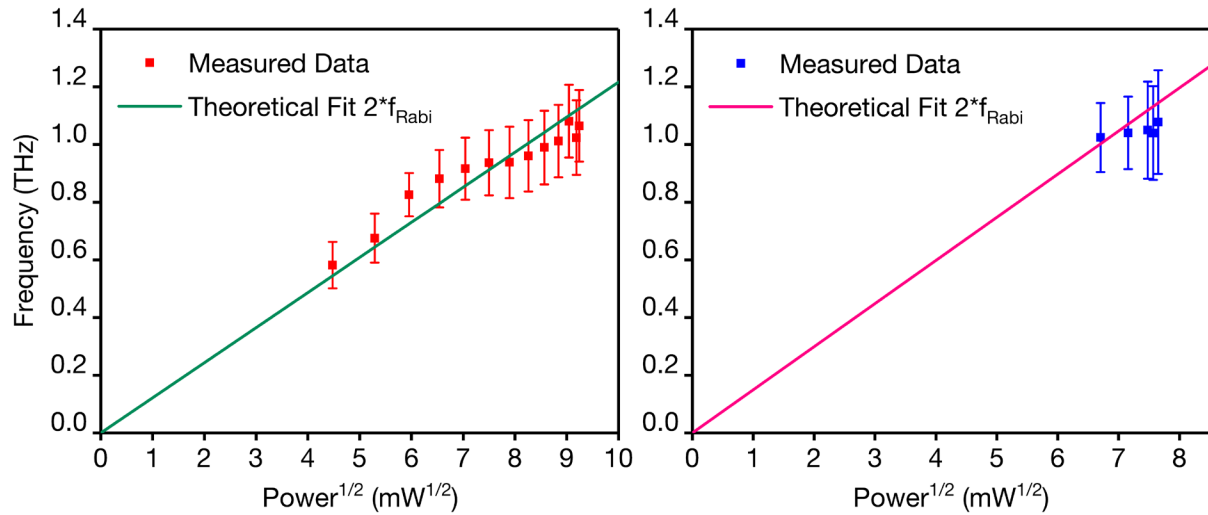
Fig 4.5 Comparison of theoretically calculated spectral distance ($2 \times f_{Rabi}$) and measured spectrum splitting. The red data (left) is measured from the red spectrum in Fig 4.1, which is an 8μm×2mm FP-QCL, and the blue data (right) is measured from the blue spectrum, which is a 4.5μm×3mm FP-QCL. Their L-I-V data can be found in Chapter 3. The error bars refer to the FWHM of one sideband.
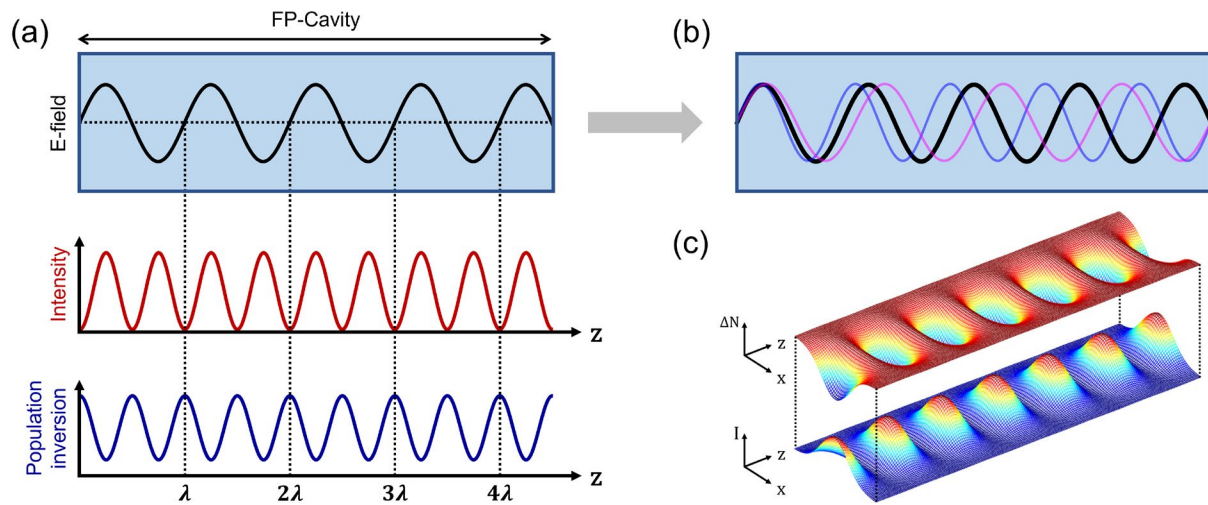
4.2.2 Spatial Hole Burning

In contrast to ring-cavity lasers, where light unidirectionally travels along the ring loop route, and the light intensity distribution in the gain medium is uniform, the two counter-propagating electromagnetic waves in the FP-cavity form a standing wave, which only flips up and down at fixed position, as shown in Fig 4.6.

(a) Travelling-wave Laser   (b) Standing-wave Laser
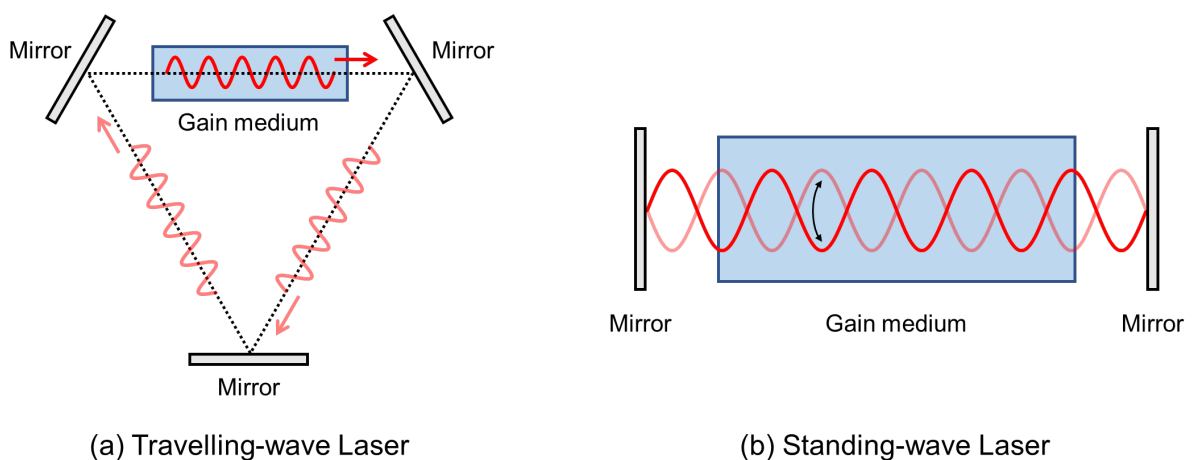
Fig 4.6 (a) Travelling wave in a ring-cavity laser. (b) Standing wave in an FP-cavity laser.

Accordingly, the distribution of light intensity, or photon density, becomes position-dependent in the FP-cavity, as one can see in Fig 4.7(a). The carriers around the antinodes of the standing wave are depleted much faster than those around the node positions, where the light intensity is always zero. This, therefore, further leads to a non-uniform distribution of electron population, and thus the population inversion, forming spatial hole burning (SHB). Such 'hole' burning can be seen very visually in a 3D diagram, as shown in Fig 4.7(c), where many holes are generated in the plane of population inversion distribution. As a result, side longitudinal modes become favoured as they have more spatial overlaps with the rich-gain

spaces, as shown in Fig 4.7(b). Also, multi-transverse mode operation is preferred, which, obviously, is another approach to reach the rich-gain spaces in the cavity.


Fig 4.7 (a) In a single longitudinal mode FP laser, the spatially non-uniform distribution of light intensity in the FP-cavity leads to a non-uniform distribution of population inversion, resulting in the spatial hole burning effect. (b) Spatial hole burning induced multimode operation, where the black wave is the primary longitudinal mode and blue/pink are adjacent modes. (c) 3D view of the non-uniform distribution of intracavity light intensity (I) and population inversion (ΔN) along the cavity.

On the other hand, if the carrier diffusion is quick enough in the gain medium, nearby carriers can then replenish to the 'holes' to mitigate the strength of the SHB effect. In other words, FP-lasers with fast carrier diffusion can remain isolated from the SHB effect. For this reason, diode lasers are less affected by the SHB effect [12][13]. In contrast, QCLs are lasers with limited carrier diffusion (i.e., compared to the ultra-fast gain recovery time at picosecond level) and therefore suffer from severe SHB. Their single-frequency operations are extremely susceptible to SHB-induced gain saturation, and side modes can subsequently rise, broadening the spectrum.

To sum up, the multimode instability of FP-QCLs, i.e., the spectrum splitting, is caused by the combined effect of Rabi oscillation and spatial hole burning. As shown in Fig 4.8, Rabi

oscillation is the temporal modulation of the electron population inversion, which is also known as population pulsation (PP) [3]. Side bands are generated in the spectrum mainly because of this mechanism. The separation between the two sidebands is roughly twice the Rabi frequency, which can further enlarge with the increment of intracavity light intensity. In contrast to the original RNGH instability, proposed based on a unidirectional travelling-wave laser, FP-QCLs are standing-wave lasers with a strong spatial hole burning effect, which is essentially spatial modulation of electron population and also known as population grating (PG) or gain grating [3]. The co-existence of these two mechanisms eventually leads to a splitting spectrum without the central mode and a lowered instability threshold.
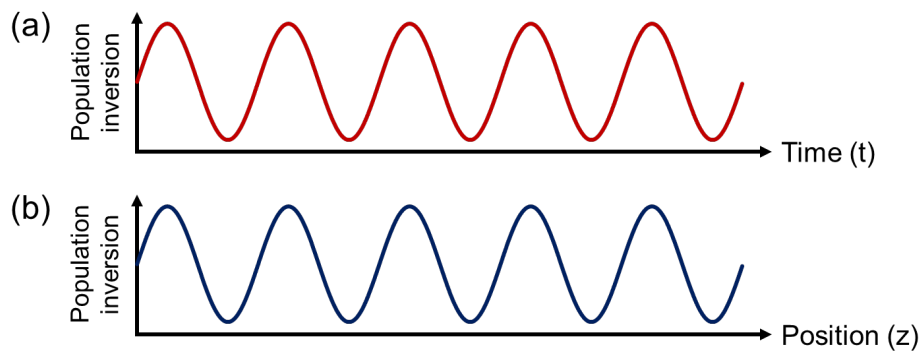
Fig 4.8 (a) Temporal modulation of electron population – Rabi oscillation or population pulsation; (b) Spatial modulation of electron population – spatial hole burning or population grating.

This problem can be mathematically studied based on the Maxwell-Bloch equations, with additional considerations of the counter-propagating electromagnetic waves (i.e., standing wave) and the population grating due to SHB. Here we only qualitatively described the mechanisms behind the odd spectrum, and the quantitative analysis will not be repeated to keep the section concise. But eventually, one will come to a theoretical spectrum with twice Rabi splitting and without the central mode, as shown in ref. [1][5].

4.3 Spatial Mode Instability

4.3.1 Origin of Beam Steering

We observed abnormal L-I curves from many of the first fabricated QCLs in the very beginning. Later, through beam profile measurement, we found that these QCLs suffered from beam steering issues. In particular, a radical beam steering was observed in CW mode QCLs. As shown in Fig 4.9, the laser initially emitted two output beams pointing at ±30°; at a certain high injection level, i.e., 0.34 A, the laser output became a single beam pointing at 20°. Most interestingly, the multimode spectral instability was completely washed out when the abrupt beam steering happened, i.e., the laser switched back to single-frequency operation.
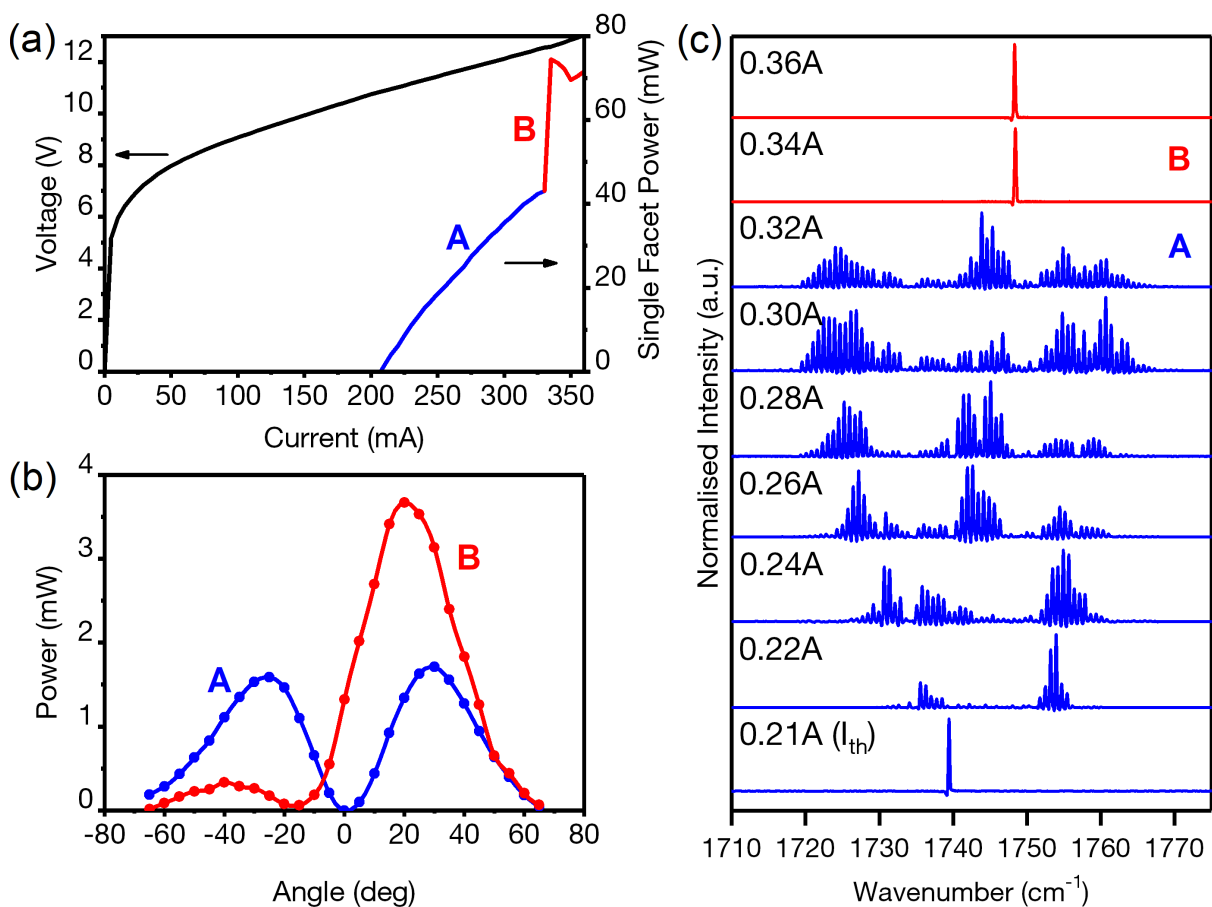
Fig 4.9 Compiled data of an 8μm×2mm QCL mounted on diamond, operating in CW mode at 20°C. (a) L-I-V, (b) beam profile, and (c) spectrum as a function of injection current.

Beam steering in QCLs has been frequently reported in the past [2][14]-[22], while most were operating in pulsed mode. In fact, this behaviour was even earlier reported in 980nm near-IR power lasers in the 1990s [23]-[26] and was perfectly explained as a result of interference between multiple coherent transverse modes. We can simply use the two lowest-order modes, i.e., the fundamental mode TM_{00} and first-order mode TM_{01}, to illustrate this, as shown in Fig 4.10. The main reason why a beam can be asymmetric is that the polarisations of the two sub-beams in the TM_{01} mode are opposite; thus, in the case of linear addition of TM_{00} and TM_{01} mode, i.e., interference, the right beam (red spot) will be further enhanced while the left beam (blue spot) is suppressed due to the negative sign of the E-field.
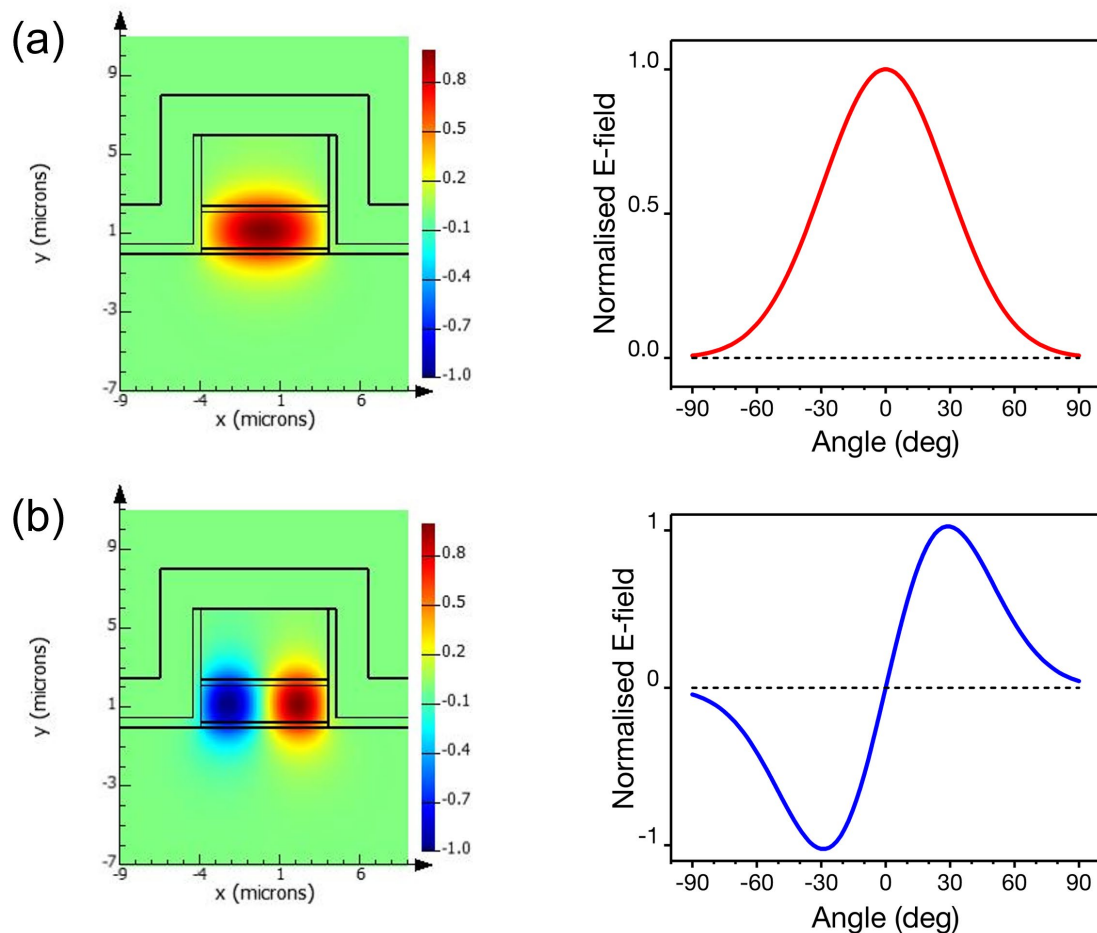
Fig 4.10 E-field distribution of different transverse modes in an 8µm-wide QCL, simulated by Lumerical. (a) Fundamental mode (TM_{00}) and the corresponding normalised x-axis far-field profile. (b) First order mode (TM_{01}) and the corresponding normalised x-axis far-field profile.

Simply add the two far-field beam profiles in Fig 4.10 together and square it, i.e., convert into intensity ($I \propto E^2$), we then obtain the resultant beam profile, as shown below, which is very similar to what we have observed in Fig 4.9(b).
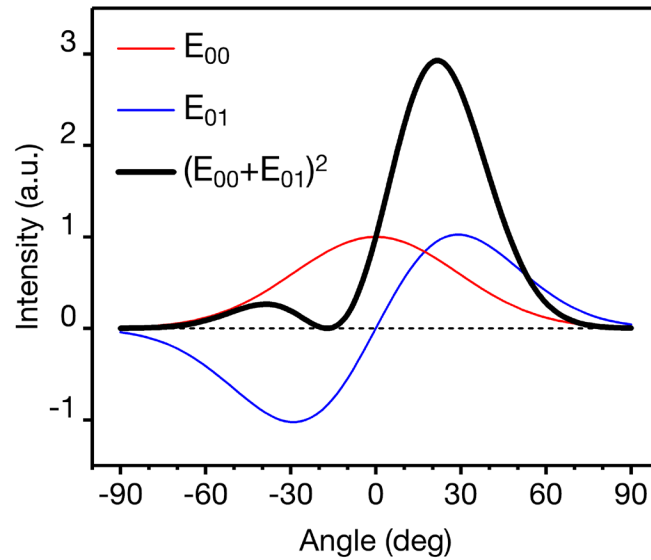
Fig 4.11 Linear addition of x-axis TM_{00} E-field profile and TM_{01} E-field profile

In the above case, the resultant beam is generated by two lowest-order transverse modes with the same amplitude and zero phase difference. Considering the different energy distributions in two transverse modes and the arbitrary phases, we can write a more general expression for the normalised resultant beam profile at the laser facet:

$$I(x) = E^2(x) = \left(\alpha E_{00}(x) + \beta E_{01}(x)\right)^2 \qquad (4.32)$$

where $E_{00}(x)$ and $E_{01}(x)$ are the normalised E-field profile of TM_{00} and TM_{01} modes. α and β are the corresponding mode coefficients. Note that this coefficient contains both amplitude and phase info. In other words, it can be either positive or negative for the E-field polarisation to flip up and down. In addition, it should be emphasised that this equation only describes the

near-field pattern of the mixed beam; therefore, the intensity is a function of position. For near- to far-field profile conversion, i.e., $I(x) \longrightarrow I(\theta)$, it is similar to a projection, but the diffraction effect needs to be considered [16].

The above analysis explained the formation of irregular beam profiles from a laser. However, this is not the end of the story because the co-existing transverse modes are not necessary to be coherent, whilst, in the previous analysis, it was taken as an absolute fact that different spatial modes are coherent. In addition, at this stage, we are still unable to explain the radical changes in the laser spectrum in Fig 4.10(c). To elaborate on this, we can re-consider the above model, i.e., a laser that operates in the superposition of TM_{00} and TM_{01} mode. For simplicity, we only consider two normalised modes with a phase difference of θ, thus:

$$I = E^2 = \left(E_{00} + E_{01}e^{i\theta}\right)^2 = E_{00}{}^2 + E_{01}{}^2 + 2E_{00}E_{01}e^{i\theta} \qquad (4.33)$$

When the two modes are coherent and phase-locked, the coherence term $2E_{00}E_{01}e^{i\theta}$ contributes to the final shape of the mixed beam; while in an incoherent case, i.e., the two modes are phase-unlocked, the average effect of the term $2E_{00}E_{01}e^{i\theta}$ is zero. Therefore, the resultant beam profile is:

$$E^2 = E_{00}{}^2 + E_{01}{}^2 \qquad (4.34)$$

This is clearly a symmetric beam profile, as shown in Fig 4.12. Despite the different shapes of the mixed beam in the coherent and incoherent coupling case, the integrated areas under the envelopes are the same, i.e., the total intensity remains unchanged, merely different in the distribution. This is totally understandable, as the integral of the coherence term is zero.
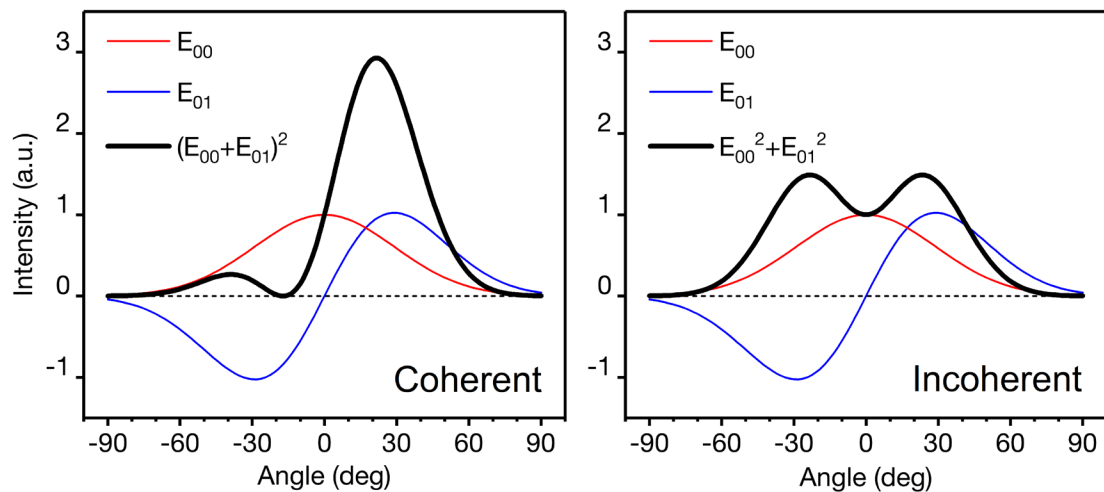
Fig 4.12 Far-field patterns of coherent and incoherent coupling of TM_{00} and TM_{01} mode

Hence, here comes the next question: how does such coherence occur between the transverse modes? This phenomenon can be linked to a bigger picture, namely *synchronisation*, because when the transverse modes move from uncorrelated to frequency- and phase-locked, this essentially implies that the beams become optically synchronised [20][25], which is the nature of the coherence. In fact, synchronisation can be seen everywhere in the world [27]. For example, as shown in Fig 4.13, two closely positioned pendulum clocks that initially swing in arbitrary phases will swing at the same frequency and phase after a certain period of time; or, in a dark forest, thousands of fireflies initially flicker arbitrarily, but eventually, they begin to flash in the same rhythm.
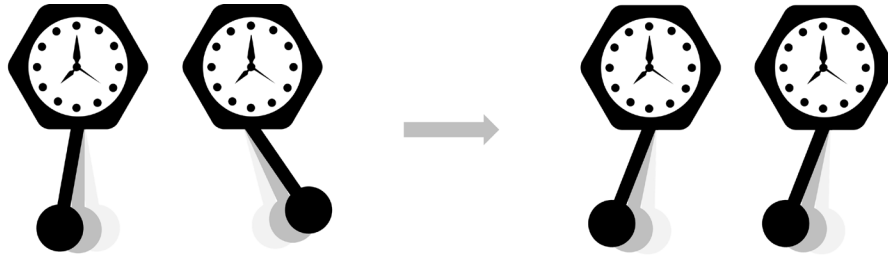
(a) Synchronisation between pendulum clocks
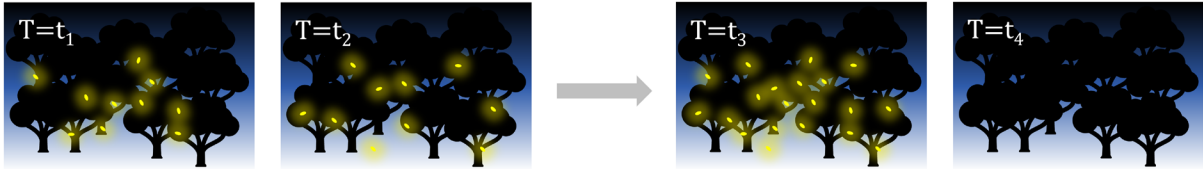
(b) Synchronisation of fireflies glowing

Fig 4.13 The picture of synchronisation [27]

Therefore, synchronisation can happen mechanically, biologically, and in our case, optically etc. In general, it indicates that when oscillators are weakly coupled, somewhat interactions can occur in between, which eventually results in motion sync. For instance, the two coupled pendulum clocks can interact with each other through the vibrations of the wall. In the laser cavity, transverse modes are spatially overlapped, travelling through the same gain medium, which definitely allows somewhat interactions to take place and leads to the synchronisation of transverse modes. This is proposed to be caused by the *Four Wave Mixing* (FWM) interactions between different transverse modes originating from the third-order nonlinearity. In ref. [16][17][18][20], self-synchronisation of laser modes is observed and explained as the result of nonlinear coupling between three transverse modes:

$$TM_{00} + TM_{02} \rightleftharpoons TM_{01} + TM_{01}$$

Nonlinear frequency conversion processes such as four wave mixing are highly phase-sensitive, and thus generated light is phase-locked [28]. Therefore, this theory is capable of explaining the spectral changes when beam steering takes place, and also providing an

answer to the origin of the modal phase-locking rather than 'assuming' that transverse modes are coherent as the starting point. Moreover, beam steering does usually happen with spectral changes. A typical case is shown in Fig 4.14 [20]. The laser initially operates in three incoherent transverse modes and thus results in a symmetric beam profile. In Fig 4.14 (d), one can see that the spectral combs of different transverse modes are closely located with slight detuning. While at a certain high injection level, three transverse modes are synchronised (red region), and only one spectral comb can be seen in the spectrum as a result of FWM-induced frequency-locking. Meanwhile, the beam profile becomes highly asymmetric due to the modal phase coherence, followed by modal interference.
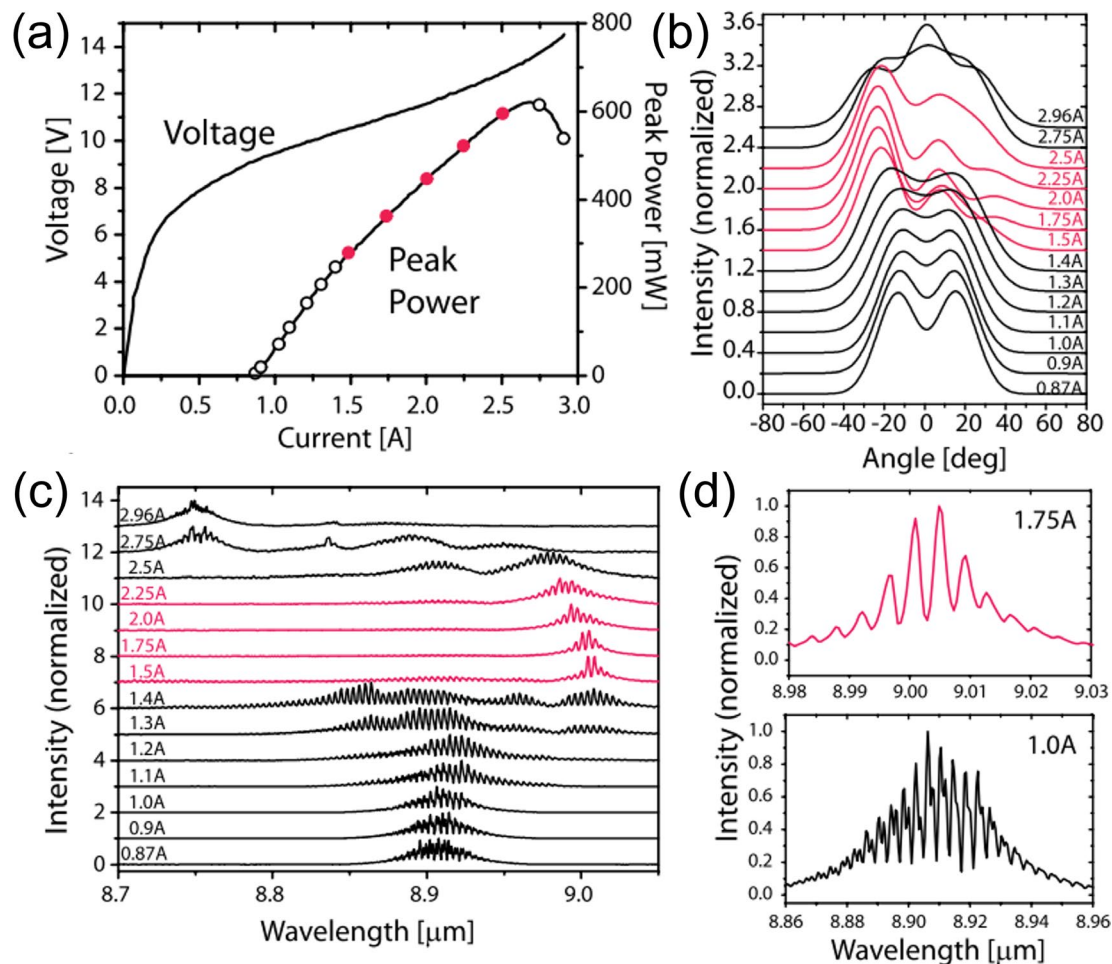
Fig 4.14 Experimental observation of synchronisation of three transverse modes, TM_{00}, TM_{01} and TM_{02}. (a) QCL pulsed mode L-I-V. (b) Evolution of beam profile. (c) Evolution of spectrum. (d) Spectrum before and after modal synchronisation (the red region refers to the synchronised operation region). Reproduced from ref. [20]. Reuse and permission obtained from the American Physical Society (APS) under the license number RNP/22/DEC/060700.

Furthermore, based on the proposed theoretical model [16][17][18][20], it was shown that transverse modes with different frequencies could eventually be synchronised to a single frequency, as shown in 4.15. The laser starts with TM_{01} mode; with the increase of gain, TM_{00} and TM_{02} modes are sequentially activated with detuned frequency; while above ~3× the threshold gain, the amplitude of each mode becomes relatively stable, and the frequencies are completely locked to the same value.
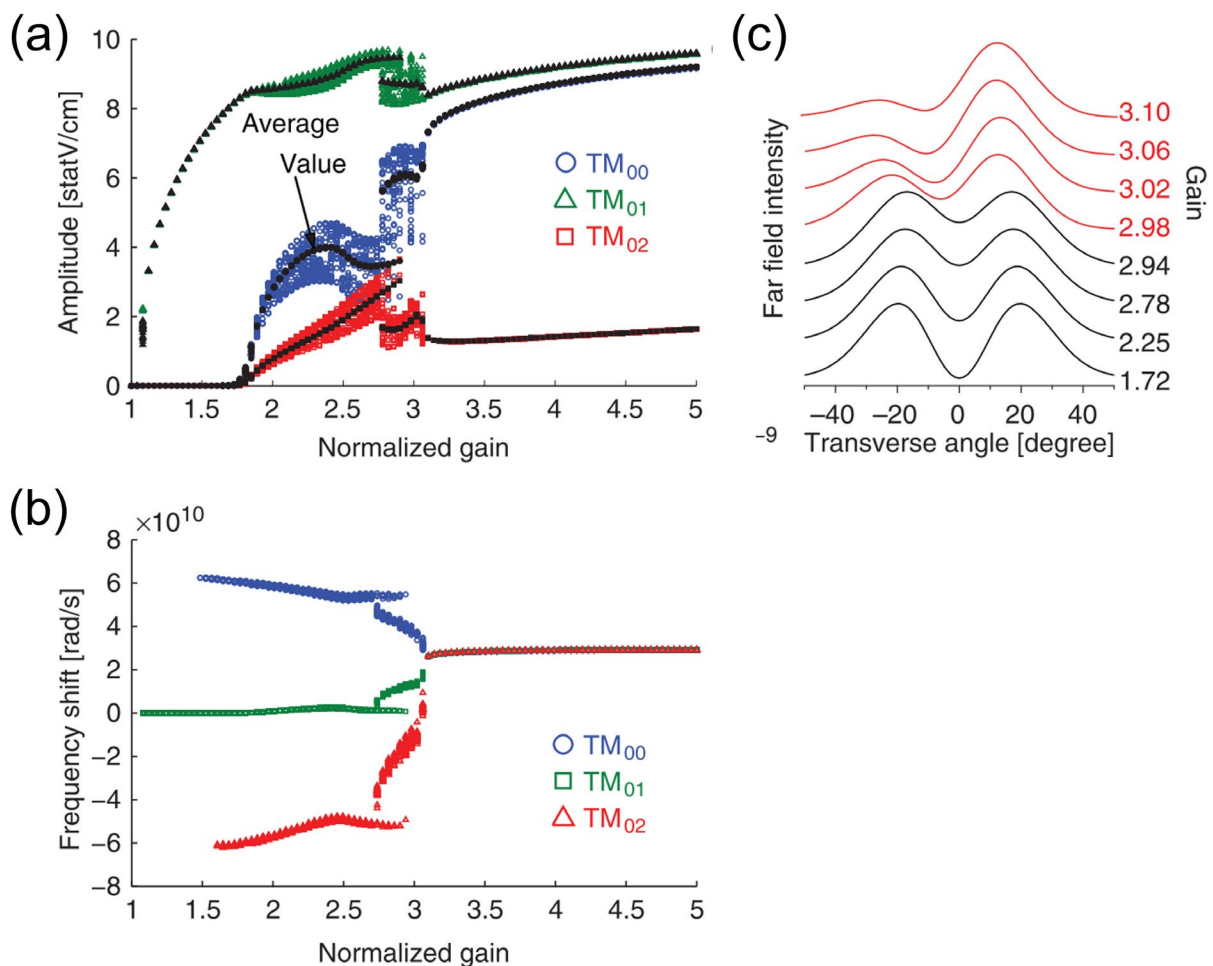
Fig 4.15 Theoretical model of synchronisation of three transverse modes, TM_{00}, TM_{01} and TM_{02}. (a) Amplitude and (b) frequency evolution of three transverse modes, starting from random conditions. (c) Corresponding evolution of the resultant beam profile. Reproduced from ref. [20]. Reuse and permission obtained from the American Physical Society (APS) under the license number RNP/22/DEC/060700.

This theoretical model seems relatively similar to what we have observed, i.e., multi-transverse mode coupling eventually results in single-frequency operation. Hence, in order to apply this theory to our observation, analysis of the beam composition is required, i.e., we need to find out whether the output beam is mixed up by two transverse modes or three transverse modes.

First, the waveguide simulation was revisited and it was found that the 8μm-wide ridge waveguide does support three transverse modes, i.e., TM_{00}, TM_{01}, and TM_{02}, as shown below.

(a) TM_{00} mode   (b) TM_{01} mode   (c) TM_{02} mode
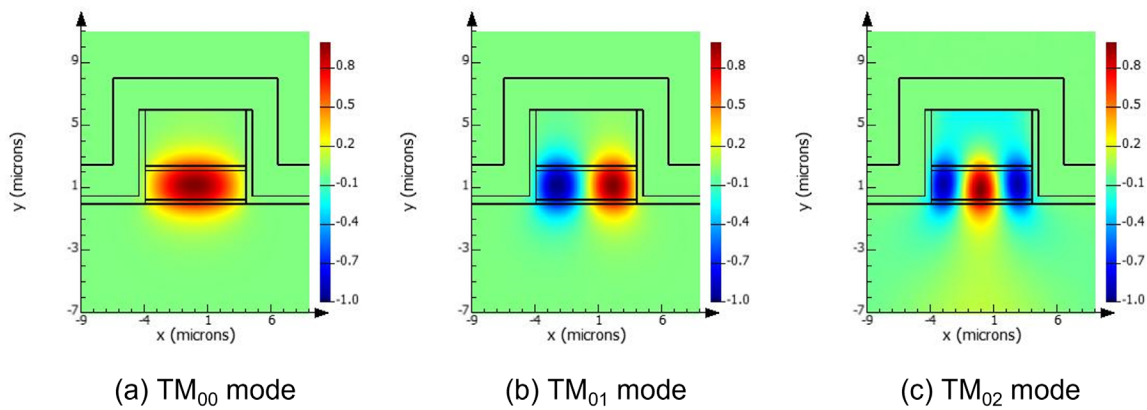
Fig 4.16 Transverse modes in an 8μm-wide QCL ridge waveguide, simulated by Lumerical.

Based on the simulation, we can obtain the gain threshold of each transverse mode, which in fact, has been done in Chapter 3; therefore, the data is directly re-compiled in Table 4.1, with the additional data of the TM_{02} mode added. Accordingly, we can roughly estimate the threshold current of each transverse mode by neglecting the transparency current and thus taking the simple linear relation that $I_{th} \propto g_{th}$ [29]. The threshold current of TM_{01} mode can be directly read from Fig 4.9(a), i.e., 210 mA, and consequently, the threshold currents of the fundamental mode and second order mode are estimated to be 211 mA and 323 mA. We can see that the threshold of TM_{02} mode is within the dynamic range of the QCL (rollover is at

~350mA) and thus, it is theoretically possible to be activated during operation. In particular, it is relatively close to the experimentally observed kink point, i.e., 330 mA.

<p style="text-align:center;">**Table 4.1** Calculated gain threshold of each mode and corresponding threshold current</p>

	Gain Threshold g_{th} [cm^{-1}]	Threshold Current I_{th} [mA]
TM$_{00}$	16.402	211 (estimated)
TM$_{01}$	16.296	210 (measured)
TM$_{02}$	25.097	323 (estimated)

With the theoretical validation of the possible presence of a third transverse mode TM$_{02}$ in the waveguide, we then moved to the experimental analysis. Similar to the case in Fig 4.14, the transverse mode composition of a mixed beam usually can be traced via the spectrum [2] because different transverse modes have slightly different effective refractive indexes due to the dissimilar spatial distribution in the cavity, which results in a marginally distinct mode spacing (FSR), recalling that $FSR = 1/(2n_{eff}L)$. The spectrum of a multi-transverse mode QCL sample is shown in Fig 4.17. One can see that an individual cluster of modes gradually rises on the right side of the main spectral comb with the increase of injection current. Intuitively, we may assume that the two combs belong to two transverse modes, and the measured FSR values can further confirm this. The right comb features slightly denser longitudinal modes, indicating a bit larger refractive index. Thus, it is considered linked to the fundamental mode TM$_{00,}$ which usually has the largest refractive index among the spatial modes due to its central location, i.e., less overlap with low refractive index materials. And consequently, the main comb should belong to TM$_{01}$ mode. In some cases, the spectral combs generated by different transverse modes are not as distinct as this example, e.g., the MR4241 sample in Fig 3.11 and Fig 4.14(d), but they are still visually distinguishable.
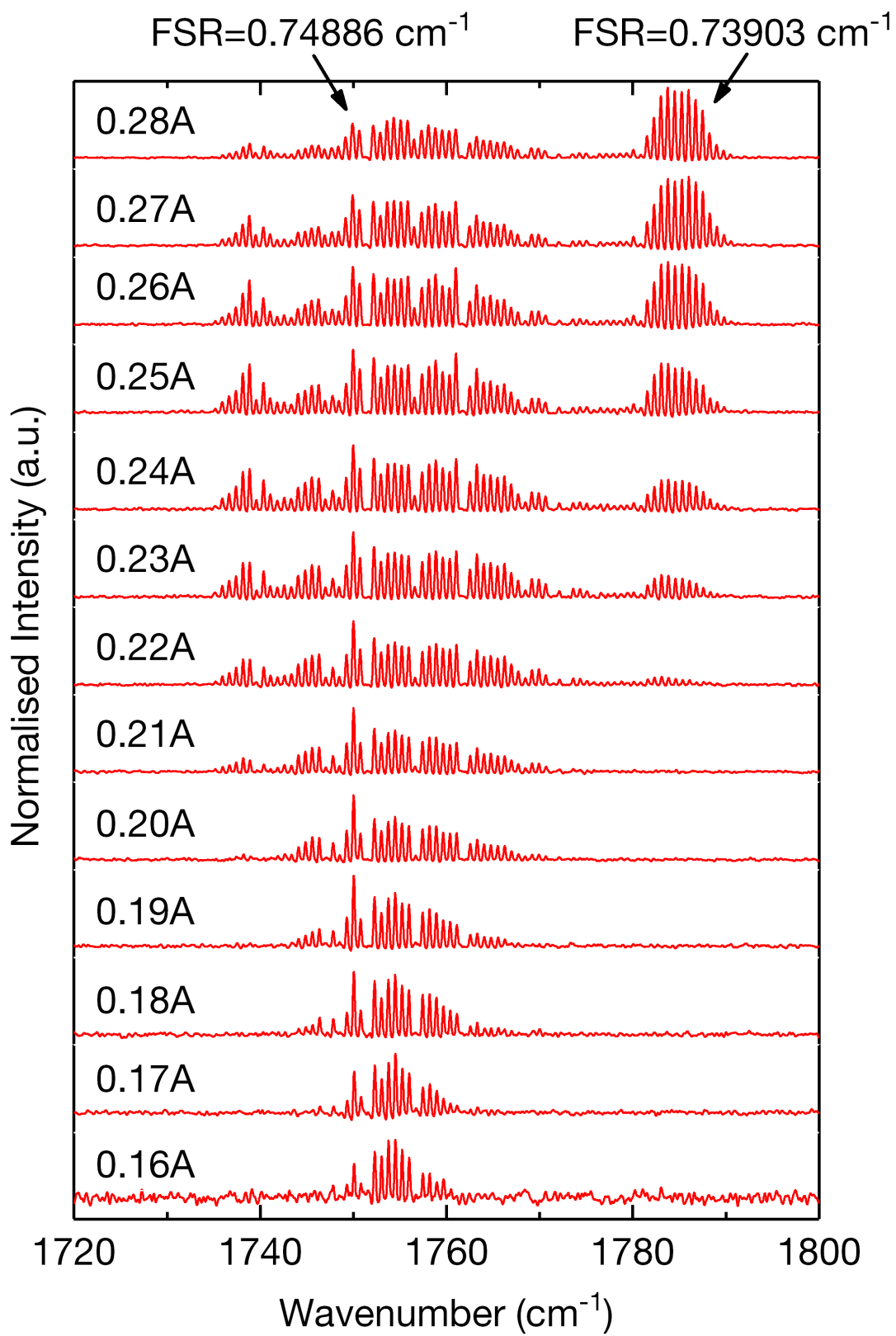
Fig 4.17 Pulsed spectra of a QCL operating at RT with 2% duty cycle, 50ns pulse width.

However, we later realised that this method worked for most of the pulsed QCLs with short-PW but was not that effective in our case, which may be the reason why most works of QCL beam steering are reported based on pulsed operations. Similar findings were mentioned in ref. [12], which is the only work we could find that reports QCL beam steering in CW mode, and they explained this as phase-locking, i.e., the spectral combs of different transverse modes are entirely overlapped.

Therefore, we have to analyse the beam composition via another approach, i.e., far-field pattern fitting. Although previously we have shown that a similar beam profile can be generated merely by considering the mixture of two lowest-order transverse modes, TM_{00} and TM_{01} (see Fig 4.11), it is more of a general explanation of beam steering. Here we need to treat it more precisely. Therefore, we first remeasured a beam profile when the radical beam steering was observed, and the QCL switched to single-frequency operation. The profile was measured in a 180° full scan (-90° to 90°) for a maximised data fitting range and then normalised. The theoretical far-field pattern of each transverse mode can be obtained from the Lumerical 2D mode simulation. With these elements prepared, we can attempt to fit the measured data points with a specific combination of transverses modes. For simplicity, we assume that the phase difference between each mode is 0, and thus the only variable is amplitude. The general fitting model is:

$$E^2 = (\alpha E_{00} + \beta E_{01} + \gamma E_{02})^2 \tag{4.35}$$

where E_{00}, E_{01}, and E_{02} are the normalised profiles of the TM_{00}, TM_{01} and TM_{02} modes, respectively, and α, β, γ are the corresponding modal coefficients. For easier comparison, we introduce the normalisation condition:

$$\alpha^2 + \beta^2 + \gamma^2 = 1 \tag{4.36}$$

In the case of two modes coupling, we can zero the amplitude γ. However, when we fit the

data points with the composition $0.65E_{00}+0.76E_{01}$, a certain mismatch did exist, as shown in Fig 4.18(a). The main peak is slightly shifted to the right side of the measured beam profile. While by adding the TM_{02} mode in and using the combination $0.7E_{00}+0.7E_{01}+0.1E_{02}$, we obtained a nearly perfect fitting, see Fig 4.18(b). This is therefore considered the second evidence to confirm the presence of TM_{02} mode in the mixed beam.
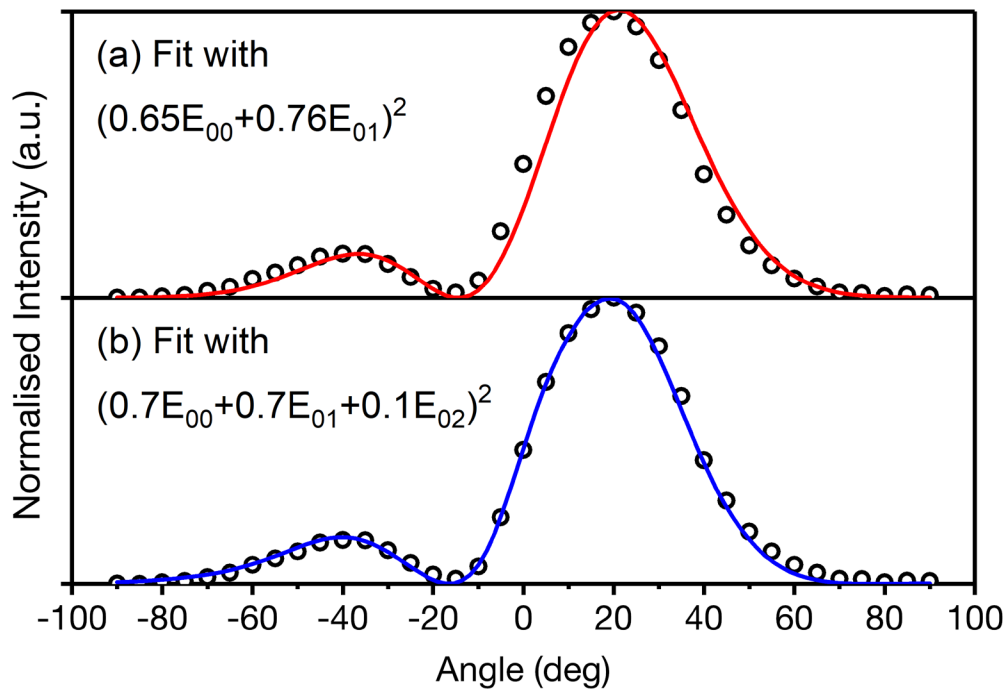
Fig 4.18 Measured beam profile data points (the circles) are fitted using (a) two theoretical models, i.e., considering only two modes mixing, and (b) three modes mixing. E_{00}, E_{01} and E_{02} are the normalised E-profiles of TM_{00}, TM_{01} and TM_{02} mode, respectively.

Furthermore, a third fact implying that the QCL can simultaneously operate in three transverse modes is the pulsed mode beam profile, as shown in Fig 4.19. For such a beam profile, one would find that it is impossible to fit with only TM_{00} and TM_{01} modes as the central dip is not zero; it has to be realised in three dimensions, i.e., TM_{00}, TM_{01}, and TM_{02}. Note that although this device operates in pulsed mode, the pulse width (PW) is 800ns, which is relatively long and thus causes a thermal shift of longitudinal modes, eventually resulting

in a smeared spectrum. Therefore, a spectral analysis of transverse modes, similar to Fig 4.17, is impossible in this case. Besides, with short pulse widths, we did not observe pronounced beam steering like this. To sum up, all the collected evidence seems to support the hypothesis that three transverse modes co-exist in the waveguide when the radical CW beam steering takes place. Therefore, the collapse of the multimode spectrum, i.e., the fascinating single-frequency operation, could be explained as the result of the four-wave mixing process between three transverse modes.
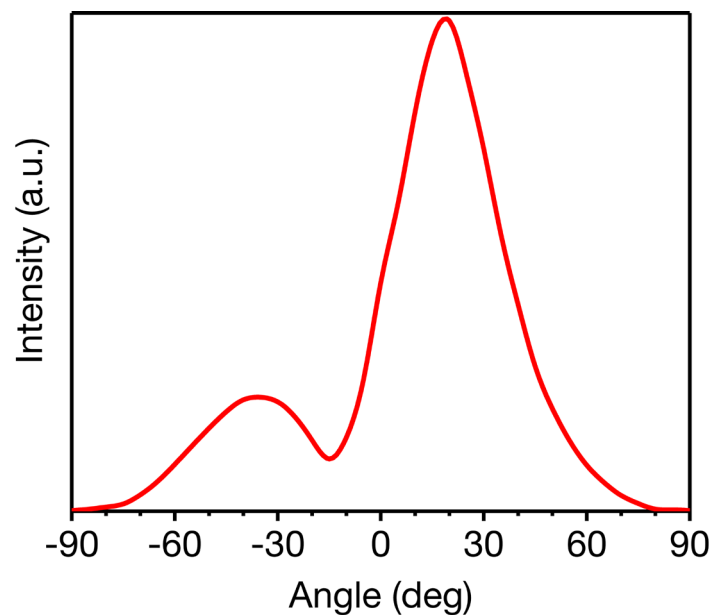
Fig 4.19 Measured beam profile of an 8µm-wide QCL in pulsed mode, DC=1%, PW=800ns.

4.3.2 Optical Bistability

Another interesting observation is that once CW beam steering is triggered, the laser can persist in operating in such ultimately synchronised mode even when decreasing the current to a much lower injection level below the trigger level, as shown in Fig 4.20. As more power can be collected by the power meter in the steering mode, the L-I curve measured by decreasing the injection current is different from the standard L-I curve measured by

increasing the injection current. The spectral and beam profile measurements also confirm that the QCL continues to operate in the synchronised mode before the region where two L-I curves are recombined, i.e., between 260 and 360 mA. When the current is reduced to 240mA, the laser switches back to the split beam and the multimode spectrum. Therefore, between 240mA and 360mA, the QCL can operate in two different modes, which depend on the 'direction' of the injection current, thus leading to optical bistability.
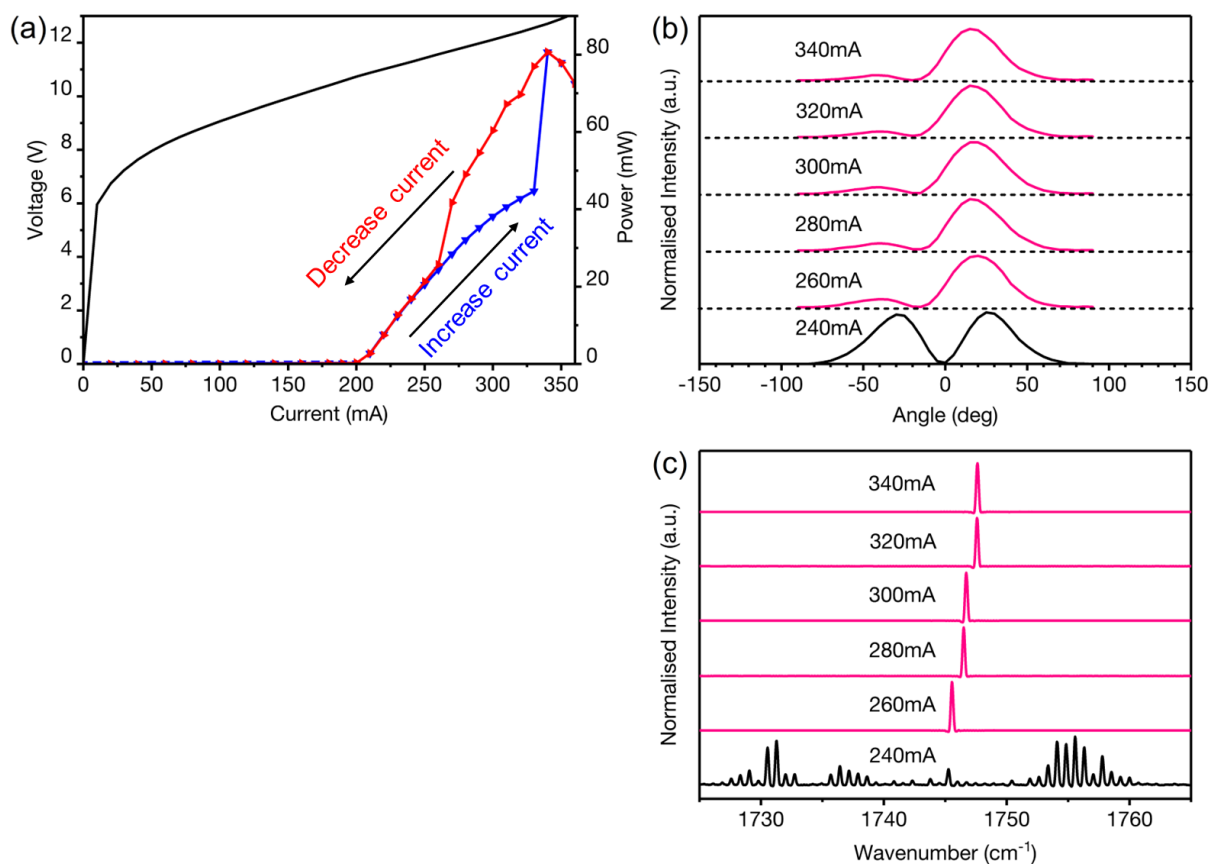
Fig 4.20 (a) CW L-I-V measured by increasing the current from 0 to 360mA and decreasing the current from 360mA to 0. The QCL continues to operate in the synchronised mode with the decrease of injection, resulting in a different L-I curve. (b) Far-field beam profile measured during decreasing current. (c) Spectra measured during decreasing current.

Such optical bistability naturally reminds us of the presence of a saturable absorber [28] in the cavity, as shown below.
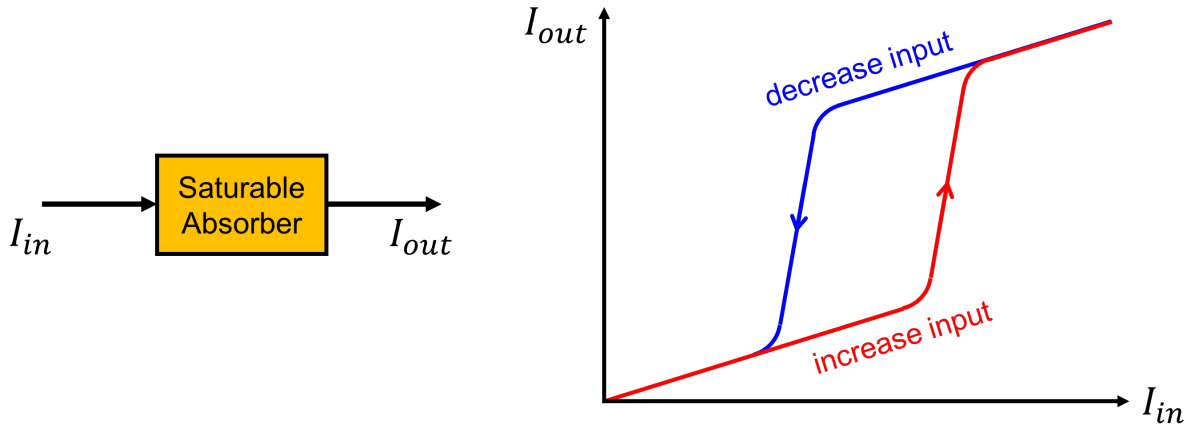
Fig. 4.21 Input light intensity vs output light intensity in a typical saturable absorber [28]

In the saturable absorber (SA), the optical loss is intensity-dependent [28]:

$$\alpha(I) = \frac{\alpha_0}{1 + \dfrac{I}{I_s}} \tag{4.37}$$

where α_0 is the loss coefficient at a low light intensity, and I_s is the saturation intensity. Consequently, a higher input intensity leads to a lower optical loss. Thus, when the injection current starts to decrease from high power, the net laser gain can remain at a higher level, if compared to the case of increasing current from 0.

But what is the nature of SA in the QCL? Considering the significantly increased local intensity of the mixed spatial mode, it is reasonable to believe that a more substantial Kerr lensing effect [30][31] can be generated in the waveguide as the refractive index becomes intracavity intensity-dependent [28]:

$$n(I) = n_0 + n_2 I \tag{4.38}$$

where n_0 is the cold cavity refractive index, and n_2 is a coefficient proportional to the third-order nonlinearity $\chi^{(3)}$, which characterises the optical nonlinearity strength. When the beam

intensity rises, the refractive index of the laser medium is also increased, which naturally generates a focal lens in the cavity, resulting in beam self-focusing, as shown in Fig 4.22.

(a) Low intensity
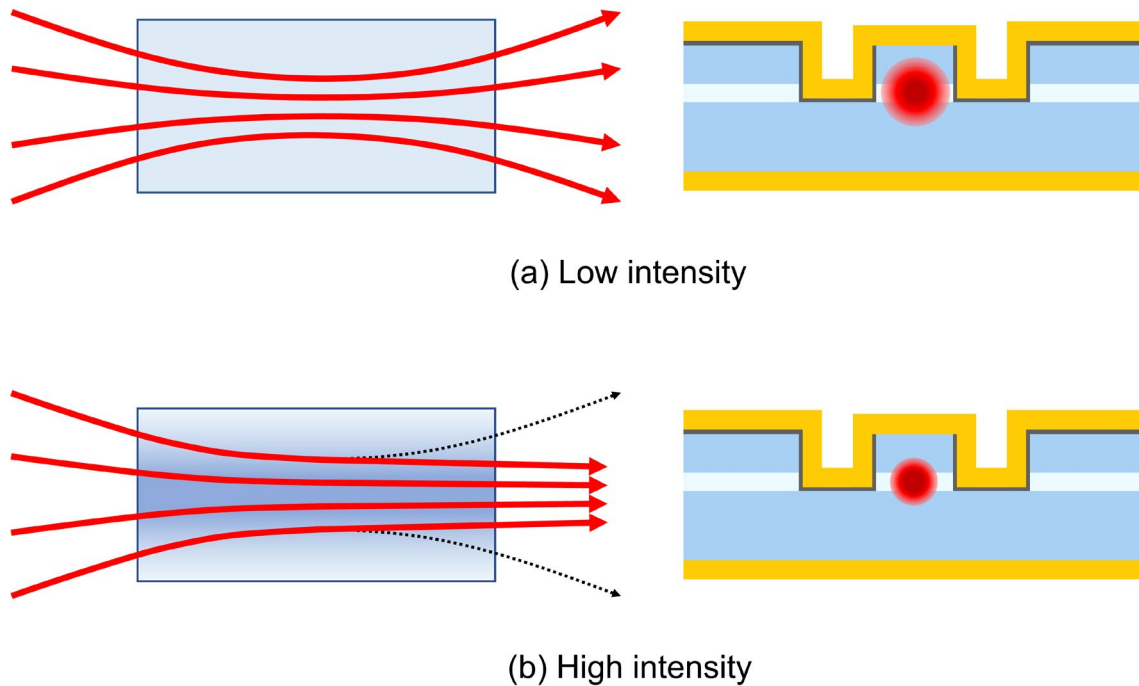
(b) High intensity

Fig 4.22 Strong Kerr lensing effect results in self-focusing of the transverse mode when the intracavity intensity is sufficiently high.

As a matter of fact, the Kerr lensing effect has been one of the main limits of further increasing the laser power, especially for those high-power mode-locking [32] or Q-switching [33] lasers, in which tremendous optical power is compressed in a short pulse. The ultra-high intracavity photon density introduces a strong 'lens', which focuses the beam to an even higher energy density. Such a vicious circle can eventually destroy the gain medium, preventing further light amplification. For this reason, one can find that chirped pulse amplification (CPA) technique [34][35] is used for ultra-high intensity pulse beam generation, which expands the pulse width in the time domain and thus lowers the beam intensity when it passes through the gain medium.

With regards to the Kerr lensing effect in QCLs, it also can be seen in the literature that the concept is used to explain some non-linear behaviours of high-performance InP-based mid-IR QCLs, such as the significantly lowered threshold of the RNGH instability [1][5] and the change of output beam divergence [31]. In line with these papers, it is reasonable to believe that a self-focusing effect in our QCL cavity could improve the net laser gain in two ways: (1) As the cross-section of the transverse mode shrinks, it leads to a larger spatial overlap between the laser beam and the laser core, i.e., an enhanced confinement factor Γ. (2) The shrunken transverse mode is then further away from the lossy sidewalls, which results in a reduced waveguide loss α_w.

Recall the simple equation we used to calculate the threshold gain of a transverse mode in Chapter 3:

$$g_{th} \downarrow = \frac{\alpha_w \downarrow + \alpha_m}{\Gamma \uparrow} \tag{4.39}$$

With a reduced waveguide loss α_w and an enhanced confinement factor Γ, the threshold gain of the transverse modes will be lowered, allowing optical bistability to take place. In particular, in our case of transverse mode coupling, the two beam spots in the waveguide (TM$_{01}$ mode) virtually combined into a single spot, which leads to a remarkably increased local light intensity and thus a stronger Kerr lensing effect.


4.4 Summary

In this chapter, the spectral and spatial instabilities observed from our fabricated QCLs were mainly discussed. The spectrum splitting of FP-QCLs is caused by the combined effect of temporal and spatial oscillations of the population inversion between the upper and lower

lasing states, namely Rabi oscillation and spatial hole burning. The theoretically estimated twice Rabi frequency fits well with the measured spectral separation between two sidebands.

The direct cause of QCL spatial instability, i.e., beam steering, is the coherent coupling of multiple transverse modes. The most interesting observation is an abrupt CW mode beam steering, where the multimode spectrum suddenly collapsed into a single longitudinal mode – an ultimate synchronisation of multiple transverse modes. We suggest that this is probably due to the activation of the second-order transverse mode TM_{02} at a high injection level and then followed by a four-wave mixing process that takes place between $TM_{00}+TM_{02}$ and $2TM_{01}$. In other words, the spatial interactions of light in the QCL gain medium can eventually affect the spectral domain.

Therefore, to link the spectral instability and spatial instability together, we come to a close loop, as shown in Fig 4.23. The QCL operates in single spectral mode near the lasing threshold but quickly runs into the multimode region due to the population pulsation and population grating; at an even higher injection level, the ultimate synchronisation of multiple transverse modes can bring the QCL back to single mode operation.
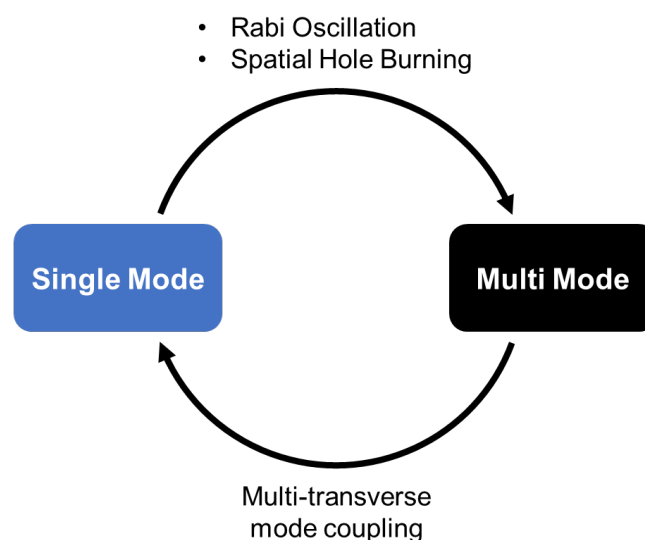
Fig 4.23 QCL runs into multi-spectral mode due to Rabi oscillation and spatial hole burning effect and runs out of the multimode regime due to multiple transverse mode coupling.

References

[1] C. Y. Wang, L. Diehl, A. Gordon, C. Jirauschek, F. X. Kärtner, A. Belyanin, D. Bour, S. Corzine, G. Höfler, M. Troccoli, J. Faist, and F. Capasso, "Coherent instabilities in a semiconductor laser with fast gain recovery," *Physical Review A*, vol. 75, no. 3, p. 031802(R), 2007.

[2] B. Hinkov, F. Fuchs, W. Bronner, K. Kohler, and J. Wagner, "Current- and temperature-induced beam steering in 7.8-µm emitting quantum-cascade lasers," *IEEE Journal of Quantum Electronics*, vol. 44, no. 11, pp. 1124–1128, 2008.

[3] T. S. Mansuripur, C. Vernet, P. Chevalier, G. Aoust, B. Schwarz, F. Xie, C. Caneau, K. Lascola, C. Zah, D. P. Caffey, T. Day, L. J. Missaggia, M. K. Connors, C. A. Wang, A. Belyanin, and F. Capasso, "Single-mode instability in standing-wave lasers: The quantum cascade laser as a self-pumped parametric oscillator," *Physical Review A*, vol. 94, no. 6, p. 063807, 2016.

[4] D. Kazakov, M. Piccardo, Y. Wang, P. Chevalier, T. S. Mansuripur, F. Xie, C. Zah, K. Lascola, A. Belyanin, and F. Capasso, "Self-starting harmonic frequency comb generation in a quantum cascade laser," *Nature Photonics*, vol. 11, no. 12, pp. 789–792, 2017.

[5] A. Gordon, C. Y. Wang, L. Diehl, F. X. Kärtner, A. Belyanin, D. Bour, S. Corzine, G. Höfler, H. C. Liu, H. Schneider, T. Maier, M. Troccoli, J. Faist, and F. Capasso, "Multimode regimes in quantum cascade lasers: From coherent instabilities to spatial hole burning," *Physical Review A*, vol. 77, no. 5, p. 053804, 2008.

[6] M. Fox, *Quantum Optics: An introduction*. Oxford: Oxford University Press, 2006.

[7]   H. Risken and K. Nummedal, "Self-pulsing in lasers," *Journal of Applied Physics*, vol. 39, no. 10, pp. 4662–4672, 1968.

[8]   R. Graham and H. Haken, "Quantum theory of light propagation in a fluctuating laser-active medium," *Zeitschrift für Physik A Hadrons and nuclei*, vol. 213, no. 5, pp. 420–450, 1968.

[9]   M. Bugajski, K. Pierscinski, D. Pierscinska, A. Szerling, and K. Kosiel, "Multimode instabilities in mid-infrared quantum cascade lasers," *Photonics Letters of Poland*, vol. 5, no. 3, pp. 85–87, 2013.

[10]   N. N. Vukovic, J. Radovanovic, V. Milanovic, and D. L. Boiko, "Analytical expression for Risken-Nummedal-Graham-Haken instability threshold in quantum cascade lasers," *Optics Express*, vol. 24, no. 23, pp. 26911–26929, 2016.

[11]   N. N. Vukovic, J. Radovanovic, V. Milanovic, and D. L. Boiko, "Low-threshold RNGH instabilities in quantum cascade lasers," in *IEEE Journal of Selected Topics in Quantum Electronics*, vol. 23, no. 6, pp. 1–16, 2017.

[12]   Y. Silberberg, D. A. Miller, A. C. Gossard, W. Wiegmann, P. W. Smith, and D. J. Eilenberger, "Passive mode locking of a semiconductor diode laser," *Optics Letters*, vol. 9, no. 11, pp. 507–509, 1984.

[13]   S. Gee, R. Coffie, P. J. Delfyett, G. Alphonse, and J. Connolly, "Intracavity gain and absorption dynamics of hybrid mode locked semiconductor lasers using multiple quantum well saturable absorbers," *Applied Physics Letters*, vol. 71, no. 18, pp. 2569–2571, 1997.

[14]   W. W. Bewley, J. R. Lindle, C. S. Kim, I. Vurgaftman, J. R. Meyer, A. J. Evans, J. S. Yu, S. Slivken, and M. Razeghi, "Beam steering in high-power CW quantum-cascade lasers," *IEEE Journal of Quantum Electronics*, vol. 41, no. 6, pp. 833–841, 2005.

[15]   N. Yu, L. Diehl, E. Cubukcu, C. Pflügl, D. Bour, S. Corzine, J. Zhu, G. Höfler, K. B. Crozier, and F. Capasso, "Near-field imaging of quantum cascade laser transverse modes," *Optics Express*, vol. 15, no. 20, pp. 13227–13235, 2007.

[16]   N. Yu, L. Diehl, E. Cubukcu, D. Bour, S. Corzine, G. Höfler, A. K. Wojcik, K. B. Crozier, A. Belyanin, and F. Capasso, "Coherent coupling of multiple transverse modes in quantum cascade lasers," *Physical Review Letters*, vol. 102, no. 1, p. 013901, 2009.

[17]   N. Yu, "Nonlinear coupling of transverse modes in quantum cascade lasers," *Optical Engineering*, vol. 49, no. 11, p. 111114, 2010.

[18]   A. K. Wójcik, N. Yu, F. Capasso, and A. Belyanin, "Nonlinear optical interactions of laser modes in quantum cascade lasers," *Journal of Modern Optics*, vol. 58, no. 9, pp. 727–742, 2011.

[19]   Y. Yao, Y. Huang, X. Wang, and C. F. Gmachl, "Modal instability and beam steering in quantum cascade lasers," *CLEO:2011 – Laser Applications to Photonic Applications*, pp. 1–2, 2011.

[20]   A. K. Wójcik, N. Yu, L. Diehl, F. Capasso, and A. Belyanin, "Self-synchronization of laser modes and multistability in quantum cascade lasers," *Physical Review Letters*, vol. 106, no. 13, p. 133902, 2011.

[21]   L. Jumpertz, S. Ferré, M. Carras, and F. Grillot, "Beam steering in quantum cascade lasers with optical feedback," *SPIE Proceedings 10111, Quantum Sensing and Nano Electronics and Photonics*, p. 101112F, 2017.

[22]   S. Ferré, L. Jumpertz, M. Carras, R. Ferreira, and F. Grillot, "Beam shaping in high-power broad-area quantum cascade lasers using optical feedback," *Scientific Reports*, vol. 7, no. 44284, 2017.

[23]   J. Guthrie, G. L. Tan, M. Ohkubo, T. Fukushima, Y. Ikegami, T. Ijichi, M. Irikawa, R. S. Mand, and J. M. Xu, "Beam instability in 980-nm power lasers: experiment and analysis," *IEEE Photonics Technology Letters*, vol. 6, no. 12, pp. 1409–1411, 1994.

[24]   M. F. Schemmann, C. J. van der Poel, B. A. van Bakel, H. P. Ambrosius, A. Valster, J. A. van den Heijkant, and G. A. Acket, "Kink power in weakly index guided semiconductor lasers," *Applied Physics Letters*, vol. 66, no. 8, pp. 920–922, 1995.

[25]   G. L. Tan, R. S. Mand, and J. M. Xu, "Self-consistent modelling of beam instabilities in 980-nm fiber pump lasers," *IEEE Journal of Quantum Electronics*, vol. 33, no. 8, pp. 1384–1395, 1997.

[26]   X. Fu, G. L. Tan, R. Gordon, and J. M. Xu, "Third-order nonlinearity induced lateral-mode frequency locking and beam instability in the high-power operation of narrow-ridge semiconductor lasers," *IEEE Journal of Quantum Electronics*, vol. 34, no. 8, pp. 1447–1454, 1998.

[27]   S. H. Strogatz, and I. Stewart, "Coupled oscillators and biological synchronization," *Scientific American*, vol. 269, no. 12, pp. 102–109, 1993.

[28]   R. W. Boyd, *Nonlinear optics*, 4th ed. London: Academic Press, an imprint of Elsevier, 2020.

[29]   M. Troccoli, S. Corzine, D. Bour, J. Zhu, O. Assayag, L. Diehl, B. G. Lee, Höfler G., and F. Capasso, "Room temperature continuous-wave operation of quantum-cascade lasers grown by metal organic vapour phase epitaxy," *Electronics Letters*, vol. 41, no. 19, pp. 1059–1060, 2005.

[30]   H. A. Haus, "Mode-locking of lasers," *IEEE Journal of Selected Topics in Quantum Electronics*, vol. 6, no. 6, pp. 1173–1185, 2000.

[31]   R. Paiella, F. Capasso, C. Gmachl, D. L. Sivco, J. N. Baillargeon, A. L. Hutchinson, A. Y. Cho, and H. C. Liu, "Self-mode-locking of quantum cascade lasers with giant ultrafast optical nonlinearities," *Science*, vol. 290, no. 5497, pp. 1739–1742, 2000.

[32]   E. P. Ippen, C. V. Shank, and A. Dienes, "Passive mode locking of the CW dye laser," *Applied Physics Letters*, vol. 21, no. 8, pp. 348–350, 1972.

[33]   J. A. Alvarez-Chavez, H. L. Offerhaus, J. Nilsson, P. W. Turner, W. A. Clarkson, and D. J. Richardson, "High-energy, high-power ytterbium-doped Q-switched fiber laser," *Optics Letters*, vol. 25, no. 1, pp. 37–39, 2000.

[34]   P. Maine, D. Strickland, P. Bado, M. Pessot and G. Mourou, "Generation of ultrahigh peak power pulses by chirped pulse amplification," *IEEE Journal of Quantum Electronics*, vol. 24, no. 2, pp. 398–403, 1988.

[35]   I. N. Ross, J. L. Collier, P. Matousek, C. N. Danson, D. Neely, R. M. Allott, D. A. Pepler, C. Hernandez-Gomez, and K. Osvay, "Generation of terawatt pulses by use of optical parametric chirped pulse amplification," *Applied Optics*, vol. 39, no. 15, pp. 2422–2427, 2000.

5 Novel Applications of Mid-IR QCLs

5.1 Introduction

With the practical and theoretical works presented in the previous two chapters, this chapter describes the novel applications we explored based on the developed $\lambda \sim 5.7$ μm QCLs. First, we aim to integrate our QCLs on the silicon platform and coupled with Ge-on-Si waveguides, which would be a promising technique for future on-chip spectroscopy or sensing applications. This work is in collaboration with the University of Southampton. In addition, we found that this QCL is also capable of melting polymers due to the roughly matched absorption. Thus, a prototype selective laser sintering (SLS) system was built, in which the conventional CO_2 laser was replaced with mid-IR QCLs.

5.2 Hybrid Integration of QCLs on Silicon

5.2.1 Background

III-V on Si has been a popular research topic for years [1]. The heterogeneous integration of III-V materials can compensate for the two main disadvantages of silicon: (1) the low

electron mobility and (2) the non-radiative property due to the indirect bandgap. In consequence, high electron mobility transistors can be realised with a fast III-V channel [2][3] on silicon, which can be an approach to maintain Moore's law. Even more attractively, this leads to the ultimate integration of photonics and electronics on silicon at the wafer scale, combining the superiorities of the two semiconductor families.

Generally, III-V on Si can be achieved via two routes: (1) monolithic integration and (2) hybrid integration. Monolithic integration refers to the direct growth of III-V on the silicon substrate. This route is promising for many attractive advantages such as large scale, the highest integration density among all technologies, low cost, high position/alignment accuracy etc. While the main challenge originates from the significant lattice constant mismatch and thermal expansion coefficient mismatch between Si and III-V materials, leading to an increase in crystal defects, such as thread dislocations (TDs) and antiphase domains (APDs), which ultimately results in severe degradation of device performance. A number of techniques have been developed to isolate the superstructures from the defects caused by lattice mismatch, such as compositional grading buffer layer [4], dislocation filter layer (DFL) [5], cyclic annealing [6], selective area growth [7], aspect ratio trapping (ATR) [8], nanovoids [9] etc. In addition, it is worth mentioning that in contrast to quantum well lasers, quantum dot lasers exhibit reduced temperature sensitivity [10] and better tolerance to dislocations because of their discrete distribution nature and therefore have achieved excellent performance on silicon via direct hetero-epitaxial growth [11].

On the other hand, hybrid integration can be achieved through several approaches, i.e., wafer bonding, micro transfer-printing (μTP), and flip-chip bonding. Wafer bonding [12] refers to the bonding of III-V wafer with silicon wafer, which can be realised either directly [13] or with the help of a thin adhesion layer [14][15]. Devices are then fabricated on the hybrid

wafer. Therefore, similar to the hetero-epitaxial growth, very high integration density and alignment accuracy can be achieved in this technique as devices are written via lithography.

In contrast, µTP and flip-chip are essentially transfer techniques – III-V devices are pre-processed and pre-tested on the native wafer, then transferred onto the target substrate. In µTP [16], III-V devices need to be grown on a sacrificial layer. Once the devices are processed, they can be released by etching the underneath sacrificial layer and then picked up by an elastomeric stamp, followed by transfer and printing. Similar to wafer bonding, devices can be directly printed onto the non-native substrate by the Van der Waals force if the bottom surface is sufficiently smooth; otherwise, adhesion layers can be used. The most attractive feature of µTP is the capability of massively parallel integration of micro-scale devices. It is therefore considered as the critical technology for the commercialisation of micro-LED (µLED) displays [17]-[19].

Flip-chip bonding [20] was introduced by IBM in the 1960s [21] and is a highly mature technique. It is more straightforward than wafer bonding or µTP in device preparation. The III-V devices are grown and fabricated in a completely traditional manner and then face-down bonded to the target substrate using a flip-chip bonder. Bonding can also be achieved in several ways, such as adhesive, soldering, thermocompression, ultrasonic etc. In short, it is a pure bonding technique, and as a matter of fact, it has been used in QCL packaging for years, i.e., epi-layer down mounting.

Table 5.1 compares the advantages and disadvantages of the abovementioned technologies in terms of integration density, alignment accuracy, throughput, cost, and maturity [22]. Usually, transfer techniques (i.e., µTP, flip chip) exhibit worse alignment accuracy as devices are positioned mechanically onto the substrate, and high throughput techniques lead to a low cost.

Table 5.1 Comparison of four heterogeneous integration technologies [22]

	Integration Density	Alignment Accuracy	Throughput	Cost	Maturity
Hetero-Growth	High	High	High	Low	R&D
Wafer Bonding	Medium	High	High	Medium	Mature
µTP	High	Medium	High	Low	R&D
Flip-Chip	Low	Medium	Low	High	Mature

With regard to QCLs, some heterogeneous integration work has also been reported. The first QCL ($\lambda \sim 4.8$ µm) on silicon was demonstrated in 2016 [23], integrated with silicon-on-nitride-on-insulator (SONOI) waveguides via direct wafer bonding. After then, the hybrid integration of DFB-QCL [24] and ICL [25] were also reported by the same group using a similar scheme. The first QCL monolithically grown on silicon was reported in 2018 [26], which was based on InAs/AlSb material system, emitting at $\lambda \sim 11$µm. Transfer-printing of QCLs onto silicon using adhesion layers was also seen in the literature [27]. In contrast to previous examples, this was the first demonstration using pre-fabricated QCLs. However, due to the critical thermal management required by QCLs, these devices only operate in pulsed mode on silicon. Another special case of QCL-on-silicon is the Si/SiGe QCL, which is inherently silicon-based. However, for this type of QCL, only theoretical works [28][29] and experimental observations of intersubband electroluminescence [30]-[33] can be found, i.e., no lasing operation has been reported so far.

Our collaborators at the University of Southampton also developed a simple and scalable integration approach, utilising the flip-chip bonding technique with enhanced z-alignment. It is widely recognised that precise facet-to-facet alignment is crucial for maximising the laser-

waveguide coupling efficiency, especially in the vertical direction (z-direction), since the laser core height is usually much smaller than the core width. For instance, the active layer thickness of our QCL is merely 1.8 µm. However, in the conventional flip-chip bonding process, the vertical position is mechanically controlled by the bonder and the solder thickness, thus resulting in a non-trivial error compared to the core thickness. In contrast, in the developed method, a support structure is constructed on the silicon substrate for physical support of the flip-chipped laser – the silicon platform and the unprocessed epitaxial surface of the laser chip are directly contacted, thus eliminating the z-alignment error caused by the flip-chip bonder. In other words, the laser and waveguide are now passively aligned in the vertical direction, and the accuracy is solely determined by the etching process, i.e., ±10 nm.

This hybrid integration method was first demonstrated on the SOI (Silicon-on-Insulator) platform using commercial lasers that emit at the communication wavelengths, i.e., near-infrared [34]. In the presented project, this integration methodology is transferred to the mid-infrared region using mid-IR QCLs. Correspondingly, the potential application of the hybrid chip is also switched from on-chip communication to on-chip sensing/spectroscopy. As the SOI waveguides exhibit a high loss above λ ~3.6 µm [35], the platform is thus transferred to germanium-on-silicon (Ge-on-Si), which is transparent up to λ ~15 µm [36]. The mid-IR QCLs are developed at the EPSRC National Epitaxy Facility in Sheffield, while the processing of the Ge-on-Si platform and flip-chip bonding of mid-IR QCLs onto the platform are undertaken by the Optoelectronics Research Centre at the University of Southampton.

In section 5.2.2, the flip-chip bonding technique is introduced. Then the first and second-generation Ge-on-Si platforms are described in section 5.2.3 and 5.2.4, respectively.

5.2.2 Flip-Chip Bonding

As introduced above, the flip-chip bonding technique allows laser chips to be face-down bonded to a prepared substrate. In this work, it is conducted through a manual sub-micron bonder, i.e., Fineplacer® Lambda from Finetech [37], as shown in Fig 5.1(a).
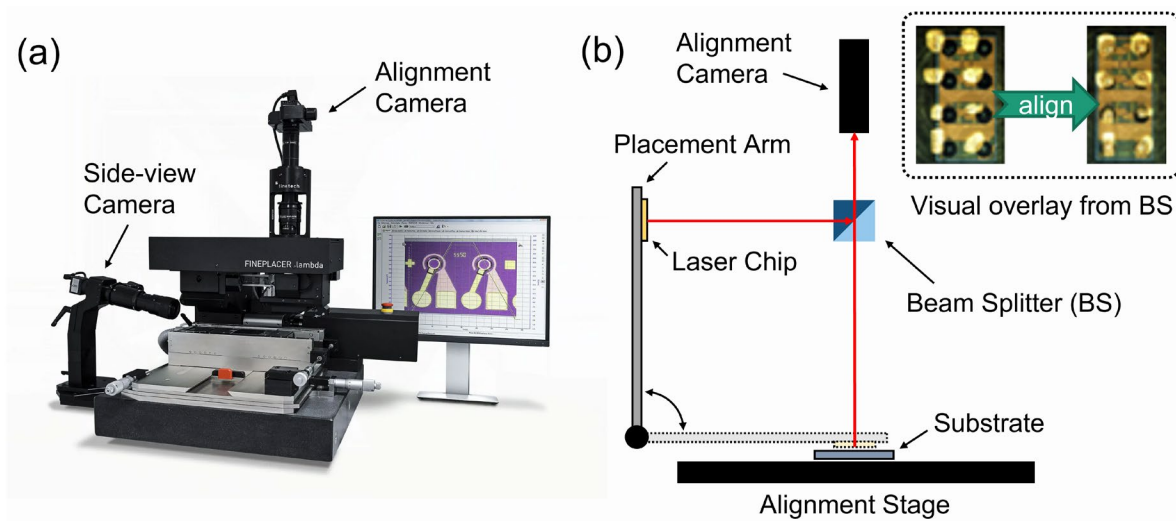
Fig 5.1 (a) Fintech Fineplacer® Lambda. (b) Schematic diagram of flip-chip bonding.

Fig 5.2(b) illustrates the working mechanism of the flip-chip bonder. Initially, a substrate is loaded onto the heating plate of the alignment stage and fixed by vacuum, with inert gas flowing surrounds the operation area. The placement arm then picks up the laser chip through vacuum suction. With the substrate on the stage and the laser chip held in the arm, they can be visually aligned in the imaging system, which consists of a camera and a calibrated beam splitter (BS). Following the visual guide, as shown in the insert of Fig 5.2(b), the operator is thus able to manually adjust the x, y position of the stage to align the bonding area to the laser chip. Once they are completely overlapped in the visual system, the placement arm will position the laser chip at the targeted region and in contact with melted liquid-phase AuSn

solder. Once the solder cools down, it solidifies; thus, the chip is face-down bonded on the substrate.

The Lambda bonder provides <0.5μm in-plane alignment accuracy, and even smaller misalignment can be achieved in a more advanced model with full automation [38]. Besides, the placement arm is equipped with a single-axis gimballed placement head, allowing 6-degree freedom, i.e., rotational in x, y, and z-direction. The use of a long laser bar can help reduce the in-plane angular misalignment.

5.2.3 Gen 1 Platform Design

The Ge-on-Si platform is processed from a 6-inch raw wafer with a 3μm germanium layer on the silicon substrate. The initial integration scheme is illustrated in Fig 5.2. As one can see, once the QCL chip is flip-chipped and bonded to the substrates, the unprocessed epitaxial surface of the QCL and the two silicon support structures are physically contacted, defining the vertical position of the QCL chip. As the distance from the QCL spatial mode centre to the epitaxial surface is fixed (~5 μm), the z-direction misalignment is solely caused by the etching process of the support structure, i.e., etching depth, which is at the level of ±10 nm. This is considerably small compared to the thickness of the QCL active layer (1.8 μm) or the germanium waveguide (3 μm), thus achieving much higher alignment accuracy than the conventional flip-chip bonding technique.

Electrical contact, or bonding, is formed between the Au-deposited bond pad and the QCL top contact layer by AuSn solder. In this approach, the solder thickness does not affect the vertical alignment, and the excessive melted liquid-phase solder will be simply squeezed into

the flow trenches on the two sides once the two support structures and the QCL wafer are firmly contacted.

(a) Front View
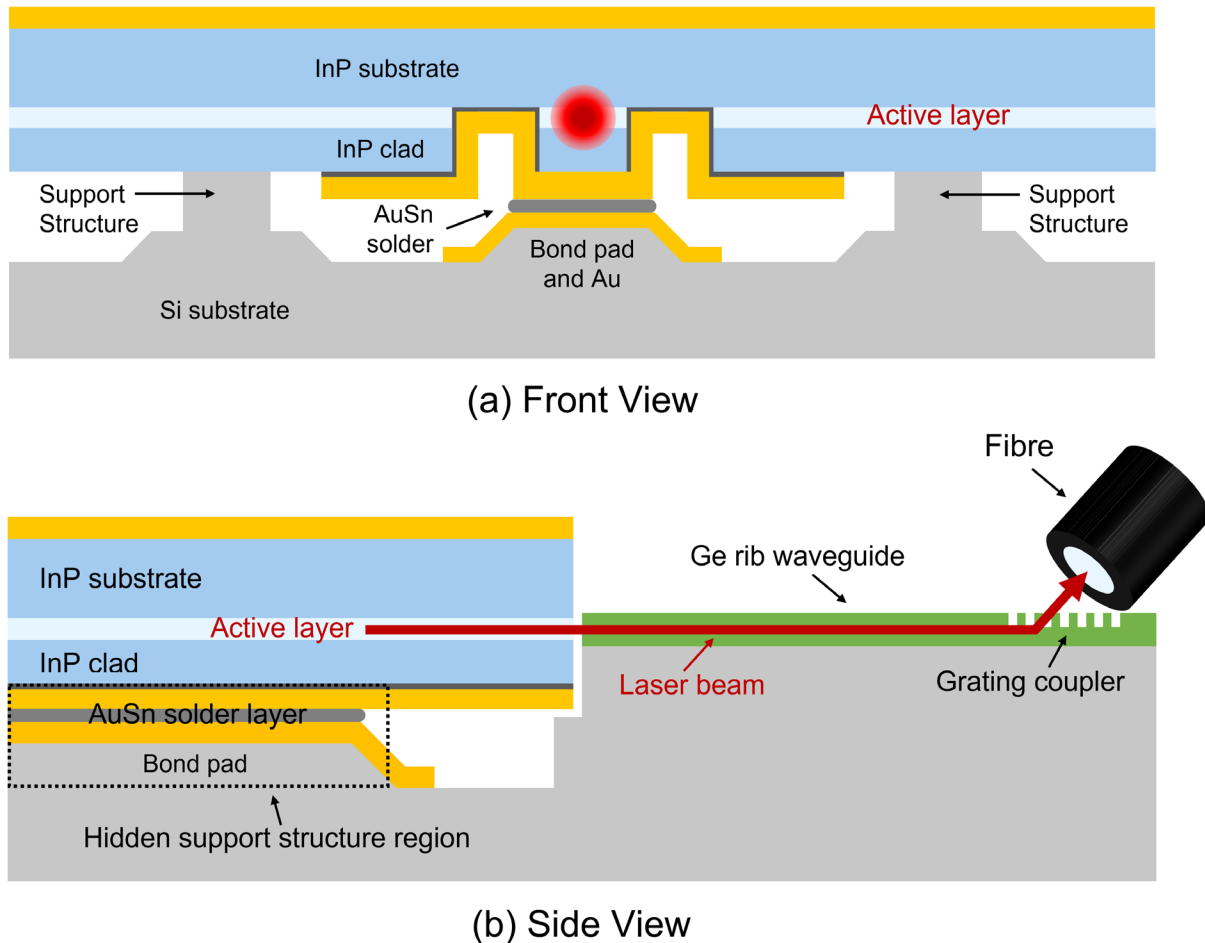
(b) Side View

Fig 5.2 (a) Front view and (b) side view of QCL integration and QCL-waveguide coupling.

The Ge-on-Si rib waveguide and grating [39] are processed by e-beam lithography (EBL) and ICP etching. The cross-section dimension of the rib waveguide is illustrated in Fig 5.3(a), which is optimised for the wavelength of 5.7 μm. The transverse mode in the rib waveguide is also simulated in Lumerical, which shows a maximum 85.6% overlap between the TM_{00} mode of the QCL and the TM_{00} mode of the waveguide. Fig 5.3(b) shows a Ge-on-Si rib waveguide under SEM [39].
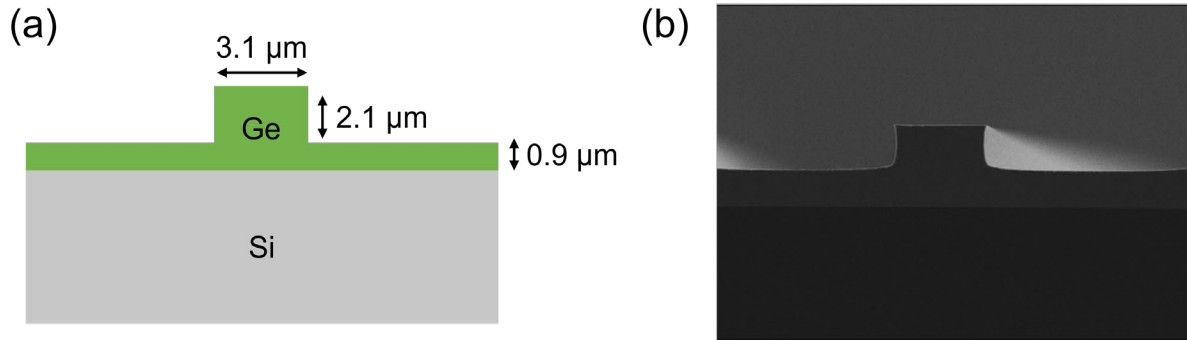
Fig 5.3 (a) Cross-section of the Ge-on-Si rib waveguide. (b) SEM photo of a Ge-on-Si waveguide [39].

The light that transmits into the Ge-on-Si rib waveguide can be measured at the grating coupler via a fibre. As shown in Fig 5.4, a standard QCL L-I-V was measured in the pulsed mode. Note that at this early stage, beam steering QCLs were used for integration, and thus the coupling efficiency was not ideal. In particular, QCLs with TM_{01} transverse mode would significantly lower the coupling efficiency as the central intensity is virtually zero. On the other hand, due to the lack of comparison, the coupling efficiency is difficult to be estimated. This is later resolved in the Gen 2 design.
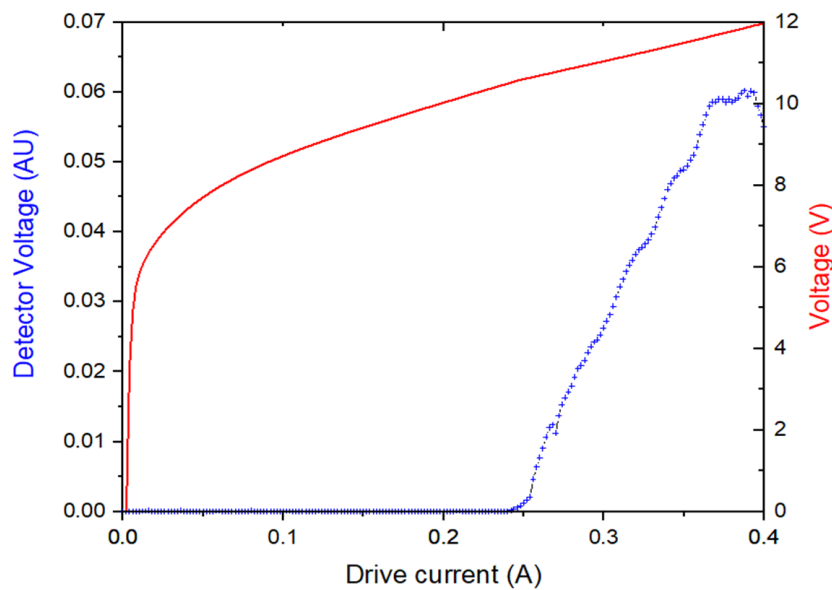
Fig 5.4 L-I-V measured (10°C) at the germanium grating via a fibre. Figure courtesy of Dr Colin J Mitchell.

Another typical issue we found with the Gen 1 integration is the unreliable electrical contact between the QCL and the bond pad. The tested integration chip is shown in Fig 5.5, where a QCL bar consisting of 24 QCLs (cavity length 2mm) is epi-side down mounted on the Si substrate via flip-chip bonding. The two ends of the long laser bar are glued for further reinforcement. 24 gold fingers can be seen on the substrate, which are the individual bonding pads deposited on the Si substrate. Note that there are no waveguide structures on this chip as this was initially made for flip-chip bonding test and because of that, a less good wafer MR3877 is used here instead of our best QCL wafer MR4243.
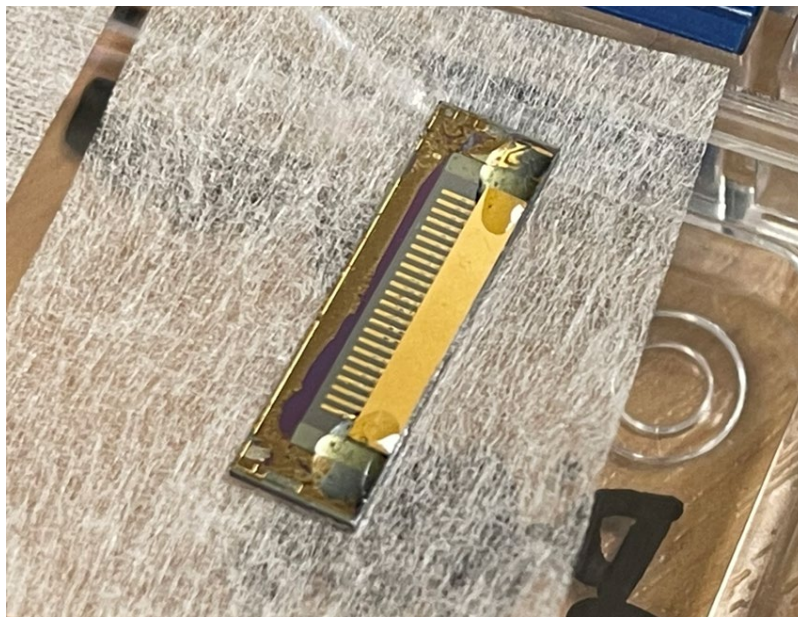
Fig 5.5 Flip-chip integrated QCL bar (2mm) on Si substrate using Gen 1 technique

Table 5.2 shows the statistical results of the integrated QCL bar in terms of the basic electrical and optical characteristics. As one can see, 2/3 of the devices (16 of 24) suffer from electric contact problems and thus the pulsed current source displayed an 'open circuit' once turned on. The 'unstable' contact means that more probe force is required for connection.

Table 5.2 Electrical and optical performance of Gen 1 integrated QCLs (6.5µm×2mm)

QCL number	Electrical contact	Lase?	Threshold
1	Good	Yes	~210 mA
2	Good	Yes	~180 mA
3	Good	No	-
4	Good	Yes	~160 mA
5	Open Circuit	-	-
6	Open Circuit	-	-
7	Good	Yes	~160 mA
8	Open Circuit	-	-
9	Open Circuit	-	-
10	Open Circuit	-	-
11	Open Circuit	-	-
12	Unstable	Yes	~190 mA
13	Open Circuit	-	-
14	Open Circuit	-	-
15	Open Circuit	-	-
16	Open Circuit	-	-
17	Open Circuit	-	-
18	Open Circuit	-	-
19	Good	No	-
20	Open Circuit	-	-
21	Good	Yes	~160 mA
22	Open Circuit	-	-
23	Open Circuit	-	-
24	Open Circuit	-	-

The cause of the contact issue is twofold. First, the metallisation of the bond pad is not uniform on Si. Second, the top contact layers of the QCLs have 'wings' at the edge, as shown in Fig 5.6, which resulted from the metal lift-off procedure and further developed during electroplating. In the case of epi-up mounting, the non-flat top contact layers will not result in any negative issues; once the devices are flip-chip bonded, the wings can then lead to unreliable contact problems. As this problem is mainly caused by the shorter gold plate side, i.e., the right side in Fig 5.6, the solution is relatively simple – we merely extended the width of the gold plate in the second fabrication so that the whole top contact area bonded with the bond pad is flat. Once the wings are far away from the bond pad and hanging above the

silicon substrate, they are no longer a problem. Also, the metal deposition of the bond pads on Si will be optimised for the Gen 2 platform. In terms of the laser performance, i.e., pulsed threshold, they are similar to the previous samples as trivial heat is generated during the pulsed operation with short pulse width and low duty cycle.
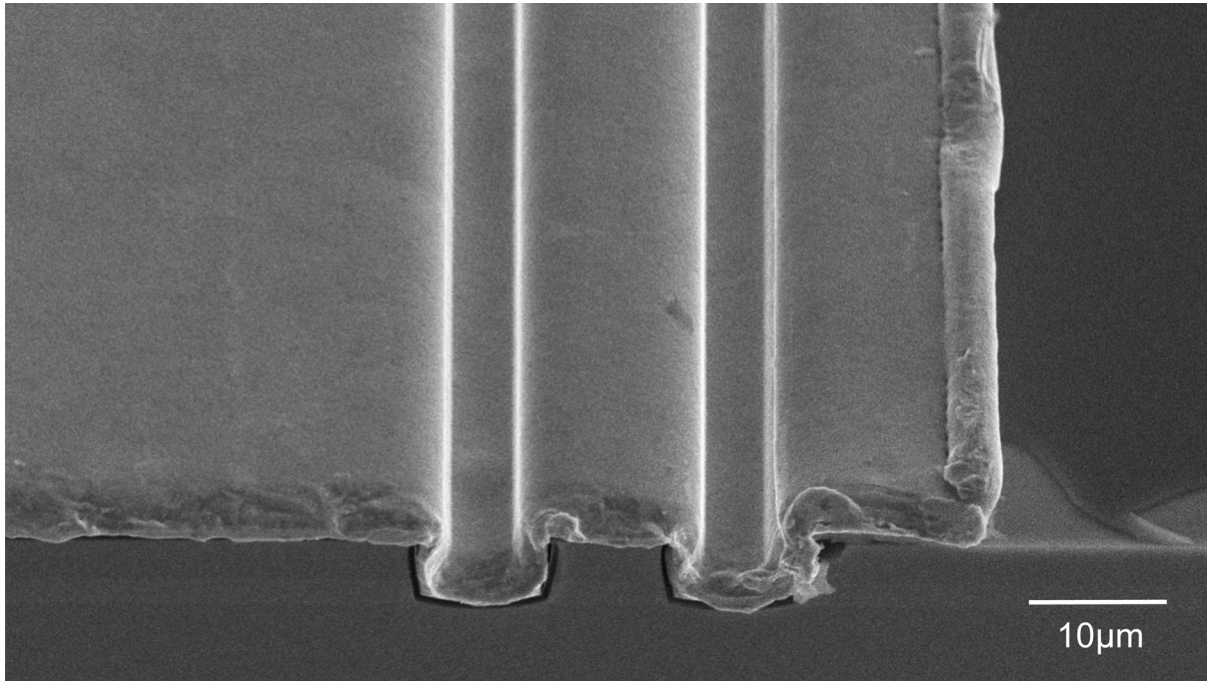
Fig 5.6 Edge wing of the gold top contact on the right side

5.2.4 Gen 2 Platform Design

The first-generation integration was demonstrated with the first fabricated QCLs that suffer from beam steering and flip-chip bonding issues, after which both the QCL and the Ge-on-Si platform were optimised. The optimisation work of QCL has been presented in Chapter 3, i.e., the second fabrication; therefore, this section mainly presents the improved design of the Ge-on-Si platform. The 2nd Gen platform design is schematically shown in Fig 5.7.
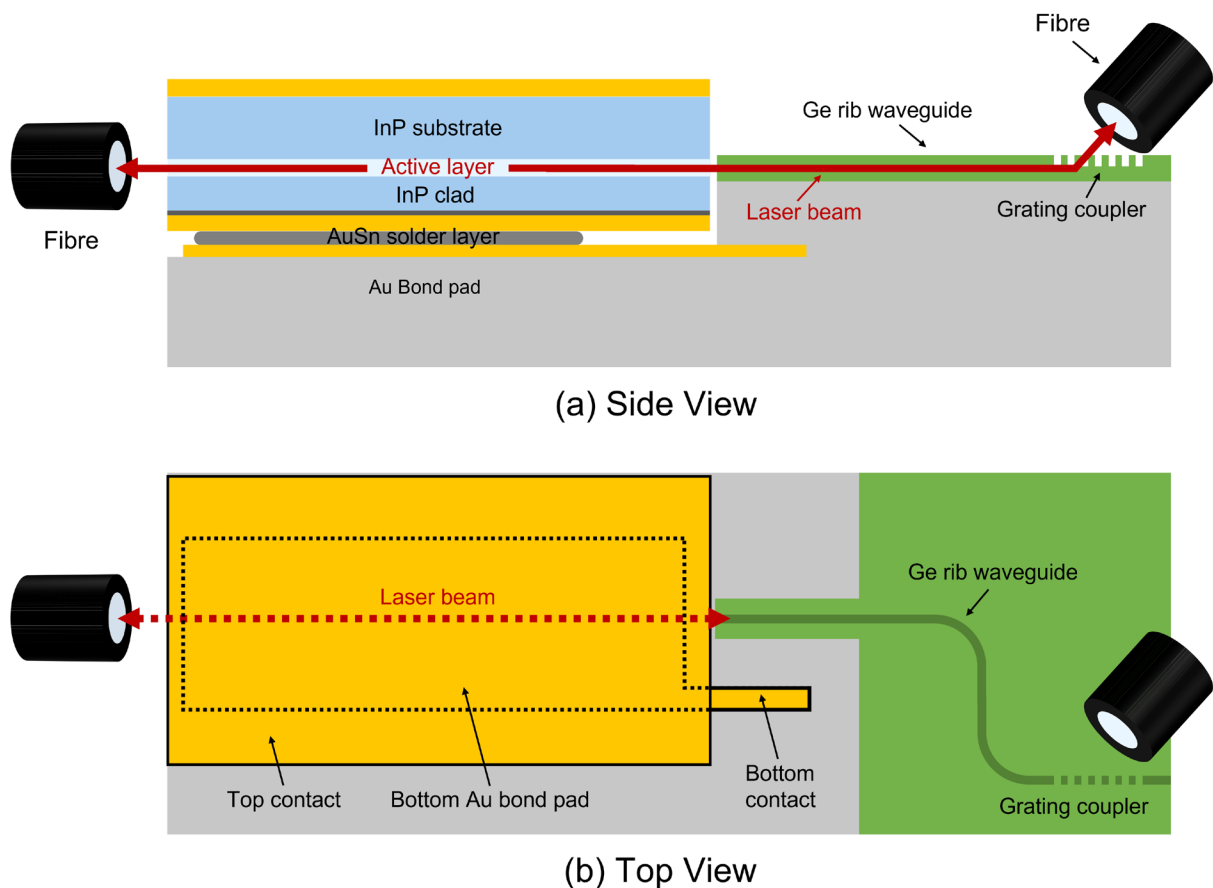
Fig 5.7 (a) Side view and (b) top view of the Gen 2 platform design.

The most pronounced improvement is that now another fibre can be directly placed at the laser back facet for real-time monitoring. Thus, the coupling efficiency can be estimated by comparing the collected signals from the two fibres. This was not allowed in Gen 1 design as the substrate was not diced at the edge of the laser; instead, the contact probe was placed behind the QCL. Correspondingly, in Gen 2 design, the bottom contact on the Si substrate is moved to the front side, next to the rib waveguide, which can be seen via the top view.

Besides, the wafer processing procedures are also simplified thanks to the developed deep vertical etching (~11 μm). An easily notable difference is that the 'step' in front of the waveguide facet in Fig 5.2(b) is now removed, resulting in a more concise geometry. Fig 5.8

shows the processed Gen 2 Ge-on-Si platform under the microscope, where the bottom Au bond pads have not been deposited yet. The germanium waveguide facet (note the sharpness of the structure) is angled to reduce the external optical feedback into the laser.
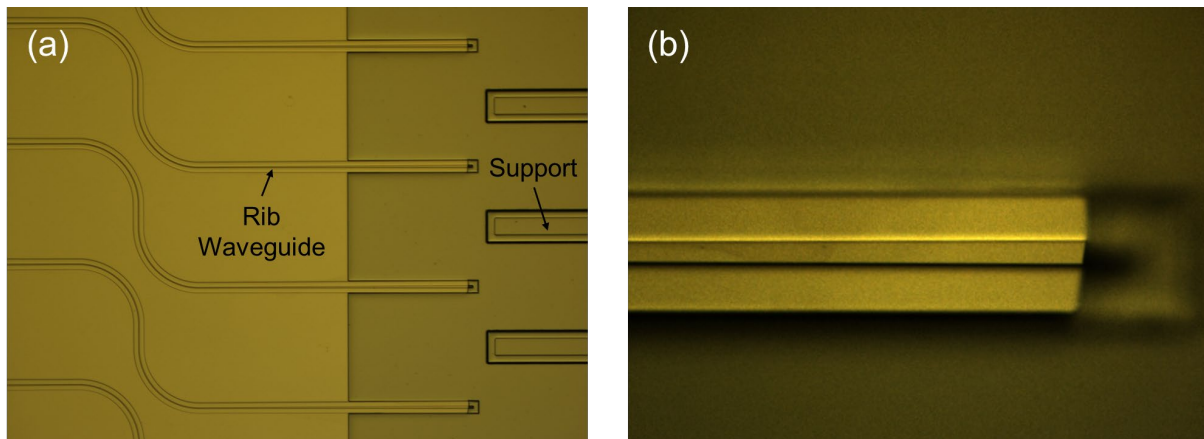
Fig 5.8 (a) Processed Ge-on-Si platform under the microscope. (b) Top view of the angled rib waveguide facet. Figure courtesy of Dr Colin J Mitchell.

As a highly scalable technique, tens of Ge-on-Si unit platforms are processed across the whole 8-inch wafer, as shown in Fig 5.9(b), and a long cleaved QCL bar can be flip-chip bonded to each unit. Fig 5.9(c) illustrates the final view of the Gen 2 integration chip. Finally, two diced integration chips are shown in Fig 5.9(d), which are labelled as B5 and B11, referring to their unit numbers on the Si wafer. The Ge waveguides can be clearly seen when imaged from a reflective angle, i.e., Fig 5.9(e). Same as Gen 1 platform, the Gen 2 platform is also designed for the integration of 24×QCLs. 6×QCLs (labelled as #1-6 on the chip) are coupled to Ge waveguides with grating couplers at the end; 17×QCLs (#7-23) are coupled with edge emitting Ge waveguides, i.e., the reflective patterns extend to the edge of the chip in Fig 5.9(e). The last QCL (#24) is the reference laser for comparison, which is not coupled to any waveguides.
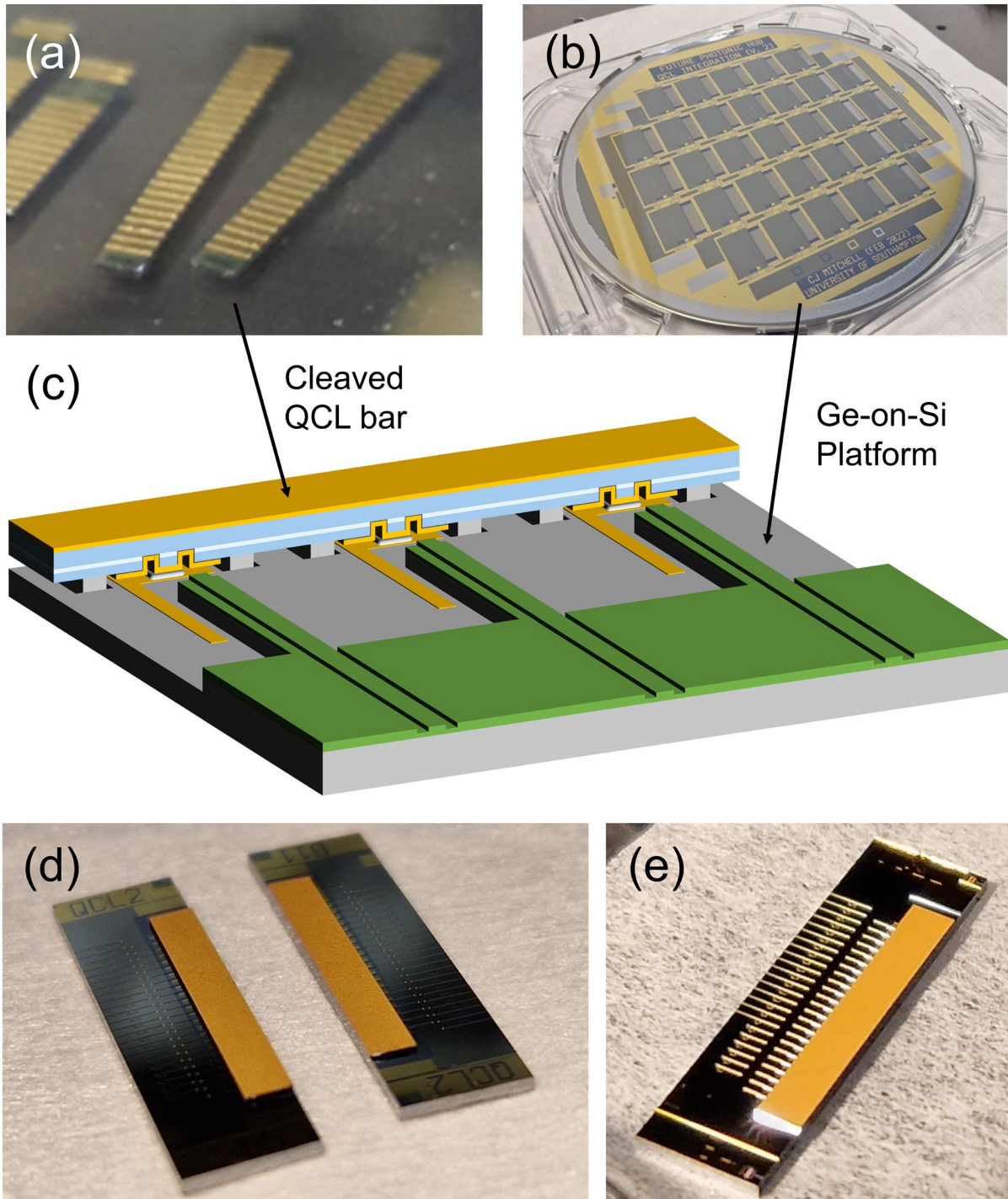
Fig 5.9 (a) Cleaved 2mm width QCL bar for integration. Wafer no. MR4243. (b) Processed 6-inch Ge-on-Si wafer. (c) 3D view of a QCL bar flip-chip bonded on the Gen 2 Ge-on-Si platform. The distance between the laser facets and Ge rib waveguides is enlarged for clarity. (d) Photos of two diced integration chips, labelled as B5 and B11. (e) A clear view of the Ge-on-Si waveguides via the reflection. Figure courtesy of Dr Colin J Mitchell.

The basic electrical and optical characteristics of B5 and B11 integration chips were then measured. B5 was first tested but it was found that no QCL optically works on the chip. Investigation under SEM reveals that most of the laser facets are covered by the excessive AuSn solders, as shown in Fig 5.10(b). The pre-deposited AuSn solder area on the bond pad can be seen in Fig 5.10(a), which is the completed Ge-on-Si platform before laser integration.
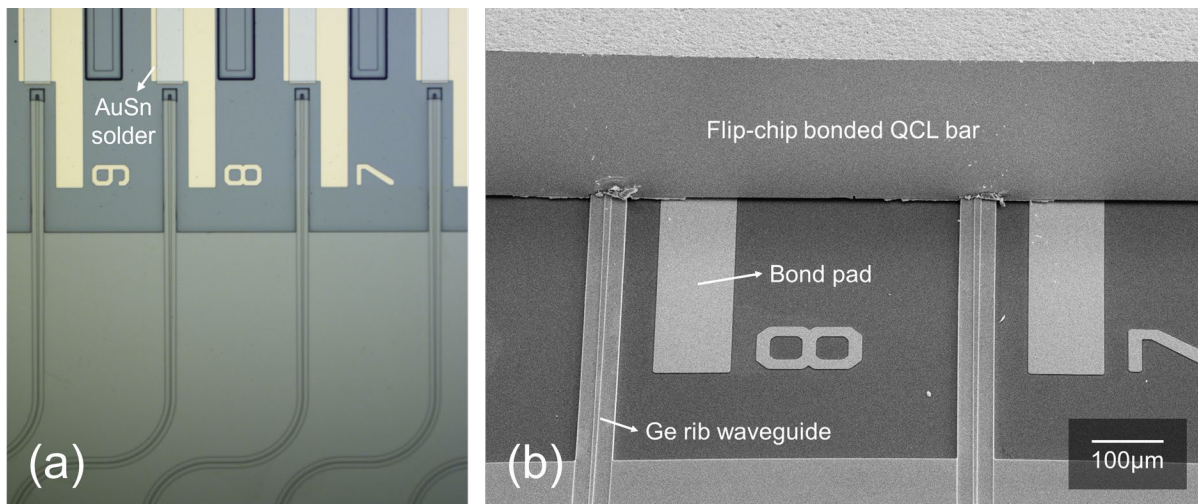
Fig 5.10 (a) The completed Ge-on-Si platform with Au bond pad and AuSn solder deposited. (b) SEM photo of the integration chip B5. The facets of QCL#7 and #8 are covered by solder.

In consequence, the basic electrical and optical performance of Gen 2 integrated QCLs was tested based on chip B11 and the result has been summarised in Table 5.3. Compared to the Gen 1 integration (see Table 5.2), the electrical contact is significantly improved as a result of the optimised QCL top contact layer and improved metallisation and uniformity of the bond pad on Si. 20 of 24 lasers now have reliable electrical contacts. The two QCLs at the two ends of the laser bar (i.e., #1 and #24) exhibit unstable contacts, which require extra probe force to enhance the contact. The laser performance, on the other hand, shows significant area

dependence – half of the laser bar is good with a uniform threshold of ~90 mA (pulsed mode, 1% DC, 250ns PW, 15°C). Note that the minimum step size of the pulsed current source is 10 mA; therefore, it does not mean that QCL#1, which has a threshold of ~80 mA, is that better than the devices with ~90 mA thresholds. With regards to this area-dependence laser performance, it could also be caused by the AuSn solder; however, destructive investigation (SEM) is not conducted on this chip at this stage since the priority is further characterisations of the working devices, e.g., spectrum, coupling efficiency etc.

Table 5.3 Statistics of Gen 2 integrated QCL (4.5µm×2mm) performance

QCL number	Electrical contact	Lase?	Threshold
1	Unstable	Yes	~80 mA
2	Open Circuit	-	-
3	Good	No	-
4	Open Circuit	-	-
5	Good	No	-
6	Good	No	-
7	Good	No	-
8	Good	No	-
9	Good	No	-
10	Good	No	-
11	Good	Yes	~110 mA
12	Good	Yes	~110 mA
13	Good	No	-
14	Good	No	-
15	Good	Yes	~90 mA
16	Good	Yes	~90 mA
17	Good	Yes	~90 mA
18	Good	Yes	~90 mA
19	Good	Yes	~90 mA
20	Good	Yes	~90 mA
21	Good	Yes	~90 mA
22	Good	Yes	~120 mA
23	Good	Yes	~90 mA
24	Unstable	Yes	~90 mA

Spectra can be easily collected from the back facets of the lasers. Fig 5.11 shows the emission spectra from a grating coupler waveguide coupled QCL (#1), a pure Ge waveguide (i.e., edge emitting) coupled QCL (#20), and the reference QCL (#24), which were all measured at the rollover point (~170 mA). One can see that the reference QCL exhibits a standard FP-laser spectrum, which consists of a series of evenly spaced longitudinal modes – a few lines are missing or significantly suppressed due to air absorption. In contrast, the emission spectra of waveguide-coupled QCLs are both affected by the external optical feedback from the waveguide facets, although the facets have been angled to reduce this effect. On the other hand, this was only observed at a certain high current injection level, i.e., close to the rollover.
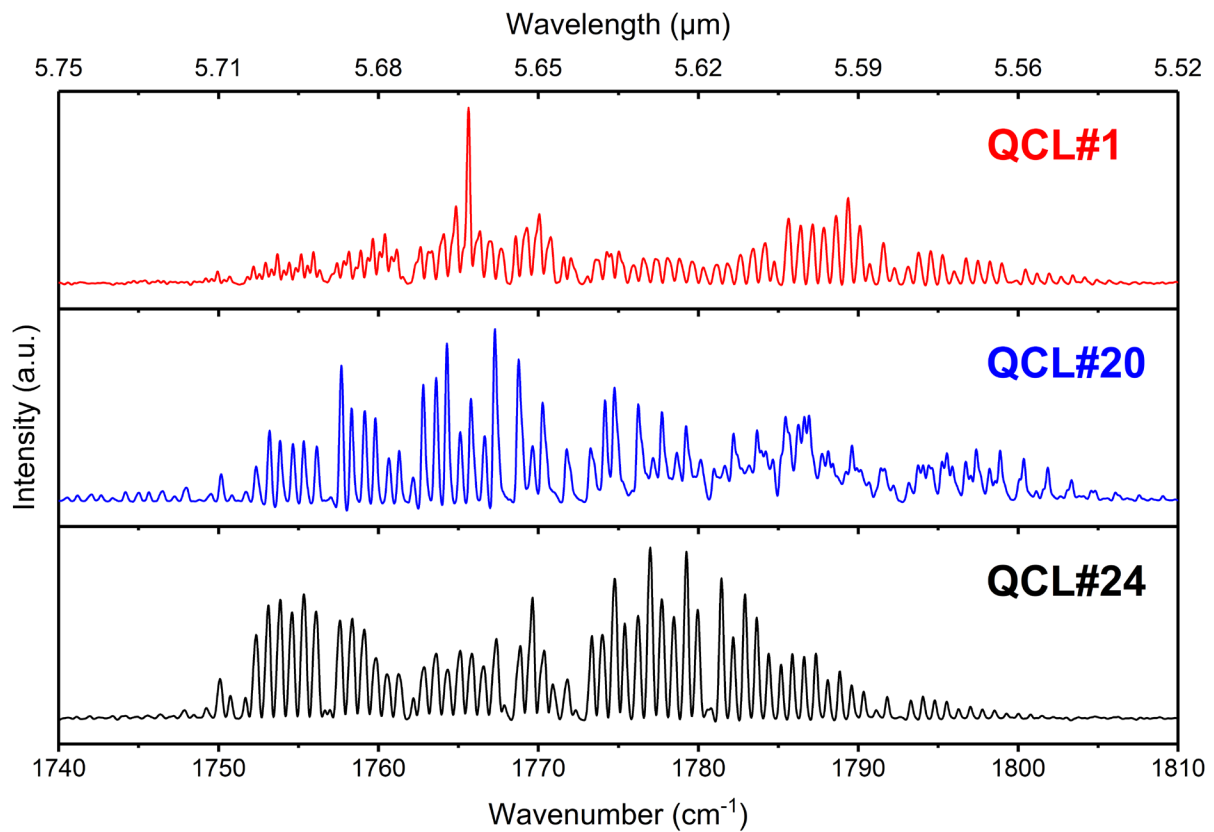
Fig 5.11 Spectra of three QCLs from the integration chip. QCL#1: coupled with Ge waveguide and grating coupler. QCL#20: coupled with pure Ge waveguide. QCL#24: the reference laser.

Due to the fact that the COVID-19 pandemic has significantly delayed the experimental progress, more characterisation works of the Gen 2 integration chip are in progress, i.e., the coupling efficiency of the Ge waveguide. To sum up, the Gen 2 platform design features several improvements – a reduced processing complexity, a lowered cost due to the decreased thickness of precious metal, significantly improved electrical contacts, an improved light coupling efficiency owing to the QCL beam optimisation, and the new compatibility of fibre coupling.

5.3 QCL-Based Polymer Selective Laser Sintering

5.3.1 Background

Additive manufacturing (AM) [40][41], also known as 3D printing, is an emerging manufacturing technology that fundamentally differs from the conventional subtractive manufacturing approach. In AM, components are constructed through layer-by-layer cross-section printing, and therefore, many complex structures that challenge the traditional manufacturing approach could become considerably more manageable in AM. In addition, AM technology features many other advantages such as low material wastage, rapid prototyping, high design freedom, economic small-volume production etc. [42][43]. It has thus attracted the attention of academia and industry.

Commonly used materials in AM are polymers, ceramics, and metals [44]. According to Wohlers Report 2022 [45], the consumption of polymer powder grew by 43.3% in 2021, overtaking photopolymers as the most used AM material for the first time. In the polymer powder bed fusion AM, two typical technologies are the inkjet-based and laser-based sintering processes [46]. The former technology employs radiation-absorbing inks to define the sintering regions, which are then irradiated by an infrared lamp and fused. Representative inkjet processes are the Multi Jet Fusion (MJF) technology [47] from Hewlett-Packard (HP) and the High Speed Sintering technology (HSS) [48] from Voxeljet. On the other hand, laser-based sintering, usually referred to as selective laser sintering (SLS) [49], utilises a high-power CO_2 laser to melt and densify the polymer particles. The laser beam is directable through the built-in optics control, thus realising in-plane selective sintering, as shown in Fig 5.12(a). SLS produces high-quality components while the efficiency is unsatisfactory due to the single dot scanning scheme, i.e., nearly 0D.

One approach to achieve high sintering efficiency while maintaining sintering quality is to deploy a laser array, thus increasing the simultaneous sintering area. In 2018, EOS introduced the LaserProFusion technology [50], where nearly one million laser diodes were integrated to form a giant laser array, as shown in Fig 5.12(c), and the total power was up to 5 kW. The whole cross-section of a component can be sintered at once, similar to a one-off projection, thus achieving ten times faster manufacturing speed than the single CO_2 laser-based SLS. However, no progress is seen after the release of the concept. A much simpler and highly scalable approach is to deploy a row of laser diodes, which is somewhat in between the slow 0D SLS and the radical 2D LaserProFusion, i.e., a 1D array scanning scheme, as shown in Fig 5.12(b). Compared to the LaserProFusion, the missing dimension can be compensated by the in-plane movement. While in contrast to the single dot SLS, the sintering efficiency is improved several times.

(a) 0D-Sintering (b) 1D-Sintering (c) 2D-Sintering
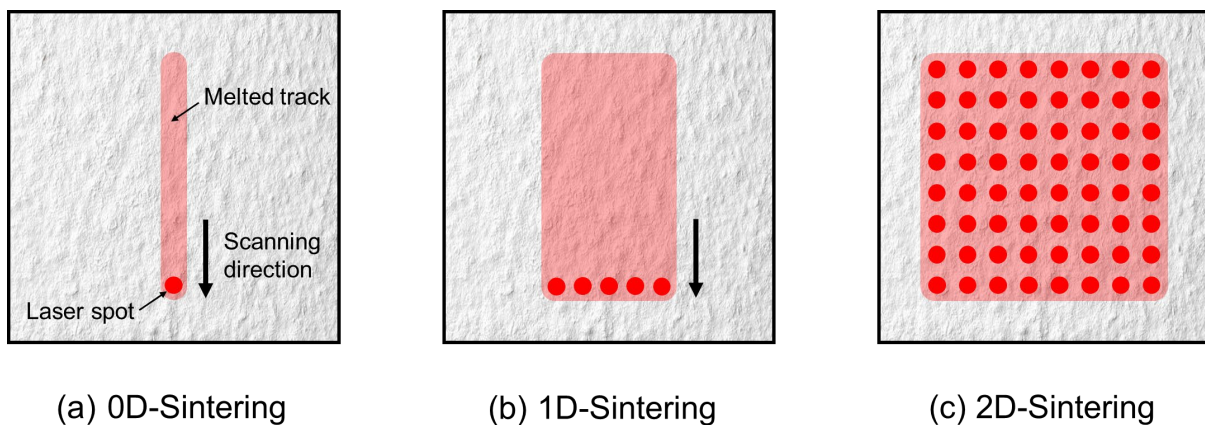
Fig 5.12 Polymer selective laser sintering schemes. (a) Standard SLS. (b) Diode area melting. (c) LaserProFusion.

Such a multi-laser parallel scanning scheme has been successfully demonstrated for AM of metallic powder using 808 nm low-power near-IR laser diodes in Sheffield, namely Diode

Area Melting (DAM) [51]-[53]. Besides, the length of the 1D laser array is extendable by deploying more individually addressable semiconductor lasers. Furthermore, extra laser rows can be added for pre- and post-heating treatments [54]. This is actually considered to be the most significant advantage of the technology rather than efficiency, as the heating/cooling process is much softer and more controllable, resulting in higher melting quality compared to the abrupt heating/cooling process using conventional high-power lasers.

On the other hand, currently, DAM of polymer powders is still limited to the utilisation of carbon black (infrared absorber) since the polymers usually exhibit strong absorptions in mid-IR rather than near-IR, while laser diodes cannot access the mid-infrared region as a result of their interband laser nature. With the addition of carbon black, i.e., an added contaminant, the finally produced components are grey, significantly reducing the manufacturing flexibility. Moreover, if the pure polymer exhibits high intrinsic absorption, i.e., in the mid-IR region, it allows us to add other colours into the feedstock for colourful polymer components manufacturing. In consequence, DAM of pure polymer remains the desired solution.

Fig 5.13 shows the transmission spectra of three common polymers in the mid-IR region, i.e., PEEK, Nylon, and TPE210. We find that TPE210 has an extreme absorption peak at 5.76 μm, which coincidentally matches the emission wavelength of our freshly developed QCL. Thus, the idea to utilise mid-IR QCLs for polymer sintering naturally comes into mind, i.e., combining the DAM scheme with mid-IR QCLs.

Before starting the experimental work, we first estimated the theoretical absorption efficiency by comparing the transmission spectrum of TPE210 with the QCL spectrum, as they are not perfectly matched. Recall that our FP-QCL can operate in two spectral modes – the single frequency mode just above the lasing threshold, and the multimode above the second threshold [55][56], as shown in Fig 5.14(a) and (b).
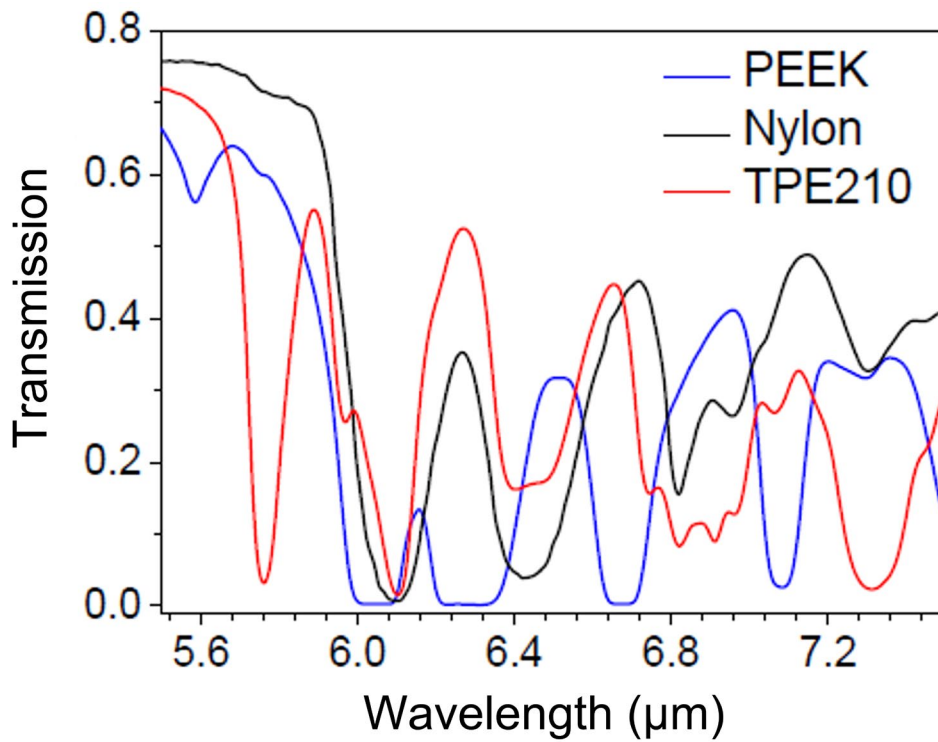
Fig 5.13 Transmission spectra of three common polymers demonstrating strong absorption fingerprint in mid-infrared (PEEK, Nylon, TPE210). Figure courtesy of Dr Dmitry G Revin.
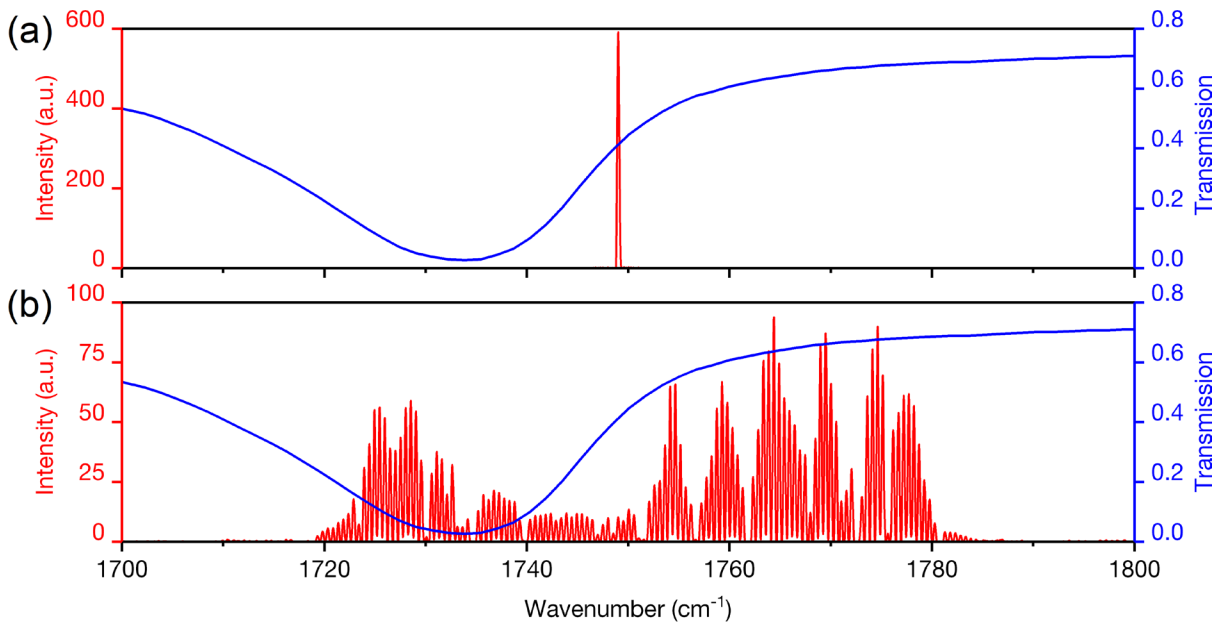
Fig 5.14 QCL spectra and TPE210 transmission spectrum. (a) QCL operates in single mode above the threshold. (b) QCL operates in multimode above the instability threshold.

The transmission (T) of the single mode can be directly read from Fig 5.14(a), i.e., ~0.41. Thus, the absorption efficiency (1–T) is ~59% if neglecting the reflection loss here. In the multimode, i.e., Fig 5.14(b), due to the spectral instability caused by the electron population pulsation and population grating [55][56], one cluster of longitudinal modes moves into the absorption peak of TPE210 while the other cluster shifts to a more transparent region. By integrating the product of the laser spectrum and the transmission spectrum, the overall absorption efficiency is calculated to be ~53.5%, a slightly lowered efficiency but will be compensated with tremendously more radiation power as this only happened at a high current injection level. Consequently, the sintering process is believed to be more effective at higher injection level, despite the quasi-RNGH instability [57][58].

In the next section, the initial experimental setup and results are presented.

5.3.2 Experiments and Results

In this section, we experimentally explored the feasibility of polymer AM using mid-IR QCLs. The schematic diagram of a QCL-based SLS system is shown in Fig 5.15. A 4.5μm×3mm diamond-mounted FP-QCL is positioned on the cooling stage and operating at a constant heatsink temperature of 15°C. For the device performance specs, please refer to Fig 3.23. The output laser beam is first collimated through an AR-coated collimating lens ($f = 1.873\ mm$) and then directed into the vertical down direction by a gold mirror. The vertically collimated beam is further focused by an AR-coated germanium aspherical lens ($f = 12.5\ mm$) at the surface of the powder bed, made from metal. Polymer powdered feedstock will be filled into the powder bed and flattened before sintering. The polymer bed is placed

on a motorised translation stage, which is movable in the xy-plane parallel to the optical bench. Thus, patterns can be engraved on powder by moving the stage. Additionally, we also introduced an in-situ monitoring system in the setup, which is a digital microscope connecting to the computer, with a magnification of up to 1000×. Once laser sintering is finished, the motorised stage will carry the powder bed to the microscope for imaging.
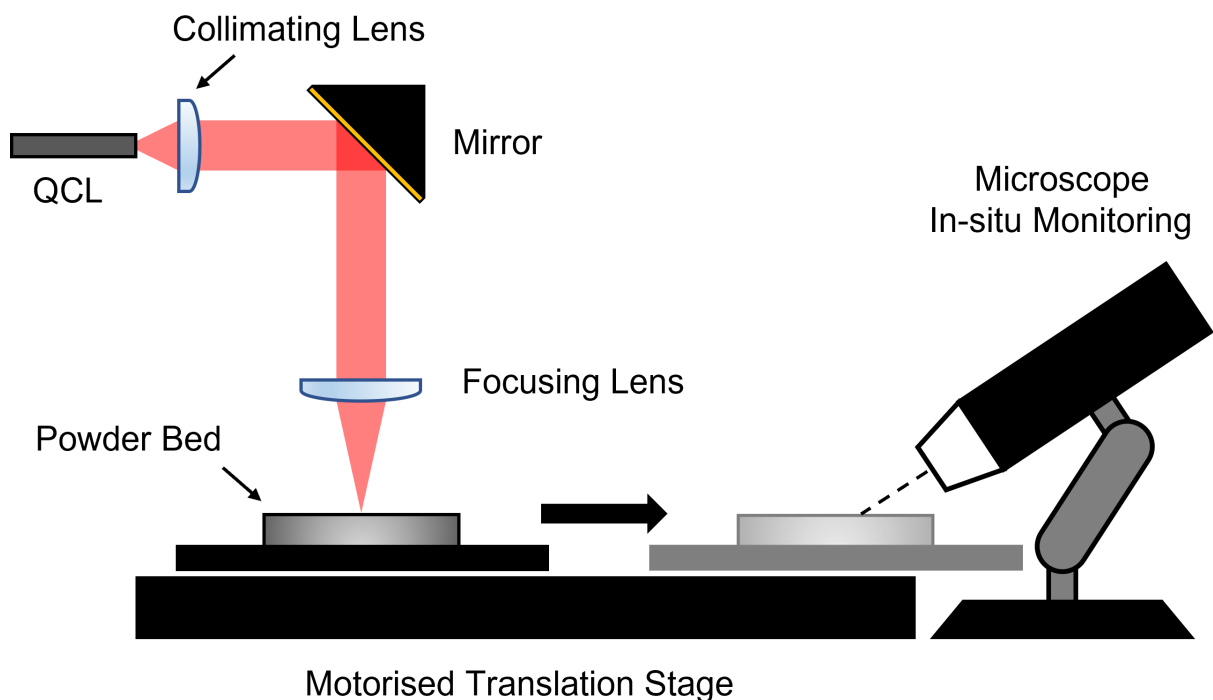
Fig 5.15 Overview of the QCL-based SLS system.

Although the absorption is very high, a typical concern of the experiment is whether the QCL is powerful enough to sinter the powder, especially considering that the conventional CO_2 lasers have watt-level power. Therefore, the focal spot size and delivered optical power are first characterised. As shown in Fig 5.16, the smallest focal spot size measured by the beam profiler is a diameter of ~32 μm at $1/e^2$ of maximum intensity and ~20 μm at FWHM.
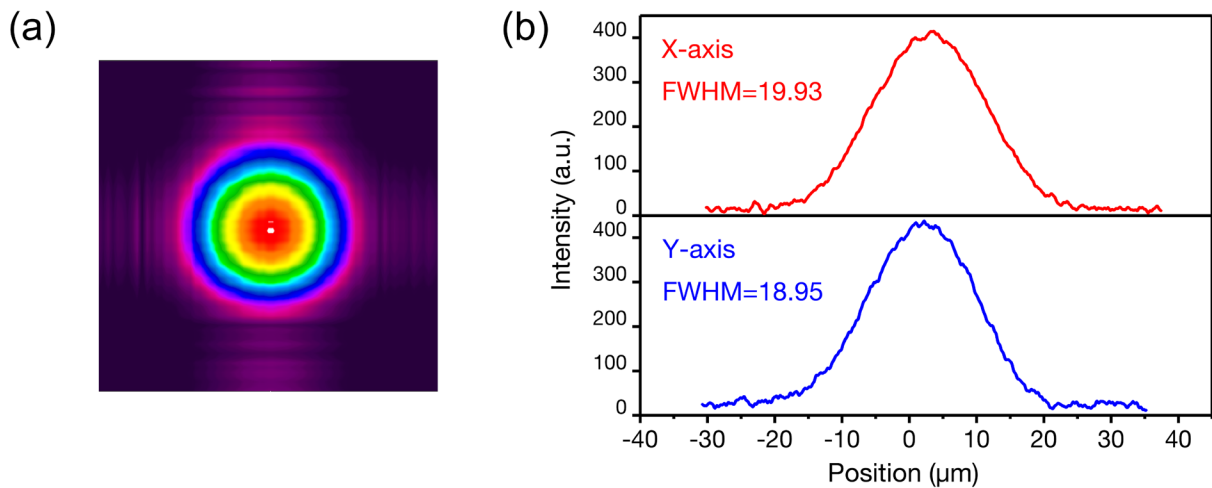
Fig 5.16 (a) Focal spot size measured by beam profiler. (b) Lateral and vertical intensity profile of the spot in (a).

The maximum delivered optical power through a collimating – reflection – focusing optical path is ~50mW at the current injection level of 0.22A, which is ~16mW lower than the power directly measured at the laser facet. This loss is most likely due to the small size of the mirror, considering that the effective reflection area could be smaller than the beam diameter after a rotation of 45°. Therefore, the average power density of the focal spot is estimated to be ~6.22 kW/cm^2. On the other hand, the actual spot size at the powder surface is more difficult to determine because (1) the laser beam is invisible, and (2) the focal length of the germanium aspherical lens is relatively short (i.e., 12.5 mm), and thus a minor change of the distance between the focusing lens and the powder bed can lead to a tens of times bigger spot size.

Finally, based on this experimental setup, we tested QCL polymer sintering with two powders, i.e., TPE210 and Nylon-12 (PA2200). As introduced previously, TPE210 exhibits strong absorption around the wavelength of ~5.7 μm. Nylon powder was mainly tested for contrast, which, in theory, is more transparent to our QCL emission. As a starting point, we

only drew straight tracks across the powder bed, and the two sockets are deposited with TPE210 and nylon powders, respectively, as shown below.
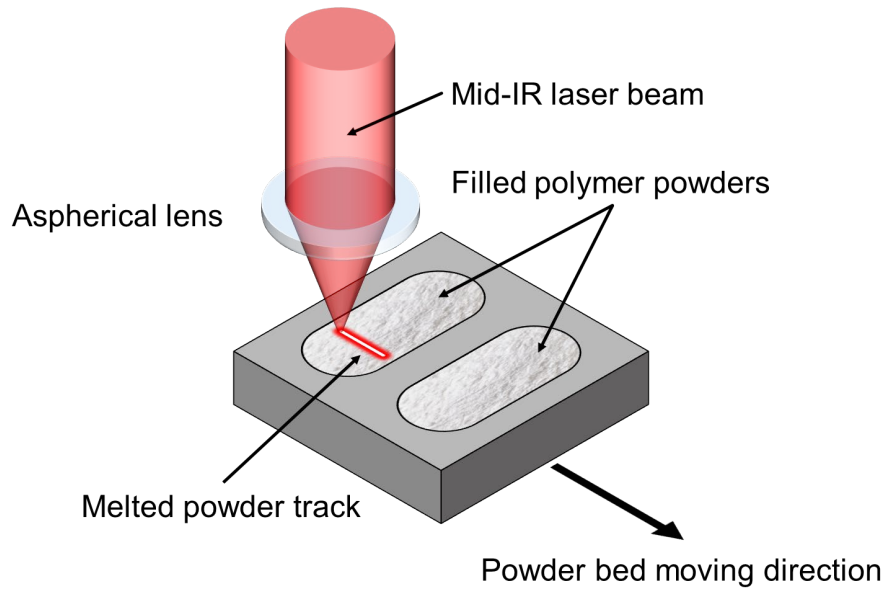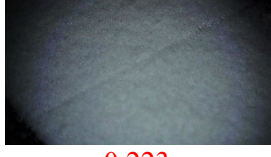
Fig 5.17 Schematic diagram of polymer powder sintering

The powders are sintered with various combinations of scanning speed (1, 2, 3, 4 mm/s) and injection current (0.16, 0.18, 0.20, 0.22 mA), thus forming a 4×4 sintering parameter matrix. The melted tracks imaged by the microscope, accordingly, become the matrix elements, as shown in Tables 5.4 and 5.5. Since the sintering marks in the white polymer powders exhibit super-low colour contrast, all the images are enhanced for clarity. Meanwhile, the linear energy density (LED) is calculated for each matrix element, defined as:

$$LED = \frac{P}{v} \tag{5.1}$$

where P is the sintering power and v is the scanning speed. The values are displayed in the unit of J/cm. The red numbers indicate that a melted track is observed.

Table 5.4 Sintering parameter matrix of TPE210 powder

	1 mm/s	2 mm/s	3 mm/s	4 mm/s
0.22 A	0.500	0.250	0.167	0.125
0.20 A	0.445	0.223	0.148	0.111
0.18 A	0.298	0.149	0.099	0.074
0.16 A	0.160	0.080	0.053	0.040

*Many tracks can be seen above the off-diagonal, where the melting LED >0.148 J/cm.

Table 5.5 Sintering parameter matrix of Nylon-12 powder

	1 mm/s	2 mm/s	3 mm/s	4 mm/s
0.22 A	0.500	0.250	0.167	0.125
0.20 A	0.445	0.223	0.148	0.111
0.18 A	0.298	0.149	0.099	0.074
0.16 A	0.160	0.080	0.053	0.040

*Only two very inconspicuous tracks can be seen at the LED of 0.500 and 0.445 J/cm.

First and foremost, as one can see from the matrices, the ~50 mW QCL is sufficiently powerful for sintering polymer powders. Also, the sintering results are highly consistent with our predictions; the TPE210 powder can be easily sintered at the wavelength of ~5.7 µm thanks to the relatively high absorption and a low melting point (148°C). On the whole, melted tracks can be seen in the top left region where LED > 0.148 J/cm. But, it was noticed that no track is observed in the left bottom box, where the LED is theoretically high enough at 0.160 J/cm. This could be caused by the laser spectral instability – recalling the laser spectrum in Fig 3.23(c), at the injection current of 0.16A, the QCL emits a harmonic-state spectrum, and the primary spectral mode is shifted to the transparent side of the TPE210 absorption spectrum, leading to a decrease in sintering efficiency.

On the other hand, only two ultra-thin and shallow tracks are obtained from the nylon powder, where the sintering energy densities are higher than 0.445 J/cm. In other words, compared to TPE210, nylon powder requires 2× more energy density to be melted due to the much lower absorption at the wavelength of 5.7µm and also the higher melting point (185°C) of the material.

In order to compare the quality of the melted tracks via different sintering parameters, all the samples were extracted from the powder bed and metallised with 200nm thick gold, after which they were sent for SEM imaging. However, it was found that the SEM photo was not ideal for sintering quality comparison, as one can see below. Fig 5.18(a) and (b) are TPE210 components, which are both covered by flakes and thus hard to tell the difference; in contrast, the fused nylon particles are slightly clearer than TPE210, as shown in Fig 5.18(c). Therefore, SEM characterisation seems unsuitable in this case. Differential scanning calorimetry (DSC) [59] will be used to characterise the sintering quality later. Meanwhile, further study of the material property of TPE210 may help us to understand the mechanism behind this.
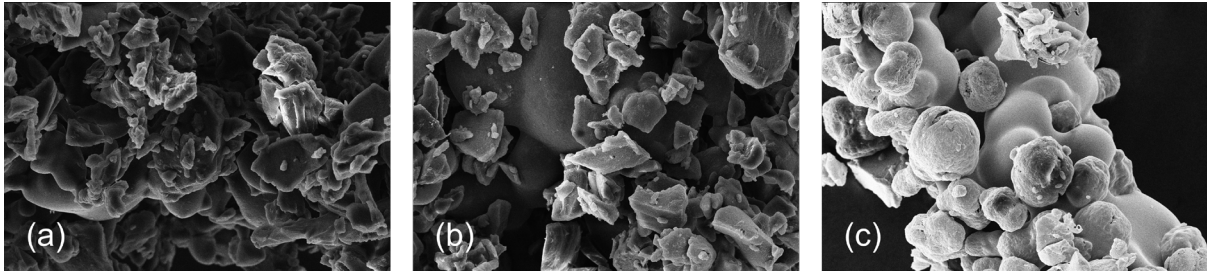
Fig 5.18 (a) and (b) are TPE210 tracks under SEM. (c) Nylon track under SEM

Followed by the single-track sintering, more complex sintering processes were tested, i.e., extending from 1D to 2D. As mentioned above, the motorised translation stage features movability in the xy-plane and is also programmable. We can therefore use the setup to produce 2D sheet parts in arbitrary shapes through software control. The sintering pattern can be directly defined in the commercial software LightBurn [60], specifically designed for laser cutter layout, editing and control. Fig 5.19(a) shows a melted circle pattern (Ø ~7 mm) at the powder surface, sintered in a zigzag routine at a track spacing of 0.25 μm, and the finally obtained sheet component is shown in Fig 5.19(b).
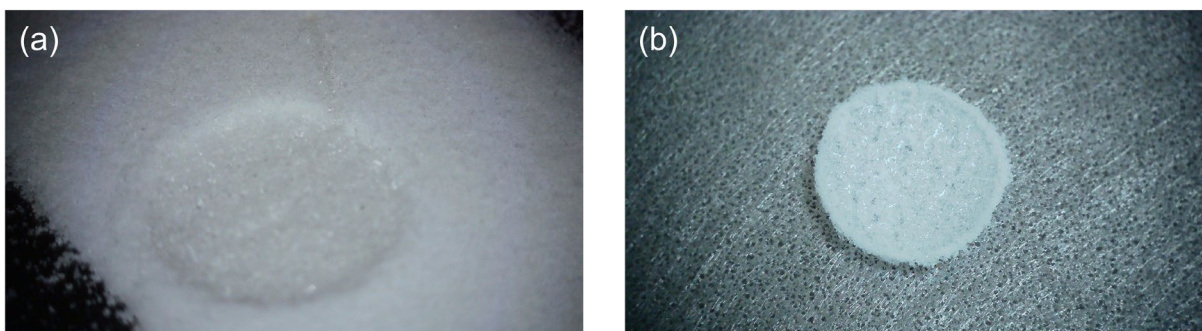
Fig 5.19 (a) Ø~7mm circular pattern sintered by QCL via a single zigzag track on the TPE210 powder. (b) The solid component that extracted from the powder after sintering.

Since the motorised stage only provides free movement in two dimensions, we cannot further extend this sintering process from 2D to 3D based on this setup via layer-by-layer stacking. Nonetheless, after all, we have successfully demonstrated the feasibility of transferring the DAM scheme to polymer AM using mid-infrared quantum cascade lasers. Despite that, the wall-plug efficiency of QCLs can hardly exceed 30% in CW mode [61], while laser diodes typically feature a WPE of up to 50% – 80% [62], the emission wavelength of QCLs can be specifically tailored to match the absorption peaks of polymers and achieve extreme absorptions. For example, a λ ~6.1 µm QCL can melt all three powders in Fig 5.13 with nearly 100% absorption efficiency. Furthermore, the mid-IR spectral range is precisely where QCLs reach their best performance – room temperature (RT) continuous-wave (CW) operation with >100 mW optical power has been demonstrated between 3.8 and 11.5 µm, and even >1 W optical output between 4 and 5 µm [63].

5.4 Summary

Two applications based on the developed mid-IR QCLs were presented in this chapter, i.e., hybrid integration of QCLs on the silicon platform and QCL-based polymer selective laser sintering. Both applications were previously demonstrated with near-IR laser diodes and are now transferred to the mid-IR region using QCLs.

Mid-IR QCLs were integrated on a Ge-on-Si platform for future on-chip sensing applications. The integration technique used in this collaboration project with the University of Southampton is flip-chip bonding with an enhanced z-direction alignment due to the support structures directly processed on the Si substrate. Gen 1 and Gen 2 integrated QCLs were

demonstrated, and the electrical contact was greatly improved on the Gen 2 platform. The QCLs can operate in RT pulsed mode while the emission spectra are influenced by the external optical feedback from the Ge waveguide facet.

The high-speed, low-power laser diode area melting (DAM) technique also has been developed for several years but is limited to metallic powder melting. Due to the nature of interband transition, i.e., cross-bandgap transition, diode lasers cannot access the mid-IR region where polymers exhibit strong absorptions. In this chapter, we demonstrated that mid-IR QCL arrays are feasible to construct a DAM system for high-speed and scalable additive manufacturing of polymer components.

References

[1]   G. T. Reed, W. R. Headley, and C. E. Png, "Silicon photonics: the early years," *SPIE Proceeding*, vol. 5730, 2005.

[2]   S. H. Kim, M. Yokoyama, N. Taoka, R. Iida, S. Lee, R. Nakane, Y. Urabe, N. Miyata, T. Yasuda, H. Yamada, N. Fukuhara, M. Hata, M. Takenaka, and S. Takagi, "Electron Mobility Enhancement of Extremely Thin Body $In_{0.7}Ga_{0.3}As$-on-Insulator Metal–Oxide–Semiconductor Field-Effect Transistors on Si Substrates by Metal–Oxide–Semiconductor Interface Buffer Layers," *Applied Physics Express*, vol. 5, no. 1, p. 014201, 2011.

[3]   K. Tomioka, M. Yoshimura, and T. Fukui, "A III–V nanowire channel on silicon for high-performance vertical transistors," *Nature*, vol. 488, no. 7410, pp. 189–192, 2012.

[4]   E. A. Fitzgerald, Y. H. Xie, M. L. Green, D. Brasen, A. R. Kortan, J. Michel, Y. J. Mii, and B. E. Weir, "Totally relaxed Ge_xSi_{1-x} layers with low threading dislocation densities grown on Si substrates," *Applied Physics Letters*, vol. 59, no. 7, pp. 811–813, 1991.

[5]   M. Tang, S. Chen, J. Wu, Q. Jiang, K. Kennedy, P. Jurczak, M. Liao, R. Beanland, A. Seeds, and H. Liu, "Optimizations of Defect Filter Layers for 1.3-μm InAs/GaAs Quantum-Dot Lasers Monolithically Grown on Si Substrates," *IEEE Journal of Selected Topics in Quantum Electronics*, vol. 22, no. 6, pp. 50–56, 2016.

[6]   M. Yamaguchi, A. Yamamoto, M. Tachikawa, Y. Itoh, and M. Sugo, "Defect reduction effects in GaAs on Si substrates by thermal annealing," *Applied Physics Letters*, vol. 53, no. 23, pp. 2293–2295, 1988.

[7]   S. A. Claussen, K. C. Balram, E. T. Fei, T. I. Kamins, J. S. Harris, and D. A. Miller, "Selective area growth of germanium and germanium/silicon-germanium quantum wells in silicon waveguides for on-chip optical interconnect applications," *Optical Materials Express*, vol. 2, no. 10, pp. 1336–1342, 2012.

[8]   J. Z. Li, J. Bai, J. Park, B. Adekore, K. Fox, M. Carroll, A. Lochtefeld, and Z. Shellenbarger, "Defect reduction of GaAs epitaxy on Si (001) using selective aspect ratio trapping," *Applied Physics Letters*, vol. 91, no. 2, p. 021114, 2007.

[9]   Y. A. Bioud, A. Boucherif, M. Myronov, A. Soltani, G. Patriarche, N. Braidy, M. Jellite, D. Drouin, and R. Arès, "Uprooting defects to enable high-performance III–V optoelectronic devices on Silicon," *Nature Communications*, vol. 10, no. 1, pp. 1–12, 2019.

[10]   D. L. Huffaker, G. Park, Z. Zou, O. B. Shchekin, and D. G. Deppe, "1.3 μm room-temperature GaAs-based quantum-dot laser," *Applied Physics Letters*, vol. 73, no. 18, pp. 2564–2566, 1998.

[11]   S. Chen, W. Li, J. Wu, Q. Jiang, M. Tang, S. Shutts, S. N. Elliott, A. Sobiesierski, A. J. Seeds, I. Ross, P. M. Smowton, and H. Liu, "Electrically pumped continuous-wave III–V quantum dot lasers on silicon," *Nature Photonics*, vol. 10, no. 5, pp. 307–311, 2016.

[12]   U. Gösele and Q. Tong, "SEMICONDUCTOR WAFER BONDING," *Annual Review of Materials Science*, vol. 28, no. 1, pp. 215–241, 1998.

[13]   C. Gui, M. Elwenspoek, N. Tas, and J. G. Gardeniers, "The effect of surface roughness on direct wafer bonding," *Journal of Applied Physics*, vol. 85, no. 10, pp. 7448–7454, 1999.

[14] F. Niklaus, G. Stemme, J. Lu, and R. J. Gutmann, "Adhesive wafer bonding," *Journal of Applied Physics*, vol. 99, no. 3, p. 031101, 2006.

[15] S. Keyvaninia, M. Muneeb, S. Stanković, P. J. Van Veldhoven, D. Van Thourhout, and G. Roelkens, "Ultra-thin DVS-BCB adhesive bonding of III-V wafers, dies and multiple dies to a patterned silicon-on-insulator substrate," *Optical Materials Express*, vol. 3, no. 1, pp. 35–46, 2013.

[16] M. A. Meitl, Z. Zhu, V. Kumar, K. J. Lee, X. Feng, Y. Y. Huang, I. Adesida, R. G. Nuzzo, and J. A. Rogers, "Transfer printing by kinetic control of adhesion to an elastomeric stamp," *Nature Materials*, vol. 5, no. 1, pp. 33–38, 2005.

[17] R. S. Cok, M. Meitl, R. Rotzoll, G. Melnik, A. Fecioru, A. J. Trindade, B. Raymond, S. Bonafede, D. Gomez, T. Moore, C. Prevatte, E. Radauscher, S. Goodwin, P. Hines, and C. A. Bower, "Inorganic light-emitting diode displays using micro-transfer printing," *Journal of the Society for Information Display*, vol. 25, no. 10, pp. 589–609, 2017.

[18] T. Wu, C. Sher, Y. Lin, C. Lee, S. Liang, Y. Lu, S. Chen, W. Guo, H. Kuo, and Z. Chen, "Mini-LED and Micro-LED: Promising Candidates for the Next Generation Display Technology," *Applied Sciences*, vol. 8, no. 9, p. 1557, 2018.

[19] X. Zhou, P. Tian, C. Sher, J. Wu, H. Liu, R. Liu, and H. Kuo, "Growth, transfer printing and colour conversion techniques towards full-colour micro-LED display," *Progress in Quantum Electronics*, vol. 71, p. 100263, 2020.

[20] J. H. Lau, "Recent Advances and New Trends in Flip Chip Technology," *Journal of Electronic Packaging*, vol. 138, no. 3, p. 030802, 2016.

[21]   E. M. Davis, W. E. Harding, R. S. Schwartz, and J. J. Corning, "Solid Logic Technology: Versatile, High-Performance Microelectronics," *IBM Journal of Research and Development*, vol. 8, no. 2, pp. 102–114, 1964.

[22]   J. Zhang, G. Muliuk, J. Juvert, S. Kumari, J. Goyvaerts, B. Haq, C. Op de Beeck, B. Kuyken, G. Morthier, D. Van Thourhout, R. Baets, G. Lepage, P. Verheyen, J. Van Campenhout, A. Gocalinska, J. O'Callaghan, E. Pelucchi, K. Thomas, B. Corbett, A. J. Trindade, and G. Roelkens, "III-V-on-Si photonic integrated circuits realized using micro-transfer-printing," *APL Photonics*, vol. 4, no. 11, p. 110803, 2019.

[23]   A. Spott, J. Peters, M. L. Davenport, E. J. Stanton, C. D. Merritt, W. W. Bewley, I. Vurgaftman, C. S. Kim, J. R. Meyer, J. Kirch, L. J. Mawst, D. Botez, and J. E. Bowers, "Quantum cascade laser on silicon," *Optica*, vol. 3, no. 5, pp. 545–551, 2016.

[24]   A. Spott, J. Peters, M. Davenport, E. Stanton, C. Zhang, C. Merritt, W. Bewley, I. Vurgaftman, C. Kim, J. Meyer, J. Kirch, L. Mawst, D. Botez, and J. Bowers, "Heterogeneously Integrated Distributed Feedback Quantum Cascade Lasers on Silicon," *Photonics*, vol. 3, no. 2, p. 35, 2016.

[25]   A. Spott, E. J. Stanton, A. Torres, M. L. Davenport, C. L. Canedy, I. Vurgaftman, M. Kim, C. S. Kim, C. D. Merritt, W. W. Bewley, J. R. Meyer, and J. E. Bowers, "Interband cascade laser on silicon," *Optica*, vol. 5, no. 8, pp. 996–1005, 2018.

[26]   H. Nguyen-Van, A. N. Baranov, Z. Loghmari, L. Cerutti, J. Rodriguez, J. Tournet, G. Narcy, G. Boissier, G. Patriarche, M. Bahriz, E. Tournié, and R. Teissier, "Quantum cascade lasers grown on silicon," *Scientific Reports*, vol. 8, no. 1, pp. 1–8, 2018.

[27]   S. Jung, J. Kirch, J. H. Kim, L. J. Mawst, D. Botez, and M. A. Belkin, "Quantum cascade lasers transfer-printed on silicon-on-sapphire," *Applied Physics Letters*, vol. 111, no. 21, p. 211102, 2017.

[28] G. Sun, H. H. Cheng, J. Menéndez, J. B. Khurgin, and R. A. Soref, "Strain-free Ge∕GeSiSn quantum cascade lasers based on L-valley intersubband transitions," *Applied Physics Letters*, vol. 90, no. 25, p. 251105, 2007.

[29] T. Grange, D. Stark, G. Scalari, J. Faist, L. Persichetti, L. Di Gaspare, M. De Seta, M. Ortolani, D. J. Paul, G. Capellini, S. Birner, and M. Virgilio, "Room temperature operation of n-type Ge/SiGe terahertz quantum cascade lasers predicted by non-equilibrium Green's functions," *Applied Physics Letters*, vol. 114, no. 11, p. 111102, 2019.

[30] G. Dehlinger, L. Diehl, U. Gennser, H. Sigg, J. Faist, K. Ensslin, Grützmacher D., and Müller E., "Intersubband Electroluminescence From Silicon-Based Quantum Cascade Structures," *Science*, vol. 290, no. 5500, pp. 2277–2280, 2000.

[31] I. Bormann, K. Brunner, S. Hackenbuchner, G. Zandler, G. Abstreiter, S. Schmult, and W. Wegscheider, "Midinfrared intersubband electroluminescence of Si/SiGe quantum cascade structures," *Applied Physics Letters*, vol. 80, no. 13, pp. 2260–2262, 2002.

[32] S. A. Lynch, R. Bates, D. J. Paul, D. J. Norris, A. G. Cullis, Z. Ikonic, R. W. Kelsall, P. Harrison, D. D. Arnone, and C. R. Pidgeon, "Intersubband electroluminescence from Si/Sige cascade emitters at terahertz frequencies," *Applied Physics Letters*, vol. 81, no. 9, pp. 1543–1545, 2002.

[33] R. Bates, S. A. Lynch, D. J. Paul, Z. Ikonic, R. W. Kelsall, P. Harrison, S. L. Liew, D. J. Norris, A. G. Cullis, W. R. Tribe, and D. D. Arnone, "Interwell intersubband electroluminescence from Si/SiGe quantum cascade emitters," *Applied Physics Letters*, vol. 83, no. 20, pp. 4092–4094, 2003.

[34] C. J. Mitchell, K. Li, R. Schachler, A. Khokhar, X. Chen, S. Stankovic, X. Wang, N. P. Sessions, K. M. Grabska, D. J. Thomson, C. Daedlow, G. T. Reed, and J. S. Wilkinson, "Tooling and procedures for hybrid integration of lasers by flip-chip technology," *2020 IEEE 8th Electronics System-Integration Technology Conference (ESTC)*, pp. 1–7, 2020.

[35] R. A. Soref, S. J. Emelett, and W. R. Buchwald, "Silicon waveguided components for the long-wave infrared region," *Journal of Optics A: Pure and Applied Optics*, vol. 8, no. 10, pp. 840–848, 2006.

[36] U. Younis, X. Luo, B. Dong, L. Huang, S. K. Vanga, A. E. Lim, P. G.-Q. Lo, C. Lee, A. A. Bettiol, and K. Ang, "Towards low-loss waveguides in SOI and Ge-on-SOI for mid-IR sensing," *Journal of Physics Communications*, vol. 2, no. 4, p. 045029, 2018.

[37] Fintech Fineplacer® Lambda 2: https://www.finetech.de/products/finetech-product-overview/sub-micron-bonder-lambda2/

[38] Fintech Fineplacer® Femto 2: https://www.finetech.de/products/finetech-product-overview/automated-die-bonder-for-prototype-and-production-fineplacer-femto2/

[39] M. Nedeljkovic, J. S. Penades, C. J. Mitchell, A. Z. Khokhar, S. Stankovic, T. D. Bucio, C. G. Littlejohns, F. Y. Gardes, and G. Z. Mashanovich, "Surface-Grating-Coupled Low-Loss Ge-on-Si Rib Waveguides and Multimode Interferometers," *IEEE Photonics Technology Letters*, vol. 27, no. 10, pp. 1040–1043, 2015.

[40] K. V. Wong and A. Hernandez, "A review of additive manufacturing," *ISRN Mechanical Engineering*, vol. 2012, pp. 1–10, 2012.

[41] I. Gibson, D. W. Rosen, B. Stucker, M. Khorasani, D. Rosen, B. Stucker, and M. Khorasani, *Additive Manufacturing Technologies*. Cham, Switzerland: Springer, 2020.

[42]   S. Ford and M. Despeisse, "Additive Manufacturing and sustainability: An exploratory study of the advantages and challenges," *Journal of Cleaner Production*, vol. 137, pp. 1573–1587, 2016.

[43]   M. Attaran, "The rise of 3-D printing: The advantages of additive manufacturing over traditional manufacturing," *Business Horizons*, vol. 60, no. 5, pp. 677–688, 2017.

[44]   D. Bourell, J. P. Kruth, M. Leu, G. Levy, D. Rosen, A. M. Beese, and A. Clare, "Materials for additive manufacturing," *CIRP Annals*, vol. 66, no. 2, pp. 659–681, 2017.

[45]   Wohlers Report 2022: https://wohlersassociates.com/press-releases/wohlers-report-2022-finds-strong-industry-wide-growth/

[46]   S. F. Shirazi, S. Gharehkhani, M. Mehrali, H. Yarmand, H. S. Metselaar, N. Adib Kadri, and N. A. Osman, "A review on powder-based additive manufacturing for tissue engineering: Selective Laser Sintering and Inkjet 3D printing," *Science and Technology of Advanced Materials*, vol. 16, no. 3, p. 033502, 2015.

[47]   Multi Jet Fusion: https://www.hp.com/uk-en/printers/3d-printers/products/multi-jet-technology.html

[48]   High Speed Sintering: https://www.voxeljet.com/case-studies/consumer-goods/hp-multi-jet-fusion-and-voxeljet-high-speed-sintering-in-comparison/

[49]   R. Brighenti, M. P. Cosma, L. Marsavina, A. Spagnoli, and M. Terzano, "Laser-based additively manufactured polymers: A review on processes and mechanical models," *Journal of Materials Science*, vol. 56, no. 2, pp. 961–998, 2020.

[50]   EOS   LaserProFusion: https://www.eos.info/en/innovations/3d-printing-of-the-future/laserpro-fusion

[51] M. Zavala-Arredondo, N. Boone, J. Willmott, D. T. D. Childs, P. Ivanov, K. M. Groom, and K. Mumtaz, "Laser diode area melting for high speed additive manufacturing of metallic components," *Materials and Design*, vol. 117, pp. 305–315, 2017.

[52] M. Zavala-Arredondo, K. M. Groom, and K. Mumtaz, "Diode area melting single-layer parametric analysis of 316l stainless steel powder," *The International Journal of Advanced Manufacturing Technology*, vol. 94, pp. 2563–2576, 2017.

[53] M. Zavala-Arredondo, H. Ali, K. M. Groom, and K. Mumtaz, "Investigating the melt pool properties and thermal effects of multi-laser diode area melting," *The International Journal of Advanced Manufacturing Technology*, vol. 97, pp. 1383–1396, 2018.

[54] M. Alsaddah, A. Khan, K. Groom, and K. Mumtaz, "Diode area melting of Ti6Al4V using 808 nm laser sources and variable multi-beam profiles," *Materials and Design*, vol. 215, p. 110518, 2022.

[55] C. Y. Wang, L. Diehl, A. Gordon, C. Jirauschek, F. X. Kärtner, A. Belyanin, D. Bour, S. Corzine, G. Höfler, M. Troccoli, J. Faist, and F. Capasso, "Coherent instabilities in a semiconductor laser with fast gain recovery," *Physical Review A*, vol. 75, no. 3, p. 031802(R), 2007.

[56] A. Gordon, C. Y. Wang, L. Diehl, F. X. Kärtner, A. Belyanin, D. Bour, S. Corzine, G. Höfler, H. C. Liu, H. Schneider, T. Maier, M. Troccoli, J. Faist, and F. Capasso, "Multimode regimes in quantum cascade lasers: From coherent instabilities to spatial hole burning," *Physical Review A*, vol. 77, no. 5, p. 053804, 2008.

[57]   H. Risken and K. Nummedal, "Self-pulsing in lasers," *Journal of Applied Physics*, vol. 39, no. 10, pp. 4662–4672, 1968.

[58]   R. Graham and H. Haken, "Quantum theory of light propagation in a fluctuating laser-active medium," *Zeitschrift für Physik A Hadrons and nuclei*, vol. 213, no. 5, pp. 420–450, 1968.

[59]   G. W. H. Höhne, W. F. Hemminger, and H. J. Flammersheim, *Differential Scanning Calorimetry*. Berlin: Springer, 2003.

[60]   LightBurn software: https://lightburnsoftware.com/

[61]   F. Wang, S. Slivken, D. H. Wu, and M. Razeghi, "Room temperature quantum cascade lasers with 22% wall plug efficiency in continuous-wave operation," *Optics Express*, vol. 28, no. 12, p. 17532, 2020.

[62]   J. Lawrence, *Advances in Laser Materials Processing: Technology, Research and Applications*. Duxford: Woodhead Publishing, an imprint of Elsevier, 2018.

[63]   Centre for Quantum Devices (CQD): http://cqd.ece.northwestern.edu/research/qcl.php

6 Conclusion and Future Work

6.1 Conclusion

The thesis presented the journey of developing a mid-IR quantum cascade laser (mid-IR QCL) with the aim of hybrid integration on the germanium-on-silicon (Ge-on-Si) platform. Mid-IR coherent sources are particularly attractive for sensing applications since a large number of molecules have their fundamental vibrational transitions lying in this region, which thus features strong and unique absorptions. For this reason, the mid-IR region is also known as the 'fingerprint' region. The motivation towards III-V on Si is simple: conventional sensing systems are bulky and high-cost; if all the components (electronics, photonics, waveguides etc.) could be integrated at the wafer scale via a high throughput manner, i.e., an on-chip sensing system, we can then obtain a compact size, portable, high energy efficiency, ultra-fast, and low-cost device and make the life more manageable. In this story, we explored the integration of QCLs on silicon via a scalable flip-chip bonding approach with enhanced vertical alignment.

Chapter 3 was dedicated to device development, starting from wafer growth. First, four mid-IR QCL wafers based on strain compensated $In_{0.6}Ga_{0.4}As/Al_{0.58}In_{0.42}As$ material system on InP substrate were grown by metal-organic vapour phase epitaxy (MOVPE), namely MR3877, MR3879, MR4241, and MR4243. The QCL adopts a classical two-phonon resonance active region design with a designed emission wavelength of ~5.4 μm. The raw wafers were then fabricated into double-trench ridge waveguide QCLs, and the actual

emission wavelength is between 5.5 and 5.7 μm due to the graded heterointerfaces. It was found that only MR4243 QCLs achieved room-temperature (RT) continuous-wave (CW) operation. In the high-temperature test, an 8μm×2mm device epi-layer up mounted on diamond remains operating in CW mode at 65°C with ~15 mW total output with an estimated T_0 value of 124 K. Despite the excellent performance, the device suffers from the beam steering problem caused by multiple transverse modes coupling. Since the laser is mainly developed for waveguide coupling on the silicon substrate, high beam quality is critically required. Therefore, to resolve this issue, the relationship between the transverse mode threshold gain and the laser core width was studied in the software Lumerical. It was found that ridge lasers always favour higher-order transverse mode operation mainly due to their lower mirror loss than the fundamental mode TM00. The simulation and analysis indicated that 5μm was the optimal width for this QCL. Finally, we fabricated 5μm QCLs. Due to the fabrication error, the actual device was 4.5μm wide, and the output beam was virtually circular. For a 3mm long uncoated device mounted on the diamond, the threshold current density in RT CW mode was as low as 1 kA/cm^2.

In Chapter 4, the spectral mode and spatial mode instabilities observed during the development of the QCL were mainly discussed. The spectral instability mainly refers to the splitting spectrum, which is caused by Rabi oscillation, i.e., oscillation of the population inversion. However, in contrast to the regular Rabi spectrum predicted in the ring cavity laser, where two side modes detuned from the primary mode by the Rabi frequency rise, the central mode in FP-QCLs is wholly suppressed. This is due to the co-existing spatial hole burning effect. The carrier diffusion is too slow compared to the QCL gain recovery time, which is at the picosecond level; therefore, FP-QCLs suffer from severe spatial burning. The spatial mode instability is the most interesting observation from the laser characterisation. It was observed that in CW mode, the multi-transverse mode synchronisation could eliminate

the spectral multimode instability and stabilise the QCL in single-frequency. This is supposed to be caused by the nonlinear coupling of three transverse modes via a four-wave mixing (FWM) process. Besides, in the synchronised mode, the QCL exhibits optical bistability. This is explained as a result of the Kerr lensing effect, which led to an increase in net laser gain at a high current injection level, i.e., a high intracavity intensity.

Chapter 5 presented the final applications based on the developed mid-IR QCL, i.e., hybrid integration of QCL on silicon coupled with germanium waveguides and QCL-based polymer selective laser sintering (SLS). This flip-chip integration method directly processes support structures on the silicon substrate to underpin the face-down laser chip. Therefore, the vertical misalignment is no longer introduced by the bonder machine but by the etching accuracy, which is at the order of 10nm, thus significantly increasing the vertical alignment accuracy. The Gen 1 Ge-on-Si platform shows problematic electrical contacts between the QCLs and the bond pads on Si and a very weak waveguide transmission due to the use of beam steering QCLs. The Gen 2 platform features simplified processing and greatly improved electrical contacts. With the beam-optimised QCLs, we would expect a significantly improved waveguide coupling efficiency as compared to Gen 1 and the characterisation work is in progress. We also demonstrated QCL-based selective laser sintering of polymer (TPE210). The relatively low power is sufficient to melt the polymers due to the high absorption and low melting point. Sheet TPE210 components were printed using the prototype setup. It is therefore validated that a QCL-based polymer diode area melting (DAM) system is possible.

6.2 Future Work

Despite the progress made in the past years, as summarised above, we are still in the early stage of the journey. There remains a great deal of work to be done, such as (1) laser performance improvement, (2) further learning and confirming the nature of multi-transverse mode synchronisation in CW mode, and (3) the next step of QCL-based applications. Future works corresponding to these three directions are suggested below.

First, there remains tremendous space to further improve the laser performance, mainly regarding output power and spectral mode control. The best performance devices we used in this thesis are uncoated ridge waveguide FP-QCLs, and epi-layer up mounted on the diamond. Commonly used approaches to improving laser output power are optimisation of thermal management and decrement of optical loss. Better thermal management can be achieved by improving the laser packaging, which includes but is not limited to a thicker top contact gold layer, thinner substrate thickness, InP lateral growth (buried-heterostructure) and epi-layer down mounting. Optical loss can be further reduced by applying HR coating at the laser back facet and increasing the cavity length. Considering that ~1 kA/cm^2 RT CW threshold current density and ~100 mW RT CW power are achieved in such a conventional package, the potential of the wafer is enormous.

In addition, QCL with a single longitudinal mode and wavelength tuneability would be the ideal choice for our applications, especially for selective laser sintering (SLS). As described in the previous chapter, the emission spectrum of our FP-QCL does not perfectly match the absorption peak of TPE210 at 5.76 μm, resulting in ~50–60% absorption efficiency. Therefore, future spectral mode control is necessary, which can be realised by employing distributed feedback grating structures in the waveguide (DFB-QCL) or an external cavity (EC-QCL). EC-QCLs typically have tens of times broader tuneable range than DFB-QCLs,

but the bulky size of the whole setup is not desired in our applications. Since we expect to eventually build QCL arrays for polymer diode area melting (DAM), compact-size lasers are required. Thus, a buried grating structure that can stabilise the longitudinal mode at 5.76 μm would be sufficient. Also, individual chips are favoured by hybrid integration and on-chip sensing. Therefore, DFB-QCL is the better choice in both cases, and the emission wavelength can be tuned electrically or thermally in a limited range.

Second, we observed multi-transverse mode synchronisation in QCL CW mode operation, which resulted in a fantastic single-frequency operation. Theoretical analysis is considered to be necessary for the future. Another fact is that this $\lambda \sim 5.7\mu m$ QCL is very close to the zero GVD (group velocity dispersion) point of InP, i.e., 5.5 μm, whilst whether this plays a role in this ultimate multi-transverse mode synchronisation remains a question. Therefore, it would be interesting to estimate the effective GVD of the waveguide via the subthreshold spectrum. Once we are more explicit about its nature, we can further look at its universality as it is now only observed from one wafer. If it can be applied to other devices with different emission wavelengths, utilising multi-transverse mode coupling would be a third way to realise high-power single-frequency QCLs other than DFB- and EC-QCLs, of course, at the cost of a steered beam.

The final discussion is on the QCL-based applications. The primary purpose of the hybrid integration project is to explore a scalable hybrid integration method. The vertical alignment error has been reduced to 10nm in the present technique. One approach to completely eradicate the misalignment error is introducing an etch stop layer underneath the QCL active region during growth. In that case, the support structures' height will remain at the wafer surface, i.e., unetched, and the QCL ridge trenches will be etched to the designed depth, i.e., to the etch stop. Thus, once the unprocessed support structure contacts the etch stop layer, no misalignment would occur. Besides, as the Ge-on-Si platform is transparent up to $\lambda \sim 15$ μm,

we could develop longer wavelength QCLs for sensing applications. For example, the wavelength of ~9 µm is promising for drug sensing.

In Chapter 5, we verified the feasibility of a QCL-based selective laser sintering system for AM of polymer components by investigating the processing of a single track using a single free-space QCL. A future extension to an array-based processing scheme similar to DAM would then require the fibre-coupling of individual QCLs and a suitable method/assembly to collimate and focus light onto the powder bed. One critical issue would be the unavailability of low-cost off-the-shelf optical components for the mid-IR, e.g., mid-IR fibre/lens. In addition to this, DFB-QCLs are also necessary to realise precisely wavelength-matched polymer selective laser sintering.